Nonlinear Large Amplitude Structural and Aeroelastic Behavior of Composite Rotor Blades at Large Static Deflection

by

Taehyoun Kim

B.S., M.E. Ajou University (1981, 1983)

M.S. The University of Texas at Austin (1987)

SUBMITTED TO THE DEPARTMENT OF AERONAUTICS AND ASTRONAUTICS IN PARTIAL FULFILLMENT OF THE REQUIREMENTS FOR THE DEGREE OF

Doctor of Philosophy

in

Aeronautics and Astronautics

at the

Massachusetts Institute of Technology

June, 1992

Signature of Author _____

Department of Aeronautics and Astronautics

May 22, 1992

Certified by _____

Professor John Dugundji

Thesis Committee Chairman, Department of Aeronautics and Astronautics

Certified by _____

Professor Norman D. Ham

Department of Aeronautics and Astronautics

Certified by _____

Professor Paul A. Lagace

Department of Aeronautics and Astronautics

Accepted by _____

Professor Harold Y. Wachman

Chairman, Department Graduate Committee

Nonlinear Large Amplitude Structural and Aeroelastic Behavior of Composite Rotor Blades at Large Static Deflection

Taehyoun Kim

SUBMITTED TO THE DEPARTMENT OF AERONAUTICS AND ASTRONAUTICS ON MAY 22, 1992 IN PARTIAL FULFILLMENT OF THE REQUIREMENTS FOR THE DEGREE OF DOCTOR OF PHILOSOPHY

Abstract

The nonlinear, large amplitude structural and aeroelastic behavior of composite rotor blades under large static deflection is investigated. A new structural model capable of handling large amplitude vibrations about large static deflections was developed, based on the previous work by Minguet and Dugundji. The model can deal with large displacements and rotations by use of Euler angles and can account for various structural couplings. The inertial model includes inertial loads due to linear and angular accelerations, centrifugal and Coriolis accelerations. The nonlinear dynamic stall was included by use of the ONERA Model. A Newton-Raphson type iterative solution technique based on numerical integration of the basic large deflection equations along with harmonic balance method is seen efficient for the present rotor blade analysis. Two different lay-ups, $[0/90]_{3s}$ and $[45/0]_s$, of graphite/epoxy beams have been selected to demonstrate the large amplitude analysis. First, the large amplitude nonrotating and rotating free vibration characteristics of the first and second bending, the first fore-and aft, and the first torsional modes are presented for varying tip static deflections and amplitudes. Both large static deflection and large amplitudes affect the fore-and-aft and torsion modes significantly, but bending modes are not influenced much by the geometrical nonlinearities. Nonrotating free vibration experiments have been performed on several different lay-ups of composite blades, and the results showed good agreement with theory. Next, large amplitude aeroelastic limit cycle analysis was performed on two-bladed models with $[0/90]_{3s}$ and $[45/0]_s$ lay-ups. Numerical results indicate that the dynamic stall is dominant in moderate range of amplitudes, but the nonlinear static-dynamic couplings in the structure, which brings much softening effects, could be equally important in large amplitude ranges.

Thesis Committee Chairman: Dr. John Dugundji
Professor
Department of Aeronautics and Astronautics

Acknowledgement

The author wishes to express much gratitude to those who supported my study at M.I.T. during the past few years. The first and the most important of all is my advisor, Professor John Dugundji, for all his insights and care, which he laid upon me with such patience and humanity. These years that I spent with him will always remain as great inspiration and encouragement in my career, and my life in general. My next gratitude goes to my thesis committee member Professor Norman Ham for his helpful suggestions and guidance during the course of my thesis work. I remember much joy and excitement that was created during each and every talk with him, technical or of human vs. human nature. I would also like to thank my third thesis committee member, Professor Paul Lagace, for his comments and careful examination of the technical quality of my thesis, and, of course, for supporting me during my first year at M.I.T..

A great deal of appreciation must go to Professor VanderVelde, who, through the Teaching Assistantship for the Multivariable Control System 1 & 2, made it possible for me to complete my thesis during the last two years. Words of thanks are also made to the following people: The members of TELAC, particularly those in room 41-317, Al Supple for his technical supports during the experimentation, and various members of the Korean Beacon Church at Harvard for their friendship and encouragement.

My deepest gratitude to my grandmother, my parents, and my brothers for their love and encouragements, and above all, my wife Sung and my son "little" Eric for their love and support throughout these difficult years. Sung has been and always will be a marvelous woman to me, and I simply don't know how to measure her enormous value in my life. My thesis righteously belongs to her.

Foreword

This research was performed in the Technology Laboratory for Advanced Composite (TELAC) of the Department of Aeronautics and Astronautics at the Massachusetts Institute of Technology, and was partially supported under U.S. Army Research Office contract DAAL03-87-K-0024, with Dr. Gary Anderson as Technical Monitor.

All of the computer codes that have been programmed and used for the present research can be found in a forthcomming TELAC Report, No. 92-4.

Contents

List of Figures

Nomenclature

A	Beam cross-sectional area
b	Semi-chord
c	Chord
C_L, C_M, C_D	Aerodynamic lift, moment, and drag coefficient
ΔC_z	Deviation of actual static lift or moment curve from linear static lift or moment
ΔC_D	Deviation of actual static drag curve from linear static drag
$[E]$	Beam stress-strain stiffness matrix
E	Young's modulus
$\underline{e}$	Hinge off-set
e_a	Distance between the reference line and the aerodynamic center
$\vec{F}_G$	Force resultant vector in global axes, x, y, z
$\vec{F}_L$	" " " " local axes, ξ, η, ζ
F_1, F_2, F_3	Force resultant components in local axes
F_x, F_y, F_z	" " " in global axes
F_{NC}, F_C	Noncirculatory and circulatory loads
f_{wi}	Beam bending modes
f_θ	Beam torsion modes
G	Shear modulus
g	Gravity
I_η	Beam area moment of inertia about ζ axis
I_ζ	" " " " " " η axis
$I_{\xi\xi}$	Beam mass moment of inertia about ξ axis
$I_{\eta\eta}$	" " " " " " ζ axis
$I_{\zeta\zeta}$	" " " " " " η axis

J	Beam torsion constant
k	Reduced frequency $= \omega b / V_0$
K_ψ	Blade lag spring constant
L	Beam length
m	Beam mass per unit length
$\vec{M}_G$	Moment resultant vector in global axes, x, y, z
$\vec{M}_L$	" " " " local axes, ξ, η, ζ
M_1, M_2, M_3	Moment resultant components in local axes
M_x, M_y, M_z	" " " " global axes
$\vec{m}_G$	Applied moment vector in global axes
m_x, m_y, m_z	" " components in global axes
$\vec{m}_{GT}$	Total applied moment vector in global axes
m_{xT}, m_{yT}, m_{zT}	" " " components in global axes
$\vec{m}_L$	Applied moment vector in local axes
m_1, m_2, m_3	" " components in local axes
N_B	Number of blades
$\vec{p}_G$	Applied load vector in global axes
p_x, p_y, p_z	" " components in global axes
$\vec{p}_{GT}$	Total applied load vector in global axes
p_{xT}, p_{yT}, p_{zT}	" " " components in global axes
$\vec{p}_L$	Applied load vector in local axes
p_1, p_2, p_3	" " components in local axes
q_{wi}	Beam generalized coordinates in flap bending
q_{vi}	Beam generalized coordinates in lag bending
q_{wi}	Beam generalized coordinates in torsion
Re	Reynolds Number
s	arc length
$[T]$	Transformation matrix

T_{ij}	Transformation matrix elements
u, v, w	Displacements along x, y, z axes
V	Resultant air velocity at aerodynamic center
V_0	Static part of V
V_2, V_3	Tangential and normal components of V
v_i	Inflow velocity
x, y, z	Global coordinates
X	Vector of unknowns
z_{0t}	Static (or average) tip vertical deflection
α	Angle of attack at the aerodynamic center
β_p	Blade preconing angle
Γ_{1z}	Linear circulatory lift or moment circulation
Γ_{2z}	Stalled circulatory lift or moment circulation
Γ_{D1}	Linear drag circulation
Γ_{D2}	Nonlinear drag circulation
$\gamma_{\xi\eta}, \gamma_{\xi\zeta}$	Beam shear strains
ϵ	Beam extension strain or a small parameter
$\dot{\epsilon}_e$	Blade equivalent pitch rate
$[\kappa]$	Curvature matrix
κ_ξ	Twist rate around ξ axis
κ_η	Bending curvature around η axis
κ_ζ	" " " ζ axis
ξ, η, ζ	Local coordinates
η_{cg}, ζ_{cg}	Mass center of blade cross section
ϕ	Total twist angle
ρ	Blade or air density
τ	Nondimensional time $= V_0 t/b$
ψ, β, θ	Euler angles

θ_r	Blade root pitch angle
θ_t	Built-in twist angle
θ_{to}	Static (or average) tip angle
θ_{ts}	Sine part of tip angle
θ_{tc}	Cosine part of tip angle
ω	Frequency
ω_ξ	Blade rotation around ξ axis
ω_η	" " " η axis
ω_ζ	" " " ζ axis
Ω	Blade rotational speed
$(\dot{\ })$	Derivative with respect to real time

Chapter 1

Introduction

1.1 Previous Work and Perspective

In designing helicopters, a major task is the prediction of the dynamic and aeroelastic behavior of the rotor blades under various flight conditions. The designer would first need an accurate structural model of the blades from which fundamental blade mode shapes and their natural vibratory frequencies can be assessed. Next, combined with general aerodynamic theories, the designer obtains the aeroelastic behavior, including divergence, flutter, ground or air resonance. In analyzing any aeroelastic system, the roles of the structural and aerodynamic parts are equally important. This is particularly true of the helicopter case where all rotor blades exhibit certain degrees of nonlinearities both in the structural and aerodynamic behavior.

The structural nonlinearities arise from the length and flexibility of the blades which allow large deflections and rotations even when the blade material still behaves in the linear stress-strain region. The study of the blade structure and dynamics dates back about forty years, and since then, it has received continuous attention from many researchers. Among notable developments, the introduction of hingeless blade construction has simplified the hub design, and increased the agility of the helicopters (Ref. 1). Other recent advances in blade construction include nonlinear twist distributions, curved blades and swept tips (Ref. 2, 3). Also, developments in advanced composite materials has introduced another design parameter through

which the static and dynamic behavior of the blades can be controlled (Ref. 4, 5, 6, 7). In particular, the designer now can aeroelastically tailor the blades both in their static deformations and dynamic characteristics by a proper lamination of the composite materials. Thus, the overall performance of the blades such as divergence or flutter can be improved (Ref. 3, 8, 9).

There are generally two different approaches in dealing with the large deflections and rotations of the flexible blades. The first approach, which has become very common practice these days, relies on various ordering schemes which lead to a set of equations of motion where large deflections and rotations are expanded into power series up to a certain order, usually quadratic or cubic (Ref. 10, 11). This formulation begins with finding nonlinear expressions for kinetic and strain energy which are later used in the Hamilton principle to get the approximate set of equations of motion. The resulting equations are usually solved by either Rayleigh-Ritz method, or Galerkin's method with appropriate use of modal expansions of the large deflections and angles. This widely known approach has caused arguments among different researchers about which ordering scheme should be used in which terms. Furthermore, the resulting nonlinear equations are sometimes too unwieldy to be manipulated, and there is always a question as to the accuracy of the procedure.

The other approach is based upon the use of Euler angles to account for the large deformation, and does not rely on any series expansion of these angles. Thus, unlike the first approach, no ordering scheme is introduced and all geometric nonlinearities are retained completely (Ref. 12, 13, 14, 15). Instead of a set of modal equations, this formulation will yield a set of nonlinear partial differential equations that constitutes a two-point boundary value problem with proper boundary conditions at the root and tip of the blades. The static solutions of these differential equations can be obtained by numerical integration scheme such as Runge-Kutta algorithm combined with Newton-Raphson type iteration. For the vibration modes and aeroelastic stability, the nonlinear equations are linearized about the solved static positions. Combined

with general unsteady aerodynamics, the linearized equations can be solved in two different methods. The first method directly obtains the influence coefficient by applying unit load at various stations in appropriate directions of degrees of freedom (usually axial, lead-lag, flap, and torsional degrees of freedom) and measuring the resulting deformation in the degree of freedom of interest (Ref. 14). Then, equations of motion can be formed using mass, aerodynamic damping, and the influence coefficient matrices, which can be solved via standard eigenvalue algorithms. The second method utilizes so-called transfer matrix method in which the basic differential equations are integrated from the tip to the root, and the determinant of the linear transfer matrix that relates the tip boundary values to the root boundary values is checked for a possible valid solution (Ref. 16). While both methods are computationally heavy compared to the first approach, the results are more accurate and reliable (Ref. 16) as a result of using fully nonlinear equations.

The modeling of unsteady aerodynamics has a long history dating back to 1930's, when Theodorsen, and, Von Karman and Sears had independently predicted theoretically the onset of sinusoidal motion or flutter of two-dimensional airfoil in the presence of constant free air stream (Ref. 17, 18). Later, Greenberg did a similar theoretical treatment of harmonic motion of airfoil submerged in pulsating air stream (Ref. 19). This analysis was particularly useful for the helicopter rotor blades because they can experience sinusoidal incoming air velocities due to possible lead-lag motion or forward flight motion of the helicopter. Much later, Loewy had suggested that in the analysis of rotor blades during hovering, the effects of spiral vortex sheets accumulated underneath the rotor disk should be accounted for (Ref. 20). These general aerodynamic theories by Theordosen, Greenberg, and Loewy have witnessed a great deal of applications among many helicopter analyses. Nowadays, with judicious use of high-speed computers the prediction of flutter of rotor blades seems fairly routine procedure.

The recognition of dynamic stall did not come until the early 50's when several

wind tunnel simulations of helicopter forward flights revealed short-period, severe torsional vibrations on the retreating side of rotor disk (Ref. 21, 22). Many researchers had continued the experimental work over decades and were able to show the effects of various parameters such as airfoil shape, mean angle of attack, oscillation amplitude, reduced frequency, Reynolds number, and Mach number, on the dynamic stalling behavior of the blades (Ref. 23). The actual modeling of the dynamic stall phenomenon has emerged later, and it generally falls into numerical and semi-empirical approaches; solution of the basic unsteady fluid equations by computational methods has provided a good estimation of the dynamic stall phenomenon (Ref. 24). Recently, a semi-empirical model called ONERA Model, that consists of a set of two second order ordinary differential equations with coefficients obtained from wind tunnel experiments of simple harmonic oscillation of airfoils, has become popular (Ref. 25). The most important advantage of the ONERA model is that, by using the basic properties of the second-order differential equations, it can adequately generate airforce hysteresis loops without going into details of the unsteady aerodynamic theories. Most applications of dynamic stall modeling using the ONERA equations have been given to the periodic response of rotor blades in forward flight (Ref. 26). On the other hand, stall flutter of isolated blades or airfoils has also been a focus of research (Ref. 27). The dynamic stall is a phenomenon that is not yet fully understood and that awaits further investigations.

Using all of the afore-mentioned structural and aerodynamic modeling techniques, most analyses of rotor blade aeroelastic behavior are traditionally based on small amplitude approximations about a given static deformation of the blade using linear or linearized aerodynamic theories. However, under certain circumstances such as high angle of attack thrust, maneuvering, or gust, a nonlinear large amplitude limit cycle may occur at different flight conditions than linear prediction would suggest. Hence, it has been of interest to explore this nonlinear aeroelastic behavior and its transition from linear behavior. Such an analysis, dealing only with geometrical

nonlinearities of the rigid blade, was given by Chopra and Dugundji (Ref. 28). Most recently, Dunn and Dugundji have given another such analysis for fixed lifting surface, this time dealing with aerodynamic stall effects only, by use of the ONERA Model (Ref. 29). Alternatively, Tang and Dowell have introduced both structural and dynamic stall in their investigation of stall limit cycles and chaotic motion of flexible, nonrotating blades (Ref. 30). The structural nonlinearities here were approximated by the moderate deflection equations and the dynamic stall was represented by the ONERA Model. Hence, a fully nonlinear aeroelastic analysis of rotating flexible blades involving both structural and aerodynamic nonlinearities would seem valuable at this point.

1.2 Research Objectives

The present research is continuation of investigation at the Technology Laboratory for Advanced Composites at M.I.T. into the basic structural behavior of composite rotor blades at large static deflections, and its application to aeroelastic problems. Emphasis is given on new exploration of nonlinear large amplitude oscillation behavior rather than small amplitude oscillation characteristics of composite blades. On the structural side, it has been known that under large static deflections, the natural frequencies and mode shapes of cantilever helicopter blades, particularly the fore-and-aft (lag) and the torsional modes, show interesting characteristics which are not apparent from their vibration behavior as undeflected cantilever blades (Ref. 14). Furthermore, for large vibration amplitudes of these modes, their frequency, static positions and mode shapes may change substantially from their linear behavior. The nonlinear, large amplitude behavior of flexible blades has never been an issue in the literature of helicopter rotor blade dynamics, and will be explored in the present research. The present research also addresses an incorporation of these large amplitude vibration effects into a nonlinear, large amplitude flutter limit cycle analysis of rotating blades in hover. For the large amplitude flutter analysis, the aerodynamics would also likely

involve nonlinear stalling effects. These aerodynamic nonlinearities are included here using the ONERA Model first introduced by Tran and Petot (Ref. 25). Thus, the specific objectives of the current investigation are: first, to explore analytically and experimentally the roles of nonlinear structure in the large amplitude free vibrations; second, to develop aerodynamic modeling that can handle large amplitude dynamic stall phenomenon accurately; and third, to develop a nonlinear method of analysis suitable for routine structural and aeroelastic check.

Chapter 2 describes the structural modeling that originates from a previous TELAC work by Minguet and Dugundji (Ref. 14). A total of twelve nonlinear partial differential equations that represent compatibility and equilibrium based on the use of Euler angles are given. General stress-strain relations including various structural couplings such as bending-twist, and extension-twist due to the use of composite materials are presented. Also, a new technique to include out-of-plane warping is introduced. Also added is the reduction of this large deflection model to a commonly used moderate deflection model for the simple case without shear, warping, and structural couplings.

Chapter 3 describes the inertial modeling that includes both linear and angular accelerations, centrifugal forces, Coriolis forces, and gravity. The resulting equations are first given in the global coordinate system. Then, using properties of transformation and rotation rate matrices, they are transformed into a local form.

Chapter 4 describes the aerodynamic modeling that includes both linear unstalled and nonlinear stalled parts. General differential equations by the ONERA model are described for the unsteady lift, moment, and drag. Calculation of the local air velocity components as well as the inflow velocity are also given. Finally, the equations for the local aerodynamic loads expressed in terms of the ONERA aerodynamic forces are described.

Chapter 5 describes the modeling of large amplitude motion in the structural and the aerodynamic parts. First, all the variables are assumed in the first harmonic form, and the transformation matrix is expanded about an arbitrarily large static

solution up to third order in terms of dynamic parts associated with the large motion. Harmonic balance method is then adopted by dropping all the higher harmonic terms and the higher order terms. For later use in the harmonic balance, the first harmonic components of the nonlinear aerodynamic forces are extracted by Fourier analysis using constant coefficients in the ONERA equations. The resulting harmonic hysteresis loops are compared against the exact numerical integrations of the ONERA equations.

Chapter 6 describes the methods of solutions for nonrotating and rotating free vibrations, static position, linear flutter, and finally large amplitude flutter. The solution procedure of the nonrotating free vibration problem by moderate deflection equations developed by Hodges and Dowell is also presented.

Chapter 7 shows the analytic results of the nonrotating free vibration for both the full nonlinear equations and the moderate deflection equations compared with each other. Also presented are some of the rotating free vibration results.

Chapter 8 describes the experimentation of the nonrotating free vibration and shows the experimental results. These results also are compared against analysis.

Chapter 9 shows the aeroelastic results including static deformation, linear and nonlinear flutter, and large amplitude stall flutter limit cycles. To distinguish the individual roles of the structure from the aerodynamics in the large amplitude limit cycle solutions, three different combinations of structure and aerodynamics were implemented in the analysis. They are, linearized structure plus nonlinear aerodynamics, nonlinear structure plus linear aerodynamics, and the full nonlinear structure plus nonlinear aerodynamics. Results from each combination are compared with each other, and relative roles of structure and aerodynamics are discussed. Most analytic results are for hingeless blades with and without structural couplings, but a lag-hinged blade with a lag spring constraint is also given analysis for illustration.

Lastly, in chapter 10 concluding remarks and recommendations for future work are mentioned.

Chapter 2

Structural Modeling

2.1 Basic Equations

For the present analysis, two types of nonlinear equations exist for flexible rotor blades; the equations which are based on various geometrical ordering schemes, and the ones which are not. The former group of equations approximate large displacements and rotations mostly up to second order (e.g., Ref. 10) while the latter group preserve the complete nonlinearities in them (e.g., Ref. 14). As will be discussed later, since strong couplings between various static and dynamic parts of the equations are expected in the nonlinear large amplitude vibrations, the set of complete nonlinear equations of the latter group is preferred. The nonlinear equations derived by Minguet and Dugundji (Ref. 14) are used here for their simplicity and immediate availability for analysis of composite blades. All of the assumptions made earlier regarding structural model in Ref. 14 are retained in this section. First, the blade itself is long enough to be treated as a one-dimensional model. Second, shear deformation and warping of the cross-section of the blade are neglected. Third, material nonlinearity is ignored.

There are twelve first-order, nonlinear partial differential equations that describe the statics and dynamics of composite blades completely. These equations are obtained by considering equilibrium, strain-displacement compatibilities, and linear stress-strain relations of a blade element. Ref. 13 contains a thorough derivation

of the equations. All the equations are derived based on the following transformation matrix that transforms the global coordinate x, y, z into the local one ξ, η, ζ (Figure 2.1), i. e. ,

$$\begin{Bmatrix} \vec{i}_\xi \\ \vec{i}_\eta \\ \vec{i}_\zeta \end{Bmatrix} = [T] \begin{Bmatrix} \vec{i}_x \\ \vec{i}_y \\ \vec{i}_z \end{Bmatrix}$$

$$[T] = \begin{bmatrix} \cos\beta\ \cos\psi & \cos\beta\ \sin\psi & \sin\beta \\ -\cos\theta\ \sin\psi & \cos\theta\ \cos\psi & \sin\theta\ \cos\beta \\ -\sin\theta\ \sin\beta\ \cos\psi & -\sin\theta\ \sin\beta\ \sin\psi & \\ \sin\theta\ \sin\psi & -\sin\theta\ \cos\psi & \cos\theta\ \cos\beta \\ -\cos\theta\ \sin\beta\ \cos\psi & -\cos\theta\ \sin\beta\ \sin\psi & \end{bmatrix} \tag{2.1}$$

Here ψ, β, θ are the local Euler angles. When the preconing angle β_p is introduced for the blade, one has to define additional transformation between the actual global coordinates x_0, y_0, z_0, and the global coordinates on the blade x, y, z as

$$\begin{Bmatrix} \vec{i}_x \\ \vec{i}_y \\ \vec{i}_z \end{Bmatrix} = [T'] \begin{Bmatrix} \vec{i}_{x0} \\ \vec{i}_{y0} \\ \vec{i}_{z0} \end{Bmatrix}$$

$$[T'] = \begin{bmatrix} \cos\beta_p & 0 & \sin\beta_p \\ 0 & 1 & 0 \\ -\sin\beta_p & 0 & \cos\beta_p \end{bmatrix} \tag{2.2}$$

Hence, the resulting transformation between the local ξ, η, ζ and the actual global system x_0, y_0, z_0 for small β_p, becomes, for small β_p

$$\begin{Bmatrix} \vec{i}_\xi \\ \vec{i}_\eta \\ \vec{i}_\zeta \end{Bmatrix} = [T''] \begin{Bmatrix} \vec{i}_{x0} \\ \vec{i}_{y0} \\ \vec{i}_{z0} \end{Bmatrix}$$

$$[T''] = \begin{bmatrix} T_{11} - \beta_p T_{13} & T_{12} & T_{13} + \beta_p T_{11} \\ T_{21} - \beta_p T_{23} & T_{22} & T_{23} + \beta_p T_{21} \\ T_{31} - \beta_p T_{33} & T_{32} & T_{33} + \beta_p T_{31} \end{bmatrix} \tag{2.3}$$

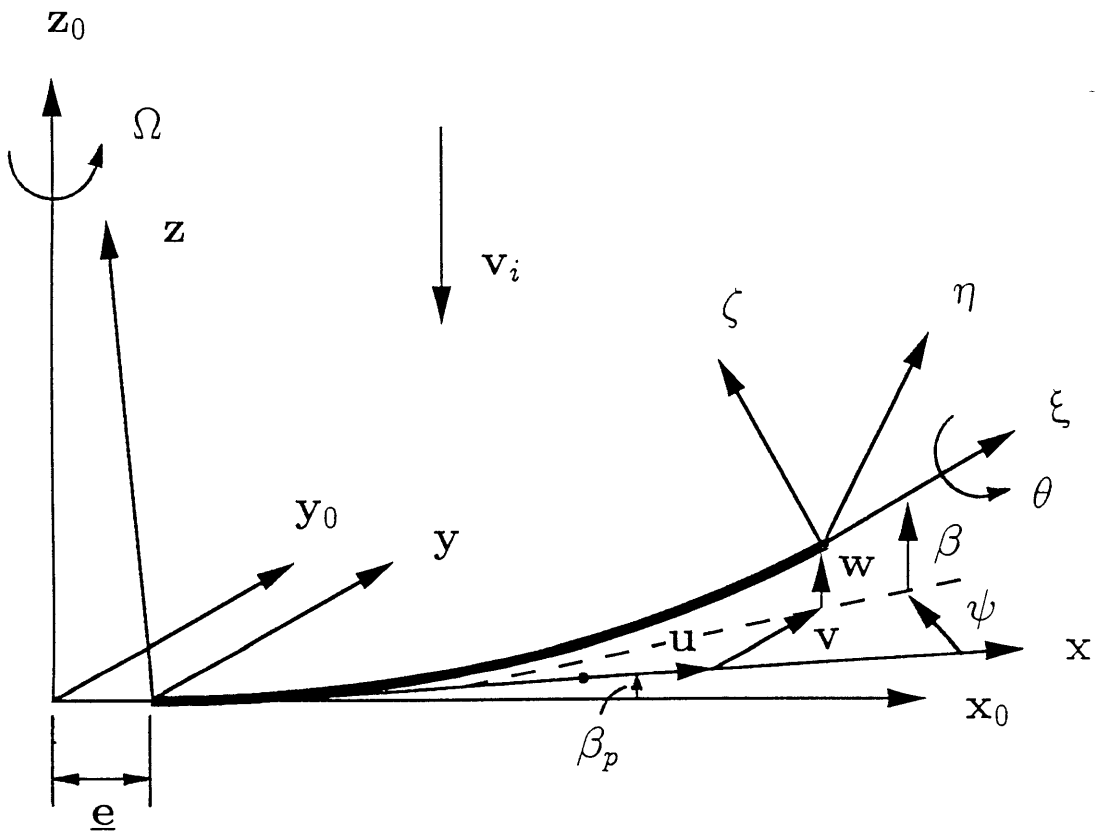

Figure 2.1: Definition of global and local axes

The transformation matrix $[T]$ is orthogonal and related to the curvature matrix as follows.

$$
\begin{aligned}
[T]^{-1} &= [T]^T \\
\frac{\partial [T]}{\partial s} &= [\kappa]\,[T]
\end{aligned}
\tag{2.4}
$$

with

$$
[\kappa] = \begin{bmatrix} 0 & \kappa_\zeta & -\kappa_\eta \\ -\kappa_\zeta & 0 & \kappa_\xi \\ \kappa_\eta & -\kappa_\xi & 0 \end{bmatrix}
\tag{2.5}
$$

where

$$
\begin{aligned}
\kappa_\xi &= \frac{\partial \theta}{\partial s} + \sin\beta \frac{\partial \psi}{\partial s} \\
&\quad \text{(twist rate around } \xi \text{ axis)} \\
\kappa_\eta &= -\cos\theta \frac{\partial \beta}{\partial s} + \sin\theta\,\cos\beta \frac{\partial \psi}{\partial s} \\
&\quad \text{(bending curvature around } \eta \text{ axis)} \\
\kappa_\zeta &= \sin\theta \frac{\partial \beta}{\partial s} + \cos\theta\,\cos\beta \frac{\partial \psi}{\partial s} \\
&\quad \text{(bending curvature around } \zeta \text{ axis)}
\end{aligned}
\tag{2.6}
$$

Inverting the above differential equation yields

$$
\begin{aligned}
\frac{\partial \theta}{\partial s} &= \kappa_\xi - \sin\theta\,\tan\beta\,\kappa_\eta - \cos\theta\,\tan\beta\,\kappa_\zeta \\
\frac{\partial \beta}{\partial s} &= -\cos\theta\,\kappa_\eta + \sin\theta\,\kappa_\zeta \\
\frac{\partial \psi}{\partial s} &= \frac{\sin\theta}{\cos\beta}\kappa_\eta + \frac{\cos\theta}{\cos\beta}\kappa_\zeta
\end{aligned}
\tag{2.7}
$$

The global displacements x, y, z are related to Euler angles via

$$
\begin{aligned}
\frac{\partial x}{\partial s} &= (1 + \epsilon)\,T_{11} \\
\frac{\partial y}{\partial s} &= (1 + \epsilon)\,T_{12} \\
\frac{\partial z}{\partial s} &= (1 + \epsilon)\,T_{13}
\end{aligned}
\tag{2.8}
$$

where ϵ is the axial strain along the reference line. In addition to the above six compatibility equations, one has to consider equilibrium of forces and moments of the

beam. The equilibrium equations can be written in either global or local coordinates. Here they are written in local coordinate in order to take into account the large deformation of the beam in space. The first three differential equations that describe the equilibrium of the local force resultants F_1, F_2, F_3 are

$$\begin{aligned}
\frac{\partial F_1}{\partial s} - \kappa_\zeta F_2 + \kappa_\eta F_3 + T_{11} p_x + T_{12} p_y + T_{13} p_z + p_1 &= 0 \\
\frac{\partial F_2}{\partial s} + \kappa_\zeta F_1 - \kappa_\xi F_3 + T_{21} p_x + T_{22} p_y + T_{23} p_z + p_2 &= 0 \\
\frac{\partial F_3}{\partial s} - \kappa_\eta F_1 + \kappa_\xi F_2 + T_{31} p_x + T_{32} p_y + T_{33} p_z + p_3 &= 0
\end{aligned} \tag{2.9}$$

with

$\vec{p}_L$: applied load vector in local axis $= p_1, p_2, p_3$

$\vec{p}_G$: applied load vector in global axis $= p_x, p_y, p_z$

The other three differential equations describe the equilibrium of the local moment resultants M_1, M_2, M_3.

$$\begin{aligned}
\frac{\partial M_1}{\partial s} - \kappa_\zeta M_2 + \kappa_\eta M_3 + T_{11} m_x + T_{12} m_y + T_{13} m_z + m_1 &= 0 \\
\frac{\partial M_2}{\partial s} + \kappa_\zeta M_1 - \kappa_\xi M_3 + T_{21} m_x + T_{22} m_y + T_{23} m_z + m_2 - F_3 &= 0 \\
\frac{\partial M_3}{\partial s} - \kappa_\eta M_1 + \kappa_\xi M_2 + T_{31} m_x + T_{32} m_y + T_{33} m_z + m_3 + F_2 &= 0
\end{aligned} \tag{2.10}$$

with

$\vec{m}_L$: applied moment vector in local axis $= m_1, m_2, m_3$

$\vec{m}_G$: applied moment vector in global axis $= m_x, m_y, m_z$

In helicopter problems, generally two kinds of loadings arise; inertial loads including normal and angular acceleration, Coriolis acceleration, centrifugal and gravitational forces; and aerodynamic loads including both steady and unsteady parts. The former group usually appears as the global $\vec{p}_G$, $\vec{m}_G$ while the latter group appears as the local $\vec{p}_L$, and $\vec{m}_L$.

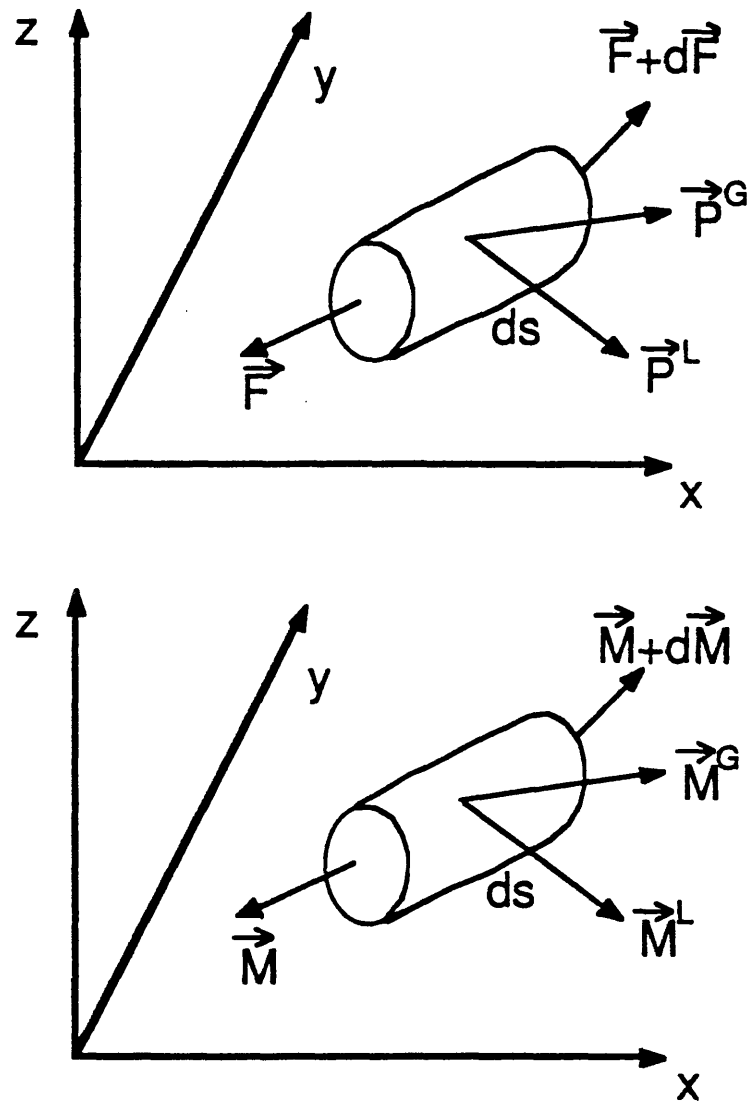

Figure 2.2: Definition of local internal forces and moments

Finally, a set of generalized stress-strain relations for a composite blade are incorporated via the following six linear equations.

$$\begin{bmatrix} F_1 \\ F_2 \\ F_3 \\ M_1 \\ M_2 \\ M_3 \end{bmatrix} = \begin{bmatrix} E_{11} & E_{12} & E_{13} & E_{14} & E_{15} & E_{16} \\ & E_{22} & E_{23} & E_{24} & E_{25} & E_{26} \\ & & E_{33} & E_{34} & E_{35} & E_{36} \\ & & & E_{44} & E_{45} & E_{46} \\ & \text{SYM} & & & E_{55} & E_{56} \\ & & & & & E_{66} \end{bmatrix} \begin{bmatrix} \epsilon \\ \gamma_{\xi\eta} \\ \gamma_{\xi\zeta} \\ \kappa_\xi \\ \kappa_\eta \\ \kappa_\zeta \end{bmatrix} \tag{2.11}$$

Here $\gamma_{\xi\eta}, \gamma_{\xi\zeta}$ represent the two transverse shear strains. In its most general case, the above stiffness matrix can be full, i.e., all of three force resultants, three moment resultants and all of six strain components can be coupled. It should be emphasized that the compatibility relations given by equations 2.7, 2.8, and the stress-strain relation 2.11 do not take either warping or transverse shear into account. To be consistent with such Bernoulli-Euler type hypothesis, both of the transverse shear strains $\gamma_{\xi\eta}$, $\gamma_{\xi\zeta}$ are not calculated during inversion of the stress-strain equation 2.11, which otherwise gives the other strain components κ_ξ, κ_η, and κ_ζ. Also, the axial strain component ϵ can be ignored since its order of magnitude is usually much higher than the other strain components.

2.2 Boundary Conditions

The basic differential equations 2.7 through 2.10 and the general stress-strain relations 2.11 constitute a two-point boundary value problem. In this section, appropriate sets of boundary conditions for several types of root construction are described.

First, for a <u>hingeless</u> blade one has:

@ root (s = 0): all displacements and Euler angles

are zero except $\theta = \theta_r$

where θ_r is collective pitch.

that is, $[x\ y\ z\ \theta\ \beta\ \psi]^T = [0\ 0\ 0\ \theta_r\ 0\ 0]^T$

@ tip (s = 1) : all local forces and moments are zero.

that is, $[F_1\ F_2\ F_3\ M_1\ M_2\ M_3]^T = [0\ 0\ 0\ 0\ 0\ 0]^T$

For a <u>lag-hinged</u> blade one has:

@ root (s = 0) : all displacements, the first two

Euler angles are zero except $\theta = \theta_r$

Resolution of moments into lag direction is zero

that is, $[x\ y\ z\ \theta\ \beta\ M_2 \sin\theta_r + M_3 \cos\theta_r]^T = [0\ 0\ 0\ \theta_r\ 0\ 0]^T$

@ tip (s = 1) : all local forces and moments are zero.

that is, $[F_1\ F_2\ F_3\ M_1\ M_2\ M_3]^T = [0\ 0\ 0\ 0\ 0\ 0]^T$

For a <u>lag-hinged</u> blade with <u>lag spring</u> one has:

@ root (s = 0) : all displacements, the first two

Euler angles are zero except $\theta = \theta_r$

Resolution of moments into lag direction

is equal to lag spring force

that is, $[x\ y\ z\ \theta\ \beta\ M_2 \sin\theta_r + M_3 \cos\theta_r]^T = [0\ 0\ 0\ \theta_r\ 0\ K_\psi \psi]^T$

@ tip (s = 1) : all local forces and moments are zero.

that is, $[F_1\ F_2\ F_3\ M_1\ M_2\ M_3]^T = [0\ 0\ 0\ 0\ 0\ 0]^T$

For a <u>flap-lag hinged</u> blade one has

@ root (s = 0) : all displacements are zero

Euler angle $\theta = \theta_r$

and two bending moments are zero

that is, $[x\ y\ z\ \theta\ M_2\ M_3]^T = [0\ 0\ 0\ \theta_r\ 0\ 0]^T$

@ tip (s = 1) : all local forces and moments are zero.

that is, $[F_1\ F_2\ F_3\ M_1\ M_2\ M_3]^T = [0\ 0\ 0\ 0\ 0\ 0]^T$

2.3 Warping and Shear Deformation

It has been noted that the structural model described in the previous section does not include warping and shear deformation. As indicated by Friedmann (Ref. 26), this model, while quite accurate for thin, high aspect-ratio composite strips, can not capture the full deformations of more realistic blades with complex cross-section configurations. In the present section, an approximate method to include both the shear deformation and out-of-plane warping of the cross-section is described. For the shear deformation part, one can introduce into equation 2.8 the shear strains $\gamma_{\xi\eta}$, $\gamma_{\xi\zeta}$ in calculating the displacements x, y, z.

$$\begin{aligned}
\frac{\partial x}{\partial s} &= (1+\epsilon)(T_{11} + T_{21}\gamma_{\xi\eta} + T_{31}\gamma_{\xi\zeta}) \\
\frac{\partial y}{\partial s} &= (1+\epsilon)(T_{12} + T_{22}\gamma_{\xi\eta} + T_{32}\gamma_{\xi\zeta}) \\
\frac{\partial z}{\partial s} &= (1+\epsilon)(T_{13} + T_{23}\gamma_{\xi\eta} + T_{33}\gamma_{\xi\zeta})
\end{aligned} \tag{2.12}$$

This formulation, first suggested by Minguet and Dugundji (Ref. 13), observes that when the blade undergoes small amount of shear deformation, the cross-section remains effectively plane but not perpendicular to the midplane of the blade. Thus, the transformation between the global x, y, z and the new local coordinates ξ, η, ζ that are defined on the deformed cross-section (Figure 2.3) is not $[T]$ but $[\gamma]\,[T]$, where

$$[\gamma] = \begin{bmatrix} 1 & \gamma_{\xi\eta} & \gamma_{\xi\zeta} \\ -\gamma_{\xi\eta} & 1 & 0 \\ -\gamma_{\xi\zeta} & 0 & 1 \end{bmatrix} \tag{2.13}$$

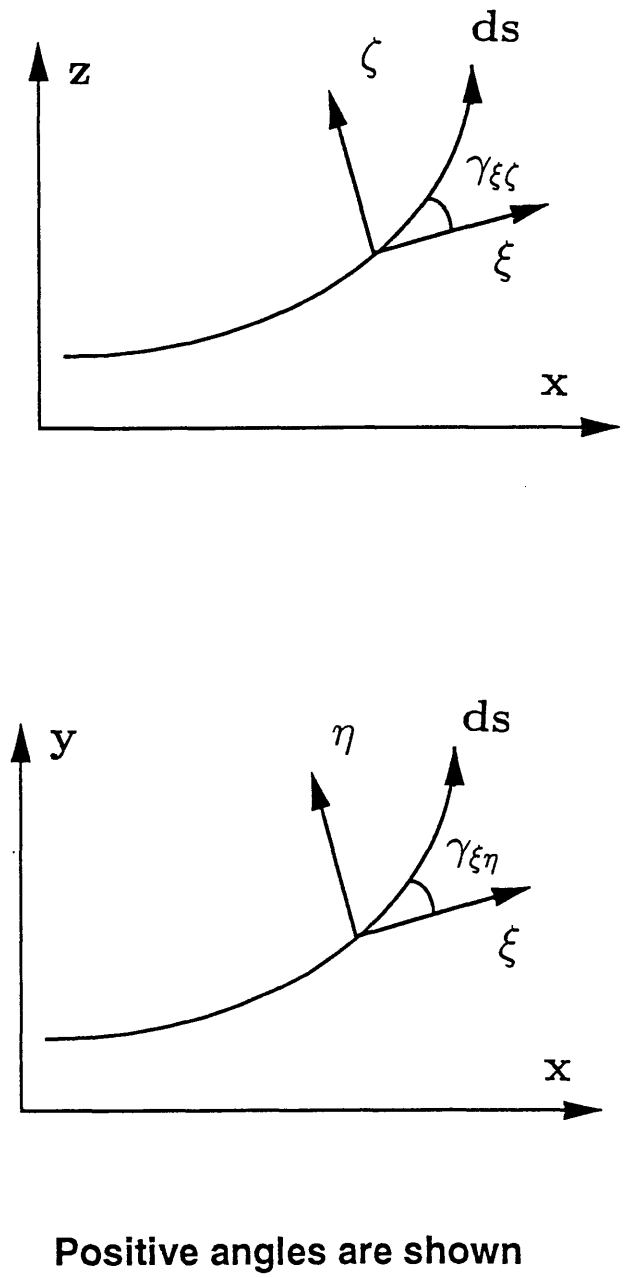

Figure 2.3: Illustration of shear deformation of cross section

For the out-of-plane warping, an analogy is invoked to classical linear twist theory that includes a warping correction term proportional to the second derivative of the twist rate θ'. This result was first obtained by Reissner and Stein (Ref. 31) by applying a partial Ritz technique to cantilever plates in which a mode shape is assumed only in the chordwise direction. Later, Crawley and Dugundji (Ref. 32) applied the same method for composite plates. To implement this correction within the current model, one should replace the twist rate by κ_ξ and introduce two additional first-order partial differential equations for κ_ξ, κ'_ξ, and a term proportional to the second derivative of κ_ξ within the twisting moment equilibrium equation as follows.

$$\begin{aligned} \frac{\partial \kappa_\xi}{\partial s} &= \kappa'_\xi \\ \frac{\partial \kappa'_\xi}{\partial s} &= \kappa''_\xi \end{aligned} \tag{2.14}$$

$$M_1 = E_{44}\,\kappa_\xi + A\,\kappa''_\xi + \text{coupling terms} \tag{2.15}$$

with additional boundary conditions

$$\kappa'_\xi(l) = 0, \quad \kappa_\xi(0) = 0 \tag{2.16}$$

where A represents the warping coefficient, and must be calculated for a given cross-section configuration (e.g., $-E_{55}c^2/12$ for flat composite strip). Note that the boundary conditions 2.16 holds true for any kind of root constructions considered in section 2.2.

When considered altogether, one can reconstruct the linear stress-strain relations 2.11 for a composite blade as

$$\begin{bmatrix} F_1 \\ F_2 \\ F_3 \\ M_1 \\ M_2 \\ M_3 \end{bmatrix} - \begin{bmatrix} E_{14} \\ E_{24} \\ E_{34} \\ E_{44} \\ E_{54} \\ E_{64} \end{bmatrix} \kappa_\xi = \begin{bmatrix} E_{11} & E_{12} & E_{13} & 0 & E_{15} & E_{16} \\ & E_{22} & E_{23} & 0 & E_{25} & E_{26} \\ & & E_{33} & 0 & E_{35} & E_{36} \\ & & & A & E_{45} & E_{46} \\ & \text{SYM} & & & E_{55} & E_{56} \\ & & & & & E_{66} \end{bmatrix} \begin{bmatrix} \epsilon \\ \gamma_{\xi\eta} \\ \gamma_{\xi\zeta} \\ \kappa''_\xi \\ \kappa_\eta \\ \kappa_\zeta \end{bmatrix} \tag{2.17}$$

At any station, equation 2.17 can be inverted to give appropriate values of $[\epsilon\, \gamma_{\xi\eta}\, \gamma_{\xi\zeta}\, \kappa''_{\xi}\, \kappa_{\eta}\, \kappa_{\zeta}]^T$ for integrating the differential equations (now fourteen equations) with the boundary conditions given in the previous section and in 2.16.

2.4 Reduction of Basic Equations for Moderate Deflections

Before proceeding with the modeling of the inertial terms in the nonlinear equations presented in the previous section, the equations of motion in u, v, w, and ϕ derived by Hodges and Dowell, Ref. 10, and Boyd, Ref. 11, for moderate deflections will be rederived from the twelve general nonlinear equations 2.7 through 2.10. By "moderate", it is meant a second order approximation to the nonlinear deflections and angles involved in simple beam theory. Only the case of isotropic blade with no mass centroid offset is considered here for illustration. Also, warping and transverse shear are not included. In this way, the approximations of the moderate deflection analysis can be assessed.

The first step in the reduction process is to rewrite the force and moment equilibrium equations in global x, y, z directions instead of local ξ, η, ζ directions. One can write the local force equilibrium equations 2.9 in vector form as

$$\frac{\partial \vec{F}_L}{\partial s} + [\kappa]^T \vec{F}_L + [T]\, \vec{p}_G + \vec{p}_L = 0 \tag{2.18}$$

where L, and G refer to local and global components. Multiplying by $[T]^T$ and noting the basic kinematic relations given by equation 2.4 gives,

$$[T]^T \frac{\partial \vec{F}_L}{\partial s} + \frac{\partial [T]^T}{\partial s} \vec{F}_L + \vec{p}_G + [T]^T \vec{p}_L = 0 \tag{2.19}$$

and upon rearranging,

$$\frac{\partial \vec{F}_G}{\partial s} + \vec{p}_{GT} = 0 \tag{2.20}$$

where one has

$$\begin{aligned}
\vec{p}_{GT} &= \vec{p}_G + [T]^T \vec{p}_L \\
\vec{F}_G &= [T]^T \vec{F}_L \\
\vec{F}_L &= [T] \vec{F}_G
\end{aligned} \tag{2.21}$$

In scalar form, equation 2.20 becomes,

$$\begin{aligned}
\frac{\partial F_x}{\partial s} &= -p_{xT} \\
\frac{\partial F_y}{\partial s} &= -p_{yT} \\
\frac{\partial F_z}{\partial s} &= -p_{zT}
\end{aligned} \tag{2.22}$$

Similarly, one can write the local moment equilibrium equations 2.10 in vector form as,

$$\frac{\partial \vec{M}_L}{\partial s} + [\kappa]^T \vec{M}_L + [T] \vec{m}_G + \vec{m}_L + \left\{ \begin{array}{c} 0 \\ -F_3 \\ F_2 \end{array} \right\} = 0 \tag{2.23}$$

Applying the same transformations as for the force equilibrium equations results in,

$$\frac{\partial \vec{M}_G}{\partial s} + \vec{m}_{GT} + [T]^T \left\{ \begin{array}{c} 0 \\ -F_3 \\ F_2 \end{array} \right\} = 0 \tag{2.24}$$

where one has defined,

$$\begin{aligned}
\vec{m}_{GT} &= \vec{m}_G + [T]^T \vec{m}_L \\
\vec{M}_G &= [T]^T \vec{M}_L \\
\vec{M}_L &= [T] \vec{M}_G
\end{aligned} \tag{2.25}$$

In scalar form, equation 2.24 becomes

$$\begin{aligned}
\frac{\partial M_x}{\partial s} + m_{xT} - T_{21} F_3 + T_{31} F_2 &= 0 \\
\frac{\partial M_y}{\partial s} + m_{yT} - T_{22} F_3 + T_{32} F_2 &= 0 \\
\frac{\partial M_z}{\partial s} + m_{zT} - T_{23} F_3 + T_{33} F_2 &= 0
\end{aligned} \tag{2.26}$$

The local force components are related to the global components from equations 2.21 as

$$\begin{aligned} F_1 &= T_{11}\,F_x + T_{12}\,F_y + T_{13}\,F_z \\ F_2 &= T_{21}\,F_x + T_{22}\,F_y + T_{23}\,F_z \\ F_3 &= T_{31}\,F_x + T_{32}\,F_y + T_{33}\,F_z \end{aligned} \tag{2.27}$$

One places the above into equations 2.26 and simplifies by using the following relations obtained from noting that $[T]^{-1} = [T]^T$ and applying Cramer's rule with $|T| = 1$.

$$\begin{aligned} T_{11} &= T_{22}\,T_{33} - T_{23}\,T_{32} \\ T_{12} &= T_{23}\,T_{31} - T_{21}\,T_{33} \\ T_{13} &= T_{21}\,T_{32} - T_{22}\,T_{31} \end{aligned} \tag{2.28}$$

This will result in the three scalar equations,

$$\begin{aligned} \frac{\partial M_x}{\partial s} + m_{xT} - T_{13}\,F_y + T_{12}\,F_z &= 0 \\ \frac{\partial M_y}{\partial s} + m_{yT} + T_{13}\,F_x - T_{11}\,F_z &= 0 \\ \frac{\partial M_z}{\partial s} + m_{zT} - T_{12}\,F_x + T_{11}\,F_y &= 0 \end{aligned} \tag{2.29}$$

Taking the derivatives of the last two equations and introducing the force equilibrium equations 2.22 gives

$$\begin{aligned} \frac{\partial^2 M_y}{\partial s^2} + \frac{\partial m_{yT}}{\partial s} + \frac{\partial}{\partial s}(T_{13}\,F_x) + T_{11}\,p_{zT} - F_z\,\frac{\partial T_{11}}{\partial s} &= 0 \\ \frac{\partial^2 M_z}{\partial s^2} + \frac{\partial m_{zT}}{\partial s} - \frac{\partial}{\partial s}(T_{12}\,F_x) - T_{11}\,p_{yT} + F_y\,\frac{\partial T_{11}}{\partial s} &= 0 \end{aligned} \tag{2.30}$$

In addition to these, it is convenient to keep the local moment equilibrium in the ξ direction,

$$\frac{\partial M_1}{\partial s} - \kappa_\zeta\,M_2 + \kappa_\eta\,M_3 + m_{1T} = 0 \tag{2.31}$$

The above moment equations together with the three global force equations 2.22 are the equivalent of equations (71 b, c) (74), and (69 a, b, c) of Hodges and Dowell (Ref. 10). No approximations have been made as yet in equations 2.22, 2.30, 2.31.

The second step in the reduction process is to look at the kinematics and to approximate the Euler angles, ψ and β in terms of global deflections, v and w in the x and y directions respectively. From the kinematic relations equations 2.8, one has

$$\begin{aligned} v' &= \frac{\partial y}{\partial s} \\ w' &= \frac{\partial z}{\partial s} \end{aligned} \tag{2.32}$$

where

$$(\ .\ )' \equiv \frac{\partial(\ .\ )}{\partial s}$$

and the axial strain ϵ has been neglected relative to unity. These equations give rise to the trigonometric relations, to second order,

$$\begin{aligned} \sin\beta &= w' \\ \cos\beta &\simeq 1 - w'^2/2 \\ \sin\psi &\simeq v' \\ \cos\psi &\simeq 1 - v'^2/2 \end{aligned} \tag{2.33}$$

so that effectively, the two Euler angles β and ψ are approximated to second order as

$$\begin{aligned} \beta &\simeq w' \\ \psi &\simeq v' \end{aligned} \tag{2.34}$$

By differentiating equations 2.33, then solving for β' and ψ' keeping terms only to second order, one obtains the same expressions as would have been obtained by simply differentiating equations 2.34 directly. Finally, substituting the β' and ψ' into the three curvature strains κ_ξ, κ_η, κ_ζ given by equations 2.6 and keeping terms to second order, results in,

$$\begin{aligned} \kappa_\xi &\simeq \theta' + w'\,v'' \\ \kappa_\eta &\simeq v''\sin\theta - w''\cos\theta \\ \kappa_\zeta &\simeq v''\cos\theta + w''\sin\theta \end{aligned} \tag{2.35}$$

The three curvature strains are now expressed, to second order, in terms of global deflections v, w and Euler rotation angle θ. Often, it is more convenient to express the twisting behavior of the blade in terms of a total twist angle ϕ which is defined as,

$$\phi = \int_0^s \kappa_\xi \, ds = \theta + \int_0^s w' \, v'' \, ds \tag{2.36}$$

In this case, the curvature strain κ_ξ and the Euler angle θ are replaced in equations 2.35 by,

$$\begin{aligned} \kappa_\xi &= \phi' \\ \theta &= \phi - \int_0^s w' \, v'' \, ds \end{aligned} \tag{2.37}$$

Since the correction to the Euler angle is a small nonlinear term, it is often neglected and the relation $\theta \simeq \phi$ is used.

The second order approximations to the Euler angles as given by equations 2.33 are also used for the general transformation matrix $[T]$. Placing these trigonometric relations into the basic transformation matrix $[T]$, equation 2.1 gives to second order,

$$[T] \simeq \begin{bmatrix} 1 - v'^2/2 - w'^2/2 & v' & w' \\ -(v' \cos\theta + w' \sin\theta) & \cos\theta\,(1 - v'^2/2) & \sin\theta\,(1 - w'^2/2) \\ (v' \sin\theta - w' \cos\theta) & -\sin\theta\,(1 - v'^2/2) & \cos\theta\,(1 - w'^2/2) \end{bmatrix} \tag{2.38}$$

The third step in the reduction process is to relate the moment resultants to the curvature strains, and then to the coordinates v, w, θ. Using the generalized linear stress-strain relations given in equation 2.11 and introducing the strain-displacement

relations of equations 2.35, one may write,

$$
\begin{aligned}
M_1 &= E_{44}\,\kappa_\xi \simeq GJ\,(\theta' + w'\,v'') \\
M_2 &= E_{55}\,\kappa_\eta \simeq EI_\eta\,(v''\sin\theta - w''\cos\theta) \\
M_3 &= E_{66}\,\kappa_\zeta \simeq EI_\zeta\,(v''\cos\theta + w''\sin\theta)
\end{aligned}
\tag{2.39}
$$

The above equations are for a blade principal axis system located along the elastic axis, where there is no coupling between the ξ, η, and ζ axes. For non-principal axes, there may be additional couplings between η and ζ and for non-elastic axis, such as in composite blades, there may be additional couplings between the ξ and η and ξ and ζ curvatures. For use in the equilibrium equations 2.30, it is also necessary to express the moments in global x, y, z directions in addition to the local ξ, η, ζ directions given by equations 2.39. From equations 2.25, one has

$$
\begin{aligned}
M_x &\equiv T_{11}M_1 + T_{21}M_2 + T_{31}M_3 \\
M_y &\equiv T_{12}M_1 + T_{22}M_2 + T_{32}M_3 \\
M_z &\equiv T_{13}M_1 + T_{23}M_2 + T_{33}M_3
\end{aligned}
\tag{2.40}
$$

This gives, to second order,

$$
\begin{aligned}
M_y &= GJ\,\theta'\,v' - (EI_\zeta\,\sin^2\theta + EI_\eta\,\cos^2\theta)\,w'' \\
&\quad -(EI_\zeta - EI_\eta)\,\cos\theta\sin\theta\,v'' \\
M_z &= GJ\,\theta'\,w' + (EI_\zeta\,\cos^2\theta + EI_\eta\,\sin^2\theta)\,v'' \\
&\quad +(EI_\zeta - EI_\eta)\,\cos\theta\sin\theta\,w''
\end{aligned}
\tag{2.41}
$$

M_x is not given above, since in the present formulation, the local moment M_1 is used rather then the global moment M_x.

Finally, to complete the reduction process, one places the moments equations 2.41, 2.39 and curvature strains equation 2.35 into the equilibrium equations 2.30, 2.31 to obtain,

$$
\begin{aligned}
&[GJ\,\theta'\,v' - (EI_\zeta\,\sin^2\theta + EI_\eta\,\cos^2\theta)\,w'' - (EI_\zeta - EI_\eta)\,\cos\theta\sin\theta\,v'']'' \\
&\quad +(w'\,F_x)' + (1 - v'^2/2 - w'^2/2)\,p_{zT} - F_z\,(v'\,v'' + w'\,w'') + m'_{yT} = 0
\end{aligned}
$$

$$[GJ\,\theta' w' + (EI_\zeta \cos^2\theta + EI_\eta \sin^2\theta)\,v'' + (EI_\zeta - EI_\eta)\cos\theta\sin\theta\, w'']''$$
$$-(v' F_x)' + (1 - v'^2/2 - w'^2/2)\,p_{yT} + F_y\,(v' v'' + w' w'') + m'_{zT} = 0 \qquad (2.42)$$

$$[GJ\,(\theta' + w' v'')]' - (EI_\zeta - EI_\eta)\,[(w''^2 - v''^2)\cos\theta\sin\theta + v'' w''\cos 2\theta]$$
$$+m_{1T} = 0$$

The force loadings F_x, F_y, F_z in the above are found from integrating the global force equations 2.22.

Although the above equations have been reduced formally to second order, some further simplifications are still made to reduce them to a simpler form. First, as mentioned in Ref. 10, by integrating the third equation, then multiplying it by v', then subtracting it from the first equation, one can eliminate the $GJ\,\theta' v'$ term, introducing only new third order terms from the third equation. Hence, to second order, the $GJ\,\theta' v'$ term can be neglected. Similarly for the $GJ\,\theta' w'$ term in the second equation. Next, the v'^2 and w'^2 terms can be neglected compared to unity for moderate deflection slopes. This would also eliminate the F_y and F_z terms since they were multiplied by $\frac{\partial T_{11}}{\partial s}$ and T_{11} is now set equal to unity as seen in equation 2.38. Along the same lines, all derivatives

$$\frac{\partial}{\partial s}$$

in these equations can be replaced by

$$\frac{\partial}{\partial x}$$

since from the kinematic relations, equations 2.8,

$$\frac{\partial}{\partial s} = \frac{\partial}{\partial x}\frac{\partial x}{\partial s} \simeq (1 - w'^2/2 - v'^2/2)\frac{\partial}{\partial x} \simeq \frac{\partial}{\partial x} \qquad (2.43)$$

Also, it is convenient to introduce the total twist variable ϕ as defined by equation 2.36 rather than deal with the Euler angle θ. With these simplifications, the previous equations can be rewritten as,

$$w: \quad [(EI_\zeta \sin^2\theta + EI_\eta \cos^2\theta)\,w'' + (EI_\zeta - EI_\eta)\cos\theta\sin\theta\, v'']''$$
$$-(w' F_x)' = p_{zT} + m'_{yT}$$

$$v: \quad [(EI_\zeta \cos^2\theta + EI_\eta \sin^2\theta)\, v'' + (EI_\zeta - EI_\eta)\cos\theta \sin\theta\, w'']'' \\ -(v'\, F_x)' = p_{yT} - m'_{yT} \tag{2.44}$$

$$\phi: \quad -(GJ\,\phi')' + (EI_\zeta - EI_\eta)\,[(w'^2 - v'^2)\cos\theta\sin\theta + v''w''\cos 2\theta] \\ = m_{1T}$$

where one has,

$$\begin{aligned} \theta &\simeq \phi - \int_0^x w'\, v''\, dx \\ F_x &\simeq -\int_x^L p_{xT}\, dx \\ \epsilon &\simeq u' + v'^2/2 + w'^2/2 = 0 \end{aligned} \tag{2.45}$$

Equations 2.44 are, effectively, the nonlinear moderate deflection equations presented by Hodges and Dowell (Ref. 10), Boyd (Ref. 11), and others. They have been shown to arise from a straightforward reduction of the general nonlinear, large deflection equations given by Minguet and Dugundji (Ref. 14), and presented here in section 2.1. Often, the relation $\theta \simeq \phi$ is used in place of the more accurate relation given by equations 2.45. The $\epsilon = 0$ relation of equations 2.45 represents an effective no stretch condition and is used to determine the axial deflection u since v and w deflections have been determined.

These equations can be further reduced by a small angle assumption. For a flat blade without built-in twist, $\theta_t = 0$, and the trigonometric functions can be expanded to second order as,

$$\begin{aligned} \sin\theta &\simeq \theta \\ \cos\theta &\simeq 1 - \theta^2/2 \end{aligned} \tag{2.46}$$

Placing these into the previous equations 2.44 gives the more useful form,

$$w: \quad [(EI_\eta\, w'' + (EI_\zeta - EI_\eta)(v''\theta + w''\theta^2)]'' \\ -(w'\, F_x)' = p_{zT} + m'_{yT}$$

$$
\begin{aligned}
v: \quad & [EI_\zeta v'' + (EI_\zeta - EI_\eta)(w''\theta - v''\theta^2)]'' \\
& \qquad -(v' F_x)' = p_{yT} - m'_{zT} \qquad (2.47)
\end{aligned}
$$

$$
\begin{aligned}
\phi: \quad & -(GJ\phi')' + (EI_\zeta - EI_\eta)[(w''^2 - v''^2)\theta + v''w''] \\
& \qquad = m_{1T}
\end{aligned}
$$

This form shows more clearly the type of nonlinear couplings involved between the w, v, and ϕ motions. These nonlinear couplings depend on the difference in bending stiffness, $(EI_\zeta - EI_\eta)$, and would give rise to linear couplings by the presence of an initial static deflection in w and v. Similar equations can be obtained for blades with an initial twist θ_t, by replacing equations 2.47 with,

$$
\begin{aligned}
\sin(\theta_t + \theta) &\simeq \sin\theta_t + \theta\cos\theta_t - \theta^2/2\sin\theta_t \\
\cos(\theta_t + \theta) &\simeq \cos\theta_t - \theta\sin\theta_t - \theta^2/2\cos\theta_t \qquad (2.48)
\end{aligned}
$$

Although the moderate deflection equations 2.47 lend themselves well to Galerkin solution, one should be careful to use a sufficient number of modes to capture the nonlinear effects when static deflections are present. They can always be checked against the general solution of the twelve nonlinear differential equations presented by Minguet and Dugundji.

Before leaving this section, it might be interesting to note that the moderate deflection equations can also be derived from an energy formulation by minimizing the total potential energy Π of the functional,

$$
\begin{aligned}
\Pi = & \frac{1}{2}\int_0^L EI_\eta (w''\cos\theta - v''\sin\theta)^2\,dx \\
& + \frac{1}{2}\int_0^L EI_\zeta (w''\sin\theta + v''\cos\theta)^2\,dx \\
& + \frac{1}{2}\int_0^L GJ(\theta' + w'v'')^2\,dx \qquad (2.49) \\
& + \frac{1}{2}\int_0^L F_x (w'^2 + v'^2)\,dx \\
& - \int_0^L (p_{yT}v + p_{zT}w - m_{yT}w' + m_{zT}v' + m_{1T}\phi)\,dx
\end{aligned}
$$

A simple application of variational methods will lead to the moderate deflection equations given by equations 2.44 and 2.47.

Chapter 3

Inertial Modeling

3.1 Global Equations

Inertial load terms can be obtained by evaluating acceleration of a particle on the blade and expressing the resulting forces and moments in the rotating axis system (Figure 2.1). That is,

$$\begin{aligned} \vec{p}_G &= -\int\int_A \rho\, \vec{a}\, dA \\ \vec{m}_G &= -\int\int_A \rho\, \vec{p} \times \vec{a}\, dA \end{aligned} \tag{3.1}$$

where

$$\vec{a} = \frac{d^2\vec{R}}{dt^2} = \ddot{\vec{r}} + 2\vec{\Omega} \times \dot{\vec{r}} + \vec{\Omega} \times (\vec{\Omega} \times \vec{r}) + \vec{g} \tag{3.2}$$

The vector $\vec{r}$ is the deformed position vector of the particle of interest, and can be represented in the global coordinate x, y, z as,

$$\vec{r}(\eta, \zeta) = \begin{Bmatrix} x + \underline{e} \\ y \\ z - \beta_p\, \underline{e} \end{Bmatrix} + \vec{p}(\eta, \zeta) \tag{3.3}$$

where

$$\vec{p}(\eta, \zeta) = T^T \begin{Bmatrix} 0 \\ \eta \\ \zeta \end{Bmatrix} \tag{3.4}$$

The first part of the position vector $\vec{r}$ above represents the position of the center of the cross-section and the second part the position in the global axes of the point on

that cross-section. The rotational speed vector $\vec{\Omega}$ and the gravity vector $g\vec{i}_{z0}$ can be written in the global system x, y, z as

$$\vec{\Omega} = \Omega \begin{Bmatrix} \beta_p \\ 0 \\ 1 \end{Bmatrix}$$

$$\vec{g} = g \begin{Bmatrix} \beta_p \\ 0 \\ 1 \end{Bmatrix} \tag{3.5}$$

Note also that the first and the second time derivatives of $\vec{r}$ become

$$\dot{\vec{r}} = \begin{Bmatrix} \dot{x} + \dot{T}_{21}\eta + \dot{T}_{31}\zeta \\ \dot{y} + \dot{T}_{22}\eta + \dot{T}_{32}\zeta \\ \dot{z} + \dot{T}_{23}\eta + \dot{T}_{33}\zeta \end{Bmatrix} \tag{3.6}$$

$$\ddot{\vec{r}} = \begin{Bmatrix} \ddot{x} + \ddot{T}_{21}\eta + \ddot{T}_{31}\zeta \\ \ddot{y} + \ddot{T}_{22}\eta + \ddot{T}_{32}\zeta \\ \ddot{z} + \ddot{T}_{23}\eta + \ddot{T}_{33}\zeta \end{Bmatrix} \tag{3.7}$$

The first term of equation 3.2 represents the translational acceleration while the second and third term represent the well known Coriolis, and centrifugal accelerations, respectively. The last term is due to the gravity field.

Substituting the above equations for $\vec{r}$, $\dot{\vec{r}}$, $\ddot{\vec{r}}$, $\vec{\Omega}$, and $\vec{g}$ into equation 3.2 and subsequently into 3.1, the resulting inertial forces per unit length of the blade in the global system x, y, z can be written as follows.

$$\begin{aligned}
p_x &= -m\,[\ddot{x} + \ddot{T}_{21}\eta_{cg} + \ddot{T}_{31}\zeta_{cg}] + 2\Omega m[\dot{y} + \dot{T}_{22}\eta_{cg} \\
&\quad + \dot{T}_{32}\zeta_{cg}] + \Omega^2 m[(x + \underline{e} - \beta_p z) + (T_{21} - \beta p T_{23})\eta_{cg} \\
&\quad + (T_{31} - \beta_p T_{33})\zeta_{cg}] - \beta_p m g \\
p_y &= -m\,[\ddot{y} + \ddot{T}_{22}\eta_{cg} + \ddot{T}_{32}\zeta_{cg}] - 2\Omega m[(\dot{x} - \beta_p \dot{z}) \\
&\quad + (\dot{T}_{21} - \beta_p \dot{T}_{23})\eta_{cg} + (\dot{T}_{31} - \beta_P \dot{T}_{33})\zeta_{cg}] \\
&\quad + \Omega^2 m[y + T_{22}\eta_{cg} + T_{32}\zeta_{cg}] \\
p_z &= -m\,[\ddot{z} + \ddot{T}_{23}\eta_{cg} + \ddot{T}_{33}\zeta_{cg}] - 2\Omega m\beta_p(\dot{y} + \dot{T}_{22}\eta_{cg} \\
&\quad + \dot{T}_{32}\zeta_{cg}) - \Omega^2 m\beta_p(x + \underline{e} + T_{21}\eta_{cg} \\
&\quad + T_{31}\zeta_{cg}) - mg
\end{aligned} \tag{3.8}$$

Likewise, the inertial moments per unit length are obtained as

$$
\begin{aligned}
m_x &= -[m(-\ddot{y}T_{23} + \ddot{z}T_{22})\eta_{cg} + m(-\ddot{y}T_{33} + \ddot{z}T_{32})\zeta_{cg} \\
&\quad +(T_{32}\ddot{T}_{23} + T_{22}\ddot{T}_{33} - T_{33}\ddot{T}_{22} - T_{23}\ddot{T}_{32})I_{\eta\zeta} \\
&\quad +(T_{22}\ddot{T}_{23} - T_{23}\ddot{T}_{22})I_{\zeta\zeta} + (T_{32}\ddot{T}_{33} - T_{33}\ddot{T}_{32})I_{\eta\eta}] \\
&\quad -2\Omega[m\{\beta_p\dot{y}T_{22} - T_{23}(\dot{x} - \beta_p\dot{z})\}\eta_{cg} + m\{\dot{y}T_{32} \\
&\quad -T_{33}(\dot{x} - \beta_p\dot{z})\}\zeta_{cg} + \{\beta_p(T_{22}\dot{T}_{32} + T_{32}\dot{T}_{22}) \\
&\quad -T_{23}(\dot{T}_{31} - \beta_p\dot{T}_{33}) - T_{33}(\dot{T}_{21} - \beta_p\dot{T}_{23})\}I_{\eta\zeta} + \{\beta_pT_{22}\dot{T}_{22} \\
&\quad -T_{23}(\dot{T}_{21} - \beta_p\dot{T}_{23})\}I_{\zeta\zeta} + \{\beta_pT_{32}\dot{T}_{32} - T_{33}(\dot{T}_{31} - \beta_p\dot{T}_{33})\}I_{\eta\eta}] \\
&\quad -\Omega^2[m\{\beta_p(x + \underline{e})T_{22} + yT_{23}\}\eta_{cg} + m\{\beta_p(x + \underline{e})T_{32} \\
&\quad +yT_{33}\}\zeta_{cg} + \{(\beta_pT_{31} + T_{33})T_{22} + (\beta_pT_{21} + T_{23})T_{32}\}I_{\eta\zeta} \\
&\quad +(\beta_pT_{21} + T_{23})T_{22}I_{\zeta\zeta} + (\beta_pT_{31} + T_{33})T_{32}I_{\eta\eta}] \\
&\quad +mg(T_{22}\eta_{cg} + T_{32}\zeta_{cg}) \\
m_y &= -[m(\ddot{x}T_{23} - \ddot{z}T_{21})\eta_{cg} + m(\ddot{x}T_{33} - \ddot{z}T_{31})\zeta_{cg} \\
&\quad +(T_{23}\ddot{T}_{31} + T_{33}\ddot{T}_{21} - T_{21}\ddot{T}_{33} - T_{31}\ddot{T}_{23})I_{\eta\zeta} \\
&\quad +(T_{23}\ddot{T}_{21} - T_{21}\ddot{T}_{23})I_{\zeta\zeta} + (T_{33}\ddot{T}_{31} - T_{31}\ddot{T}_{33})I_{\eta\eta}] \\
&\quad +2\Omega[m\{\beta_p\dot{y}T_{21} + T_{23}\dot{y}\}\eta_{cg} - m\dot{y}(T_{33} - \beta_pT_{31})\zeta_{cg} \\
&\quad +\{\beta_p(T_{21}\dot{T}_{32} + T_{31}\dot{T}_{22}) + T_{23}\dot{T}_{32} + T_{33}\dot{T}_{22}\}I_{\eta\zeta} \\
&\quad +\{-\beta_pT_{21}\dot{T}_{22} - T_{23}\dot{T}_{22}\}I_{\zeta\zeta} - \{\beta_pT_{31}\dot{T}_{32} + T_{33}\dot{T}_{32}\}I_{\eta\eta}] \\
&\quad +\Omega^2[m\{\beta_p(x + \underline{e})T_{21} + (x + \underline{e} - \beta_pz)T_{23}\}\eta_{cg} \\
&\quad +m\{\beta_p(x + \underline{e})T_{31} + (x + \underline{e} - \beta_pz)T_{33}\}\zeta_{cg} \\
&\quad +\{T_{21}T_{33} + T_{23}T_{31} + 2\beta_p(T_{21}T_{31} - T_{23}T_{33})\}I_{\eta\zeta} \\
&\quad +\{T_{21}T_{23} + \beta_p(T_{21}^2 - T_{23}^2)\}I_{\zeta\zeta} \\
&\quad +\{T_{31}T_{33} + \beta_p(T_{31}^2 - T_{33}^2)\}I_{\eta\eta}] \\
&\quad -mg\{(T_{21} - \beta_pT_{23})\eta_{cg} + (T_{31} - \beta_pT_{33})\}\zeta_{cg} \\
m_z &= -[m(\ddot{y}T_{21} - \ddot{x}T_{22})\eta_{cg} + m(\ddot{y}T_{31} - \ddot{x}T_{32})\zeta_{cg}
\end{aligned}
$$

$$
\begin{aligned}
&+(T_{21}\ddot{T}_{32} + T_{31}\ddot{T}_{22} - T_{22}\ddot{T}_{31} - T_{32}\ddot{T}_{21})I_{\eta\zeta} \\
&+(T_{21}\ddot{T}_{22} - T_{22}\ddot{T}_{21})I_{\zeta\zeta} + (T_{31}\ddot{T}_{32} - T_{32}\ddot{T}_{31})I_{\eta\eta}] \\
&-2\Omega[m\{(\dot{x} - \beta_p\dot{z})T_{21} + \dot{y}T_{22}\}\eta_{cg} + m\{(\dot{x} - \beta_p\dot{z})T_{31} \\
&+\dot{y}T_{32}\}\zeta_{cg} + \{T_{21}(\dot{T}_{31} - \beta_p\dot{T}_{33}) + T_{31}(\dot{T}_{21} - \beta_p\dot{T}_{23}) \\
&+T_{22}\dot{T}_{32} + T_{32}\dot{T}_{22}\}I_{\eta\zeta} + \{T_{21}(\dot{T}_{21} - \beta_p\dot{T}_{23}) \\
&+T_{22}\dot{T}_{22}\}I_{\zeta\zeta} + \{T_{31}(\dot{T}_{31} - \beta_p\dot{T}_{33)} + T_{32}\dot{T}_{32}\}I_{\eta\eta}] \\
&-\Omega^2[m\{-yT_{21} + (x + \underline{e} - \beta_p z)T_{22}\}\eta_{cg} \\
&+m\{-yT_{31} + (x + \underline{e} - \beta_p z)T_{32}\}\zeta_{cg} \\
&-\beta_p(T_{22}T_{33} + T_{32}T_{23})I_{\eta\zeta} - \beta_p T_{22}T_{23}I_{\zeta\zeta} \\
&-\beta_p T_{32}T_{33}I_{\eta\eta}] - \beta_p mg(T_{22}\eta_{cg} + T_{32}\zeta_{cg})
\end{aligned}
\tag{3.9}
$$

where

$$
\begin{aligned}
m\,\eta_{cg} &= \int\int_A \rho\eta\,dA, \quad m\,\zeta_{cg} = \int\int_A \rho\zeta\,dA \\
I_{\zeta\zeta} &= \int\int_A \rho\eta^2\,dA, \quad I_{\eta\eta} = \int\int_A \rho\zeta^2\,dA \\
I_{\eta\zeta} &= \int\int_A \rho\eta\zeta\,dA
\end{aligned}
\tag{3.10}
$$

These are well-known quantities of the cross-section and for practical purposes, it is often assumed that $\zeta_{cg} \approx 0$ and $I_{\eta\zeta} \approx 0$.

3.2 Local Equations

Since the basic equilibrium equations 2.9 and 2.10 are written in the local coordinates ξ, η, ζ rather than in the global x, y, z, it is useful to obtain inertial loads in the local coordinate system. This can be done simply by expanding the local expressions in terms of the global ones via

$$
\begin{aligned}
p_i &= T_{i1}p_x + T_{i2}p_y + T_{i3}p_z \\
m_i &= T_{i1}m_x + T_{i2}m_y + T_{i3}m_z
\end{aligned}
\tag{3.11}
$$

where $i = 1, 2, 3$. In these expansions, one can take advantage of the following useful relations.

$$
\begin{aligned}
T_{11} &= T_{22}\,T_{33} - T_{23}\,T_{32} \\
T_{12} &= T_{23}\,T_{31} - T_{21}\,T_{33} \\
T_{13} &= T_{21}\,T_{32} - T_{22}\,T_{31} \\
T_{21} &= T_{13}\,T_{32} - T_{12}\,T_{33} \\
T_{22} &= T_{11}\,T_{33} - T_{13}\,T_{31} \\
T_{23} &= T_{12}\,T_{31} - T_{11}\,T_{32} \\
T_{31} &= T_{12}\,T_{23} - T_{13}\,T_{22} \\
T_{32} &= T_{13}\,T_{21} - T_{11}\,T_{23} \\
T_{33} &= T_{11}\,T_{22} - T_{12}\,T_{21}
\end{aligned}
\tag{3.12}
$$

$$
\begin{aligned}
T_{11}^2 + T_{12}^2 + T_{13}^2 &= 1 \\
T_{21}^2 + T_{22}^2 + T_{23}^2 &= 1 \\
T_{31}^2 + T_{32}^2 + T_{33}^2 &= 1
\end{aligned}
$$

$$
\begin{aligned}
T_{11}\,T_{21} + T_{12}\,T_{22} + T_{13}\,T_{23} &= 0 \\
T_{11}\,T_{31} + T_{12}\,T_{32} + T_{13}\,T_{33} &= 0 \\
T_{21}\,T_{31} + T_{22}\,T_{32} + T_{23}\,T_{33} &= 0
\end{aligned}
\tag{3.13}
$$

Equations 3.12 and 3.13 are results of the orthogonality identities $[T]^{-1} = [T]^T$ and $|T| = 1$, respectively. Also, one can observe that

$$
\begin{aligned}
\dot{T}_{1i} &= \omega_\zeta\,T_{2i} - \omega_\eta\,T_{3i} \\
\dot{T}_{2i} &= \omega_\xi\,T_{3i} - \omega_\zeta\,T_{1i} \\
\dot{T}_{3i} &= \omega_\eta\,T_{1i} - \omega_\xi\,T_{2i}
\end{aligned}
\tag{3.14}
$$

$$
\begin{aligned}
\ddot{T}_{1i} &= -(\omega_\eta^2 + \omega_\zeta^2)T_{1i} + (\dot{\omega}_\zeta + \omega_\xi\omega_\eta)T_{2i} \\
&\quad + (-\dot{\omega}_\eta + \omega_\xi\omega_\zeta)T_{3i} \\
\ddot{T}_{2i} &= (-\dot{\omega}_\zeta + \omega_\xi\omega_\eta)T_{1i} - (\omega_\xi^2 + \omega_\zeta^2)T_{2i} \\
&\quad + (\dot{\omega}_\xi + \omega_\eta\omega_\zeta)T_{3i} \\
\ddot{T}_{3i} &= (\dot{\omega}_\eta + \omega_\xi\omega_\zeta)T_{1i} + (-\dot{\omega}_\xi + \omega_\eta\omega_\zeta)T_{2i} \\
&\quad - (\omega_\xi^2 + \omega_\eta^2)T_{3i}
\end{aligned} \tag{3.15}
$$

where $i = 1, 2, 3$. Equations 3.14 and 3.15 are results of the following relations of the time derivatives of $[T]$ to the rotation rate matrix $[\omega]$.

$$
[\dot{T}] \equiv \frac{\partial[T]}{\partial t} = [\omega][T]
$$

$$
[\ddot{T}] = \frac{\partial[\omega][T]}{\partial t} = ([\dot{\omega}] + [\omega][\omega])[T] \tag{3.16}
$$

with

$$
[\omega] = \begin{bmatrix} 0 & \omega_\zeta & -\omega_\eta \\ -\omega_\zeta & 0 & \omega_\xi \\ \omega_\eta & -\omega_\xi & 0 \end{bmatrix} \tag{3.17}
$$

where

$$
\begin{aligned}
\omega_\xi &= \frac{\partial\theta}{\partial t} + \sin\beta\,\frac{\partial\psi}{\partial t} \\
&\quad \text{(rotation rate around } \xi \text{ axis)} \\
\omega_\eta &= -\cos\theta\,\frac{\partial\beta}{\partial t} + \sin\theta\,\cos\beta\,\frac{\partial\psi}{\partial t} \\
&\quad \text{(rotation rate around } \eta \text{ axis)} \\
\omega_\zeta &= \sin\theta\,\frac{\partial\beta}{\partial t} + \cos\theta\,\cos\beta\,\frac{\partial\psi}{\partial t} \\
&\quad \text{(rotation rate around } \zeta \text{ axis)}
\end{aligned} \tag{3.18}
$$

Equations 3.18 are indeed identical to equation 2.6 with ∂s replaced by ∂t. Use of the rotation rate matrix $[\omega]$ will avoid the time derivatives of $[T]$ which are cumbersome to deal with.

After substituting the global expression equations 3.8 and 3.9 into equation 3.11, and using the above relations, one can summarize the inertial forces and moments in the local coordinates as follows.

$$
\begin{aligned}
p_1 &= -m[\ddot{x}T_{11} + \ddot{y}T_{12} + \ddot{z}T_{13} + (-\dot{\omega}_\zeta + \omega_\xi\omega_\eta)\eta_{cg}] \\
&\quad + 2\Omega m[\dot{y}T_{11} - (\dot{x} - \beta_p\dot{z})T_{12} - \beta_p\dot{y}T_{13} \\
&\quad - \omega_\xi(T_{23} + \beta_p T_{21})\eta_{cg}] \\
&\quad + \Omega^2 m[(x + \underline{e} - \beta_p z)T_{11} + yT_{12} - \beta_p(x + \underline{e})T_{13} \\
&\quad - \{T_{13}T_{23} + \beta_p(T_{11}T_{23} + T_{13}T_{21})\}\eta_{cg}] \\
&\quad - mg(\beta_p T_{11} + T_{13}) \\
p_2 &= -m[\ddot{x}T_{21} + \ddot{y}T_{22} + \ddot{z}T_{23} - (\omega_\xi^2 + \omega_\zeta^2)\eta_{cg}] \\
&\quad + 2\Omega m[\dot{y}T_{21} - (\dot{x} - \beta_p\dot{z})T_{22} - \beta_p\dot{y}T_{23} \\
&\quad + \{\omega_\xi(T_{13} + \beta_p T_{11}) + \omega_\zeta(T_{33} + \beta_p T_{31}\}\eta_{cg}] \\
&\quad + \Omega^2 m[(x + \underline{e} - \beta_p z)T_{21} + yT_{22} - \beta_p(x + \underline{e})T_{23} \\
&\quad + (1 - T_{23}^2 - 2\beta_p T_{21}T_{23})\eta_{cg}] \\
&\quad - mg(\beta_p T_{21} + T_{23}) \\
p_3 &= -m[\ddot{x}T_{31} + \ddot{y}T_{32} + \ddot{z}T_{33} + (\dot{\omega}_\xi + \omega_\eta\omega_\zeta)\eta_{cg}] \\
&\quad + 2\Omega m[\dot{y}T_{31} - (\dot{x} - \beta_p\dot{z})T_{32} - \beta_p\dot{y}T_{33} \\
&\quad - \omega_\zeta(T_{23} + \beta_p T_{21})\eta_{cg}] \\
&\quad + \Omega^2 m[(x + \underline{e} - \beta_p z)T_{31} + yT_{32} - \beta_p(x + \underline{e})T_{33} \\
&\quad - \{T_{23}T_{33} + \beta_p(T_{31}T_{23} + T_{33}T_{21})\}\eta_{cg}] \\
&\quad - mg(\beta_p T_{31} + T_{33})
\end{aligned}
\tag{3.19}
$$

$$
\begin{aligned}
m_1 &= -I_{\xi\xi}\dot{\omega}_\xi - (I_{\zeta\zeta} - I_{\eta\eta})\omega_\eta\omega_\zeta \\
&\quad - m(\ddot{x}T_{31} + \ddot{y}T_{32} + \ddot{z}T_{33})\eta_{cg} \\
&\quad - 2\Omega[m\{(\dot{x} - \beta_p\dot{z})T_{32} - \dot{y}(T_{31} - \beta_p T_{33})\}\eta_{cg} \\
&\quad + \omega_\zeta(T_{23} + \beta_p T_{21})I_{\zeta\zeta} + \omega_\eta(T_{33} + \beta_p T_{31})I_{\eta\eta}]
\end{aligned}
$$

$$
\begin{aligned}
& -\Omega^2 m[-yT_{32} - (x+\underline{e}-\beta_p z)T_{31} + \beta_p(x+\underline{e})T_{33}]\eta_{cg} \\
& -\Omega^2[T_{23}T_{33} + \beta_p(T_{21}T_{33} + T_{23}T_{31})](I_{\zeta\zeta} - I_{\eta\eta}) \\
& +mg(T_{33} + \beta_p T_{31})\eta_{cg} \\
m_2 \;=\; & -I_{\eta\eta}(\dot{\omega}_\eta + \omega_\xi\omega_\zeta) \\
& -2\Omega[\omega_\xi T_{33} - \beta_p\omega_\xi(T_{22}T_{13} + T_{23}T_{12})]I_{\eta\eta} \\
& -\Omega^2[T_{33}T_{13} + \beta_p(T_{31}T_{13} + T_{33}T_{11})]I_{\eta\eta} \\
m_3 \;=\; & -I_{\zeta\zeta}(\dot{\omega}_\zeta - \omega_\xi\omega_\eta) \\
& +m(\ddot{x}T_{11} + \ddot{y}T_{12} + \ddot{z}T_{13})\eta_{cg} \\
& -2\Omega[m\{-(\dot{x}-\beta_p\dot{z})T_{12} + \dot{y}(T_{11}-\beta_p T_{13})\}\eta_{cg} \\
& -\omega_\xi(T_{23}+\beta_p T_{21})I_{\zeta\zeta}] \\
& -\Omega^2 m[yT_{12} + (x+\underline{e}-\beta_p z)T_{11} - \beta_p(x+\underline{e})T_{13}]\eta_{cg} \\
& +\Omega^2[T_{23}T_{13} + \beta_p(T_{21}T_{13} + T_{23}T_{11})]I_{\zeta\zeta} \\
& -mg(T_{13} + \beta_p T_{11})\eta_{cg}
\end{aligned}
\tag{3.20}
$$

Here, $I_{\xi\xi} = I_{\eta\eta} + I_{\zeta\zeta}$ is the mass moment of inertia of the blade about the reference axis per unit length. In the above expressions, the mass centroid ζ_{cg} and the cross product of inertia $I_{\eta\zeta}$ have been neglected.

Chapter 4

Aerodynamic Modeling

4.1 Dynamic Stall Modeling

For the present research, one needs an aerodynamic tool that can adequately describe both linear unstalled and nonlinear stalled aerodynamic loads with ease and simplicity. In particular, its form must be such that it can be immediately applied to the stability and response analysis for the composite rotor blades using a simple harmonic method. Among such linear models, the Greenberg's or Loewy's aerodynamic theories with constant inflow model has been traditionally used for the stability analysis of rotary wing problems (Ref. 33, 34). Also, quasi-steady aerodynamics with dynamic inflow concept is frequently used (Ref. 35, 36).

As for the dynamic stall modeling part, the ONERA Model that consists of two ordinary differential equations has recently become popular recently (Ref. 25). However, most of the applications of ONERA Model in rotary wing problems have exclusively focused on the periodic responses and stabilities of forward flight cases (Ref. 37, 38, 39). In forward flight, the dynamic stall phenomenon near retreating blade side does not produce stall flutter because of its short period of presence. On the other hand, dynamic stall in hovering flight, if it ever exists, can develop into flutter oscillations. The periodic responses in this case are self-excited oscillations that are sustained over a long period of time. For a simple analysis of nonlinear flutter problems only first few harmonics are adequate to capture the amplitude levels as well as

the associated frequency and dynamic pressure. In the present analysis, only the first harmonics are extracted from the nonlinear ONERA Model.

The ONERA Model was first developed at the *Office National d'Etudes et de Recherches Aerospatiales* by Tran and Petot (Ref. 25). The model is a semi-empirical, unsteady, nonlinear model based upon quasi-linear, small amplitude oscillation experimental data. It consists of two ordinary differential equations. The first equation incorporates a single lag term on the linear part of the airfoil's static force curve, and is, thus, analogous to the Theodorsen function for linear theory. The second equation incorporates two lag terms on the nonlinear (i.e., stalling) portion of the airfoil's static force curve. The ONERA model was later investigated by Peters (Ref. 39) in an attempt to differentiate the roles of angle of attack due to pitching and angle of attack due to plunging, and also to include the unsteady free-stream, large angles of attack, and reversed flow. The coefficients of the linear part were thus chosen such that it fits the theoretical Theodorsen or Greenberg function within the linear domain of operation. More recently, Tran and Petot (Ref. 40) presented a unified version of the ONERA equations which, in addition to all of the previous revisions, add the effect of compressibility and the stalled drag. The final equations appear as circulations rather than lift and moment coefficients as per Peters' suggestion.

The original version of ONERA model expressed in lift and moment coefficients has been used by Dunn and Dugundji (Ref. 29) along with harmonic balance method for the nonlinear response analysis of fixed wing surfaces. Most recently, Barwey et al (Ref. 41) have used the complete version including the stalled drag in evaluating lag damping of rotor blades in forward flight. The present analysis is a further extension of these models including the effects of large angle of attack, pulsating incoming velocity, drag stall, and the effect of stall delay. Following the suggestions of Peters (Ref. 39), Tran and Petot (Ref. 40), and Barwey et. al (Ref. 41), the basic ONERA equations appropriate for rotary wing problems can be written in real time as follows.

Lift & Moment;

$$
\begin{aligned}
F_{NC} &= \frac{1}{2}\rho S_z (s_z b \dot{V}_3 + l_z b V \dot{\epsilon}_e + k_z b^2 \ddot{\epsilon}_e) \\
F_C &= \frac{1}{2}\rho S_z (V\Gamma_{1z} + V\Gamma_{2z})
\end{aligned} \tag{4.1}
$$

where

$$
\begin{aligned}
\Gamma_{1z} &= a_{0z} V_0 \alpha_0 + \Gamma_{11z} \\
\dot{\Gamma}_{11z} + \lambda_z \frac{V_0}{b}\Gamma_{11z} &= \lambda_z a_{0z} \frac{V_0}{b} V_3 + \lambda_z \sigma_z V_0 \dot{\epsilon}_e \\
&\quad + \gamma_z a_{0z} \dot{V}_3 + \gamma_z \sigma_z b \ddot{\epsilon}_e \\
\ddot{\Gamma}_{2z} + a_z \frac{V_0}{b}\dot{\Gamma}_{2z} + r_z \frac{V_0^2}{b^2}\Gamma_{2z} &= -r_z [\frac{V_0^2}{b^2}\Delta\Gamma_z + e_z \frac{V_0}{b}\frac{\partial \Delta\Gamma_z}{\partial t}] \\
\text{with} \quad \Delta\Gamma_z &\equiv V\Delta C_z
\end{aligned} \tag{4.2}
$$

and the subscript $z = L$ or M for lift or moment.

Drag;

$$
D = \frac{1}{2}\rho c (V\Gamma_{D1} + V\Gamma_{D2}) \tag{4.3}
$$

where

$$
\begin{aligned}
\Gamma_{D1} &= V C_{D0} \\
\ddot{\Gamma}_{D2} + a_D \frac{V_0}{b}\dot{\Gamma}_{D2} + r_D \frac{V_0^2}{b^2}\Gamma_{D2} &= -[r_D \frac{V_0^2}{b^2}\Delta\Gamma_D + e_D \frac{V_0}{b}\dot{V}_3] \\
\text{with} \quad \Delta\Gamma_D &\equiv V\Delta C_D
\end{aligned} \tag{4.4}
$$

Here, using the low Reynolds number characteristics of NACA 0012 airfoil (Ref. 42), the following coefficients have been assumed for lift and moment.

$$
S_L = c, \quad s_L = \pi, \quad l_L = 0, \quad k_L = 0.5\pi
$$

$$
a_{0L} = \sigma_L = 5.9
$$

$$\lambda_L = 0.15, \quad \gamma_L = 0.55$$

$$\begin{aligned}
a_L &= 0.25 + 0.1\,(\Delta C_L)^2 \quad \text{if } Re \geq 340,000 \\
&\ 0.25 + 0.4\,(\Delta C_L)^2 \quad \text{if } Re \leq 340,000 \\
r_L &= [0.2 + 0.1\,(\Delta C_L)^2]^2 \quad \text{if } Re \geq 340,000 \\
&\ [0.2 + 0.23\,(\Delta C_L)^2]^2 \quad \text{if } Re \leq 340,000 \\
e_L &= -0.6\,(\Delta C_L)^2 \quad \text{if } Re \geq 340,000 \\
&\ -2.7\,(\Delta C_L)^2 \quad \text{if } Re \leq 340,000
\end{aligned}$$

$$S_M = c^2, \quad s_M = l_M = -\frac{\pi}{4}, \quad k_M = -\frac{3\pi}{16}$$

$$a_{0M} = \sigma_M = \lambda_M = \gamma_M = 0$$

$$a_M = a_L, \quad r_M = r_L, \quad e_M = e_L$$

For the drag part, a cubic form of quasi-static drag curve is invoked (Ref. 29) and the coefficients suggested by Tran and Petot (Ref. 40), Barwey et. al (Ref. 41) are employed.

$$\begin{aligned}
C_{D0} &= 0.014 \\
a_D &= 0.32 \\
r_D &= (0.2 + 0.1\,\Delta C_L^2)^2 \\
e_D &= -0.015\,\Delta C_L^2
\end{aligned}$$

The lift and moment equations of the ONERA Model, like the classical Theodorsen equations, are separated into the noncirculatory or apparent mass F_{NC}, and circulatory F_C parts. ΔC_L, ΔC_M, and ΔC_D each represents the deviation of the linear static curve from the quasi static curve for the lift, moment, and drag coefficient,

respectively (Figure 4.1). $\Delta\Gamma_L$, $\Delta\Gamma_M$, $\Delta\Gamma_D$ can then be interpreted as deviations in the circulations associated with stalled region. These deviations are identically zero in the linear unstalled region, and are effective only in the nonlinear stalled region. In the unstalled case, the above lift and moment equations are reduced to the form of the Greenberg's expression with the first order Pade approximation for the Theodorsen function $C(k)$ (Ref. 43). One can further improve the stall model by introducing the so called *stall delay* in the the lift deviation ΔC_L. This is equivalent to assuming that no lift stall will occur and the lift coefficient will follow the linear straight line with slope of 5.9 during the delay time $\Delta\tau$ after the angle of attack has passed the stall angle α_Δ. This delay is not to be confused with the time delay that has already been introduced implicitly by use of second order differential equations. The introduction of this additional stall delay has been necessitated by the observation that the delay effect by the differential equations alone is not enough to account for the actual initial delay phenomenon found from experiments. The concept of stall delay has been common, but was not introduced in recent applications including Dunn and Dugundji (Ref. 29) and Barwey et al. (Ref. 41). A delay of $\Delta\tau = 10$ in the non-dimensional time seems to be norm (Ref. 44), therefore this value is used in the present analysis. The normal downwash air velocity V_3 at the aerodynamic center appears as a boundary term in the linear parts of the lift and moment equations. It is noted that V_3 corresponds to the term $V\alpha - \dot{h}$ in the original linear aerodynamic theory by Theodorsen (Ref. 43), which is an approximate expression of the normal downwash velocity for small angles of attack. The role of V_3 is thus to account for large angles of attack in the linear parts of the ONERA equations. Likewise, the so called equivalent pitch rate $\dot{\epsilon}_e$ has replaced $\dot{\theta}$ in the original Theodorsen equations and enters as another important boundary term. Here it is defined as

$$\dot{\epsilon}_e \;=\; \omega_\xi + \Omega\,(T_{13} + \beta_p T_{11}) \tag{4.5}$$

According to Greenberg (Ref. 19), this new pitch rate includes the effect of the rotational speed in addition to the kinematical pitch rate ω_ξ.

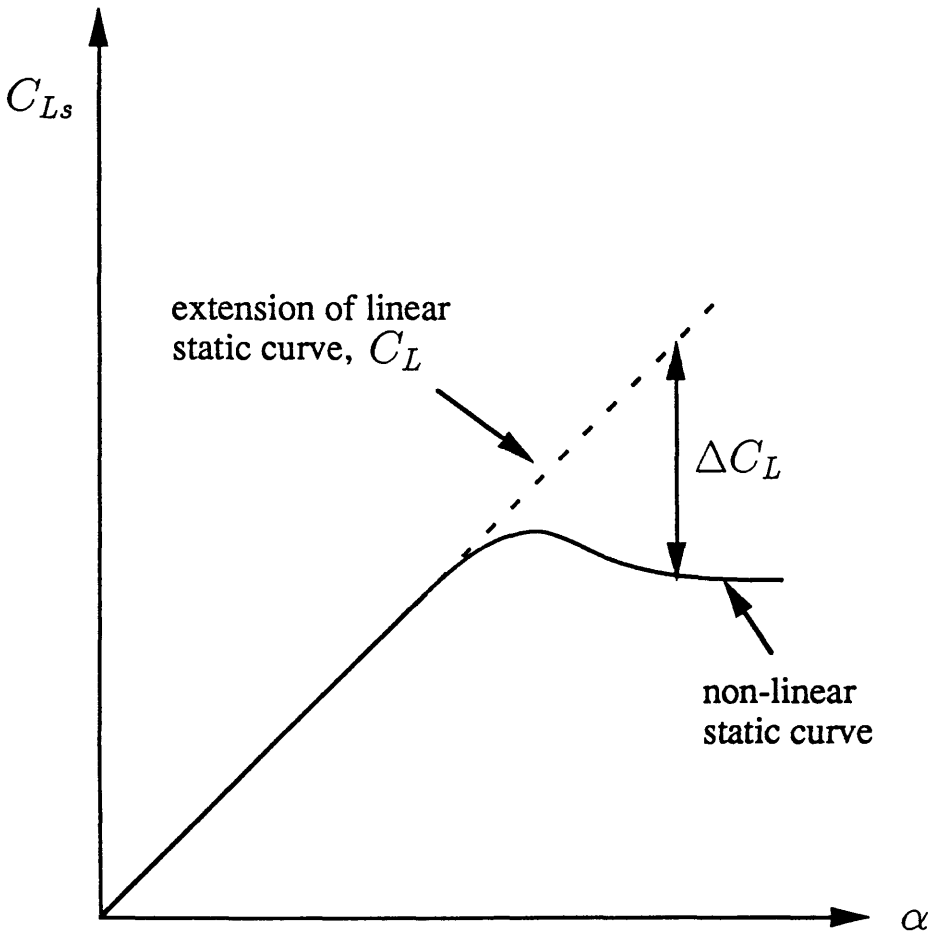

Figure 4.1: Definition of lift deficiency

4.2 Calculation of Air Velocities

The velocity vector of a blade particle at the aerodynamic center on a specific cross-section can be given in vector form as

$$\vec{V} = \vec{\Omega} \times \vec{r} + \dot{\vec{r}} + \vec{v}_i \tag{4.6}$$

where $\vec{r}$ is the distance between the origin and the aerodynamic center of the cross-section of interest and is given in the global system x, y, z as

$$\vec{r} = \begin{Bmatrix} x + \underline{e} + T_{21}\eta_r \\ y + T_{22}\eta_r \\ z - \beta_p \underline{e} + T_{23}\eta_r \end{Bmatrix} \tag{4.7}$$

where η_r represents the distance between the reference axis and the aerodynamic center on the cross-section. The rotational speed vector $\vec{\Omega}$ in the global system was given in equation 3.5, and the inflow velocity vector $\vec{v}_i$ in the global system is

$$\vec{v}_i = v_i \begin{Bmatrix} \beta_p \\ 0 \\ 1 \end{Bmatrix} \tag{4.8}$$

Note that the vector representation 4.6 is the total velocity of the blade particle against air particles incoming from above the blades. Substituting the expressions for $\vec{\Omega}$, $\vec{r}$, $\vec{v}_i$ into 4.6 yields the following three global components of $\vec{V}$.

$$\begin{aligned} V_{G1} &= -\Omega\,(y + T_{22}\eta_r + v_i\beta_p) + \dot{x} + \dot{T}_{21}\eta_r \\ V_{G2} &= \Omega\,(x - z\beta_p + T_{21}\eta_r - \beta_p T_{23}) + \dot{y} + \dot{T}_{22}\eta_r \\ V_{G3} &= \Omega\beta_p\,(y + T_{22}\eta_r) + v_i\,\dot{z} + \dot{T}_{23}\eta_r \end{aligned} \tag{4.9}$$

The local tangential and normal components of the air velocity V_2 and V_3 at the aerodynamic center, defined in the positive η, ζ directions, are then obtained by the transformation

$$\begin{aligned} V_2 &= T_{21}V_{G1} + T_{22}V_{G2} + T_{23}V_{G3} \\ V_3 &= -T_{31}V_{G1} - T_{32}V_{G2} - T_{33}V_{G3} \end{aligned}$$

Or in full expression,

$$
\begin{aligned}
V_2 &= \Omega\left[(x + \underline{e} - z\beta_p)T_{22} + y\left(\beta_p T_{23} - T_{21}\right)\right] \\
&\quad + \dot{x}\,T_{21} + \dot{y}\,T_{22} + \dot{z}\,T_{23} + v_i\left(T_{23} + \beta_p T_{21}\right) \\
V_3 &= -\Omega\left[(x + \underline{e} - z\beta_p)T_{32} + y\left(\beta_p T_{33} - T_{31}\right)\right] \\
&\quad - \dot{x}\,T_{31} - \dot{y}\,T_{32} - \dot{z}\,T_{33} - \eta_r\,\dot{\epsilon}_e - v_i\left(T_{33} + \beta_p T_{31}\right)
\end{aligned}
\tag{4.10}
$$

The total resultant air velocity at the aerodynamic center is then

$$
V = \sqrt{V_2^2 + V_3^2} \tag{4.11}
$$

The inflow velocity $v_i(s)$ at a given station is assumed to be constant, and can be obtained by considering a momentum equilibrium of a circular ring element. If it is assumed that the induced velocity is normal to the plane of the rotation, then equating a momentum change across the rotor over the ring element ds with the increment in the total thrust gives

$$
4\pi\rho(x + \underline{e} - \beta_p z)v_i^2 = N_B[(\beta_p T_{21} + T_{23})p_2^L + (\beta_p T_{31} + T_{33})p_3^L] \tag{4.12}
$$

Regardless of existence of stall, the right hand side is a complicated function of v_i itself. Hence, in order to get the exact solution, a Newton Raphson type iteration technique with an appropriate initial guess should be used. For example, the initial value of v_i can be assigned by solving the quadratic equation

$$
\begin{aligned}
&8\pi(x + \underline{e} - \beta_p z)v_i^2 + N_B\Omega(x + \underline{e} - \beta_p z)^2 c C_{L\alpha}(T_{33} \\
&\quad + \beta_p T_{31})\frac{v_i}{V_2} - N_B\Omega^2(x + \underline{e} - \beta_p z)^2 c C_{L\alpha}\frac{V_3}{V_2} = 0
\end{aligned}
\tag{4.13}
$$

in the linear unstalled region, or

$$
\begin{aligned}
&8\pi(x + \underline{e} - \beta_p z)v_i^2 + N_B\Omega(x + \underline{e} - \beta_p z)^2 c a_{ss}(T_{33} \\
&\quad + \beta_p T_{31})\frac{v_i}{V_2} - N_B\Omega^2(x + \underline{e} - \beta_p z)^2 c(a_{ss}\frac{V_3}{V_2} + b_{ss}) = 0
\end{aligned}
\tag{4.14}
$$

in the nonlinear stalled region. Again, these equations are obtained by considering the momentum balance of a ring element with small angle of attack approximation. In the first equation the static lift curve is simply $C_{L\alpha}\,\alpha$, whereas in the second equation it is assumed by a single break point approximation, $a_{ss}\,\alpha + b_{ss}$.

4.3 Local Aerodynamic Loads

The aerodynamic loads given in equations 4.1 through 4.4 are located at the aerodynamic center of the blade cross-section. When the local airloads about the local coordinates ξ, η ζ, are calculated the following assumptions are then made. First, the apparent mass lift L_{NC} acts normal to the airfoil. Second, the circulatory lift L_C is normal to the resultant air velocity V, while the drag D is always parallel to the resultant air velocity. See Figure 4.4. The resulting local airloads are then expressed as

$$
\begin{aligned}
p_1 &= 0 \\
p_2 &= L_C \sin\alpha - D\cos\alpha \\
&= \rho\, b\,[V_3(\Gamma_{1L} + \Gamma_{2L}) - V_2(\Gamma_{1D} + \Gamma_{2D})] \\
p_3 &= L_C \cos\alpha + D\sin\alpha + L_{NC} \\
&= \rho\, b\,[V_2(\Gamma_{1L} + \Gamma_{2L}) + V_3(\Gamma_{1D} + \Gamma_{2D})] + L_{NC} \\
m_1 &= M_C + M_{NC} + (p_3^L - L_{NC})\,e_a \\
&= 2\,\rho\, b^2\, V(\Gamma_{1M} + \Gamma_{2M}) + M_{NC} + (p_3^L - L_{NC})\,e_a \\
m_2 &= 0 \\
m_3 &= 0
\end{aligned}
\tag{4.15}
$$

where

$$\alpha = \tan^{-1}\left(\frac{V_3}{V_2}\right) \tag{4.16}$$

is the effective angle of attack at the aerodynamic center. It is noted that in multiplying the local p_3 by its moment arm e_a in calculating m_1, the noncirculatory part

L_{NC} is not included because this apparent mass effect has already been accounted in M_{NC}, given by equation 4.1.

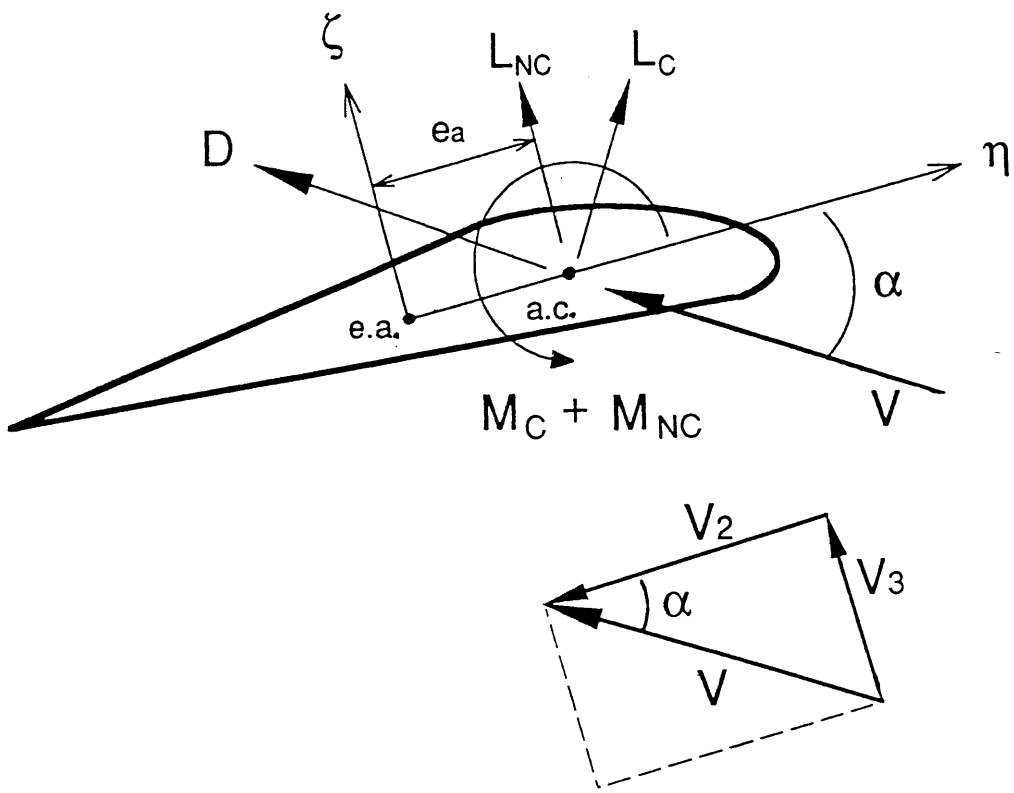

Figure 4.2: Illustration of air loads and velocities

Chapter 5

Modeling of Large Amplitude Motion

5.1 Harmonic Balance Method

In most of rotor blade applications, the basic equations are linearized about a given static position to make a small, perturbed free or flutter vibration problem. An appropriate eigenvalue problem is then solved to find the various mode shapes, their associated natural frequencies, and damping coefficients. This eigen method is not useful for the present analysis because, once the amplitudes become large, the frequency of a particular mode becomes a function of amplitude level of that mode due to couplings which may develop between the static and dynamic components in the governing equations. Furthermore, in the case of self-excited flutter problems it is expected that the critical rotational speed that yields a particular limit cycle solution may be different than the linear solution would predict. Thus, basic characteristics that distinguish the nonlinear, large amplitude vibration from the linear, small vibration can be summarized as follows:

(1) The frequency of a particular mode may change as its amplitude increases.

(2) The critical rotational speed changes from the linearly predicted one.

(3) The mode shapes can be altered from the linear ones.

(2) The static mean position of the beam can also change as a function of amplitude.

Two popular methods for the solution of general nonlinear dynamic problems are

direct numerical time integration of the basic equations, and the harmonic balance method. The former method will give the exact solution which shows the effects of all possible harmonics, while the latter method will yield a solution with only first few harmonics. The direct time integration requires a set of governing equations that contain only time t as independent variable. Thus, starting with the set of twelve basic partial differential equations described in chapter 2 including all the structural couplings, one has to reduce them into equations of motion involving only the four displacements u, v, w, θ such as equations 2.47, and then by performing appropriate modal series expansions, must reduce the equations into a modal form expressing them in terms of generalized coordinates. Usually, a large amount of computing time is used until the solutions reach their final steady states.

In the present analysis, the harmonic balance method is preferred because we do not want a set of approximate modal equations which are based on an ordering scheme, but rather use the large deflection equations to account for the fully nonlinear nature of the large amplitude problems. These twelve differential equations contain all the twelve variables, i. e. three Euler angles, three force resultants and three moment resultants, in addition to the usual three displacements x, y, z as their independent variables. In such a situation, it is more insightful to assume the time dependency of the solution in the the first harmonic form, and use numerical integration in space instead of in time. In doing so one loses, of course, the effects of higher harmonics, but the key argument is that in most of the nonlinear analysis, amplitudes associated with the first harmonics have the largest magnitudes, therefore are most critical in determining its response and stability. This is traditionally done for "describing function" methods of nonlinear vibration analysis.

Thus for the purpose of present analysis, all quantities are assumed to be of the following form

$$X(\Omega, \omega, t) = X_0(\Omega, \omega) + X_s(\Omega, \omega) \sin \omega t + X_c(\Omega, \omega) \cos \omega t \tag{5.1}$$

where X_0, X_s and X_c represent the static part and the associated amplitude (not a small quantity) around that static part, respectively. That X_s and X_c are not small quantities is reflected in the dependency of X_0, X_s and X_c on the rotational speed and frequency. Hence, unlike small vibration problem, a one-to-one correspondence between amplitude level and a combination of critical Ω, ω exist.

The analytic modeling consists of substituting the above expression for each variable into the twelve (fourteen if warping is included) governing equations. As a result of multiplications involving $\sin\omega t$ and $\cos\omega t$, this will produce many higher harmonics such as $\sin 2\omega t$, $\sin 3\omega t$,..., and $\cos 2\omega t$, $\cos 3\omega t$,...., etc.. These higher harmonic terms would be terms of higher order of magnitudes if the amplitude of motion were small. For details of how these multiplications are performed and the resulting coefficients, see the Appendices A, B, C. A harmonic balance method is then employed to retain only three kinds of terms; the ones that are constants and the ones that are coeffcients of $\sin\omega t$ and $\cos\omega t$. All the higher harmonic terms are left out. As explained in the Appendices, since there are many trigonometric functions involved in the twelve basic differential equations, it is essential to rely on a series expansion expressions of these trigonometric functions in order to extract the harmonic functions out of these trigonometric expressions. Then, it is inevitable that after truncating the higher harmonic terms, many of the remaining terms will still contain higher order of magnitude terms, for example, $\sin^4\omega t$ produces the constant 3/8 even after neglecting its higher harmonic components $\cos 2\omega t$ and $\cos 4\omega t$. It is clear that keeping all these higher order of magnitude terms will make the equations extremely long and unwieldy. Hence, an ordering scheme that keeps magnitudes of up to third order is employed to maintain a consistent level of nonlinearities in all of the equations. See the Appendix A. It is emphasized that this ordering scheme does not mean

$$\cos\theta \sim 1 - \frac{\theta^2}{2} + \text{H. O. T.}$$

but rather

$$\cos\theta \sim \cos\theta_0 - \sin\theta_0\,\Delta\theta - \frac{1}{2}\cos\theta_0\,(\Delta\theta)^2 + \frac{1}{6}\sin\theta_0\,(\Delta\theta)^3 + \text{H. O. T.}$$

where $\theta = \theta_0 + \Delta\theta$, and the θ_0 and $\Delta\theta = \theta_s \sin\omega t + \theta_c \cos\omega t$ represent the static and dynamic components of θ. Thus, the complete nonlinearity in the large rotations and deflections is still kept in a static sense; however strategically, terms only up to third order are kept in the dynamic counterparts.

Application of the harmonic balance followed by the approximating schemes will render the final thirty-six (forty-two, if warping is included) equations gradually incompatible as the amplitude level is raised. More specifically, these coupled equations would not satisfy equilibrium, geometric compatibilities, and stress-strain relations perfectly as their original twelve versions would. Therefore, one should expect deterioration in the degree of compatibility as amplitudes increase. Normally this would mean loss of accuracy in the solutions, or in the worst case, even the loss of convergence. However, as shown later in this report, this does not impose serious computational limits in most of reasonable range of amplitudes.

5.2 Fourier Analysis of Nonlinear Aerodynamics

For use in the harmonic balance method, it is necessary to be able to evaluate the lowest order frequency components of the ONERA nonlinear aerodynamic force coefficients when given a harmonic input. For the aerodynamic part, a variable X is assumed as

$$X(\Omega, k, \tau) = X_0(\Omega, k) + X_s(\Omega,\ k)\sin k\tau + X_c(\Omega, k)\cos k\tau \tag{5.2}$$

where

$$k = \text{reduced frequency} = \frac{\omega b}{V_0}$$

$$\tau = \text{non-dimensional time} = \frac{V_0 t}{b}$$

Here, V_0 is the time-averaged value of V at a given station along the blade. The effective angle of attack α is also expanded in the first harmonic form

$$\begin{aligned} \alpha(\tau) &= \alpha_0 + \alpha_s \sin k\tau + \alpha_c \cos k\tau \\ &= \alpha_0 + \alpha_V \sin\varphi \end{aligned} \tag{5.3}$$

where

$$\begin{aligned} \alpha_V &= \text{oscillation amplitude} \\ &= \sqrt{\alpha_s^2 + \alpha_c^2} \\ \varphi &= k\tau + \xi \\ \xi &= \sin^{-1}\frac{\alpha_c}{\alpha_V} \end{aligned} \tag{5.4}$$

Next, assume harmonic motion for ΔC_z in the non-dimensional time φ.

$$\Delta C_z(\varphi) = \Delta C_{z0} + \Delta C_{zVs} \sin\varphi + \Delta C_{zVc} \cos\varphi + \text{H.O.T.} \tag{5.5}$$

where by use of Fourier integrals

$$\begin{aligned} \Delta C_{z0} &= \frac{1}{\pi}\int_{-\frac{\pi}{2}}^{\frac{\pi}{2}} \Delta C_z(\varphi)\, d\varphi \\ \Delta C_{zVs} &= \frac{2}{\pi}\int_{-\frac{\pi}{2}}^{\frac{\pi}{2}} \Delta C_z(\varphi) \sin\varphi\, d\varphi \\ \Delta C_{zVc} &= \frac{2}{\pi}\int_{-\frac{\pi}{2}}^{\frac{\pi}{2}} \Delta C_z(\varphi) \cos\varphi\, d\varphi \end{aligned} \tag{5.6}$$

In general, the deviation ΔC_z can be described in any manner desired. For example, ΔC_z could be described by straight line fits between discrete points in the stalled domain. See Figure 5.1. That is, assuming that total N number of line fits are available, the general formula for the deviation ΔC_z is expressed as

$$\Delta C_z = 0 \qquad \text{if } \alpha \leq \alpha_\Delta$$

$$\Delta C_z = \sum_{i=1}^{j} a_{zi}(\alpha - \alpha_i) \text{ if } \alpha_j \leq \alpha < \alpha_{j+1}$$

$$\Delta C_z = \sum_{i=1}^{N} a_{zi}(\alpha - \alpha_i) \text{ if } \alpha \geq \alpha_N \tag{5.7}$$

where $\alpha_1 = \alpha_\Delta$ is the static stall angle of attack. For simplicity, following Dunn and Dugundji (Ref. 29), ΔC_z was defined by only two straight line fits of low Reynolds number static curves of NACA 0012 airfoil (see Figure 5.2, 5.3, 5.4). See Appendix D for the full description of the coefficients $a'_{zi}s$. This approximation of the actual stalled curves using only a few straight lines would not seem to affect the Fourier components of ΔC_z much because these are in fact smeared properties assessed over one cycle of the motion.

As indicated in section 4.1, to improve upon the aerodynamic modeling the stall delay of 10 units in the nondimensional time τ is implemented in the current harmonic model by simply taking out an initial part of the stalled region in the Fourier integrals. This stall delay model, as expected, will delay the onset of the actual stall by reducing the effective amounts of the Fourier integrals 5.6. In Appendix D, the details of an example of full Fourier analysis is given using a simple single line fit of ΔC_z and introducing the stall delay of 10 as suggested. One can extend this single line approximation to any number of line approximations by repeating the same procedure within each region $\alpha_j \leq \alpha \leq \alpha_{j+1}$, and then sum the resulting harmonic coefficients over the whole region according to 5.7.

After completing the Fourier analysis of the deviations ΔC_z, these harmonic expressions are substituted into the equations 4.1 through 4.4 to yield the harmonic components of the linear and nonlinear circulations, Γ_{1z}, Γ_{D1}, and, Γ_{2z}, Γ_{D2}. These components then define the total noncirculatory and circulatory lift, moment, and drag.

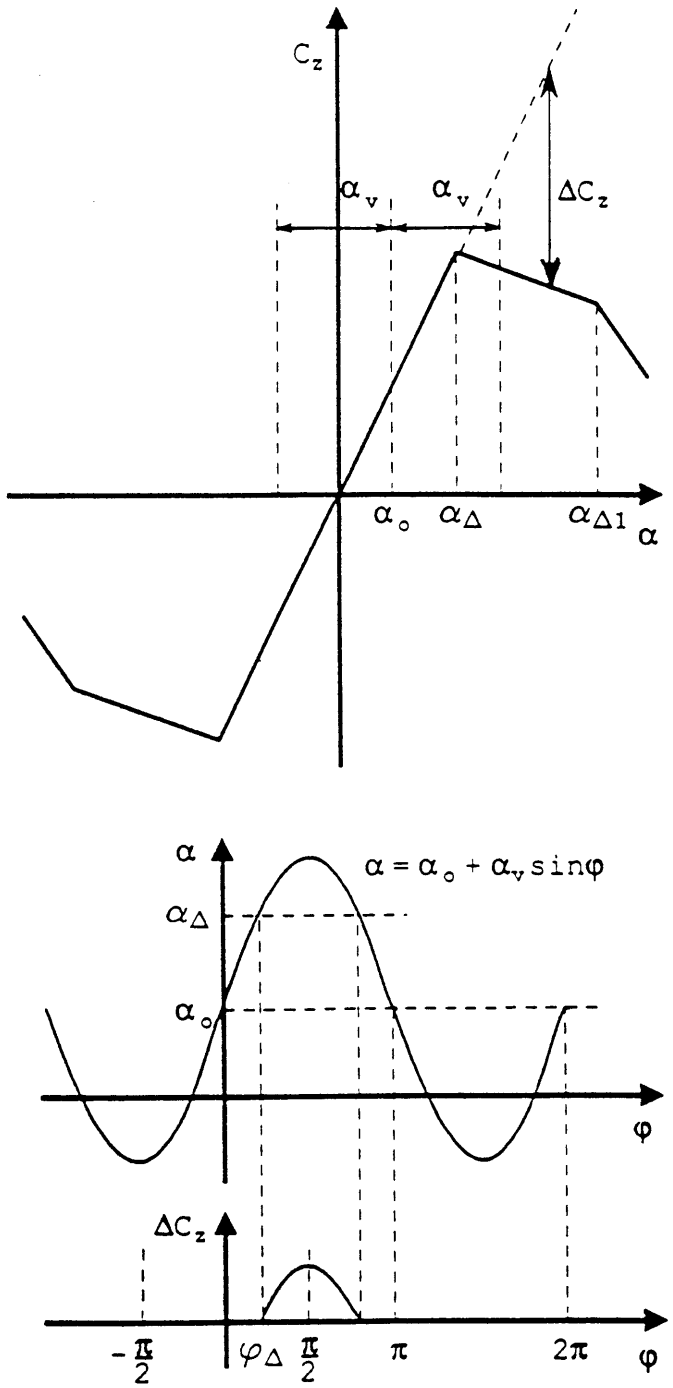

Figure 5.1: Example of oscillation stall angle on aerodynamic curve and in-phase domain

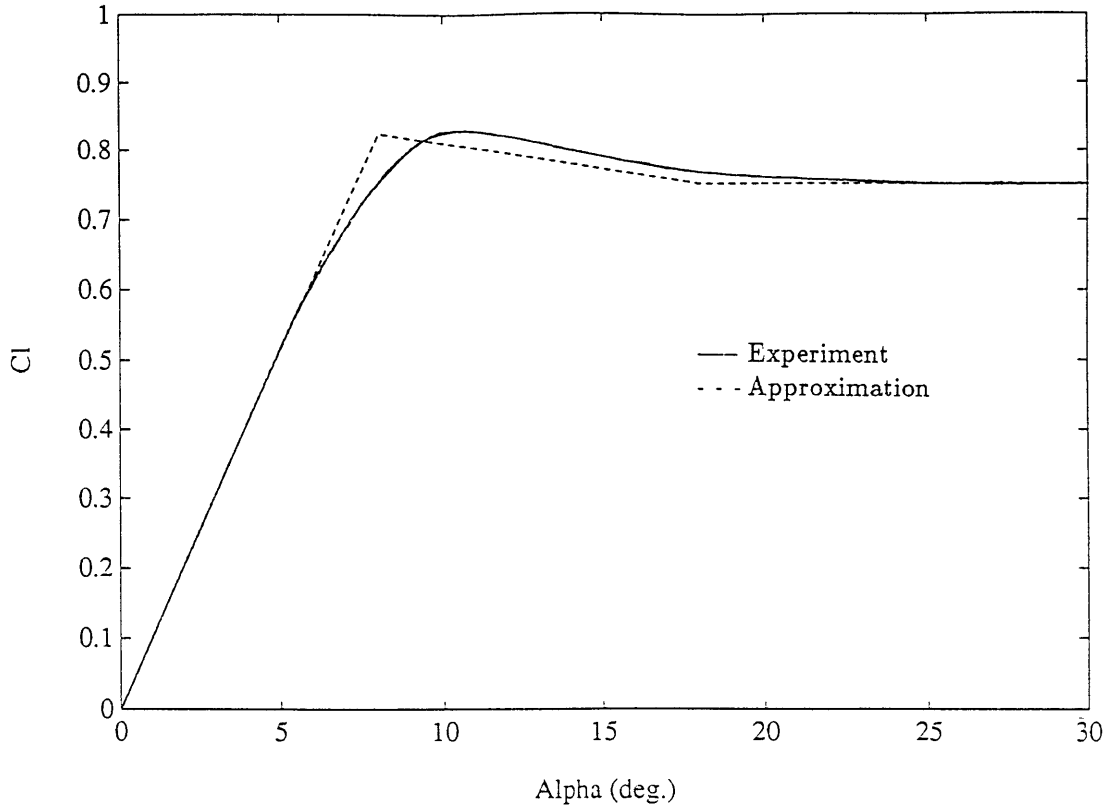

Figure 5.2: NACA-0012 low Reynolds number static lift curve

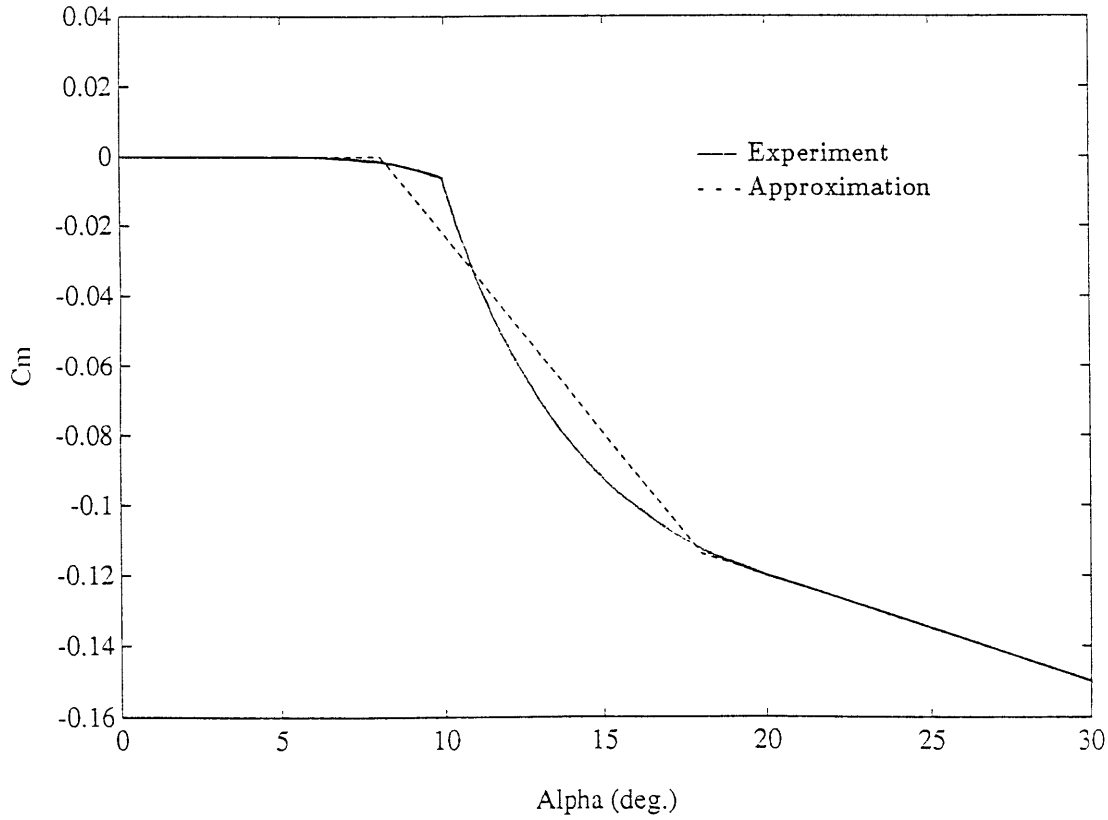

Figure 5.3: NACA-0012 low Reynolds number static moment curve

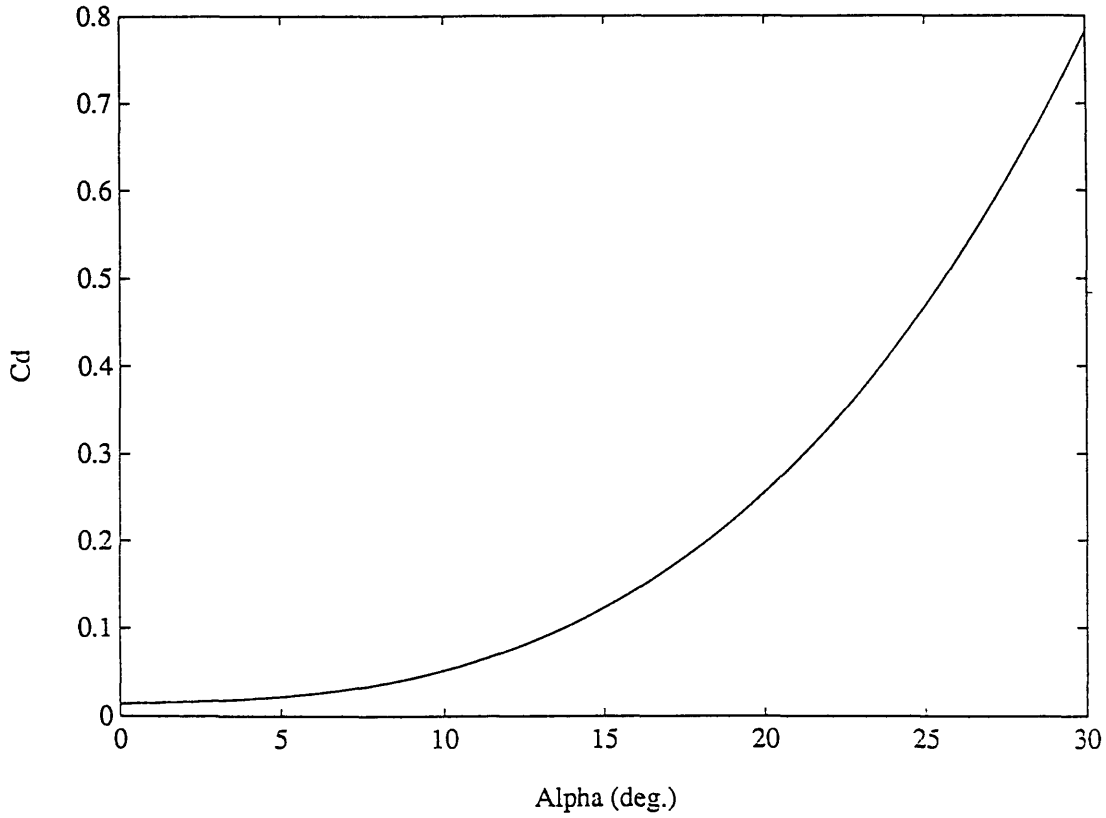

Figure 5.4: NACA-0012 low Reynolds number static drag curve

Noncirculatory part;

$$F_{NC} = F_{NC0} + F_{NCs} \sin k\tau + F_{NCc} \cos k\tau$$

where

$$\begin{aligned}
F_{NC0} &= \frac{1}{2} \rho S_z l_z b \{V_0 \dot{\epsilon}_{e0} + 0.5 (V_s \dot{\epsilon}_{es} + V_c \dot{\epsilon}_{ec})\} \\
F_{NCs} &= \frac{1}{2} \rho S_z [- s_z k V_0 V_{3c} + l_z b (V_c \dot{\epsilon}_{e0} + V_0 \dot{\epsilon}_{ec}) - k_z k b V_0 \dot{\epsilon}_{ec}] \\
F_{NCc} &= \frac{1}{2} \rho S_z [s_z k V_0 V_{3s} + l_z b (V_s \dot{\epsilon}_{e0} + V_s \dot{\epsilon}_{ec}) + k_z k b V_0 \dot{\epsilon}_{es}]
\end{aligned} \tag{5.8}$$

Linear circulatory part;

$$\begin{aligned}
\Gamma_{1z} &= a_{0z} V_0 \alpha_0 + \Gamma_{11zs} \sin k\tau + \Gamma_{11zc} \cos k\tau \\
\Gamma_{D1} &= \Gamma_{D10} + \Gamma_{D1s} \sin k\tau + \Gamma_{D1c} \cos k\tau
\end{aligned}$$

where

$$\begin{aligned}
\Gamma_{11zs} &= F_z(k) L_{zs}(k) - G_z(k) L_{zc}(k) \\
\Gamma_{11zc} &= G_z(k) L_{zs}(k) + F_z(k) L_{zc}(k)
\end{aligned} \tag{5.9}$$

$$\begin{aligned}
\Gamma_{D10} &= 0.014 V_0 \\
\Gamma_{D1s} &= 0.014 V_s \\
\Gamma_{D1c} &= 0.014 V_c
\end{aligned} \tag{5.10}$$

Nonlinear circulatory part;

$$\begin{aligned}
\Gamma_{2z} &= \Gamma_{2z0} + \Gamma_{2zs} \sin k\tau + \Gamma_{2zc} \cos k\tau \\
\Gamma_{D2} &= \Gamma_{D20} + \Gamma_{D2s} \sin k\tau + \Gamma_{D2c} \cos k\tau
\end{aligned}$$

where

$$\begin{aligned}
\Gamma_{2z0} &= -\Delta\Gamma_{z0} \\
\Gamma_{2zs} &= \frac{k_{z1} k_{z3} + k_{z2} k_{z4}}{k_{z1}^2 + k_{z2}^2} \\
\Gamma_{2zc} &= \frac{k_{z1} k_{z4} - k_{z2} k_{z3}}{k_{z1}^2 + k_{z2}^2}
\end{aligned} \tag{5.11}$$

$$
\begin{aligned}
\Gamma_{D20} &= -\Delta\Gamma_{D0} \\
\Gamma_{D2s} &= \frac{m_1 m_3 + m_2 m_4}{m_1^2 + m_2^2} \\
\Gamma_{D2c} &= \frac{m_1 m_4 - m_2 m_3}{m_1^2 + m_2^2}
\end{aligned} \tag{5.12}
$$

The expressions for $\Delta\Gamma_z$, $\Delta\Gamma_D$ as well as other coefficients are defined in the Appendix E. In the above Fourier components 5.9, the time-averaged part of Γ_{11z} has been replaced by the static linear airforce expression $a_{0z}V_0\alpha_0$. This modification is necessary because the differential equation for Γ_{11z} can not give the correct static term. Thus, Γ_{11z} is assumed to have only unsteady parts, Γ_{11zs} and Γ_{11zc}.

5.3 Hysteresis Generation of Aerodynamic Coefficients

In this section, several approximate methods of calculating the aerodynamic force hysteresis will be described and compared against the exact method. The problem arises as follows. In strict sense, when evaluating the coefficients a_z, r_z, e_z, and a_D, r_D, e_D defined in section 4.1 in the nonlinear part of the ONERA equations, one has to use full unsteady expressions for the lift deviation ΔC_L. Naturally, the simplest way of of approximating the unsteady ΔC_L is to use well defined static parts of ΔC_L in the coefficients as follows.

$$
\begin{aligned}
a_L &= 0.25 + 0.4\,[\Delta C_L(\alpha_0)]^2 \\
a_L &= 0.25 + 0.4\,(\Delta C_{L0})^2
\end{aligned}
$$

The first of these uses the constant value of ΔC_L at the mean angle of attack α_0. If the mean angle of attack is below the stall angle but the amplitude is large enough to cross into the stalled region, this approximation does not yield accurate asset of a_L because the formulation gives no stall effects. On the other hand, the second approximation takes this effect into account by using the mean value ΔC_{L0} obtained from Fourier analysis through the cycle. Thus, it is likely a better approximation.

The third approximation is to use full harmonic expression for ΔC_L.

$$a_L = 0.25 + 0.4\,[\Delta C_{L0} + \Delta C_{Ls} \sin\omega t + \Delta C_{Lc} \cos\omega t]^2$$

This approximation, though an improvement over the first two, results in a complicated algebraic formulas when substituted into the ONERA equations, from which the fundamental harmonics of the aerodynamic coefficients can not be readily extracted. The computation involved in the extraction procedure may well be comparable to that of using direct numerical integration scheme.

The last method, which is the exact one, is to let the lift deviation ΔC_L as well as the coefficients a_z, r_z, e_z, and a_D, r_D, e_D completely unsteady, use numerical integration to get steady state responses of the aerodynamic coefficients from the ONERA equations, and then extract the first harmonics using Fourier integrals numerically. In this method, basic variables in the ONERA equations such as $V, V_3, \dot{\epsilon}_e$ are still assumed to be of the first harmonic form whose elements are obtained from harmonic balance method. Usually, starting with some initial condition, the numerical integration should march over several periods until it reaches convergence. Thus, though exact, it requires a large number of computations and may not be appropriate to be used along with harmonic balance scheme.

It is without question that as the angle of attack and the reduced frequency becomes higher, the higher order methods such as the direct integration or the third approximation should be used. The second approximation can be recommended if the nonlinearity is moderate, i.e., if the angle of attack is moderate, and if the unsteadiness of the stalled motion is moderate, i.e., if the reduced frequency is in moderate range. However, the first approach is not recommended at all because of the reason described above.

All of Fourier components of the nonlinear aerodynamics in the current analysis is based on the second approach in which ΔC_L is approximated by its time-averaged ΔC_{L0}. The most important advantage of this approximation is that the resulting

formula is very simple and easy to be implemented while it still attempts to include the *smearing* effect of large angle of attack into stall region.

To illustrate accuracy of using ΔC_{L0} for moderate values of α and k, a series of Fourier analyses were performed on the lift, moment, and drag coefficients for pure pitching motion of the blade at its quarter-chord aerodynamic center with constant incoming velocity V_0. A set of ONERA equations suitable for this pure pitching motion are

<u>Lift & Moment;</u>

$$\begin{aligned} F_{NC} &= \frac{1}{2}\rho S_z (s_z b V_0 \dot{\theta} + l_z b V_0 \dot{\theta} + k_z b^2 \ddot{\theta}) \\ F_C &= \frac{1}{2}\rho S_z (V_0^2 C_{1z} + V_0^2 C_{2z}) \end{aligned} \tag{5.13}$$

where

$$\begin{aligned} \dot{C}_{1z} + \lambda_z \frac{V_0}{b} C_{1z} &= \lambda_z a_{0z} \frac{V_0}{b}\theta + \lambda_z \sigma_z \dot{\theta} \\ &\quad + \gamma_z a_{0z} \dot{\theta} + \gamma_z \sigma_z \frac{b}{V_0}\ddot{\theta} \\ \ddot{C}_{2z} + a_z \frac{V_0}{b}\dot{C}_{2z} + r_z \frac{V_0^2}{b^2} C_{2z} &= -r_z [\frac{V_0^2}{b^2}\Delta C_z + e_z \frac{V_0}{b}\frac{\partial \Delta C_z}{\partial t}] \end{aligned} \tag{5.14}$$

<u>Drag;</u>

$$D = \frac{1}{2}\rho c (V_0^2 C_{D1} + V_0^2 C_{D2}) \tag{5.15}$$

where

$$\begin{aligned} C_{D1} &= C_{D0} \\ \ddot{C}_{D2} + a_D \frac{V_0}{b}\dot{C}_{D2} + r_D \frac{V_0^2}{b^2} C_{D2} &= -[r_D \frac{V_0^2}{b^2}\Delta C_D + e_D \frac{V_0}{b}\dot{\theta}] \end{aligned} \tag{5.16}$$

Note that these equations have been written in terms of the force coefficients C_z, C_D rather than the circulation coefficients Γ_z, Γ_D because the free stream velocity

is not pulsating anymore. Furthermore, for the sake of simplicity, the large angle of attack in the linear parts was not accounted for, i.e., $V_0\theta$ was used instead of V_3 in the ONERA equations 4.2 and 4.4. Fourier analysis of the new ONERA equations 5.13 through 5.16 based on the simple straight line approximation of deviations 5.7 lead to first harmonics expressions similar to equations 5.8 through 5.12. For the direct numerical integration, these equations are converted into a set of first order equations in the form

$$\frac{d\vec{X}}{dt} = \vec{f}(\vec{X}, t)$$

which then can be solved by fourth-order Runge-Kutta integration with appropriate initial conditions at $t = 0$. Usually the initial value of nonlinear coefficient C_{2z} is assigned zero while the linear C_{1z} is given the linear slope of 5.9 and 0, for the lift and moment, respectively. The stall delay can also be implemented in the numerical integration scheme simply by delaying the activation of the nonlinear part of the ONERA lift equation for $\Delta\tau = 10$ after the pitch angle θ has passed the stall angle. If the pitch angle returns back to the stall angle before the delay time has passed in the time domain, however, the blade is experiencing light stall, and the nonlinear part should not be used, i.e., no stall is introduced. This stall strategy that the stall be introduced only in deep stall case has also been implemented in the Fourier modeling parts.

In Figures 5.2 through 5.5, the solid curves represent experimental lift and moment hysteresis for pure pitching motion at the aerodynamic center (Ref. 42). In order to show how much the inclusion of the additional stall delay would improve the ONERA Model, two other curves by broken lines, one with the delay and the other without the delay, are also drawn via direct numerical integration of the ONERA equations. All of the results were obtained at Reynolds number of 4.9×10^5, and the reduced frequencies chosen were moderate values ranging between 0.1 and .16. As seen in the figures the stall delay is essential in improving the accuracy of the ONERA Model. In the next figures, Figure 5.6 through 5.11, the solid curves are complete lift, moment

and drag hystereses resulting from direct numerical integration of the same ONERA results with the stall delay. The solid ellipses are obtained by taking the Fourier integrals of these complete solutions numerically over one cycle. Then, the dashed ellipses represent the first harmonics obtained by harmonic balance assuming constant aerodynamic coefficients. As expected, there are generally good agreements between the two ellipses at low values of α and k, but at high values, they are not well matched. Note also that the the lift and drag loops are in general better matched with the exact harmonic loops than the moment loops.

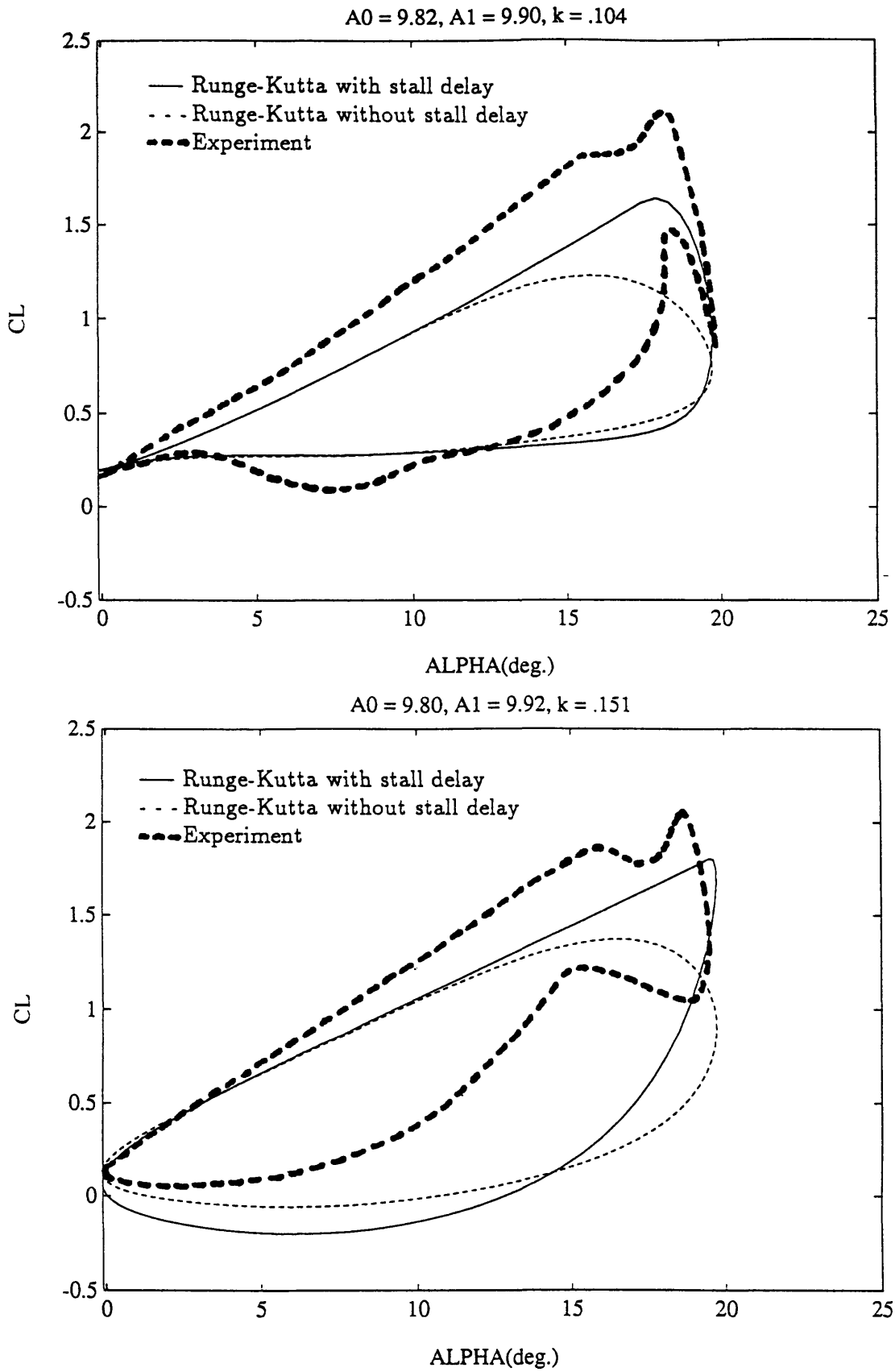

Figure 5.5: 2-D lift coefficient hysteresis loops; Experiment vs. ONERA Model for NACA 0012 airfoil, $Re = 4.9 \times 10^5$

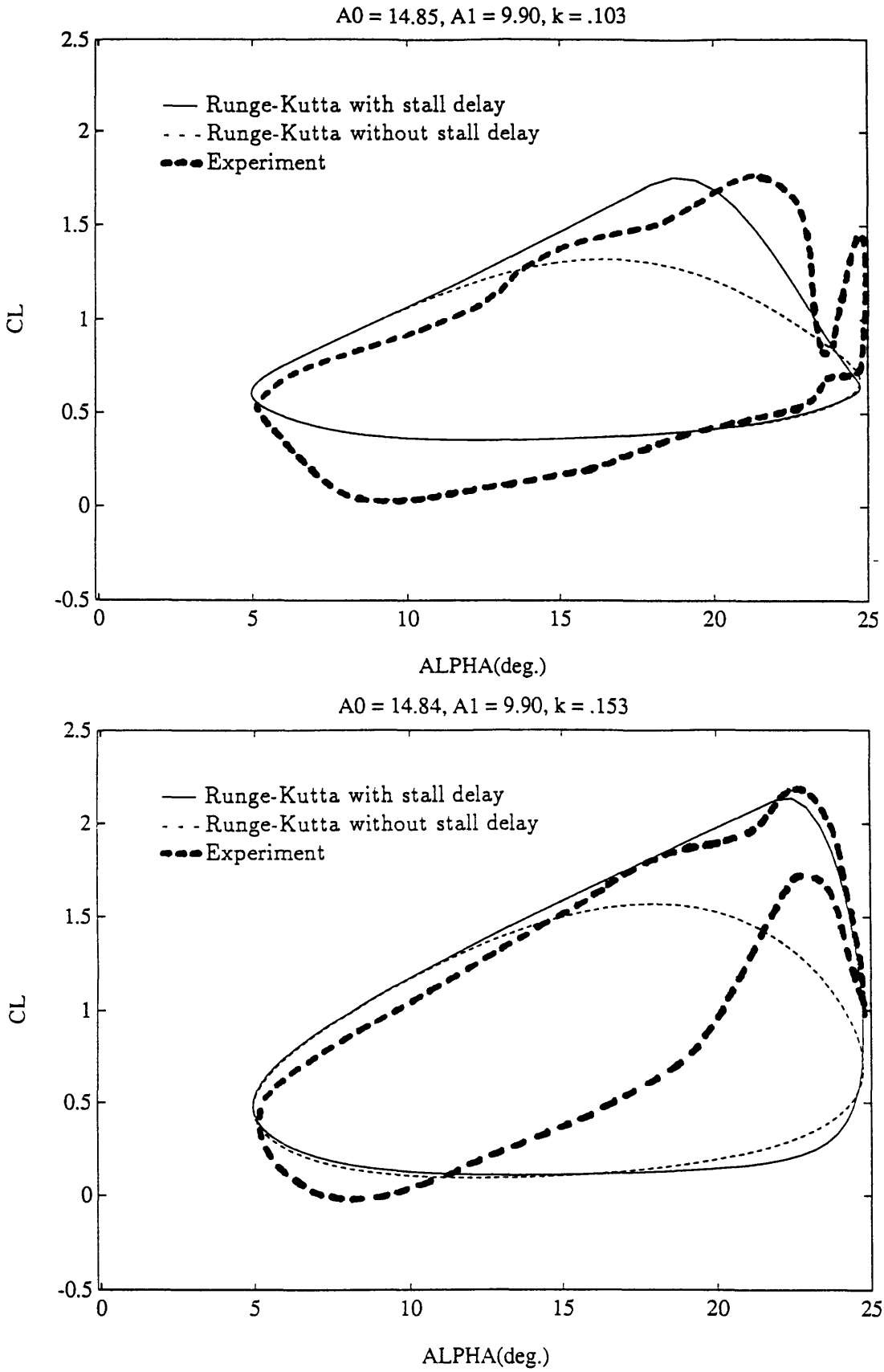

Figure 5.6: 2-D lift coefficient hysteresis loops; Experiment vs. ONERA Model for NACA 0012 airfoil, $Re = 4.9 \times 10^5$

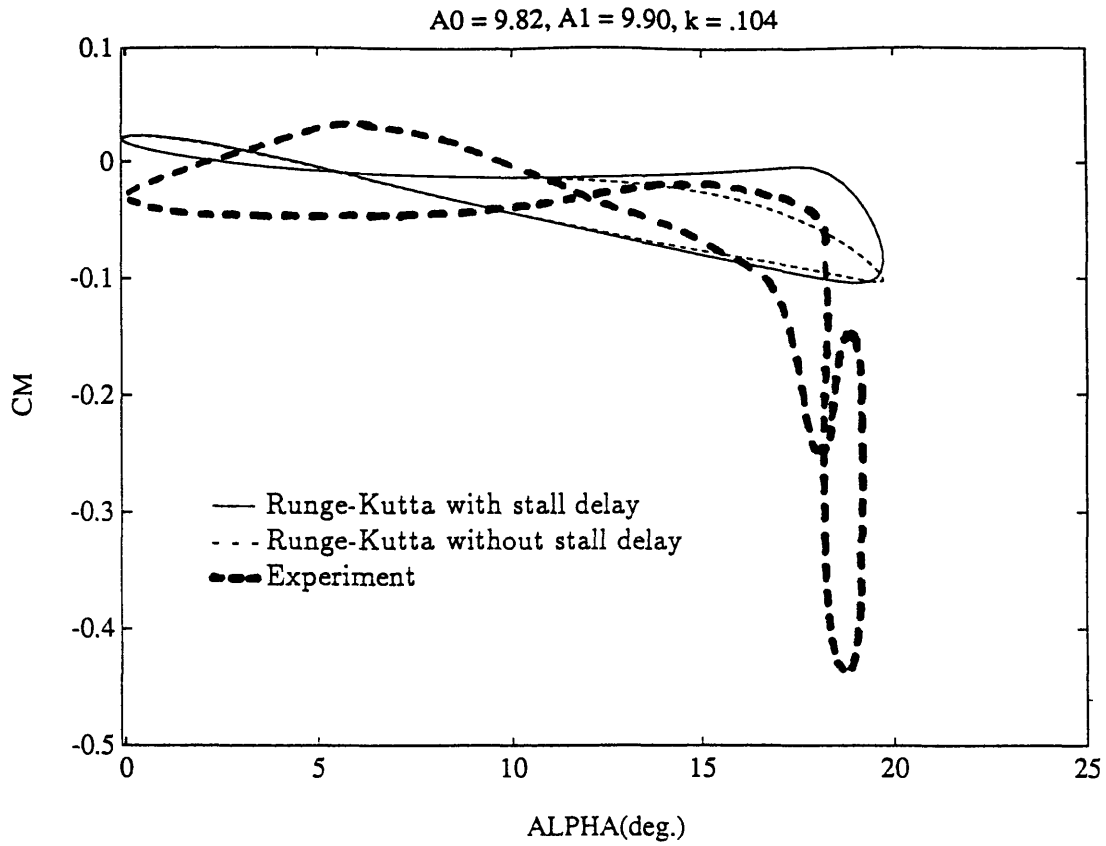

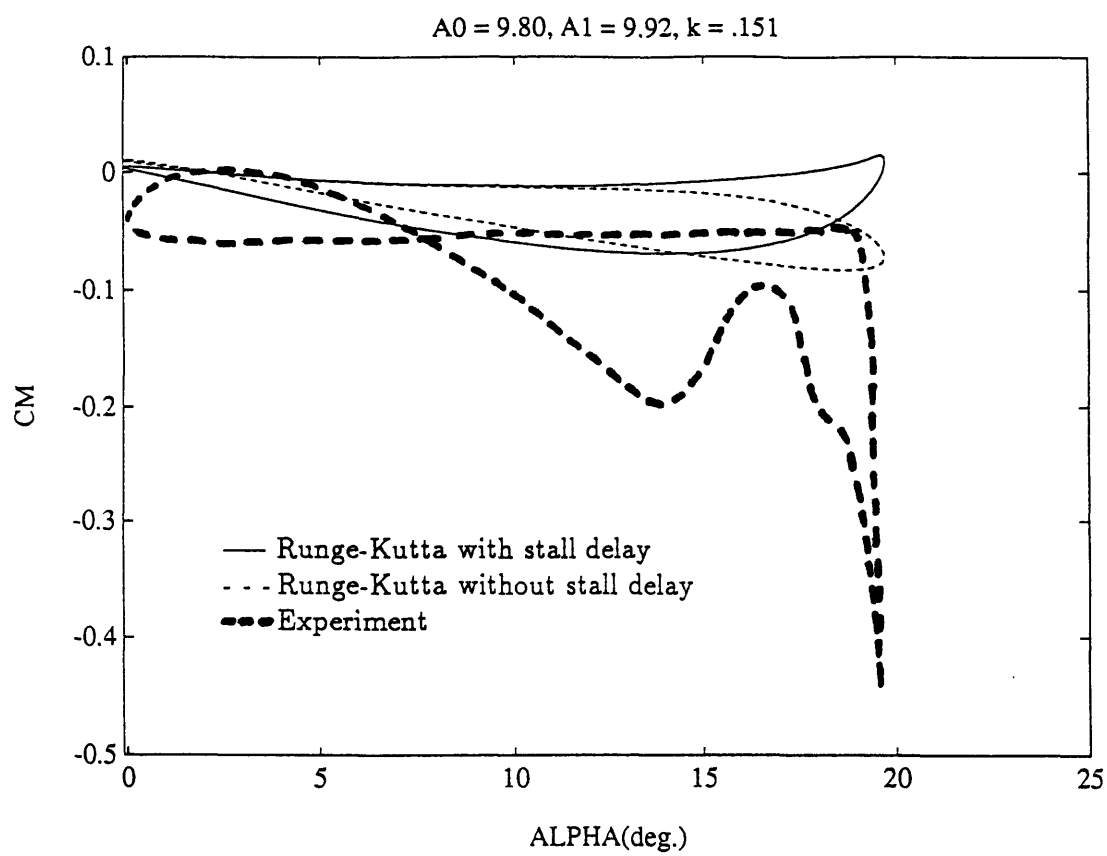

Figure 5.7: 2-D moment coefficient hysteresis loops; Experiment vs. ONERA Model for NACA 0012 airfoil, $Re = 4.9 \times 10^5$

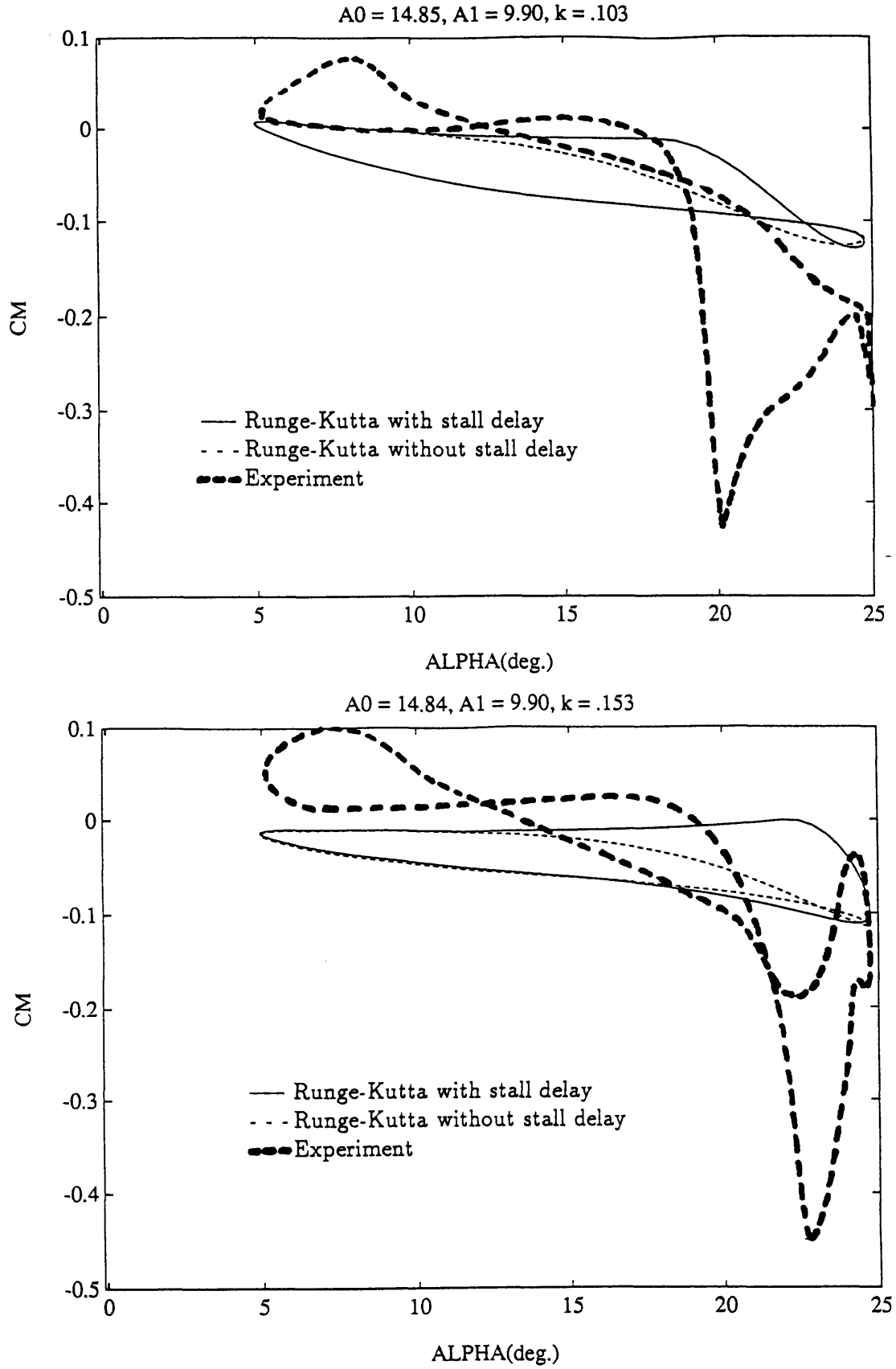

Figure 5.8: 2-D moment coefficient hysteresis loops; Experiment vs. ONERA Model for NACA 0012 airfoil, $Re = 4.9 \times 10^5$

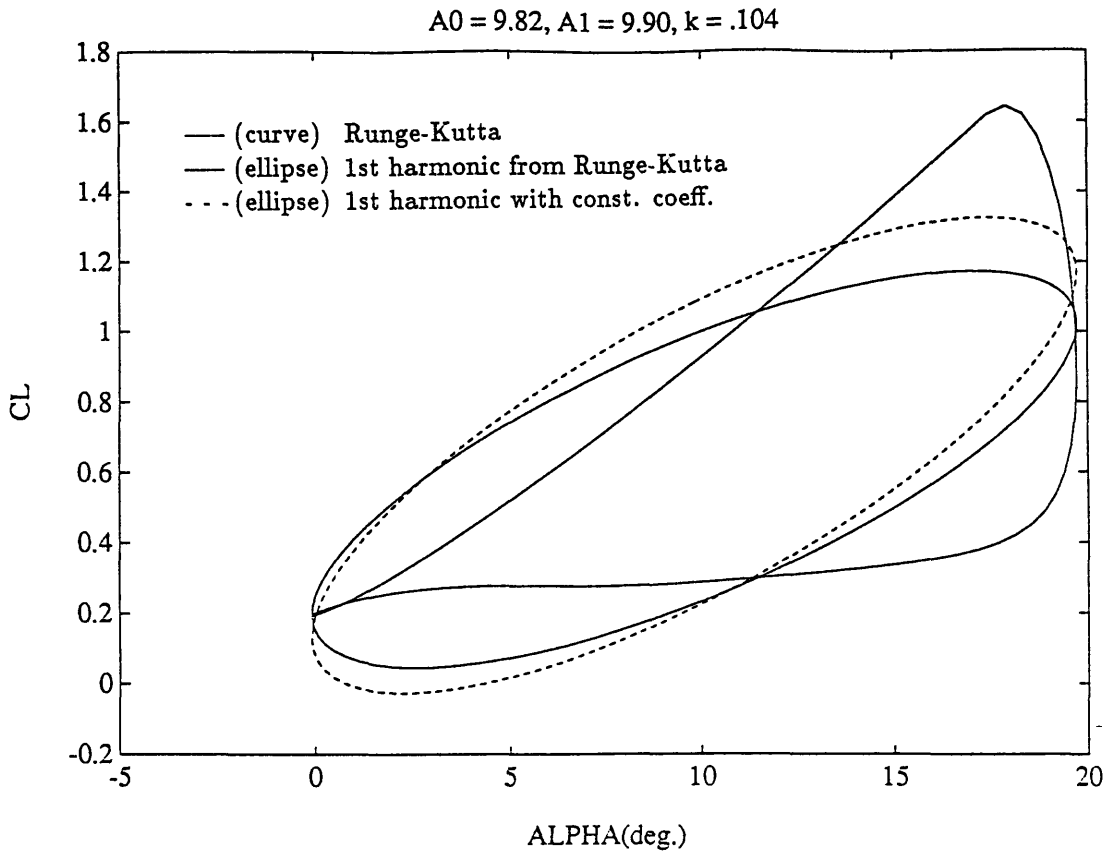

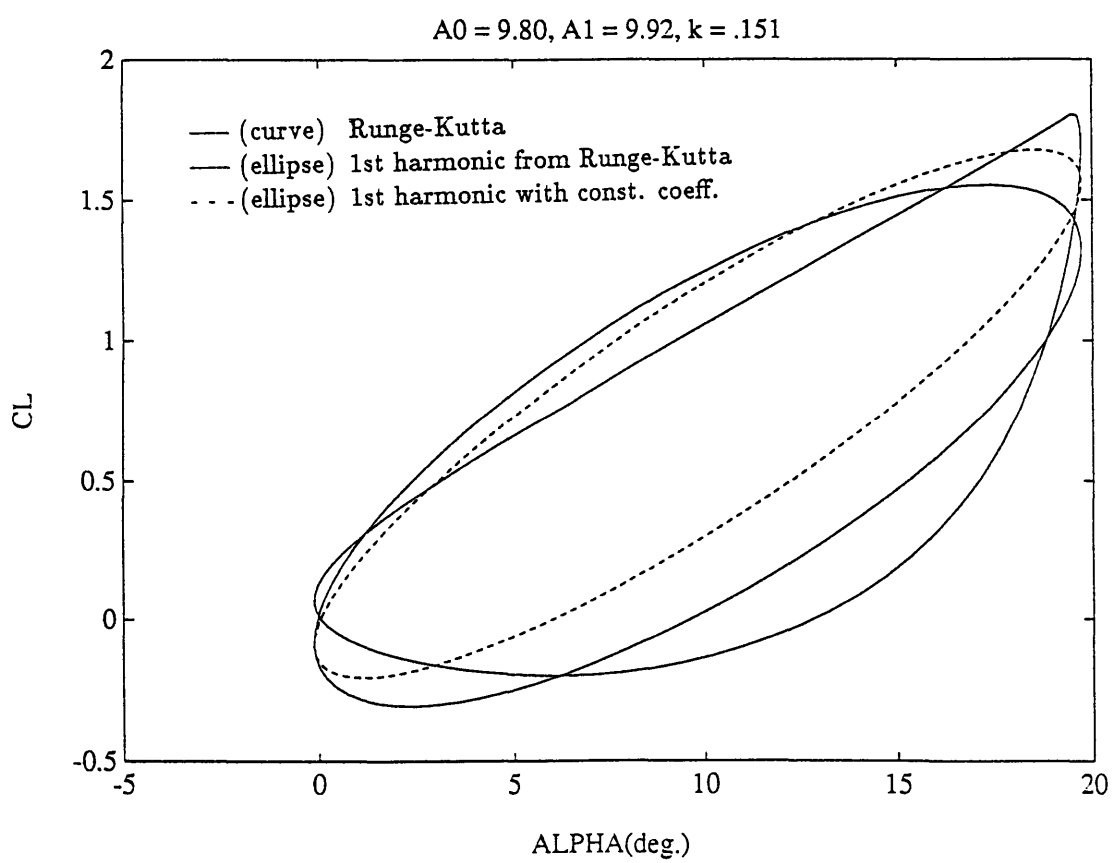

Figure 5.9: 2-D lift coefficient hysteresis loops vs. first harmonic loops; for NACA 0012 airfoil, $Re = 4.9 \times 10^5$

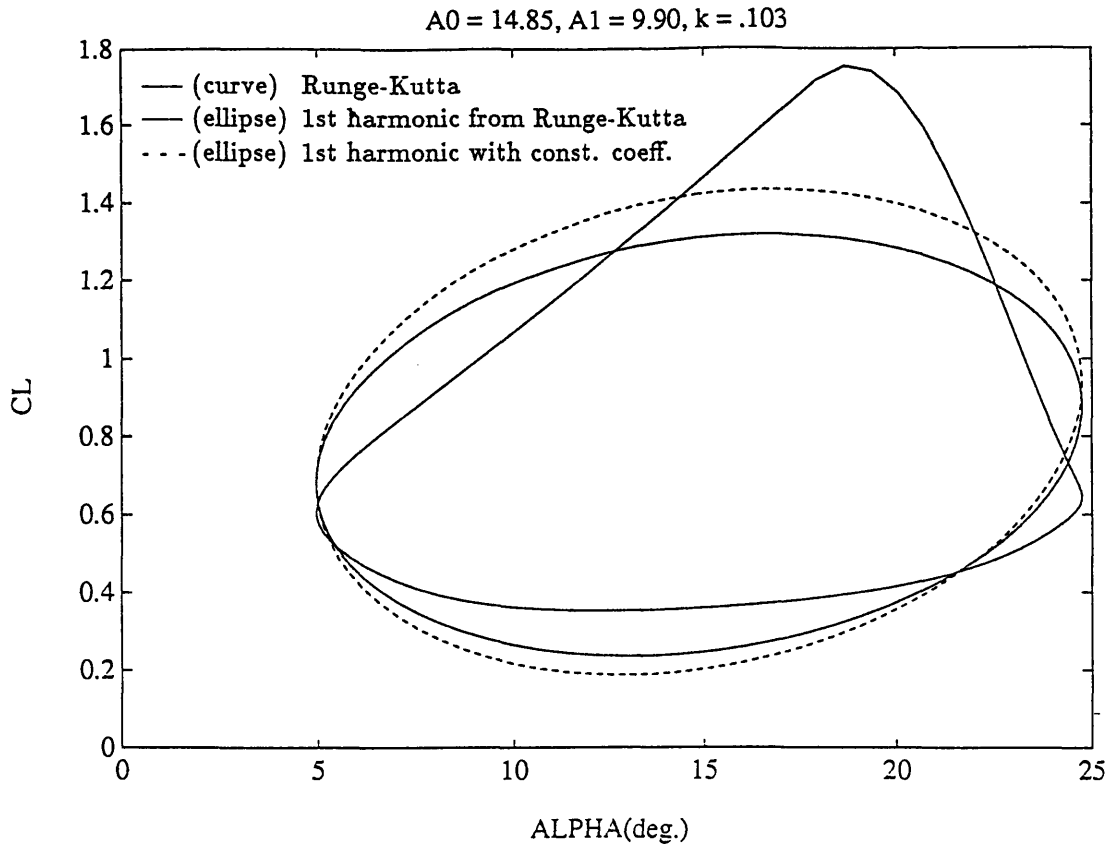

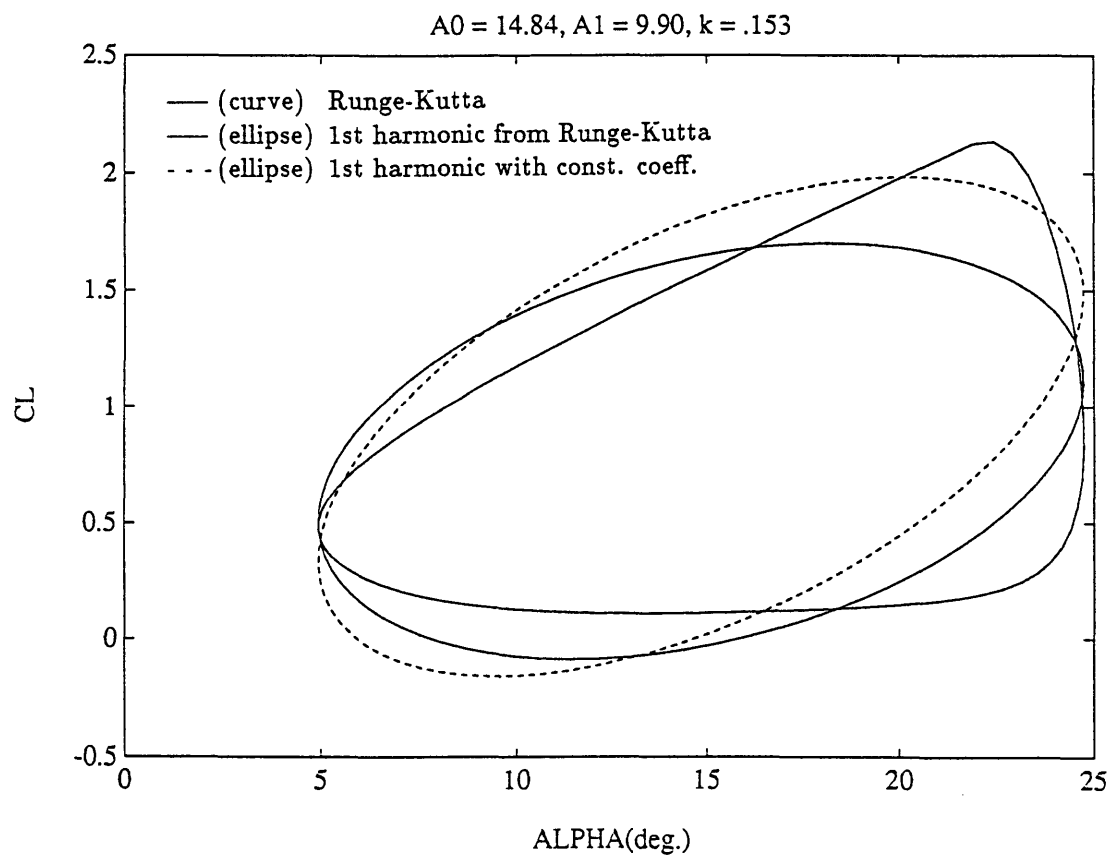

Figure 5.10: 2-D lift coefficient hysteresis loops vs. first harmonic loops; for NACA 0012 airfoil, $Re = 4.9 \times 10^5$

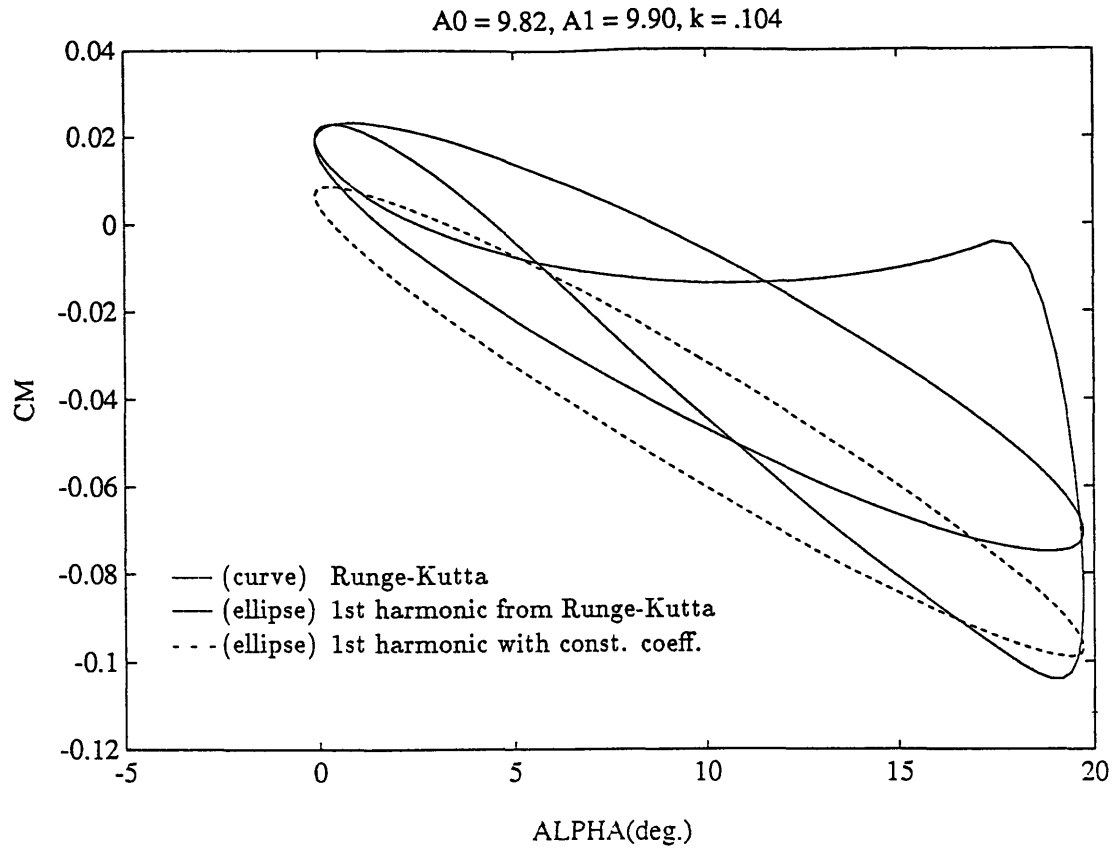

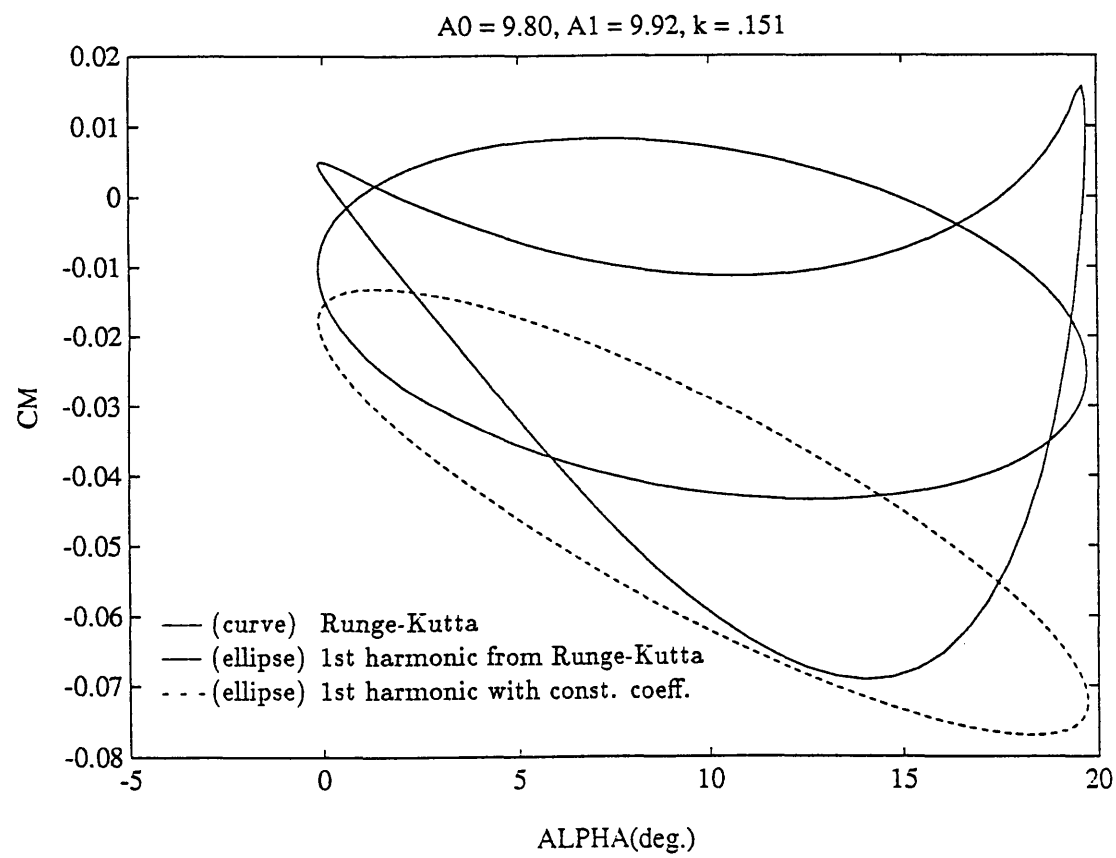

Figure 5.11: 2-D moment coefficient hysteresis loops vs. first harmonic loops; for NACA 0012 airfoil, $Re = 4.9 \times 10^5$

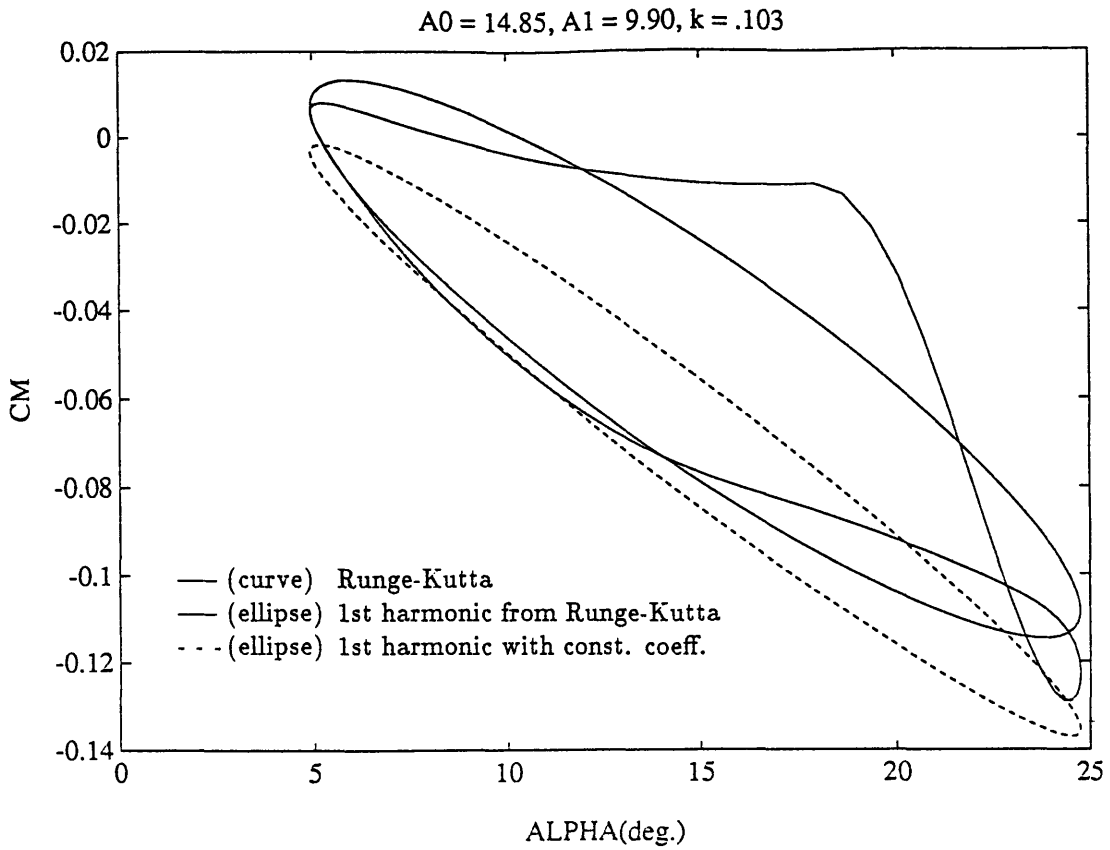

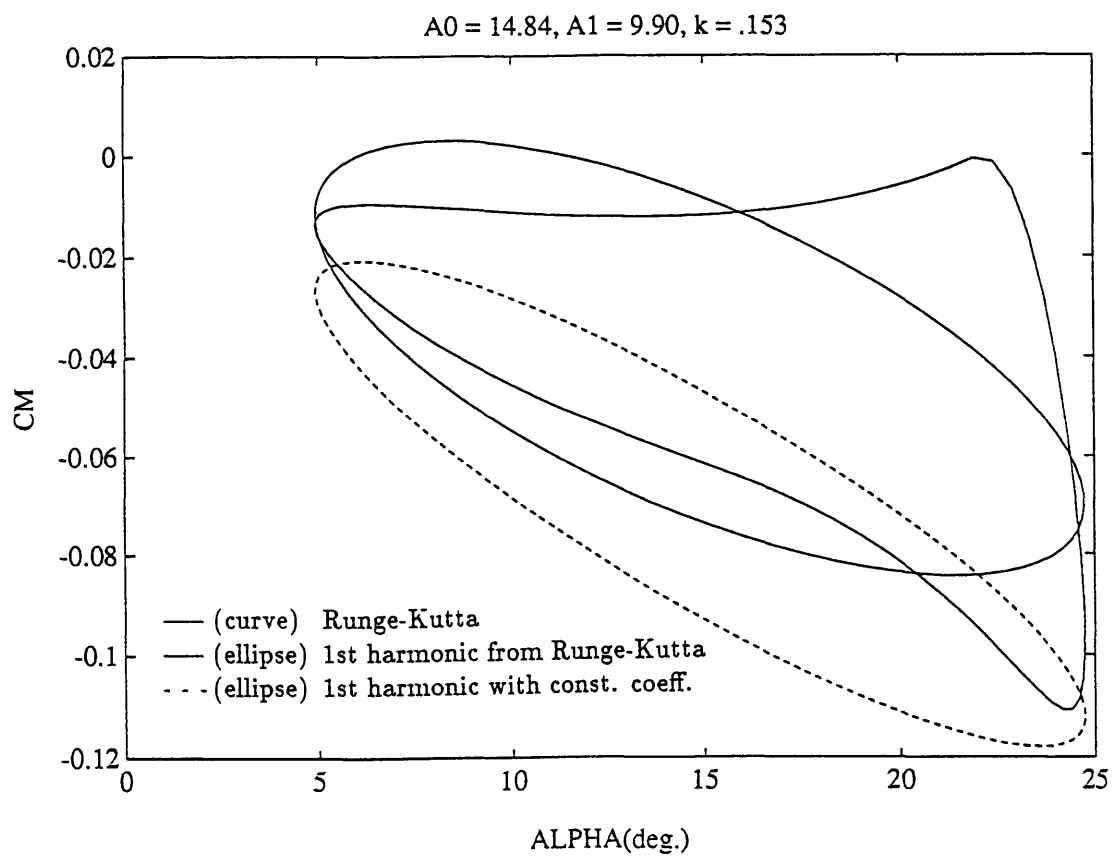

Figure 5.12: 2-D moment coefficient hysteresis loops vs. first harmonic loops; for NACA 0012 airfoil, $Re = 4.9 \times 10^5$

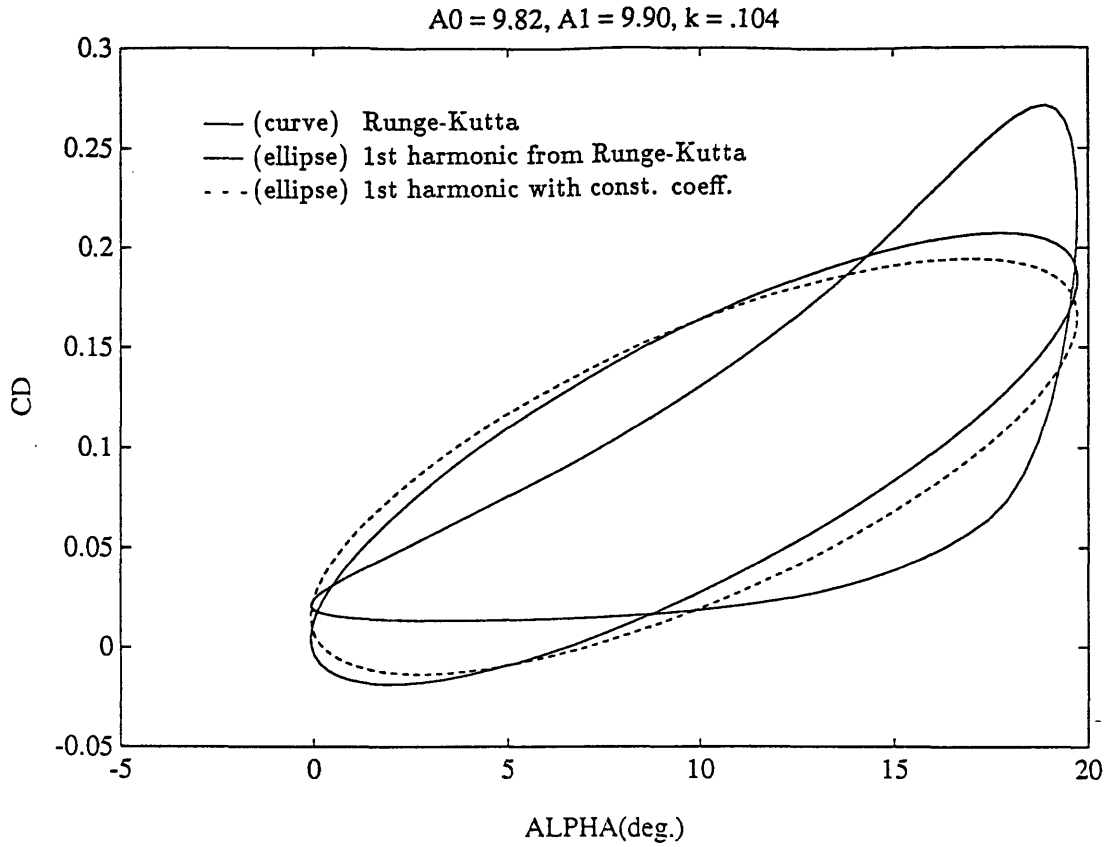

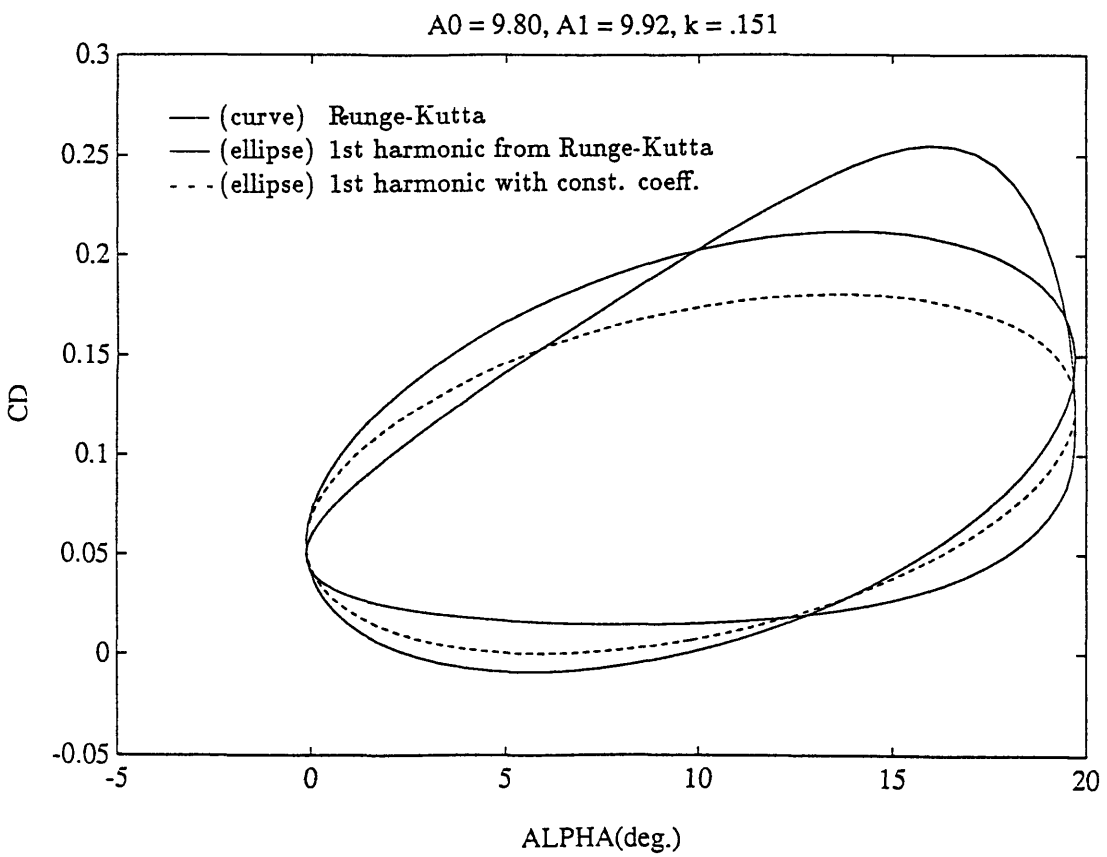

Figure 5.13: 2-D drag coefficient hysteresis loops vs. first harmonic loops; for NACA 0012 airfoil, $Re = 4.9 \times 10^5$

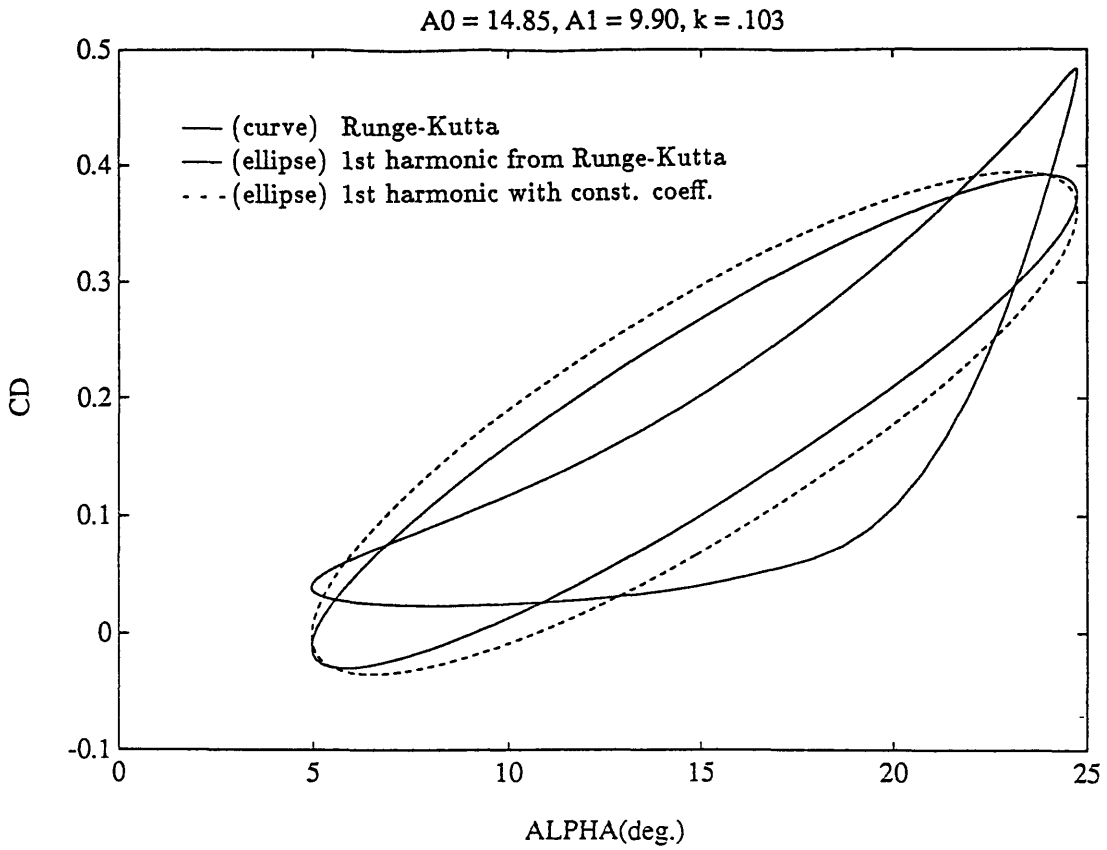

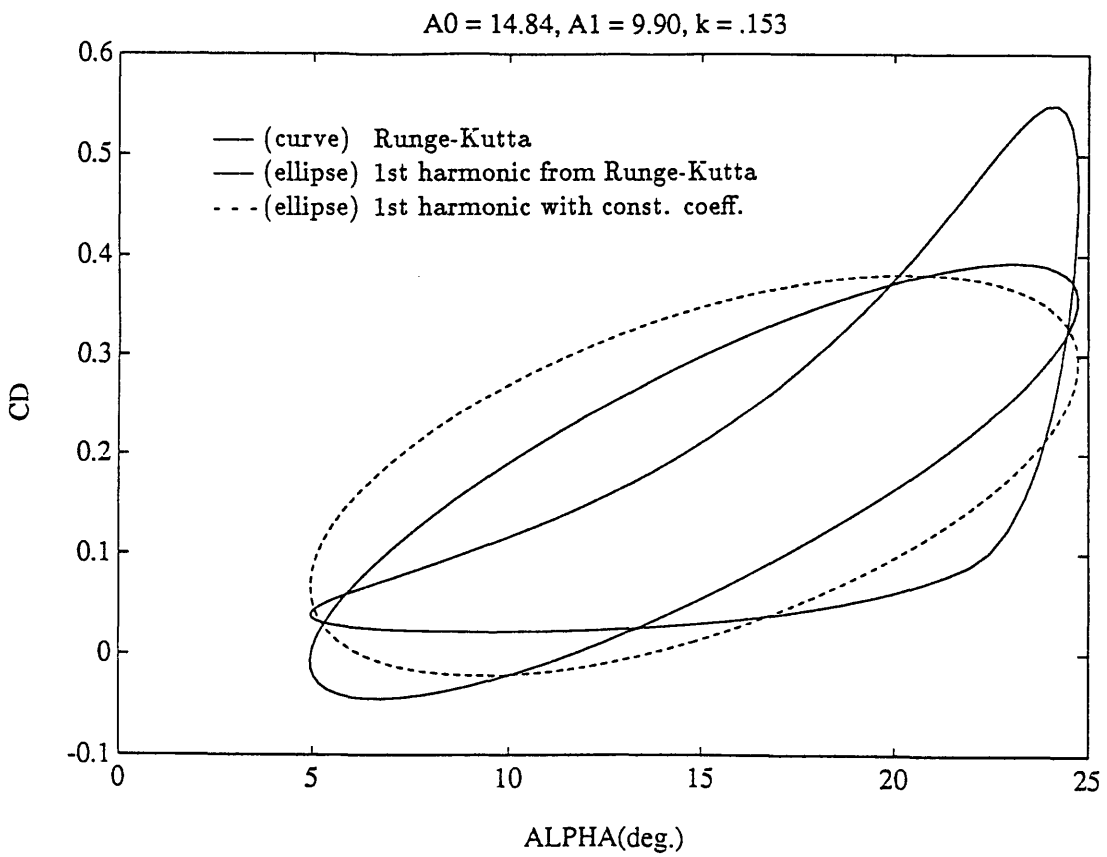

Figure 5.14: 2-D drag coefficient hysteresis loops vs. first harmonic loops; for NACA 0012 airfoil, $Re = 4.9 \times 10^5$

Chapter 6

Methods of Solution

6.1 Nonrotating Free Vibration

For the nonrotating large amplitude free vibration problems, all the aerodynamic forces discussed in chapter 4 are dropped. Also any inertial loading terms multiplied by the rotational speed Ω are dropped. Hence, the only applied loadings are inertial terms due to translational and rotational accelerations, and due to gravity. In this case it is convenient to express the inertial forces in global coordinate and inertial moments in local coordinate as follows.

$$\begin{aligned} p_x &= -m\left[\ddot{x} + \ddot{T}_{21}\eta_{cg}\right] - \beta_p mg \\ p_y &= -m\left[\ddot{y} + \ddot{T}_{22}\eta_{cg}\right] \\ p_z &= -m\left[\ddot{z} + \ddot{T}_{23}\eta_{cg}\right] - mg \end{aligned} \tag{6.1}$$

$$\begin{aligned} m_1 &= -I_{\xi\xi}\dot{\omega}_\xi - (I_{\zeta\zeta} - I_{\eta\eta})\omega_\eta\omega_\zeta \\ &\quad - m(\ddot{x}T_{31} + \ddot{y}T_{32} + \ddot{z}T_{33})\eta_{cg} \\ &\quad + mg(T_{33} + \beta_p T_{31})\eta_{cg} \\ m_2 &= -I_{\eta\eta}(\dot{\omega}_\eta + \omega_\xi\omega_\zeta) \\ m_3 &= -I_{\zeta\zeta}(\dot{\omega}_\zeta - \omega_\xi\omega_\eta) \\ &\quad + m(\ddot{x}T_{11} + \ddot{y}T_{12} + \ddot{z}T_{13})\eta_{cg} \\ &\quad - mg(T_{13} + \beta_p T_{11})\eta_{cg} \end{aligned} \tag{6.2}$$

where ζ_{cg} and $I_{\eta\zeta}$ have been neglected. For a flat composite laminated blade example, η_{cg} and β_p are also set to zero. Furthermore, one can ignore the rotary inertia around η axis, and approximate the rotation rate $\dot{\omega}_\xi$ by $\ddot{\theta}$. Thus, the resulting global and local loads can be summarized as

$$\begin{aligned} p_x &= -m\,\ddot{x} \\ p_y &= -m\,\ddot{y} \\ p_z &= -m\,\ddot{z} - mg \end{aligned} \tag{6.3}$$

and

$$\begin{aligned} m_1 &= -I_{\xi\xi}\ddot{\theta} \\ m_2 &= m_3 = 0 \end{aligned} \tag{6.4}$$

In nonrotating free vibration problems, no phase difference exists between different stations of the blade. Therefore, dropping one of the sinusoidal terms, one can assume that all of the variables are of the form

$$X(\omega, t) = X_0(\omega) + X_s(\omega)\sin\omega t$$

After substituting the global inertial loadings described above into the force and moment equilibrium equations in section 2.1 and performing harmonic balancing, one can express the resulting ordinary differential equations in symbolic vector form

$$\underset{(12\times 1)}{\frac{dX_0}{ds}} = \underset{(12\times 1)}{g_0(X_0, X_s, \omega)} \tag{6.5}$$

and

$$\frac{dX_s}{ds} = g_s(X_0, X_s, \omega) \tag{6.6}$$

$$(12 \times 1) \qquad (12 \times 1)$$

where

$$X_0 = [\, F_{10}\, F_{20}\, F_{30}\, M_{10}\, M_{20}\, M_{30}\, x_0\, y_0\, z_0\, \theta_0\, \beta_0\, \psi_0 \,]^T$$

$$X_s = [\, F_{1s}\, F_{2s}\, F_{3s}\, M_{1s}\, M_{2s}\, M_{3s}\, x_s\, y_s\, z_s\, \theta_s\, \beta_s\, \psi_s \,]^T$$

The two vector function arrays g_0 and g_s contain many product terms involving multiplications of two, or three harmonic quantities. They, of course, originate from the twelve basic equations that are presented in section 2.1. Multiplications of harmonics and calculations of the coefficients of the resulting new harmonics can be easily implemented according to the formulae in the Appendices A, B, and C, with all $\cos \omega t$ terms dropped.

To solve this system, all of the twenty four equations (now twelve for the static part, twelve for the dynamic part. twenty eight if warping is included) are first integrated from the tip to the root of the blade once. Minguet and Dugundji used a finite-difference iteration method for the solution of static deformation, sweeping from the tip to the root and vice versa a few times until all the residues become very small. When applying this scheme to the solution of mode shapes and their frequencies, one has to be cautious because this finite-difference iteration will usually converge to the first mode only. To obtain higher modes, one must consider other integration techniques which do not sweep back and forth along the span but are more appropriate for boundary value type problems. Among such, Runge-Kutta integration is frequently used and very effective. Currently, a fourth order Runge-Kutta algorithm is used.

In the early step of numerical integration, one has to guess the boundary values of displacements and rotations at the tip as well as the frequency that will make, for a given mode shape, all the displacements and rotations at the root as close to

the prescribed values as possible. For instance, a linear eigensolution by Minguet and Dugundji can provide a good guess for tip values X_t and the frequency ω. The functional relationships between these two sets of boundary values at the root and at the tip can be written as

$$\underset{(12\times 1)}{X_r} = \underset{(12\times 1)}{f(X_t,\omega)} \tag{6.7}$$

where

$$X_t = [x_0\, x_s\, y_0\, y_s\, z_0\, z_s\, \theta_0\, \theta_s\, \beta_0\, \beta_s\, \psi_0\, \psi_s]^T$$

at the tip, and X_r is set equal to one of the root boundary values given in section 2.2. For example, for a hingeless blade with collective pitch θ_r at the root, one needs

$$X_r = [0\,0\,0\,0\,0\,0\,\theta_r\,0\,0\,0\,0\,0]^T$$

at the root.

Since the initial guess for the twelve components of X_t can not be perfect, there will be nonzero residues R by the time the integration reaches the root. A Newton-Raphson type algorithm can then be used to produce a better set of boundary values based on the current values. This will produce a series of the following set of boundary values.

$$X_t^{n+1} = X_t^n - J(X_t^n,\omega^n)^{-1} R^n \tag{6.8}$$

where

$$R^n \equiv f(X_t^n,\omega^n) - X_r$$

and

$$J:\ (12\times 12) \text{ Jacobian matrix}$$

Here the superscript n refers to the n-th iterative values, and X_r refers to the desired values at the root. The n-th boundary values X_t^n at the tip will eventually march to

the true solution, provided it exists. Currently two algorithms called F. D. G. (finite difference Gauss' method) and F. D. L. M. (finite difference Levenberg-Marquardt method) (Ref. 45), respectively are used to evaluate the Jacobian matrix numerically. The former is simply a numerical version of Newton-Raphson method, and in the latter case, an efficient relaxation scheme is added.

It is noted that whatever algorithm is used, it must take iterations on the frequency as well as the boundary values, since it is not known in advance at which frequency a mode will happen for a given amplitude level. Therefore, one of the six boundary amplitudes at the tip $x_s, y_s,\ z_s, \theta_s, \beta_s, \psi_s$, is replaced by the frequency ω, and the replaced displacement is fixed throughout iterations. Which one has to be fixed depends on the mode being sought. For instance, if bending modes are of concern it will be z_s; for torsional modes θ_s is fixed. The iteration will march until the boundary conditions at the root are met, i. e. , the residues R^n are zeros or at least less than some small parameter ϵ where $\epsilon \ll 1$.

As a final notion, the above solution procedure, when applied to linear problems, is similar to the so called transfer matrix technique used to obtain helicopter blade vibration modes by Isakson and Eisley (Ref. 46).

6.2 Nonrotating Free Vibration by Moderate Deflection Equations

In the present section, analysis of the nonrotating large amplitude free vibration problem is described by use of the nonlinear equations of motion 2.47, developed by Hodges and Dowell, and Boyd. These equations are valid only up to the second order of magnitude in the deflections and rotations of the blade, and also do not include any structural coupling effects such as bending-twist, extension-twist, etc.. Even though the equations are known to yield fairly accurate linear vibration results at moderate amount of deformations, this may not be the case for the large amplitude vibrations. The major purpose of this section is then to present an iterative solution technique

based on harmonic balance method, and identify nonlinear terms which differentiate the large amplitude vibration from small amplitude motion.

For nonrotating uniform blades without either structural couplings or mass centroid off-set, one can rewrite equations 2.47 as

$$m\ddot{w} + EI_\eta w'''' + (EI_\zeta - EI_\eta)[v''\theta + w''\theta^2]'' = -mg \tag{6.9}$$

$$m\ddot{v} + EI_\zeta v'' + (EI_\zeta - EI_\eta)[w''\theta - v''\theta^2)]'' = 0 \tag{6.10}$$

$$I_{\xi\xi}\ddot{\theta} - (GJ\phi')' + (EI_\zeta - EI_\eta)[(w''^2 - v''^2)\theta + v''w''] = 0 \tag{6.11}$$

Now assume for the displacement

$$\begin{aligned} w &= w_0 + w_1 \sin\omega t \\ v &= v_1 \sin\omega t \\ \theta &= \theta_1 \sin\omega t \end{aligned}$$

Note that static deformation can not exist in the chordwise bending v and twist θ for the type of blades under consideration. Substituting these expressions into equation 6.9, 6.10 6.11, and balancing each of the static, $\sin\omega t$ gives

<u>Static part</u>

$$EI_\eta w_0'''' + (EI_\zeta - EI_\eta)[\underline{\underline{\frac{1}{2}\theta_1 v_1''}} + \underline{\underline{\frac{1}{2}\theta_1^2 w_0''}}]'' = -mg \tag{6.12}$$

<u>Dynamic part</u>

$$-m\omega^2 w_1 + EI_\eta w_1'''' = 0 \tag{6.13}$$

$$-m\omega^2 v_1 + EI_\zeta v_1'''' + (EI_\zeta - EI_\eta)[\underline{\underline{-\frac{3}{4}\theta_1^2 v_1''}} + \underline{\theta_1 w_0''}]'' = 0 \tag{6.14}$$

$$-I_{\xi\xi}\omega^2\theta_1 - GJ\theta_1'' + (EI_\zeta - EI_\eta)[(\underline{w_0''^2} - \underline{\underline{\frac{3}{4}v_1''^2}})\theta_1 + \underline{w_0''v_1''}] = 0 \tag{6.15}$$

All the underlined terms represent the linear couplings between the static w_0 and the first order terms v_1, θ_1 that always exist regardless of the magnitudes of the amplitudes. The double underlined are higher order terms that would be absent if the amplitudes were small. From the static equation for w_0, it is immediately seen that the vertical static deformation will exactly be that of flat beams if amplitudes v_1 and θ_1 are restricted to be small. Hence, as both amplitudes become large the time-averaged position of w will change from the linearly predicted one in proportion to the difference in the bending stiffness $EI_\zeta - EI_\eta$. As for the vibration part of w, the equation reveals that the free vibration modes in w are exactly those of flat beams, and are completely decoupled from the modes in v, θ. However, the dynamic equations for v and θ have higher order nonlinear couplings, and are, therefore, expected to change their modes as amplitude become large. These qualitative insights on the behavior of the large amplitude motion of blades were not possible to attain in the previous section when dealing with fully nonlinear differential equations, and should serve as preliminary information before proceeding further.

In the remainder of the section, the solutions for w_1 will not be sought because they are the well known bending modes for flat beams. See, for example, Meirovitch (Ref. 47). To solve equations 6.12, 6.14, 6.15, assume modal expansions in the form

$$\begin{aligned} w_0(x) &= \sum_{i=1}^{Nw} f_{wi}(x)\, q_{wi} \\ v_1(x) &= \sum_{i=1}^{Nv} f_{wi}(x)\, q_{vi} \\ \theta_1(x) &= \sum_{i=1}^{Nt} f_{\theta i}(x)\, q_{\theta i} \end{aligned} \tag{6.16}$$

where f_{wi}'s, f_θ's are beam bending modes and torsion modes. q_{wi}'s, q_{vi}'s, and $q_{\theta i}$'s are the associated generalized coordinates. These mode shapes can be selected arbitrarily provided that they satisfy both geometric and natural boundary conditions at both ends in order to comply with Galerkin's method. Note that the same bending mode shapes f_{wi}'s are used for both the flapwise bending and chordwise bending. In the

following formulation, which is similar to that used by Boyd (Ref. 11), the beam bending and torsion modes at flat position are employed. These are well defined in, for example, Meirovitch (Ref. 47). After placing the modal expansions into the equations 6.12, 6.14, 6.15, Galerkin's method is applied by multiplying the resulting equations by the mode shapes f_{wi}'s, f_{wi}'s, and $f_{\theta i}$'s respectively, followed by integrations in space. The results are total number of $N_w + N_v + N_t$ nondimensional nonlinear algebraic equations in the generalized coordinates $q_{wi}, q_{vi}, q_{\theta i}$:

$$\pi^4 N_j^4 \bar{q}_{wj} + \frac{1}{2}(\tau - 1) \sum_{\mu=1}^{Nv} \sum_{\nu=1}^{Nt} H_{\nu j \mu} q_{\theta \nu} \bar{q}_{v\mu} + \frac{1}{2}(\tau - 1) \cdot \sum_{\mu=1}^{Nt} \sum_{\nu=1}^{Nt} \sum_{i=1}^{Nw} R_{ij\nu\mu} q_{\theta\nu} q_{\theta\mu} \bar{q}_{wi} + \frac{mgl^3}{EI_\eta}\left(\frac{-2B_j}{N_j \pi}\right) = 0$$

$$\text{with} \quad j = 1, 2, 3, ..., N_w \tag{6.17}$$

$$\pi^4 N_j^4 \left(\tau - \frac{\omega^2}{\omega_{wj}^2}\right) \bar{q}_{vj} - \frac{3}{4}(\tau - 1) \sum_{\nu=1}^{Nt} \sum_{\mu=1}^{Nt} \sum_{i=1}^{Nv} R_{ij\mu\nu} q_{\theta\nu} q_{\theta\mu} \bar{q}_{vi} + (\tau - 1) \sum_{\nu=1}^{Nt} \sum_{\mu=1}^{Nw} H_{\nu\mu j} q_{\theta\nu} \bar{q}_{w\mu} = 0$$

$$\text{with} \quad j = 1, 2, 3, ..., N_v \tag{6.18}$$

$$\frac{1}{2}\pi^2 (j - \frac{1}{2})^2 \frac{GJ}{EI_\eta}\left(1 - \frac{\omega^2}{\omega_{\theta j}^2}\right) q_{\theta j} + (\tau - 1) \sum_{\nu=1}^{Nw} \sum_{\mu=1}^{Nw} \sum_{i=1}^{Nt} R_{\mu\nu ji} \bar{q}_{w\nu} \bar{q}_{w\mu} - \frac{3}{4}(\tau - 1) \sum_{\nu=1}^{Nv} \sum_{\mu=1}^{Nv} \sum_{i=1}^{Nt} R_{\mu\nu ji} \bar{q}_{v\mu} \bar{q}_{v\nu} q_{\theta i} + (\tau - 1) \sum_{\nu=1}^{Nv} \sum_{\mu=1}^{Nw} H_{j\nu\mu} \bar{q}_{v\nu} \bar{q}_{w\mu} = 0$$

$$\text{with} \quad j = 1, 2, 3, ..., N_t \tag{6.19}$$

where for the j-th mode

$$\tau \equiv \frac{EI_\zeta}{EI_\eta}$$

$$\bar{q}_{wj} \equiv \frac{q_{wj}}{l}$$

$$\bar{q}_{vj} \equiv \frac{q_{vj}}{l}$$

$$\omega_{\theta j} \equiv \pi(j - 1/2)\sqrt{\frac{GJ}{I_{\xi\xi} l^2}} = \text{j-th torsion frequency}$$

$$\omega_{wj} \equiv \pi^2 N_j^2 \sqrt{\frac{EI_\eta}{ml^4}} = \text{j-th flap bending frequency}$$

$$B_j \equiv \frac{\sin \pi N_j - \sinh \pi N_j}{\cosh \pi N_j + \cos \pi N_j}$$

N_j's are given as follows (Ref. 47).

$$\begin{aligned} N_1 &= 0.596864162695 \\ N_2 &= 1.494175614274 \\ N_3 &= 2.500246946168 \\ N_4 &= 3.499989319849 \\ N_5 &= 4.500000461516 \\ & \text{etc.} \end{aligned}$$

Both $H_{j\mu\nu}$ and $R_{ij\mu\nu}$ represent some numerical integrations associated with products of mode shapes for the j-th mode:

$$\begin{aligned} H_{j\mu\nu} &\equiv \int_0^1 f_{\theta j}\, f''_{w\mu}\, f''_{w\nu}\, d\bar{x} \\ R_{ij\mu\nu} &\equiv \int_0^1 f''_{wi}\, f''_{wj}\, f_{\theta\mu}\, f_{\theta\nu}\, d\bar{x} \\ \text{with} \quad \bar{x} &\equiv x/l \end{aligned}$$

As expected, all of the nonlinear terms are multiplied by the same factor $\tau - 1$, which is a measure of the bending stiffness difference $EI_\zeta - EI_\eta$. Thus, one should expect weak nonlinearities as τ gets close to an order of unity (i.e., EI_ζ close to EI_η), or vice versa.

One can put equations 6.17 through 6.19 in a compact matrix form

$$\begin{bmatrix} [K_1] & 0 & 0 \\ 0 & -\omega^2 [M_1] + [K_2] & 0 \\ 0 & 0 & -\omega^2 [M_2] + [K_3] \end{bmatrix} \begin{bmatrix} \{\bar{q}_w\} \\ \{\bar{q}_v\} \\ \{q_\theta\} \end{bmatrix} = \begin{bmatrix} \{F_g\} \\ 0 \\ 0 \end{bmatrix} + \begin{bmatrix} \{\bar{Q}_w\} \\ \{\bar{Q}_v\} \\ \{Q_\theta\} \end{bmatrix} \tag{6.20}$$

where the first term on the right hand side represents the linear gravity forces, and $\{\bar{Q}_w\}$, $\{\bar{Q}_v\}$, $\{Q_\theta\}$ are nonlinear vector functions of the generalized coordinate vectors $\{\bar{q}_w\}$, $\{\bar{q}_v\}$, and $\{q_\theta\}$. The dimension of the matrix is $(N_w+N_v+N_\theta)$ by $(N_w+N_v+N_\theta)$. Matrix equation 6.20 is solved via a Newton-Raphson method similar to the one in section 6.1. Thus, the sine component of one of the modes (usually the first mode of motion of interest) is set to a desired amplitude level. The problem statement still retains the same number of unknowns as equations, since we have now replaced the fixed mode by the unknown frequency and iterate on the amplitudes of the remaining modes as well as the frequency. As before, one can rely on linear free vibration results such as ones by Minguet and Dugundji to start off the iteration procedure.

6.3 Rotating Free Vibration

The basic solution procedure for the rotating large amplitude free vibration problems remains the same as for the nonrotating case in the absence of any aerodynamic terms, except that now we have all the inertial loads including centrifugal, Coriolis terms. Thus, we need both first harmonic functions $\sin\omega t$ and $\cos\omega t$ in the Fourier expansion to account for phase differences which may arise from the Coriolis accelerations. Thus, after finishing harmonic balancing one has three sets of (12×1) differential equations in symbolic vector form

$$\underset{(12\times 1)}{\frac{dX_0}{ds}} = \underset{(12\times 1)}{h_0(X_0, X_s, X_c, \Omega, \omega)} \tag{6.21}$$

and

$$\underset{(12\times 1)}{\frac{dX_s}{ds}} = \underset{(12\times 1)}{h_s(X_0, X_s, X_c, \Omega, \omega)} \tag{6.22}$$

$$\frac{dX_c}{ds} = h_c(X_0, X_s, X_c, \Omega, \omega) \tag{6.23}$$

$$(12 \times 1) \qquad (12 \times 1)$$

where

$$\begin{aligned} X_0 &= [\,F_{10}\,F_{20}\,F_{30}\,M_{10}\,M_{20}\,M_{30}\,x_0\,y_0\,z_0\,\theta_0\,\beta_0\,\psi_0\,]^T \\ X_s &= [\,F_{1s}\,F_{2s}\,F_{3s}\,M_{1s}\,M_{2s}\,M_{3s}\,x_s\,y_s\,z_s\,\theta_s\,\beta_s\,\psi_s\,]^T \\ X_c &= [\,F_{1c}\,F_{2c}\,F_{3c}\,M_{1c}\,M_{2c}\,M_{3c}\,x_c\,y_c\,z_c\,\theta_c\,\beta_c\,\psi_c\,]^T \end{aligned}$$

As in the nonrotating case, given a rotational speed Ω, one has to guess boundary values of displacements and rotations at the tip and the frequency ω to start with. Since all of the rotating modes are expected to follow the nonrotating modes closely in their shapes, any of the linear nonrotating mode shapes such as ones given by Ref. 14 can be used as an initial guess for either $\sin\omega t$ or $\cos\omega t$ part of the boundary values at the tip. For the initial guesses at the frequencies, however, one needs to raise the nonrotating frequencies slightly to account for the centrifugal effects. The functional relationships between the two sets of boundary values at the root and the tip in this case can be written as

$$X_r = f(X_t, \Omega, \omega) \tag{6.24}$$

$$(18 \times 1) \quad (18 \times 1)$$

where

$$X_t = [x_0\,x_s\,x_c\,y_0\,y_s\,y_c\,z_0\,z_s\,z_c\,\theta_0\,\theta_s\,\theta_c\,\beta_0\,\beta_s\,\beta_c\,\psi_0\,\psi_s\,\psi_c]^T$$

at the tip. Once again, with appropriate initial value of X_t and a root boundary condition X_r given in section 2.2, the above relationship leads to a Newton-Raphson iterative algorithm

$$X_t^{n+1} = X_t^n - J(X_t^n, \omega^n)^{-1} R^n \tag{6.25}$$

where

$$R^n \equiv f(X_t^n, \omega^n) - X_r$$

and

$$J: \ (18 \times 18) \text{ Jacobian matrix}$$

One of the six boundary amplitudes at the tip $x_s, y_s, z_s, \theta_s, \beta_s, \psi_s$ is replaced by the frequency ω, and the replaced displacement is fixed throughout iterations.

6.4 Solution of Static Position

For a given rotational speed Ω and a root pitch angle θ_r, the static analysis of the blade proceeds as follows. First, all the dynamic terms are dropped leaving twelve (fourteen if warping and shear are included) static differential equations in the form,

$$\frac{dX_0}{ds} = p_0(X_0) \tag{6.26}$$

$$(12 \times 1) \quad (12 \times 1)$$

where

$$X_0 = [\, F_{10}\, F_{20}\, F_{30}\, M_{10}\, M_{20}\, M_{30}\, x_0\, y_0\, z_0\, \theta_0\, \beta_0\, \psi_0 \,]^T$$

Then the resulting twelve differential equations are integrated leading to a relationship between tip variables and root variables as

$$X_r = f(X_t) \tag{6.27}$$

$$(6 \times 1) \quad (6 \times 1)$$

where

$$X_t = [x_0\, y_0\, z_0\, \theta_0\, \beta_0\, \psi_0]^T$$

at the tip. Since only static variables are involved, the initial guesses for the tip value X_t can be fairly arbitrary as far as they are geometrically reasonable. Thus,

with appropriate initial value of X_t and a root boundary condition X_r, the functional relationship can be used to form a series of Newton-Rahpson algorithm,

$$X_t^{n+1} = X_t^n - J(X_t^n)^{-1} R^n \tag{6.28}$$

where

$$R^n \equiv f(X_t^n) - X_r$$

$$J: \ (6 \times 6) \text{ Jacobian matrix}$$

The algorithm will eventually converge to the solution as the iteration goes on provided that the initial value for X_t is reasonable.

6.5 Solution of Linear Flutter

For a linear flutter solution, all the higher order magnitude terms are dropped out leaving only the first order dynamic terms in the differential equations. Hence, the structural part will be linearized about an arbitrary static position, and the aerodynamic part will be also linearized about static angle of attack. The static solution has just been obtained from the previous section.

$$\underset{(12 \times 1)}{\frac{dX_s}{ds}} = \underset{(12 \times 1)}{q_s(X_s, X_c, \omega)} \tag{6.29}$$

and

$$\underset{(12 \times 1)}{\frac{dX_c}{ds}} = \underset{(12 \times 1)}{q_c(X_s, X_c, \omega)} \tag{6.30}$$

where

$$X_s = [F_{1s}\, F_{2s}\, F_{3s}\, M_{1s}\, M_{2s}\, M_{3s}\, x_s\, y_s\, z_s\, \theta_s\, \beta_s\, \psi_s]^T$$

$$X_c = [F_{1c}\, F_{2c}\, F_{3c}\, M_{1c}\, M_{2c}\, M_{3c}\, x_c\, y_c\, z_c\, \theta_c\, \beta_c\, \psi_c]^T$$

It is noted that these differential equations are completely decoupled from the static solution X_0, and become functions of ω only after the static solution has been found.

Since the equations are linear, a linear transformation between tip values and root values exists in the form,

$$X_r = T_r(\omega) X_t \tag{6.31}$$

$$(12 \times 1) \quad (12 \times 1)$$

where

$$X_t = [x_s\, x_c\, y_s\, y_c\, z_s\, z_c\, \theta_s\, \theta_c\, \beta_s\, \beta_c\, \psi_s\, \psi_c]^T$$

at the tip, and

$$X_r = [0\,0\,0 \ldots 0]^T$$

This transformation is called the transition matrix and its i-th column can be obtained by integrating the twenty four differential equations corresponding to initial tip boundary condition (12×1) $[0\,0\,0 \ldots, 0\,1\,0 \ldots 0]^T$ where the nonzero unity enters at the i th element. For any flutter solution to exist for a given static solution and a frequency ω, the transition matrix T_r must be singular. In addition, all of its 11x11 submatrices must be singular since the phases of the tip boundary values could be arbitrary. Hence, T_r must have rank deficieny of two. To check this, one can first check the determinant of T_r, and if the determinant is sufficiently small, solve the eigenvalue problem equation 6.31 for an arbitrary combination of amplitude and phase. Then for the eigensolution X_t at the tip, the twenty-four differential equations are integrated. If the resulting root vector X_r is indeed zero or close to zero for the chosen X_t, then the corresponding Ω, ω and the boundary value X_t yield a flutter solution. If not, a different combination of Ω and ω should be tried. Hence, a typical flutter solution needs more than a few iterations between the static analysis and the eigen analysis described in this section.

In the remainder of section, an example of linear flutter solution technique described above will be given for the case of torsional flutter. In this procedure, the sine part of the torsional amplitude θ_s is fixed at the tip at desired level while the corresponding cosine part θ_c is set to zero.

Step 1;

Given Ω, θ_r, and a root boundary condition X_r, solve for the static deformation of the blade following the procedure described in section 6.4. Save the results.

Step 2;

Linearize the equations of motion about the static position by dropping all the higher order magnitude terms higher than the first order. This can be implemented simply by dropping the higher order terms in the formulas given in Appendices A, B, and C. Also, linearize the unsteady aerodynamics about the given static angle of attack α_0 at each station. If α_0 is below stall angle, the aerodynamic coefficients must reduce to Greenberg's formula. If α_0 is above the stall angle, then the ONERA nonlinear equations are linearized about it.

Step 3;

With θ_c set to zero at the tip and a chosen value of ω, integrate the twenty four linearized differential equations to form the following matrix relation

$$X_r' = T_r'(\omega)\, X_t' \tag{6.32}$$

$$(12 \times 1) \quad (11 \times 1)$$

where

$$X_t' = [\theta_s\, \beta_s\, \beta_c\, \psi_s\, \psi_c\, x_s\, x_c\, y_s\, y_c\, z_s\, z_c\,]^T$$

at the tip, and

$$X_r' = [\theta_s\, \theta_c\, \beta_s\, \beta_c\, \psi_s\, \psi_c\, x_s\, x_c\, y_s\, y_c\, z_s\, z_c\,]^T$$

at the root which is not a zero vector until a flutter solution is found. The i-th column of the (12×11) matrix T_r' can be obtained by integrating the twenty four differential equations corresponding to initial tip boundary condition (11×1) $[0\,0\,0\ldots, 0\,1\,0\ldots 0]^T$ where the nonzero unity enters at the i th element.

Step 4;

Form an (11×11) matrix A such that

$$A = \begin{bmatrix} \text{1st row of } T_r' \\ \text{3rd row of } T_r' \\ \text{4th row of } T_r' \\ \text{etc.} \\ \text{12th row of } T_r' \end{bmatrix}$$

Step 5;

Check if $det\, A$ is zero, or close to zero.

Step 6;

If yes, get eigensolution $[\theta_s\, \beta_s\, \beta_c\, \psi_s\, \psi_c\, x_s\, x_c\, y_s\, y_c\, z_s\, z_c]^T$ at the tip with $\theta_s = 1$ and $\theta_c = 0$ at the tip, by solving the (12×11) matrix equation. Call this $[1\, \beta_{st}\, \beta_{ct}\, \psi_{st}\, \psi_{ct}\, x_{st}\, x_{ct}\, y_{st}\, y_{ct}\, z_s\, z_{ct}]^T$.

Step 7;

Check the residue in θ_{cr} at the root by multiplying the second row of T_r' matrix by the eigensolution as

$$\theta_{cr} = T_r'(2,1) + T_r'(2,2)\beta_{st} + T_r'(2,3)\beta_{ct} + \ldots + T_r'(2,11)\, z_{ct}$$

If θ_{cr} is zero or close to zero, then a flutter solution has been found. If not, then go back to Step 1 and repeat the subsequent steps for different set of Ω and ω until a flutter point is found.

6.6 Solution of Large Amplitude Flutter Limit Cycles

In this section, solution technique of nonlinear flutter that may evolve from linear flutter solutions is described. Unlike its linear counterpart, the nonlinear flutter problem is coupled with static parts of the solution. Furthermore, there is one-to-one correspondence between pair of given (Ω, ω) and an amplitude level of the solution. Thus, one can express the coupled nonlinear differential equations in vector form

$$\frac{dX_0}{ds} = r_0(X_0, X_s, X_c, \Omega, \omega) \tag{6.33}$$

$$(12 \times 1) \qquad (12 \times 1)$$

and

$$\frac{dX_s}{ds} = r_s(X_0, X_s, X_c, \Omega, \omega) \tag{6.34}$$

$$(12 \times 1) \qquad (12 \times 1)$$

$$\frac{dX_c}{ds} = r_c(X_0, X_s, X_c, \Omega, \omega) \tag{6.35}$$

$$(12 \times 1) \qquad (12 \times 1)$$

where

$$\begin{aligned} X_0 &= [\,F_{10}\,F_{20}\,F_{30}\,M_{10}\,M_{20}\,M_{30}\,x_0\,y_0\,z_0\,\theta_0\,\beta_0\,\psi_0\,]^T \\ X_s &= [\,F_{1s}\,F_{2s}\,F_{3s}\,M_{1s}\,M_{2s}\,M_{3s}\,x_s\,y_s\,z_s\,\theta_s\,\beta_s\,\psi_s\,]^T \\ X_c &= [\,F_{1c}\,F_{2c}\,F_{3c}\,M_{1c}\,M_{2c}\,M_{3c}\,x_c\,y_c\,z_c\,\theta_c\,\beta_c\,\psi_c\,]^T \end{aligned}$$

The vector function arrays r_0, r_s and r_c contain many product terms involving multiplications of two, or three harmonic quantities. They originate from the twelve basic equations that are presented in section 2.1. Multiplications of harmonics and calculations of the coefficients of the resulting new harmonics are implemented according to formulas in the Appendices A, B, and C.

First, all of the thirty-six equations (now twelve for the static part, twenty four for the dynamic part) are first integrated from the tip to the root of the blade once. One has to guess tip boundary value X_t as well as the rotational speed and frequency that will make X_r at the root as close to the prescribed values as possible. Since the nonlinear solutions are assumed to evolve from linear solutions, the linear eigensolution and the critical Ω, ω obtained in the previous sections are used for the initial X_t, Ω, and ω. Once the integration starts, the functional relationships between these two sets of boundary values can be written as

$$X_r = f(X_t, \Omega, \omega) \tag{6.36}$$

$$(18 \times 1) \quad (18 \times 1)$$

where

$$X_t \;=\; [x_0\, x_s\, x_c\, y_0\, y_s\, y_c\, z_0\, z_s\, z_c\, \theta_0\, \theta_s\, \theta_c\, \beta_0\, \beta_s\, \beta_c\, \psi_0\, \psi_s\, \psi_c]^T$$

at the tip. Since for a given level of amplitude the initial eighteen components of X_t can not be perfect, a Newton-Raphson algorithm is employed to produce a better set of boundary values based on the current values. This will produce a series of the following set of boundary values.

$$X_t^{n+1} \;=\; X_t^n \;-\; J(X_t^n, \Omega^n, \omega^n)^{-1} R^n \tag{6.37}$$

where

$$R^n \;\equiv\; f(X_t^n, \Omega^n, \omega^n) \;-\; X_r$$

$$J: \; (18 \times 18) \text{ Jacobian matrix}$$

This algorithm must take iterations on the Ω and ω as well as the boundary values, since it is not known in advance at which rotational speed and frequency a nonlinear flutter will exist for a given amplitude level. Therefore, one of sine parts of the boundary amplitudes at the tip $x_s, y_s,\ z_s, \theta_s,$ is replaced by Ω, and is fixed at a given level throughout iterations. Also, the corresponding cosine part of the amplitude is replaced by ω, and is fixed at zero value. This is done because the associated phases of various amplitudes can be assigned any value. Which pair of amplitude should be replaced depends on the flutter mode shape of interest, but the torsional amplitude pair θ_s, θ_c is usually selected.

For each amplitude level the iteration stops when the residue vector R at the root becomes sufficiently small. Beginning with very small amplitude level which essentially corresponds to the linear flutter solution, the solution method marches with increased amplitude until there the algorithm diverges, i.e., there exists no nonlinear solution.

Chapter 7

Analytic Results of Large Amplitude Free Vibration

7.1 Nonrotating results using Fully Nonlinear Equations

The prescribed algorithm in section 6.1 has been used to investigate the first and second bending modes, first fore-and-aft modes, and first torsion modes of cantilevered blades with the lay-ups $[0/90]_{3s}$, $[45/0]_s$ of graphite/epoxy for various tip deflections. These blade models were also used by Minguet and Dugundji in Ref. 14. The modes chosen have the lowest natural frequencies, and hence should converge easily. Furthermore, they are important from an aeroelastic perspective. The configuration of the blades investigated is 560 mm long, 30 mm wide. Beam material properties of these lay-ups are listed on Table 7.1. To see how these coefficients are calculated, refer to section 2.6 of Ref. 13. The warping coefficients for these blades are fairly small, of an order of magnitude of 10^{-4}, so warping and transverse shear were not included in all of calculations.

The static deflections were varied by imposing and adjusting uniform gravity level $\vec{g}$ throughout the blade. As stated earlier, one of the six boundary amplitudes at the tip was replaced by ω, and the replaced amplitude was fixed throughout the iterations. The z_s, y_s, and θ_s were fixed for bending, fore-and-aft, and torsional modes, respectively. For simplicity of analysis, none of the hinge-offset, preconing angle, root

pitch, root coning, or root lag was introduced ($\underline{e} = \beta_p = \theta_0 = 0$). A total of 16 node points were used along the blades. Note that the same number of nodes was also used in Ref. 14. All of the cases were guided by the linear results by Ref. 14. That is, the linear mode shapes and their natural frequencies provide reasonable trial values which, after a few iterations, would lead to nontrivial solutions. All the runs were made on a DEC Microvax computer with typical number of iterations from 5 to 10 for convergence. Each iteration took approximately between 15 to 30 seconds of CPU time, longer times being required for cases with strong structural couplings. Often, it was necessary to use under-relaxation, i.e., only a portion of the full Newton-Raphson increment, to lead iterations smoothly to the final solution without causing divergence or any sudden jump into another nonlinear solution (In fact, both F. D. G. and F. D. L. M. algorithms assume use of certain under-relaxations). Each analysis was continued until the amplitude could not be further increased. At this point, the Jacobian matrix became almost singular and the solution did not converge.

Before illustrating the results in detail, it is worthwhile to mention that in linear problems with small perturbations, the present analysis would be slightly superior to that of Ref. 14. The present analysis is based on a continuous model while Ref. 14 is based on a lumped, finite difference model.

As the moderate deflection equations in section 6.2 show, the large amplitude effects in the structure as well as large static deformation, largely depend on the chordwise vs. flapwise bending stiffness ratio EI_ζ/EI_η. Sine both blade models under consideration possess very high stiffness ratios (390 and 6930 respectively), these effects are expected to be prominent in the results. These trend, however, will diminish if the effective chordwise bending stiffness is reduced via., for example, direct reduction in EI_ζ or use of lag hinge.

The first example is the $[0/90]_{3s}$ specimen. Figure 7.1, 7.2, and 7.3 show changes of natural frequencies of various modes as functions of amplitudes z_s,y_s, and θ_s at the tip, at three different static tip deflection levels, 0 mm, 59 mm, and 210 mm (1B,

2B - first and second bending modes, 1F - first fore-and-aft or lead-lag mode, 1T - first torsional mode). Also, Figure 7.4 and 7.5 represent the variations of the average deflection z_0 at the tip as functions of the tip amplitudes for the static tip deflections 59 mm and 210 mm. From the figures the following two observations can be made.

(1) Increasing amplitude level has slight stiffening effects in 1B, 2B (or any bending modes, presumably) whereas it has significant softening effects in 1F, 1T modes, particularly for moderate range of static tip deflections. Consequently, the natural frequencies of bending modes rise slightly with amplitude level while those of 1F and 1T modes always drop.

(2) The above frequency changes are accompanied by changes in the average static deflections (centershifts). Increasing amplitude levels has slight effects on the centershifts of bending modes except for the 2B mode. However, it causes significant centershift increase for the 1F mode and a centershift decrease for the 1T mode, particularly for moderate static tip deflections. The behavior of these centershifts seem relevant to the linear findings in Ref. 13 (see Figure 7.9).

Figure 7.6 presents the effects of second harmonics on the natural frequencies of 1F modes at three different levels of static tip deflections, 24 mm (small), 59 mm (moderate), and 210 mm (large). It was found that including terms involving the second harmonic $\cos 2\omega t$ in two-dimensional sense was enough to capture the missing second harmonics in 1F modes. In other words, only F_1,F_3,M_2, and β,x,z were expressed in the form

$$X(\omega, t) = X_0(\omega) + X_s(\omega)\sin\omega t + X_{2c}(\omega)\cos\ 2\omega t$$

with all other variables containing only the first harmonics as before. This was done based on the intuition that second harmonics will mostly appear in x_s, z_s and their motion should be initially 90 degrees out of phase with the rest of amplitudes. Then a new set of formulae that performs multiplications of harmonics was implemented in the computer program. These are different from the previous ones in the Appendices in that they now have to deal with $\cos 2\omega t$ as well. The resulting Jacobian is then

(15×15) instead of (18×18) which would result if $\cos 2\omega t$ were introduced in all of the variables. It was found that 1F modes exhibit significant second harmonic contents in z_s motion at moderate to large amplitude levels when static tip deflections are small. On the other hand, at either zero or moderate to large static tip deflections the effects of the second harmonic term were almost unrecognizable even at high level of amplitudes. In fact, z_s has no first harmonic content in 1F modes. An effort was also made to seek for any second harmonics in 1T, 1B and 2B bending modes at, but they have been found very weak and are not presented here.

Figure 7.10 through 7.21 show mode shapes at two extreme amplitude levels under the three different static tip deflections, 0 mm, 59 mm, and 210mm. For most of the amplitude range, the nonlinear modes remain almost identical to linear modes in their shapes even though their frequencies change.

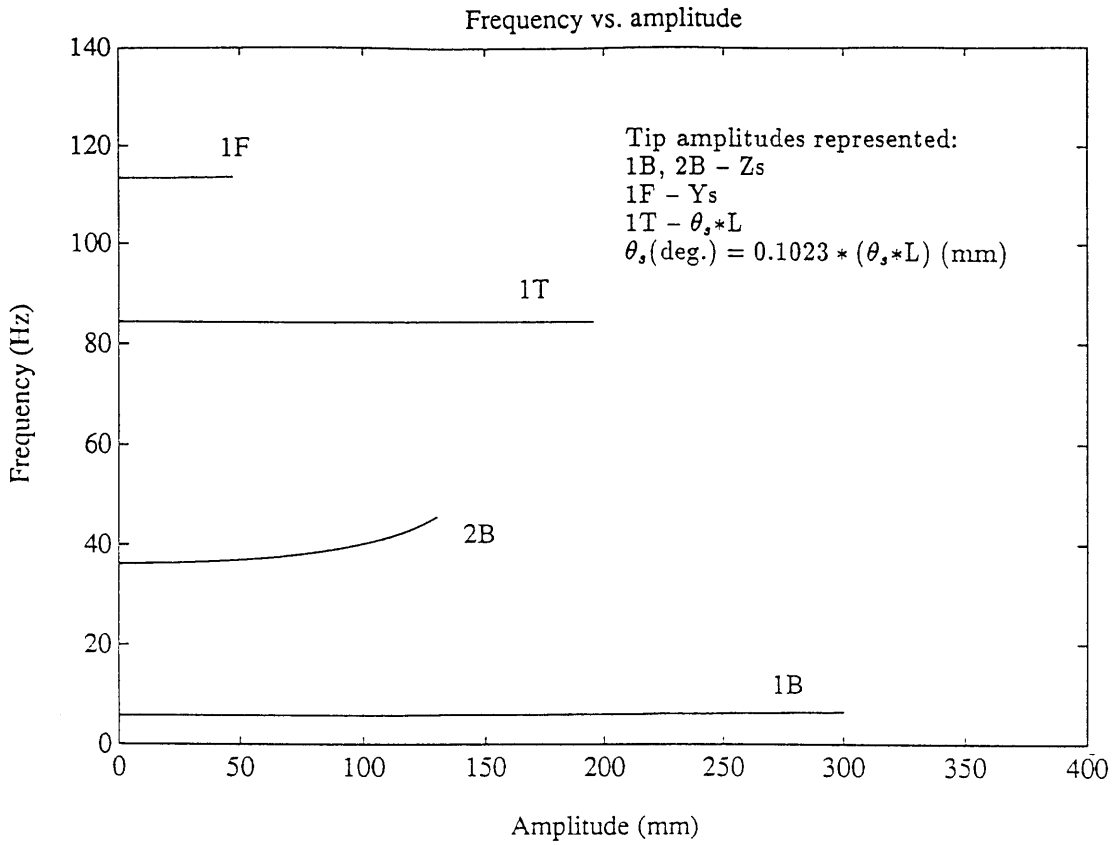

Figure 7.1: Frequency vs. amplitude; $[0/90]_{3s}$, 0 mm tip deflection

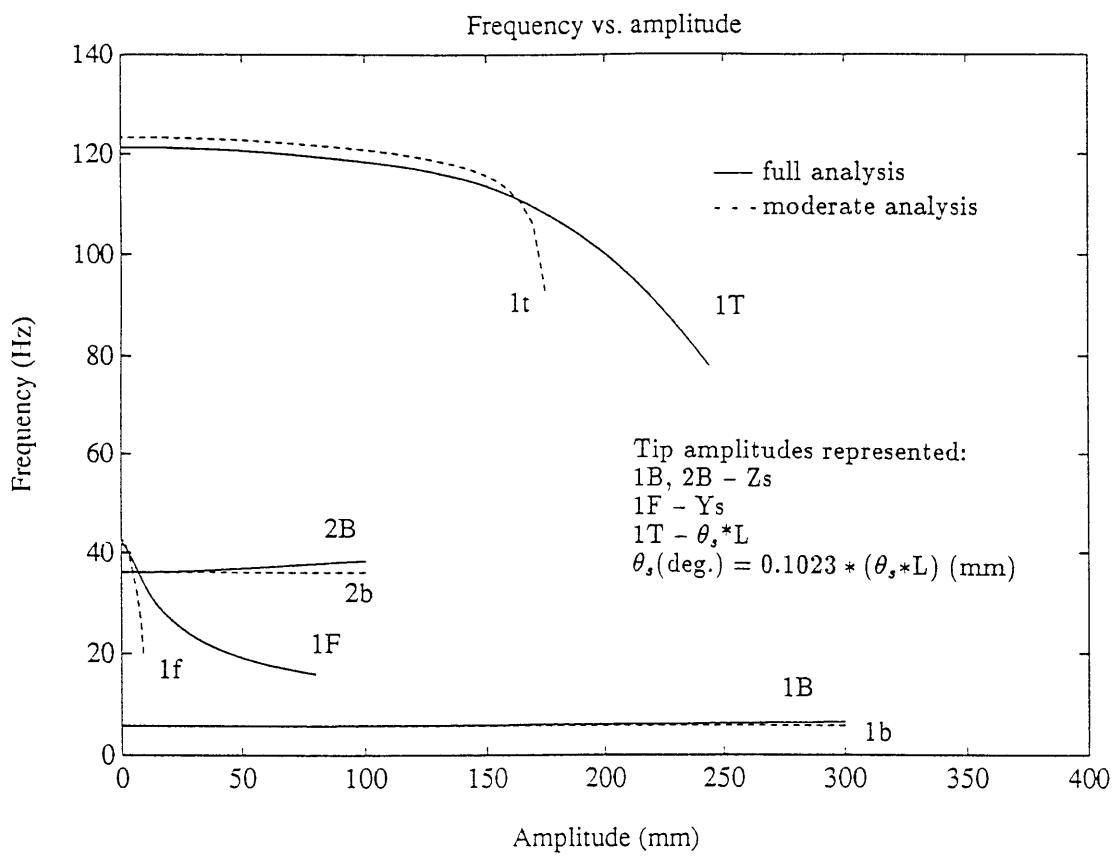

Figure 7.2: Frequency vs. amplitude; $[0/90]_{3s}$, 59 mm tip deflection

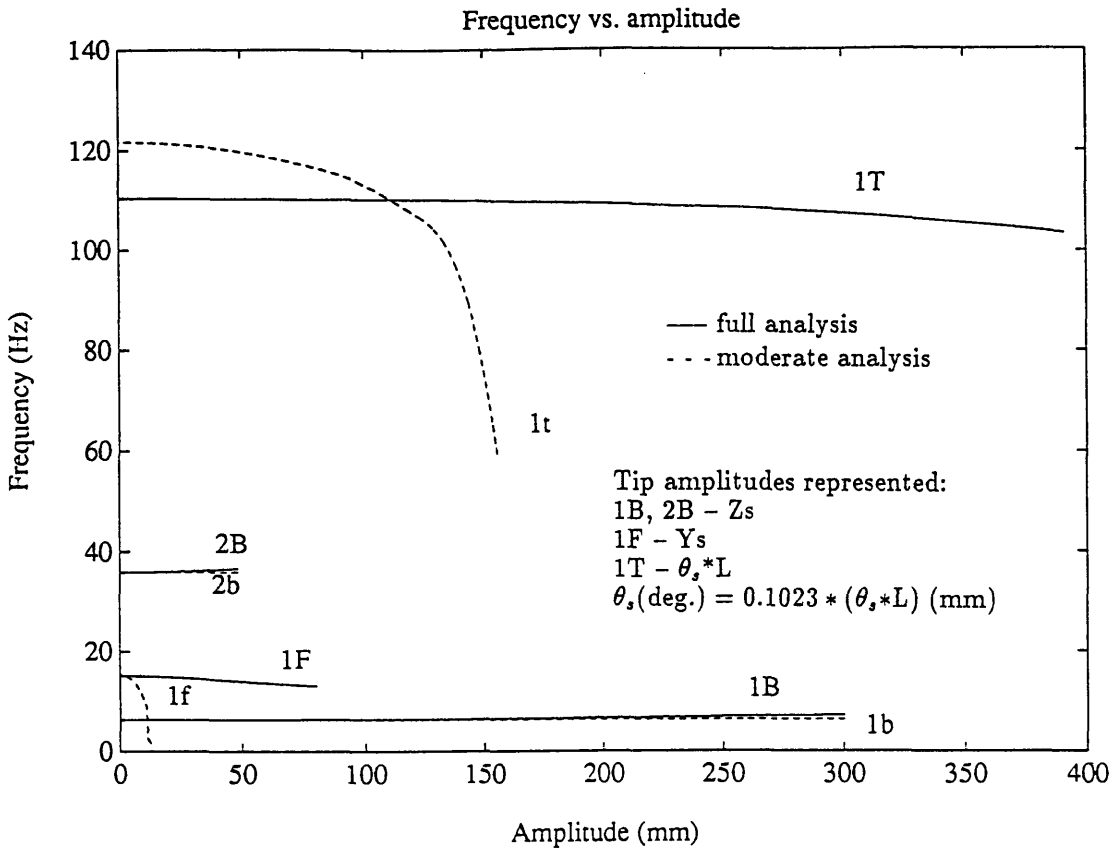

Figure 7.3: Frequency vs. amplitude; $[0/90]_{3s}$, 210 mm tip deflection

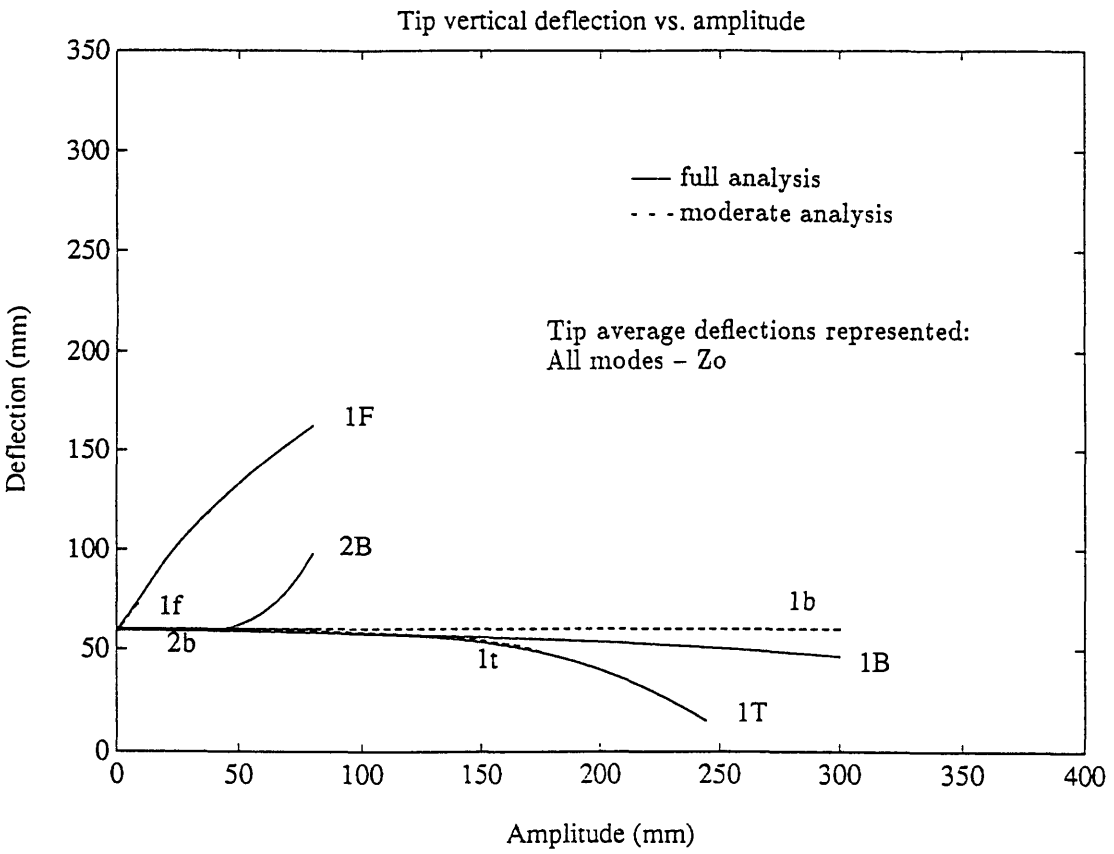

Figure 7.4: Tip average deflection vs. amplitude; $[0/90]_{3s}$, 59 mm tip deflection

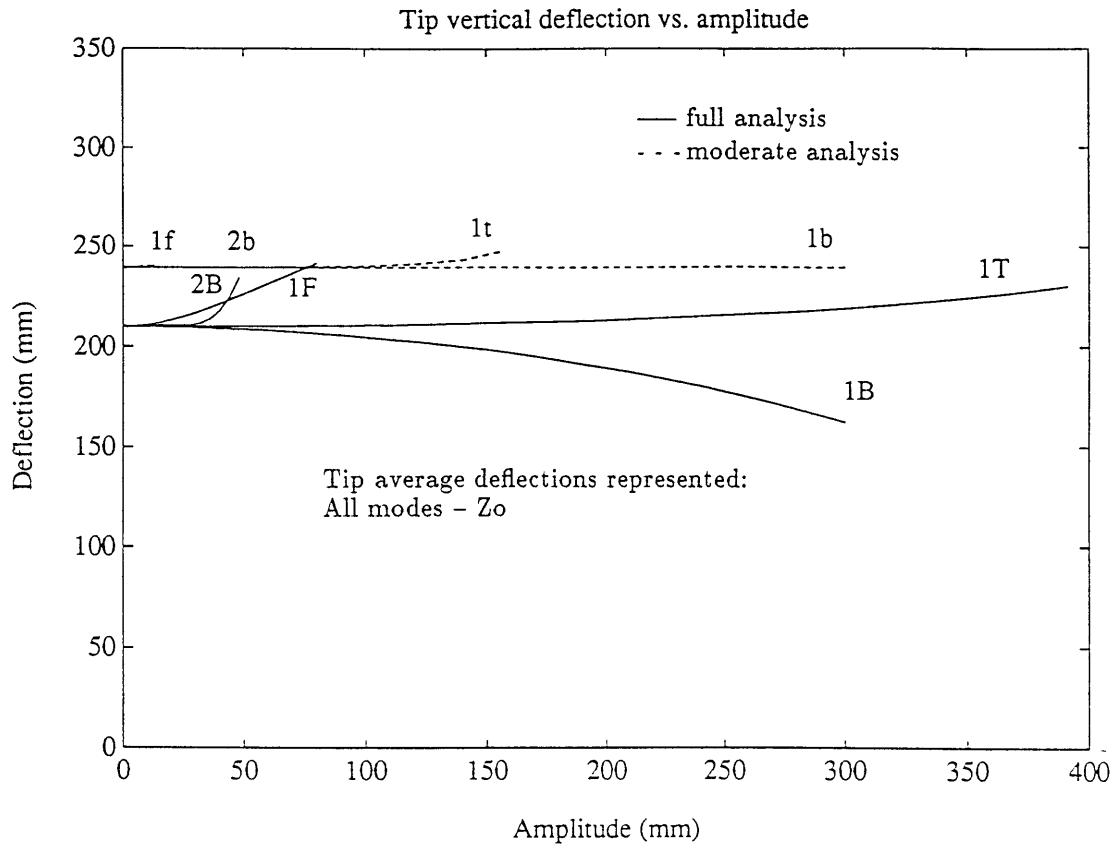

Figure 7.5: Tip average deflection vs. amplitude; $[0/90]_{3s}$, 210 mm tip deflection

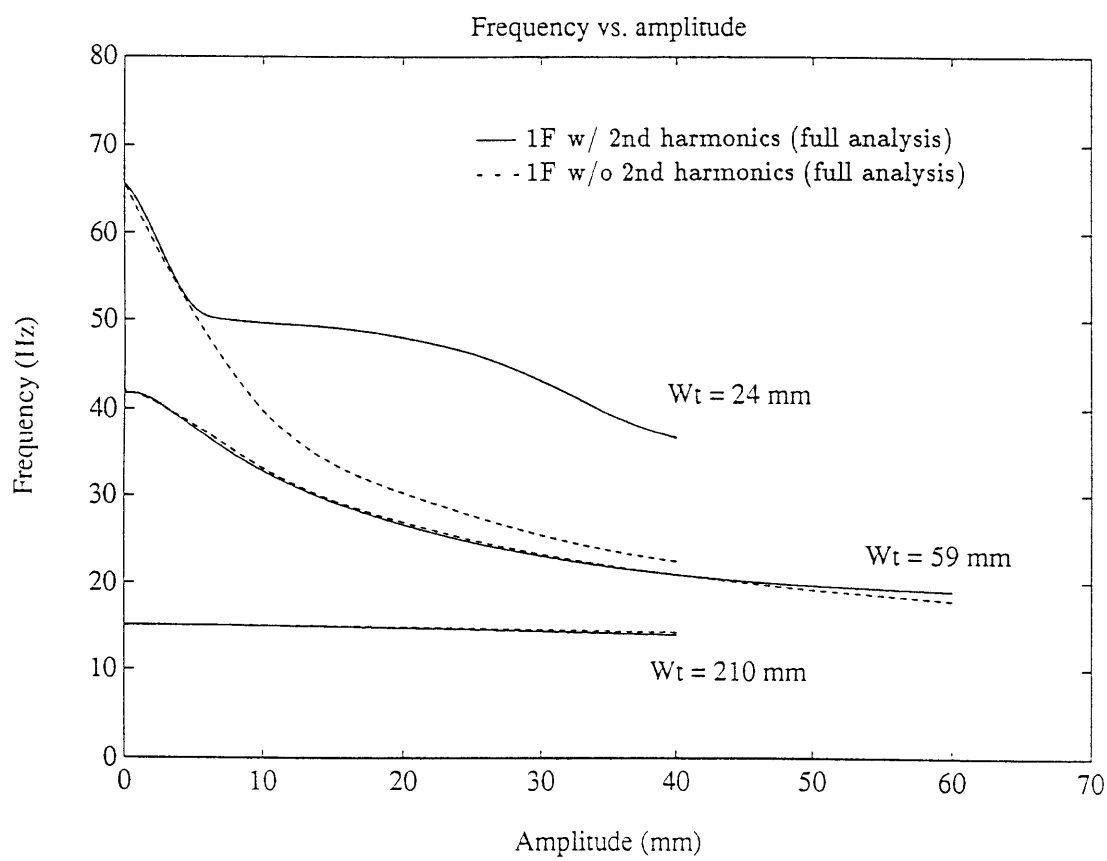

Figure 7.6: Frequency vs. amplitude w/ and w/o 2nd harmonics; $[0/90]_{3s}$, 24 mm, 59 mm, and 210 mm tip deflection

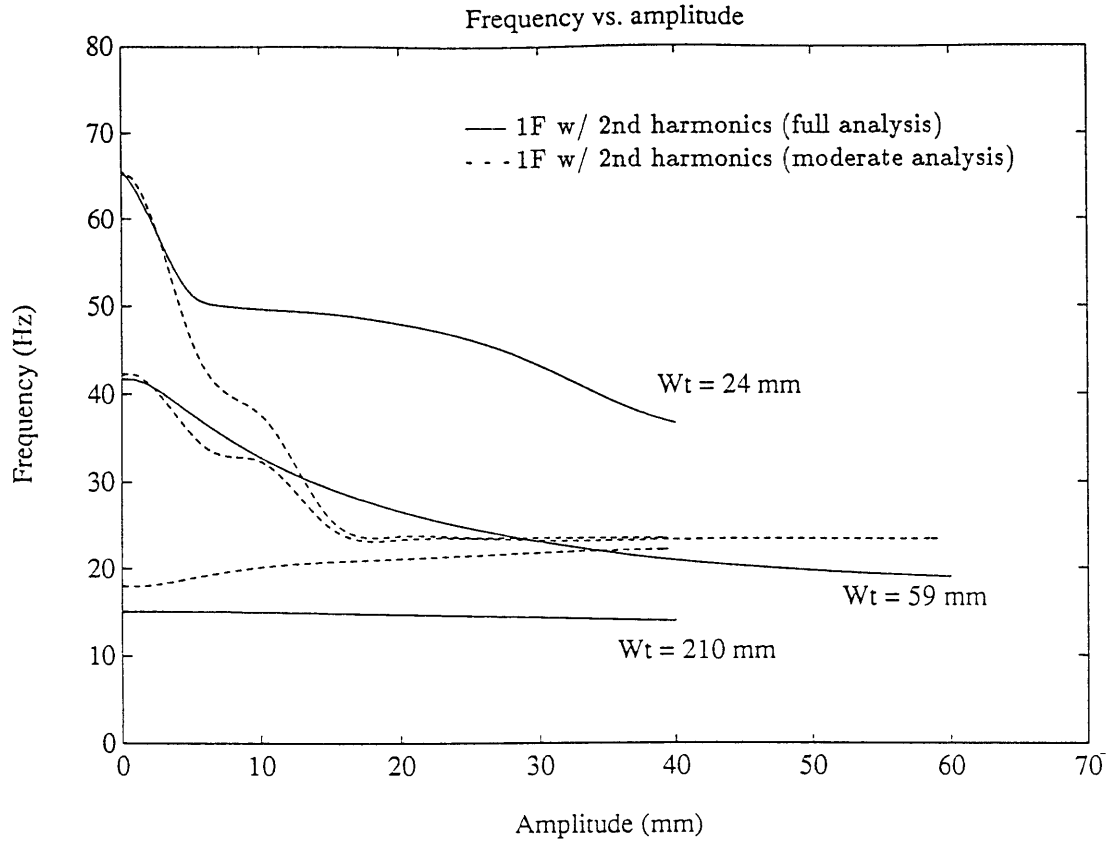

Figure 7.7: Frequency vs. amplitude w/ 2nd harmonics; $[0/90]_{3s}$, 24 mm, 59 mm, and 210 mm tip deflection

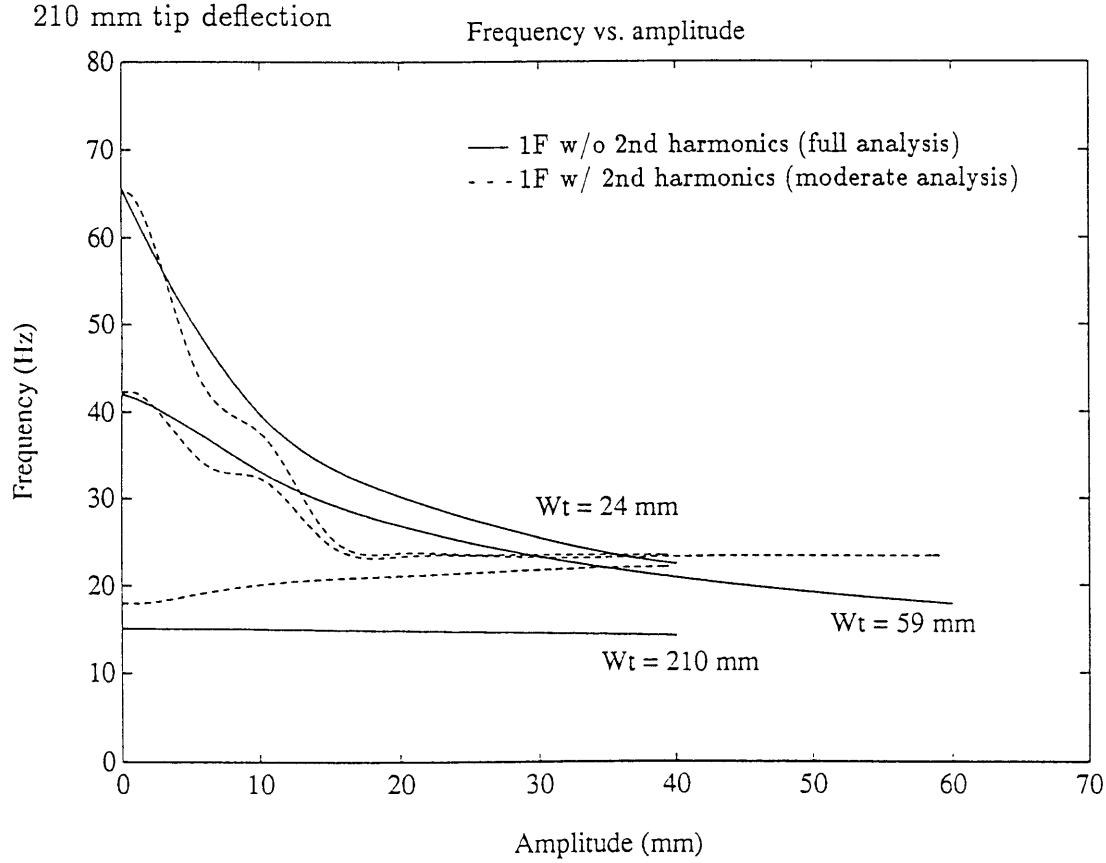

Figure 7.8: Frequency vs. amplitude w/ and w/o 2nd harmonics; $[0/90]_{3s}$, 24 mm, 59 mm, and 210 mm tip deflection

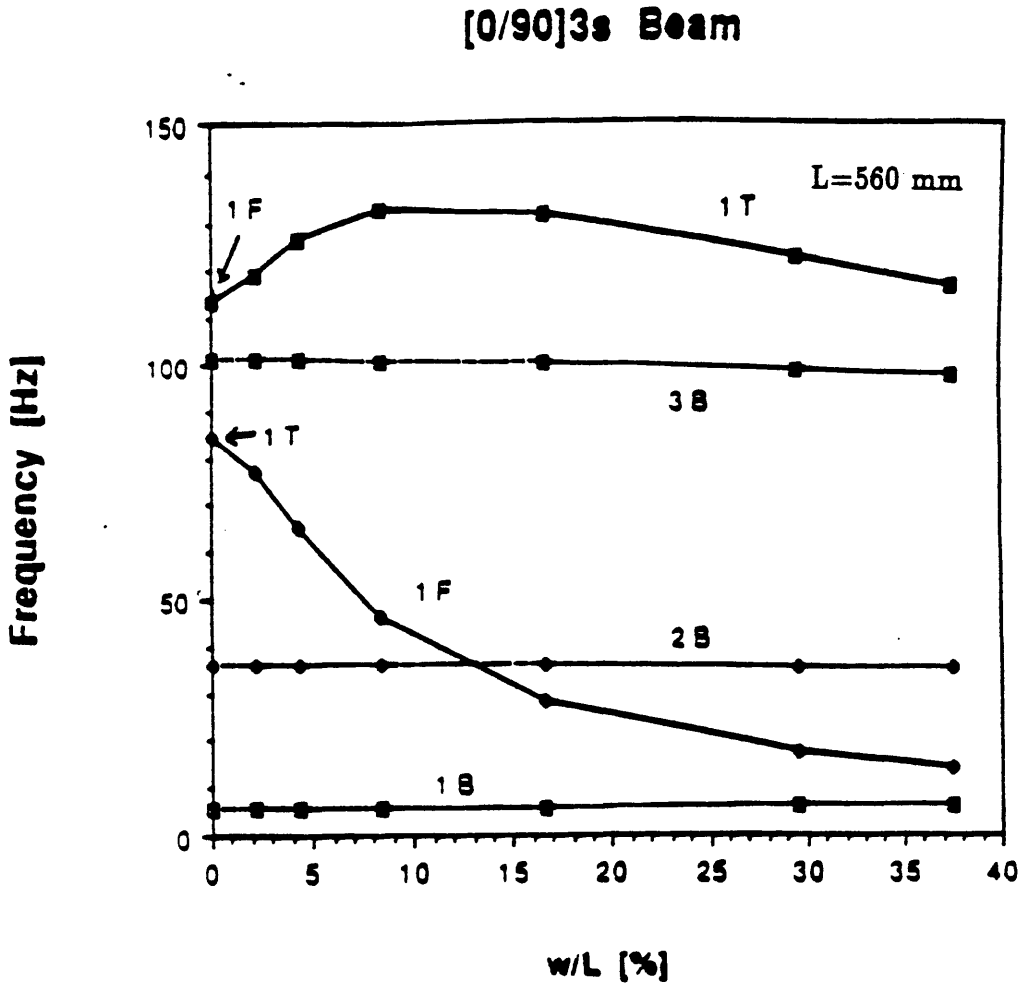

Figure 7.9: Natural frequencies of $[0/90]_{3s}$ beam as a function of tip deflection (from Ref. 13)

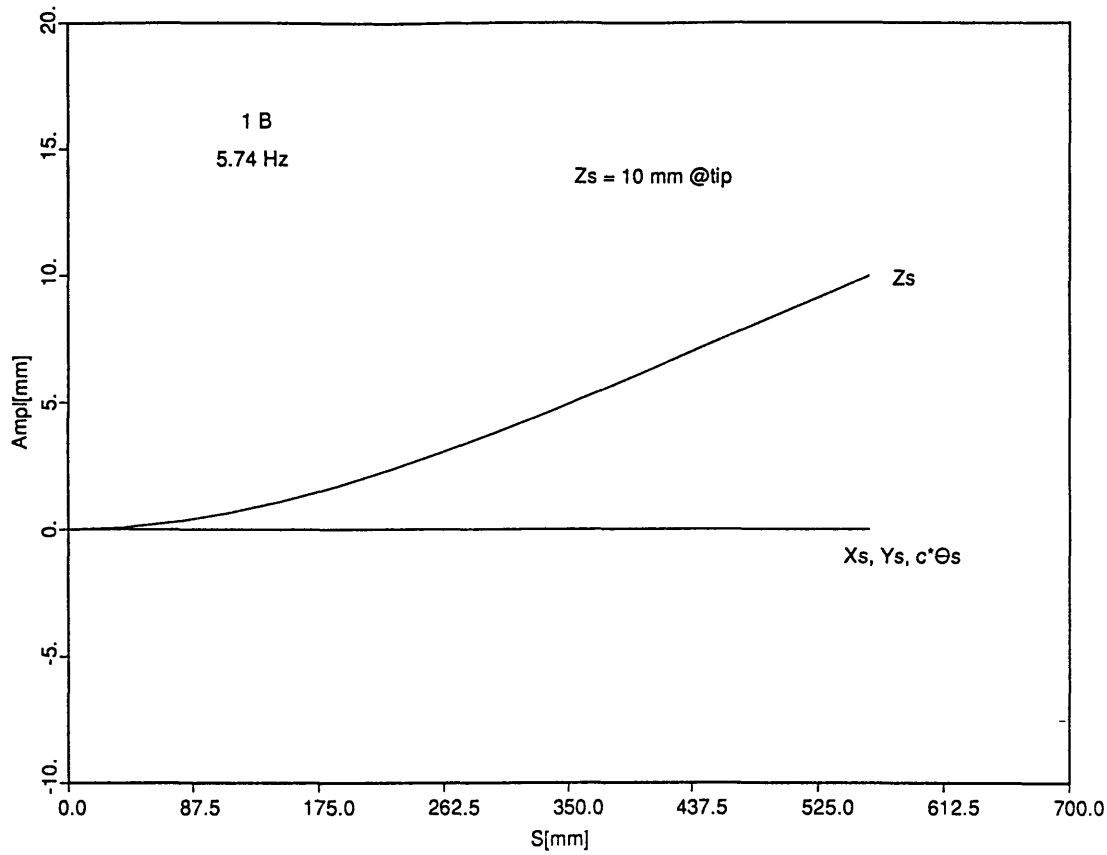

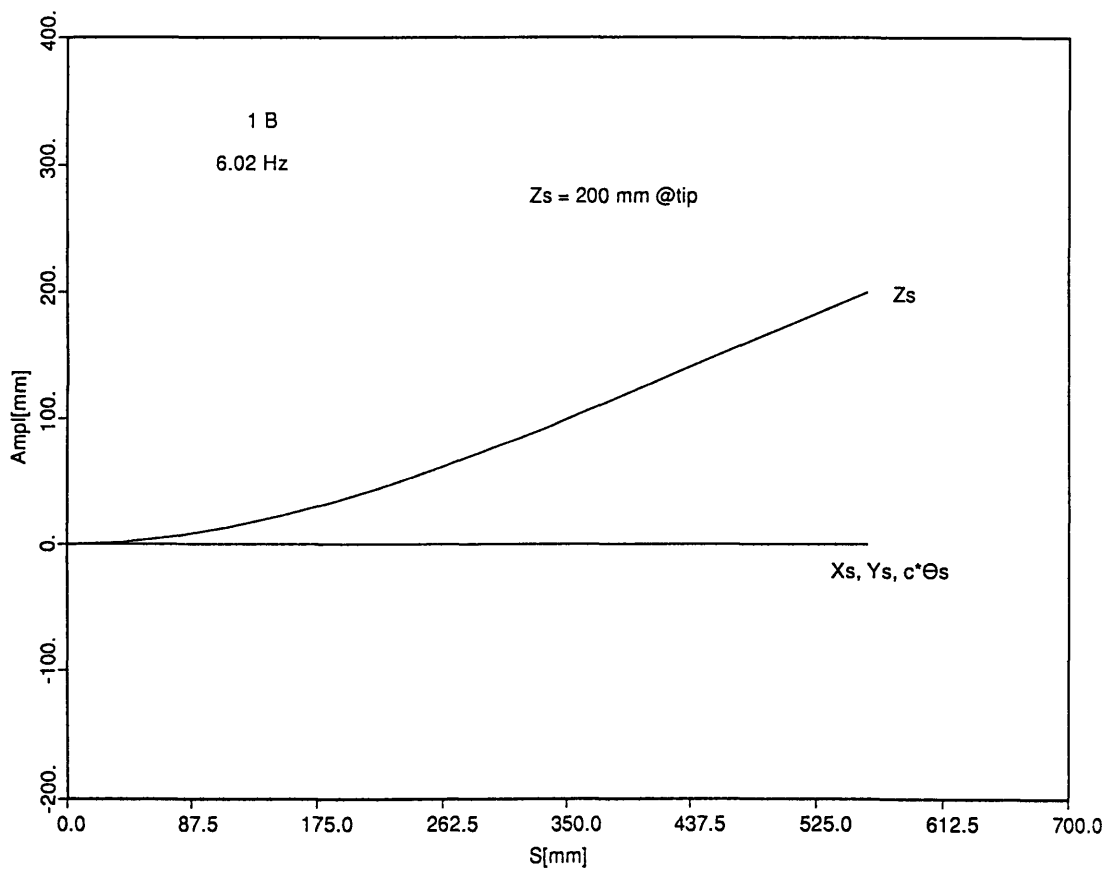

Figure 7.10: First Bending Mode; $[0/90]_{3s}$, 0 mm tip deflection, Zs=10, 200 mm

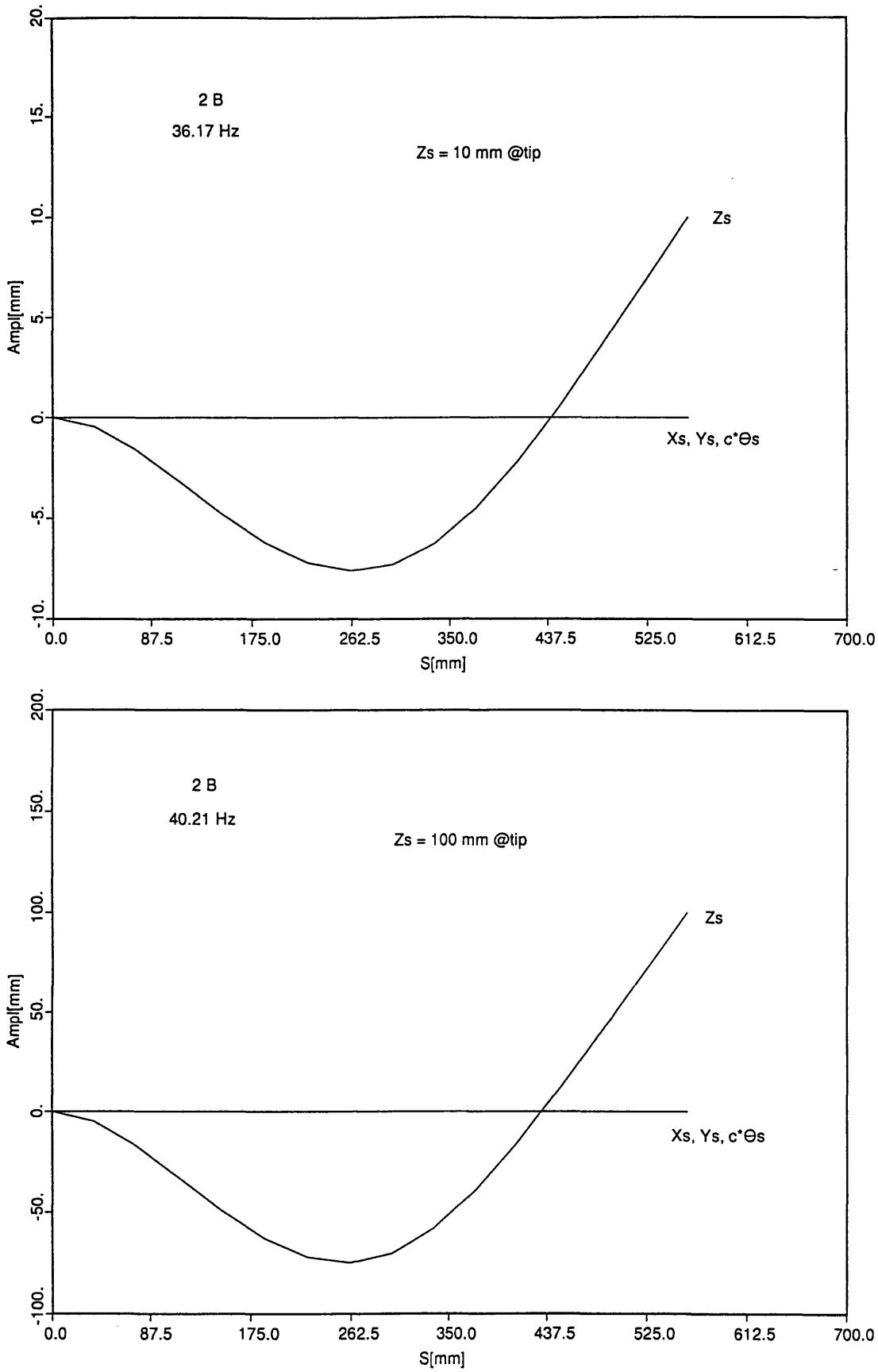

Figure 7.11: Second Bending Mode; $[0/90]_{3s}$, 0 mm tip deflection, Zs=10, 100 mm

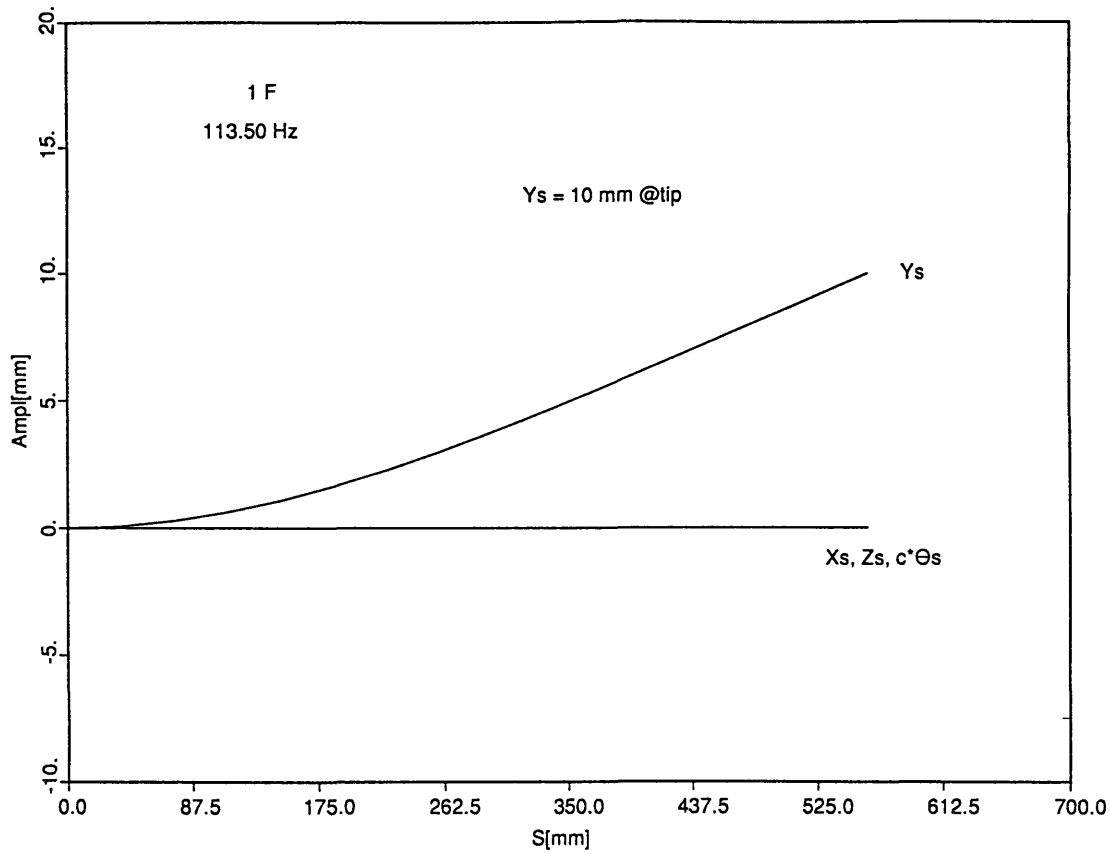

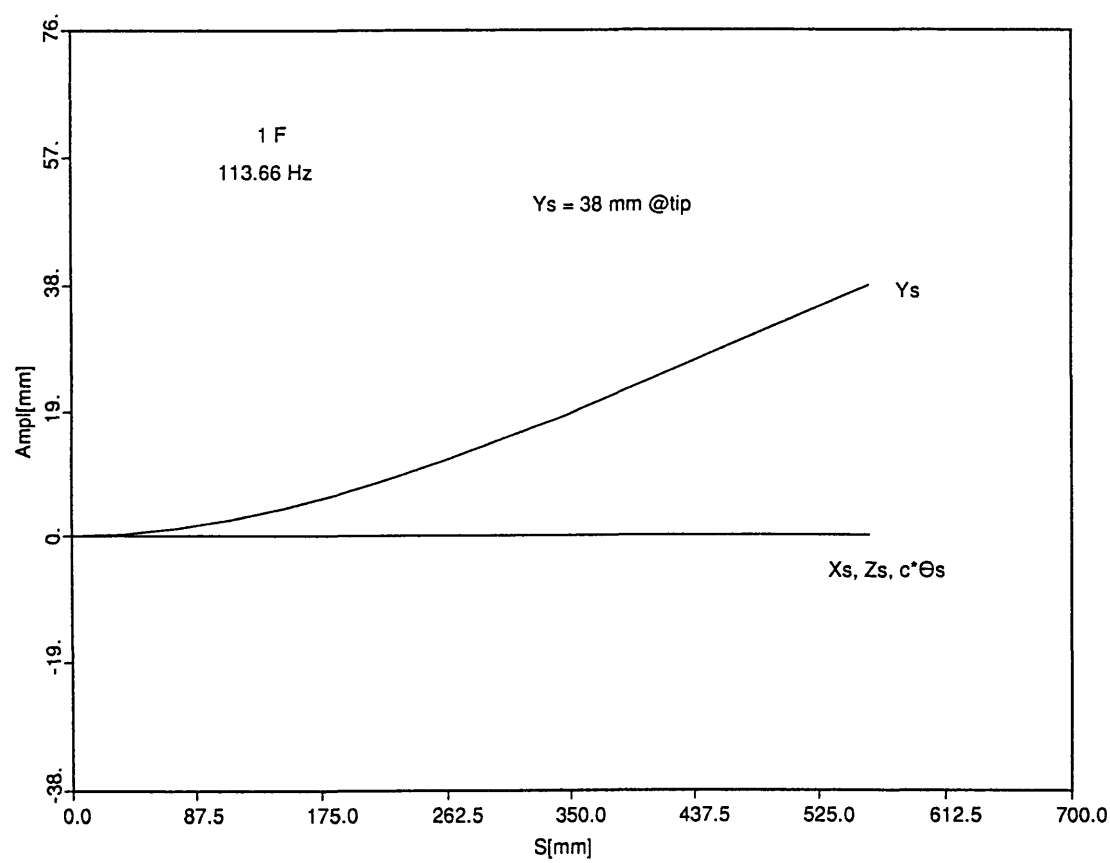

Figure 7.12: First Fore-and-Aft Mode; $[0/90]_{3s}$, 0 mm tip deflection, Ys=10, 38 mm

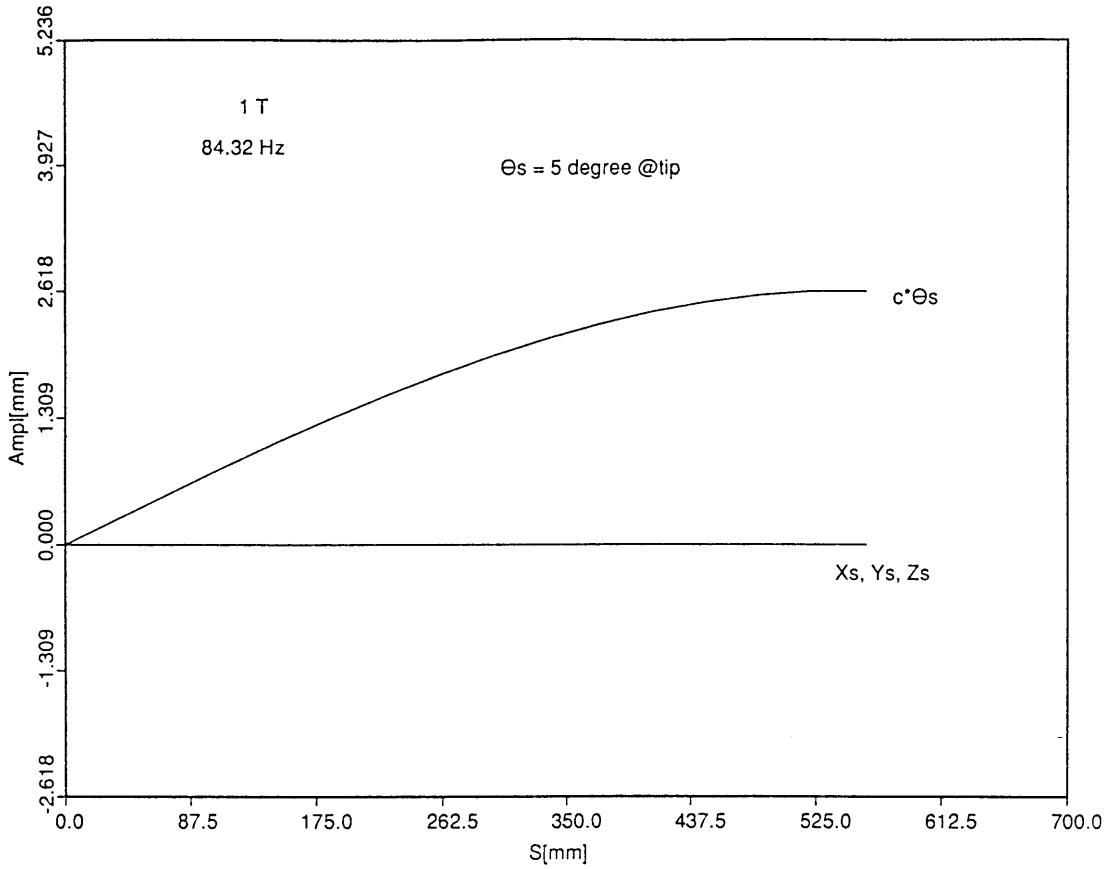

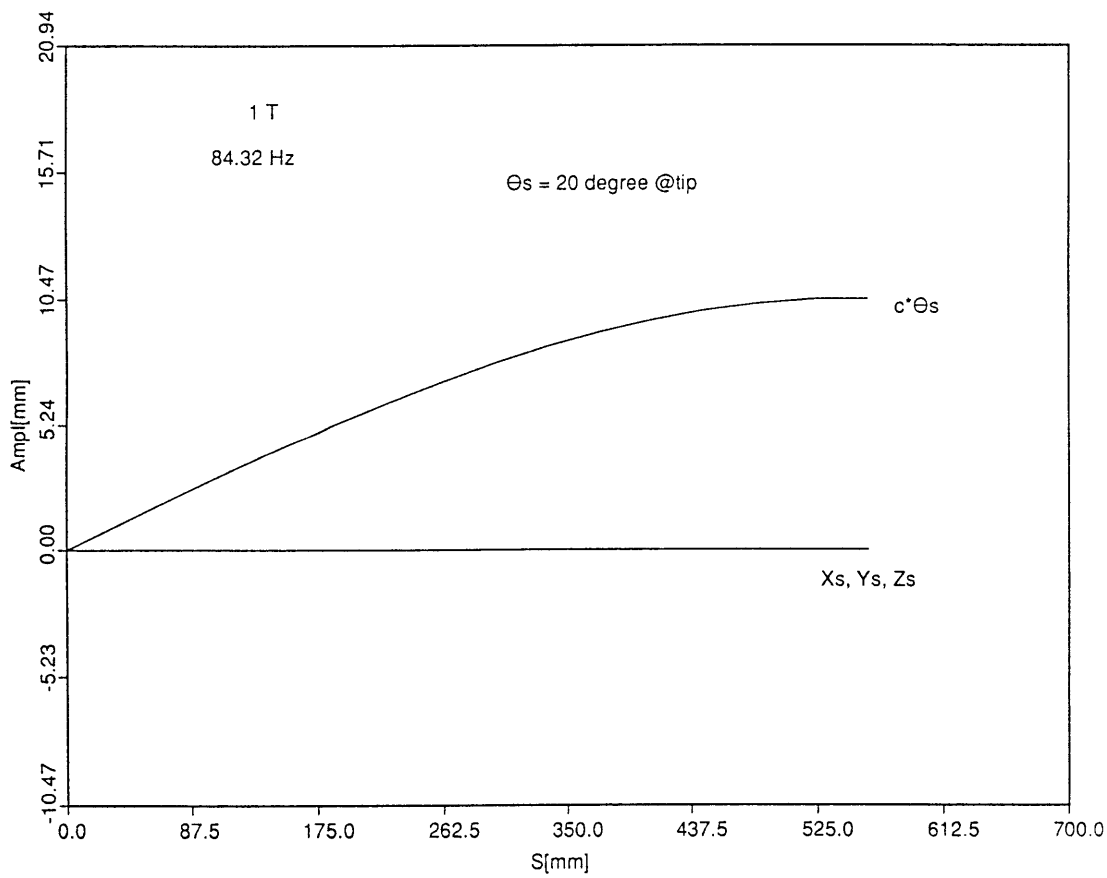

Figure 7.13: First Torsion Mode; $[0/90]_{3s}$, 0 mm tip deflection, θ_s=5, 20 deg.

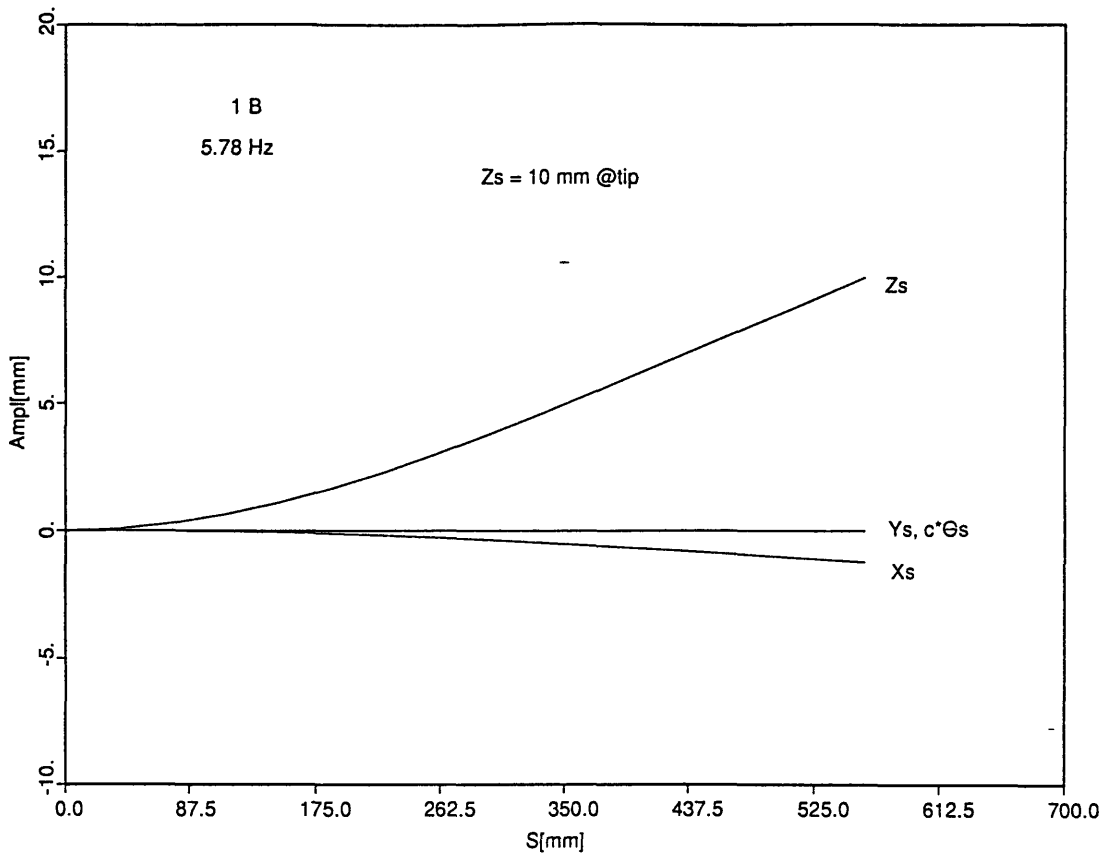

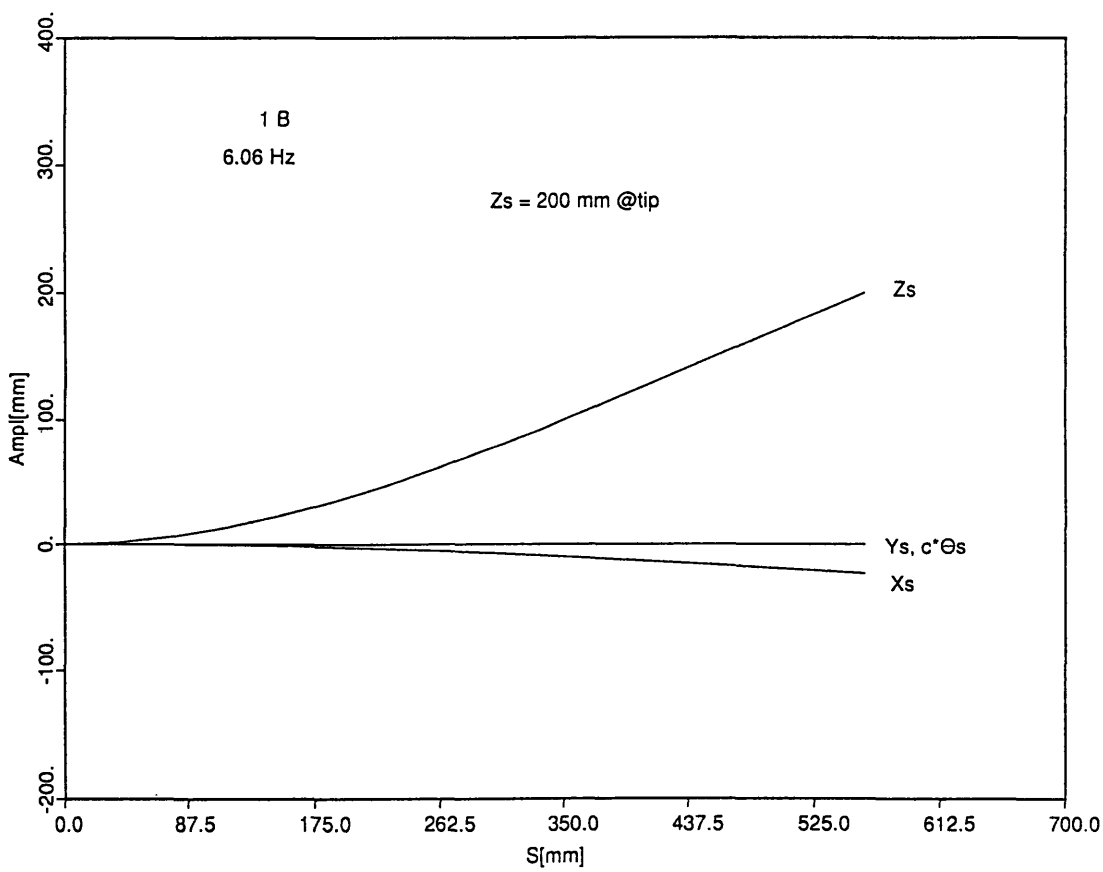

Figure 7.14: First Bending Mode; $[0/90]_{3s}$, 59 mm tip deflection, Zs=10, 200 mm

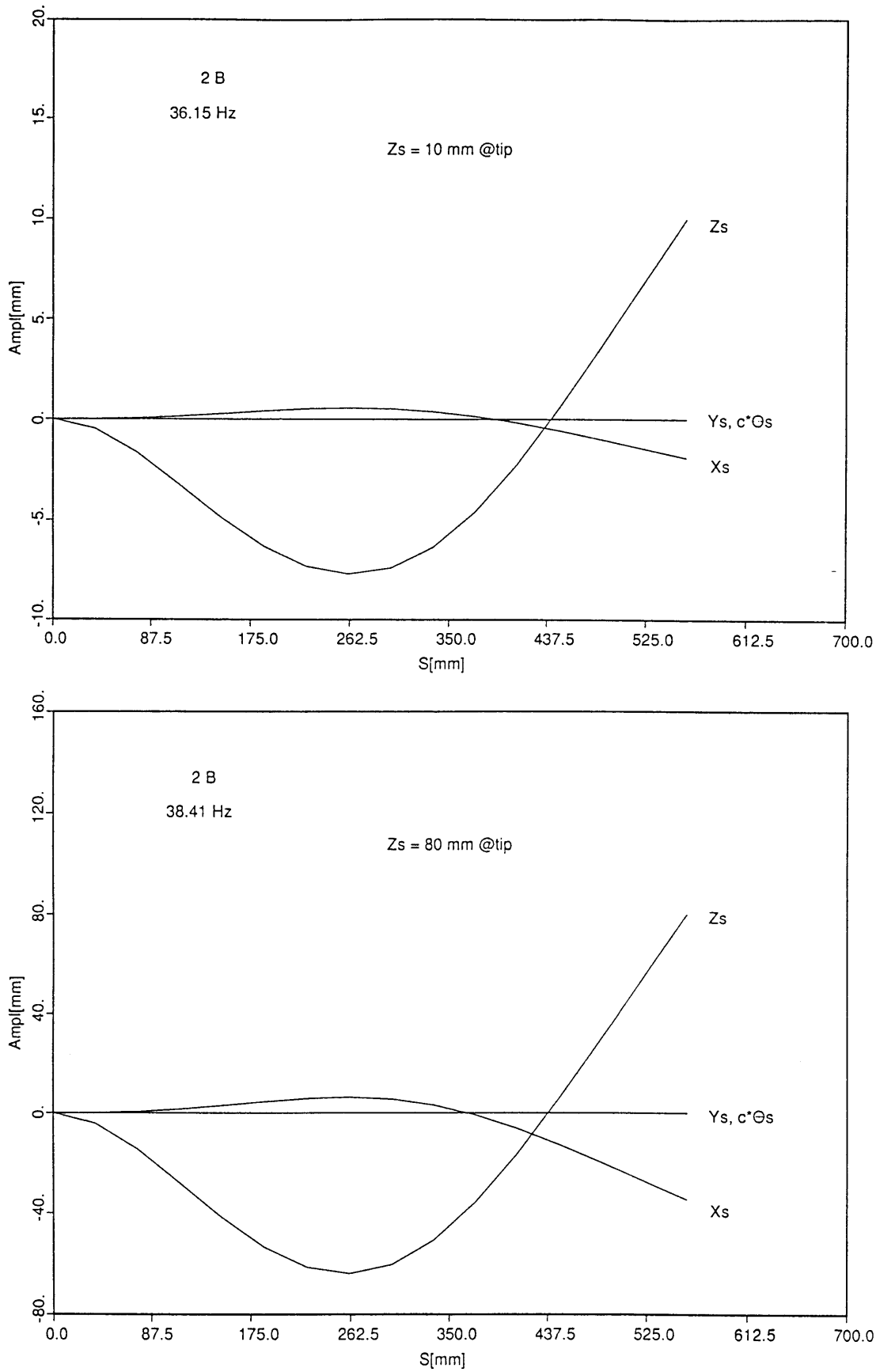

Figure 7.15: Second Bending Mode; $[0/90]_{3s}$, 59 mm tip deflection, Zs=10, 80 mm

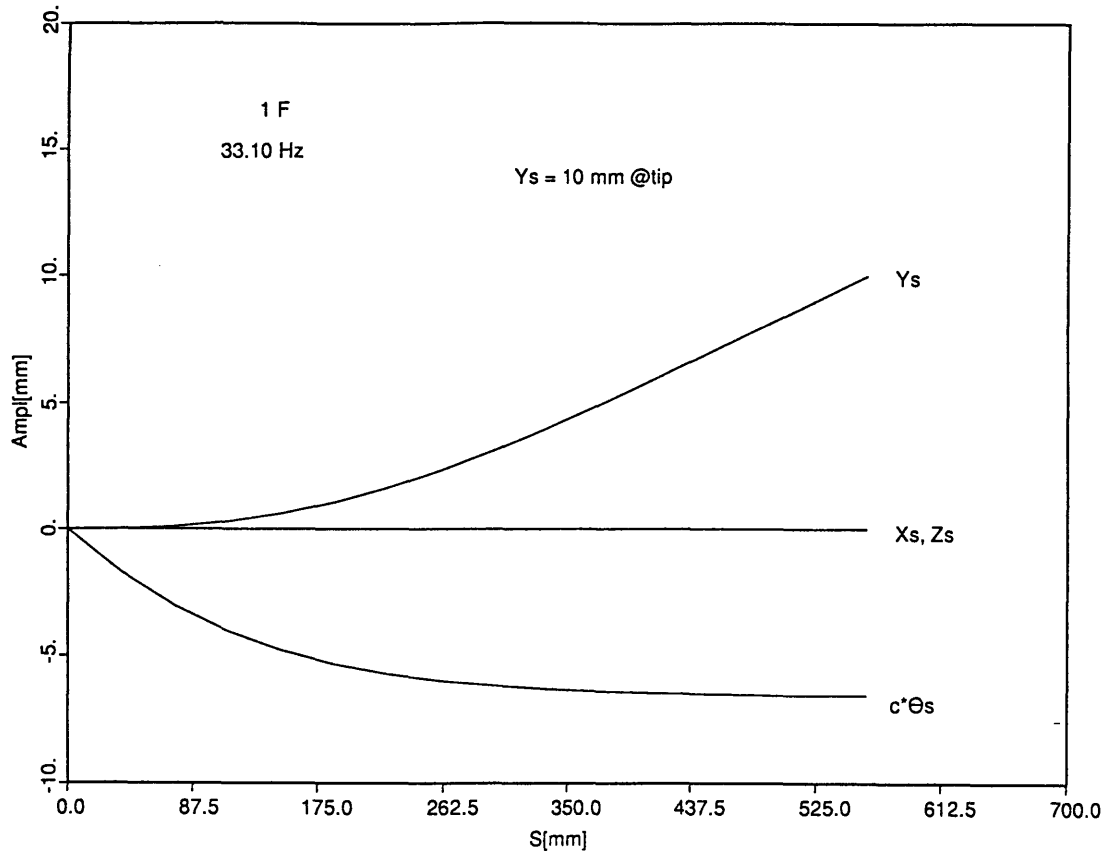

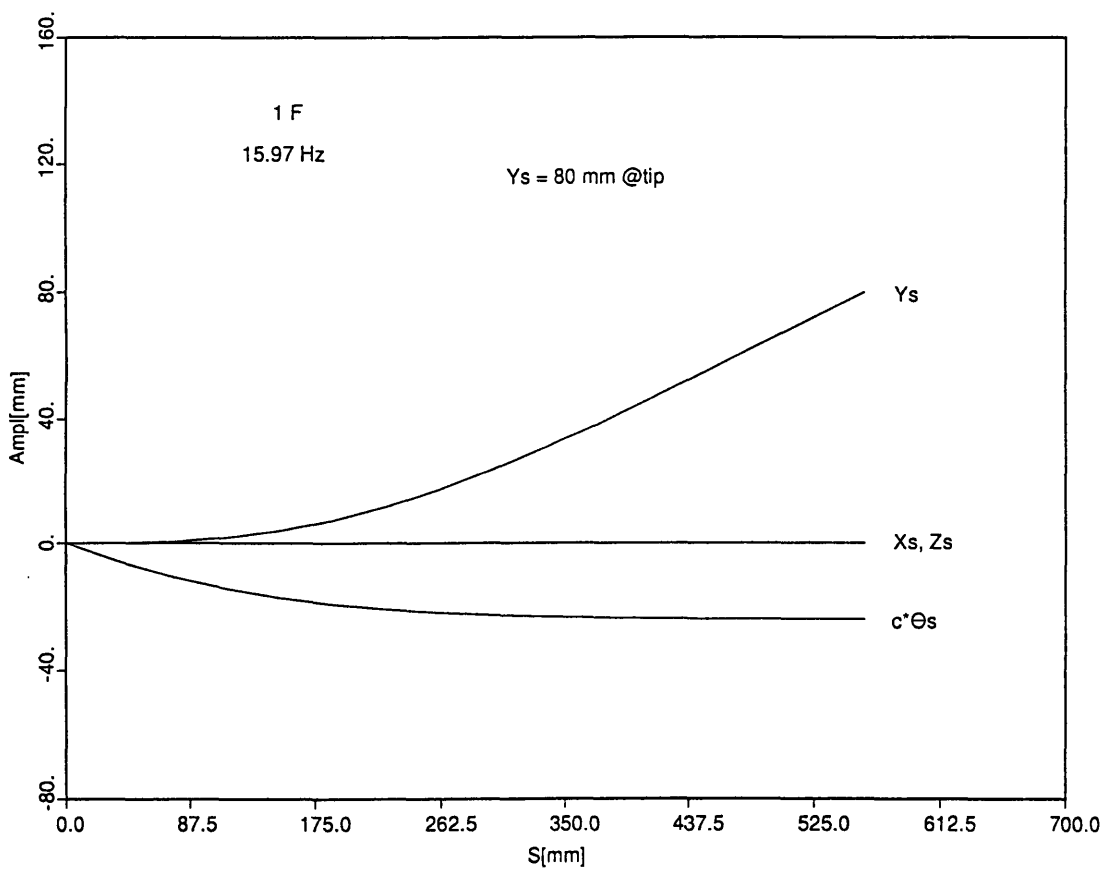

Figure 7.16: First Fore-and-Aft Mode; $[0/90]_{3s}$, 59 mm tip deflection, Ys=10, 80 mm

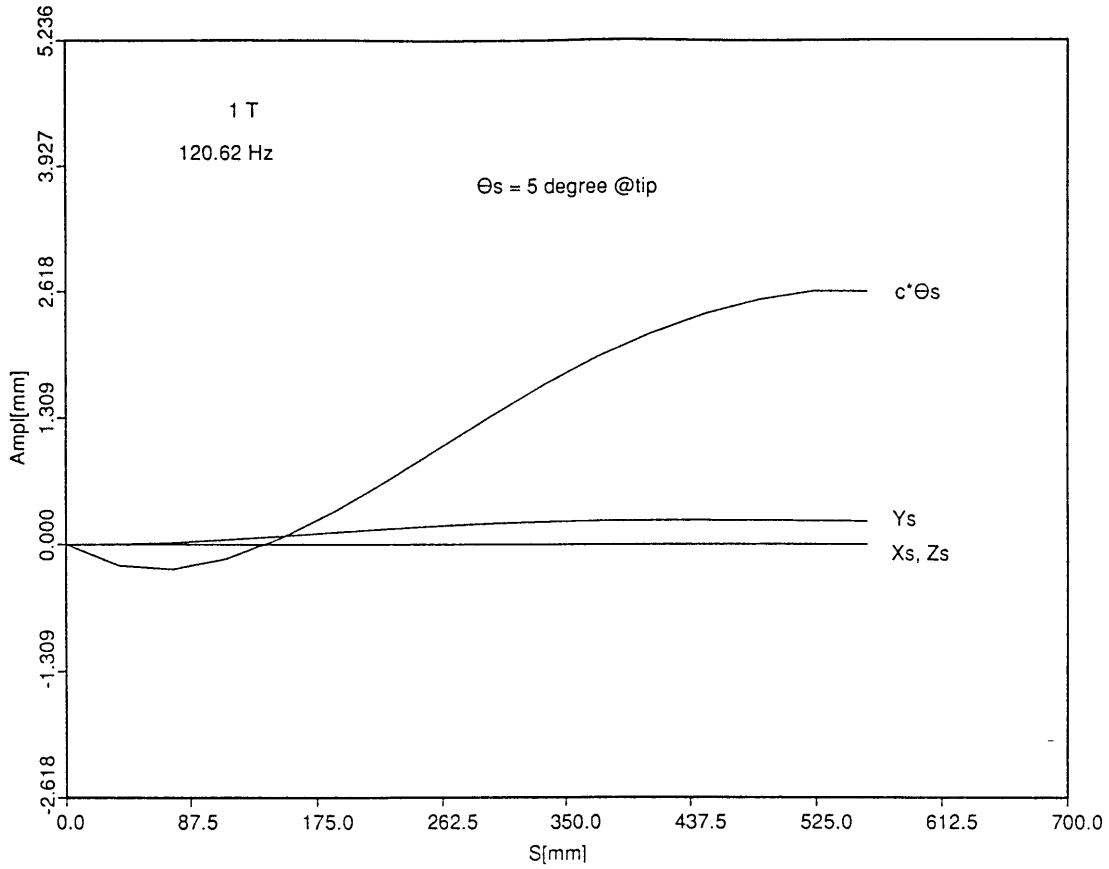

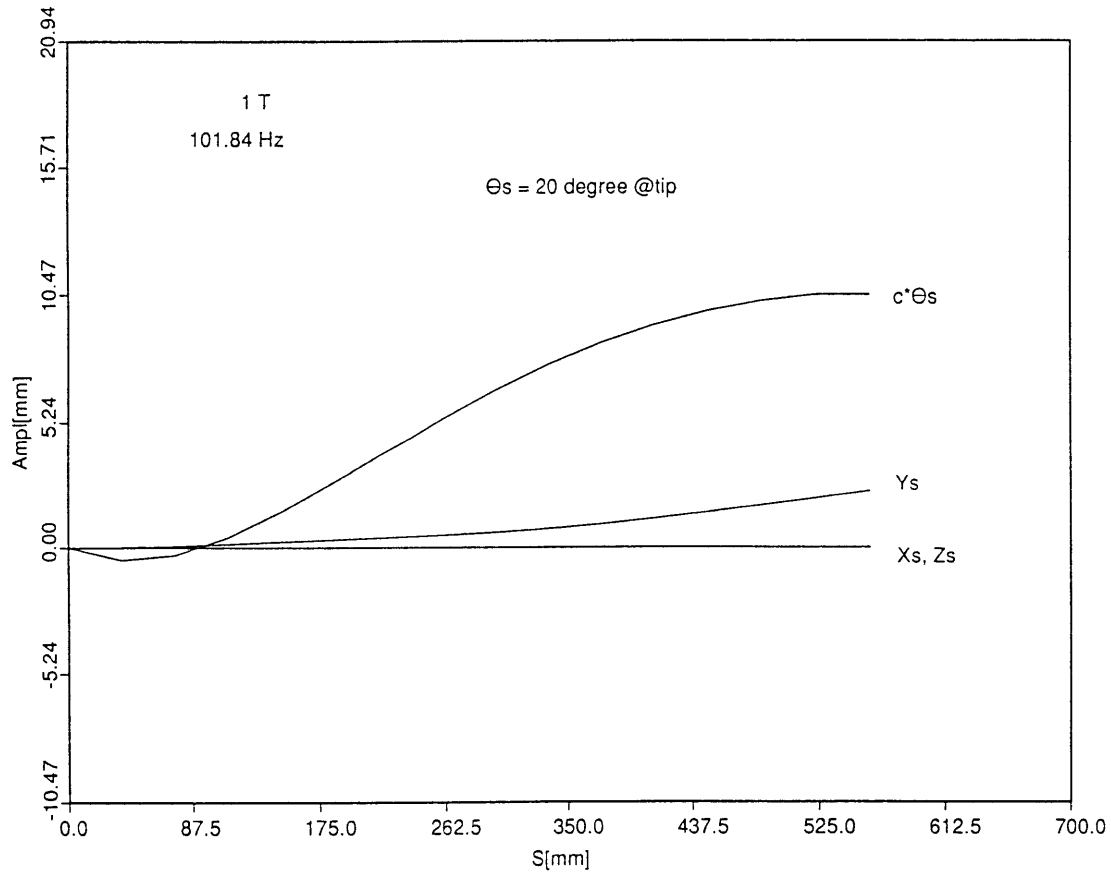

Figure 7.17: First Torsion Mode; $[0/90]_{3s}$, 59 mm tip deflection, θ_s=5, 20 deg.

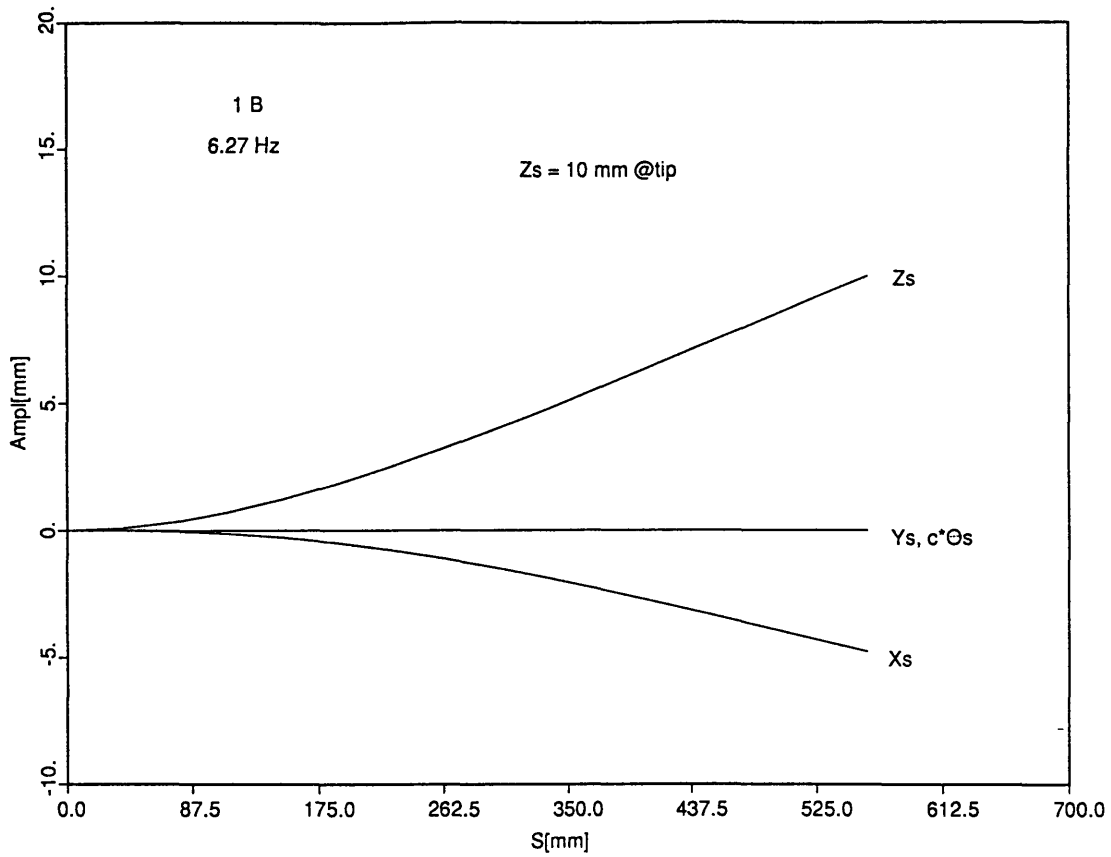

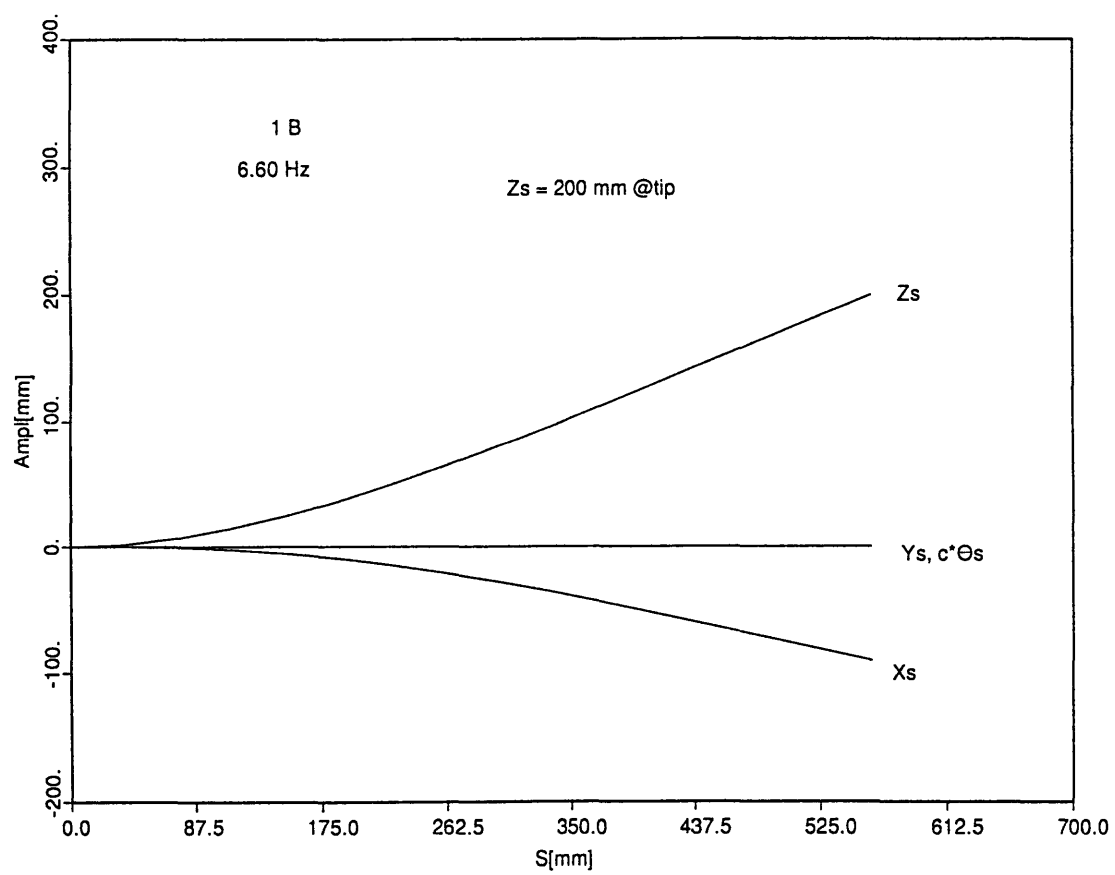

Figure 7.18: First Bending Mode; $[0/90]_{3s}$, 210 mm tip deflection, Zs=10, 200 mm

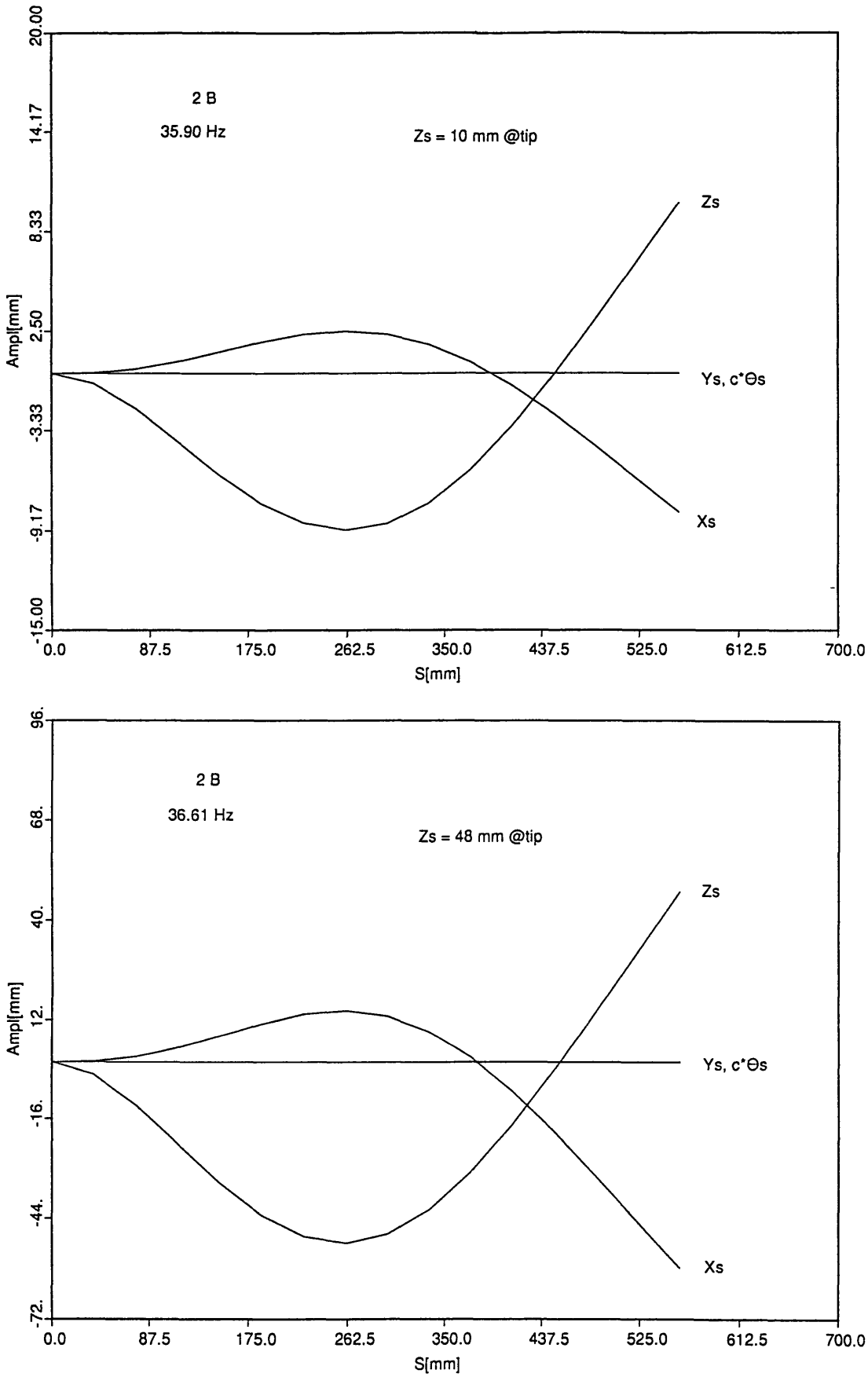

Figure 7.19: Second Bending Mode; $[0/90]_{3s}$, 210 mm tip deflection, Zs=10, 48 mm

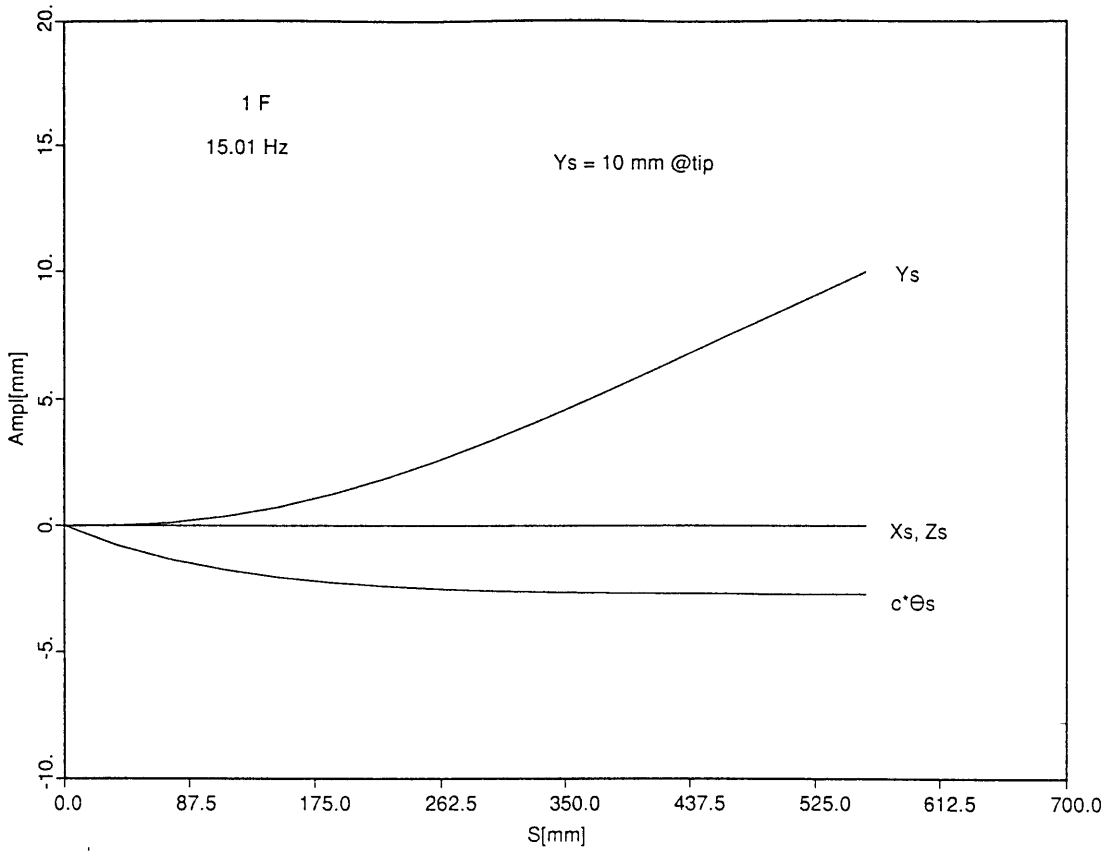

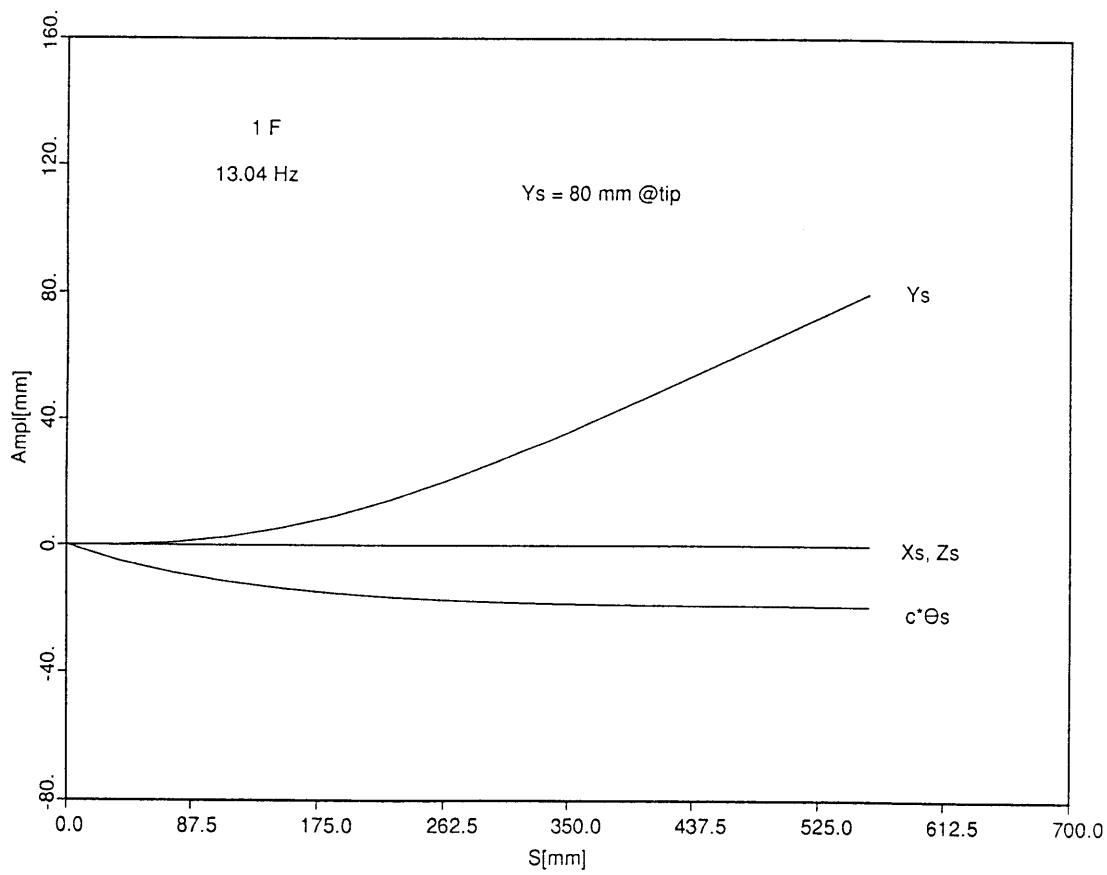

Figure 7.20: First Fore-and-Aft Mode; $[0/90]_{3s}$, 210 mm tip deflection, Ys=10, 80 mm

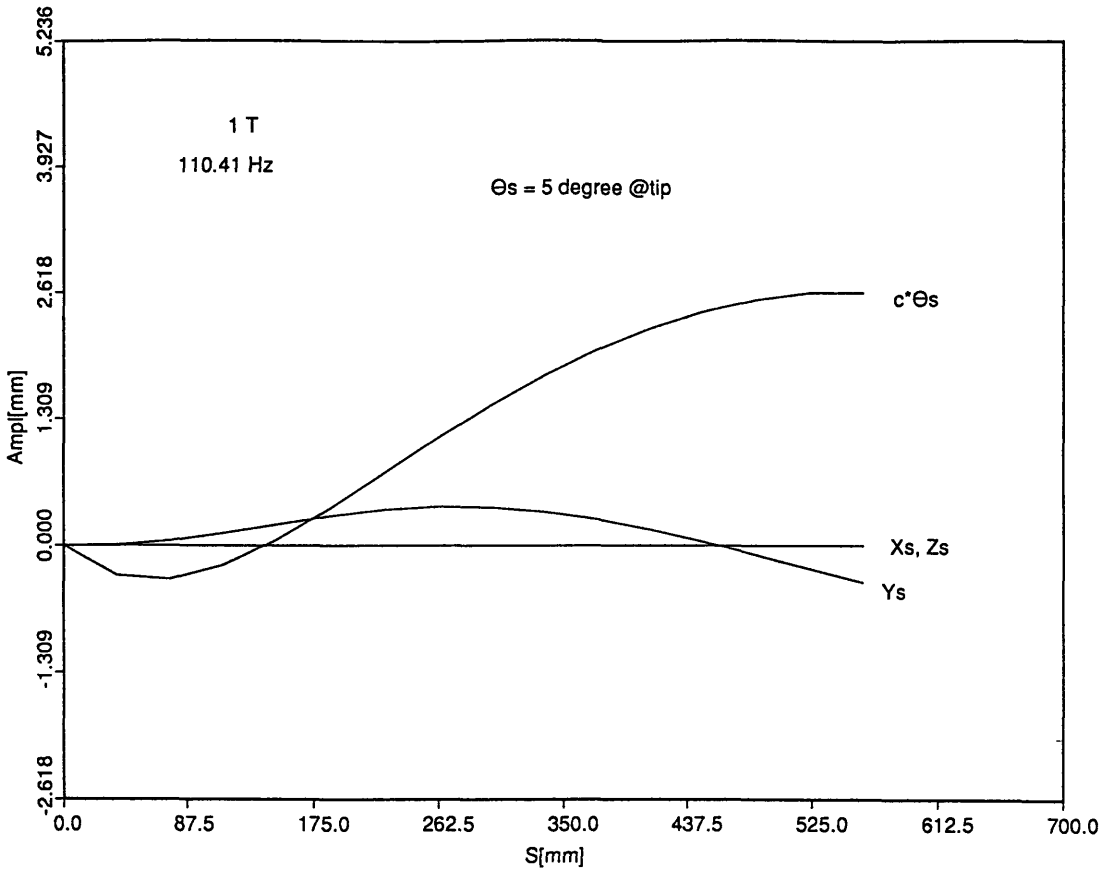

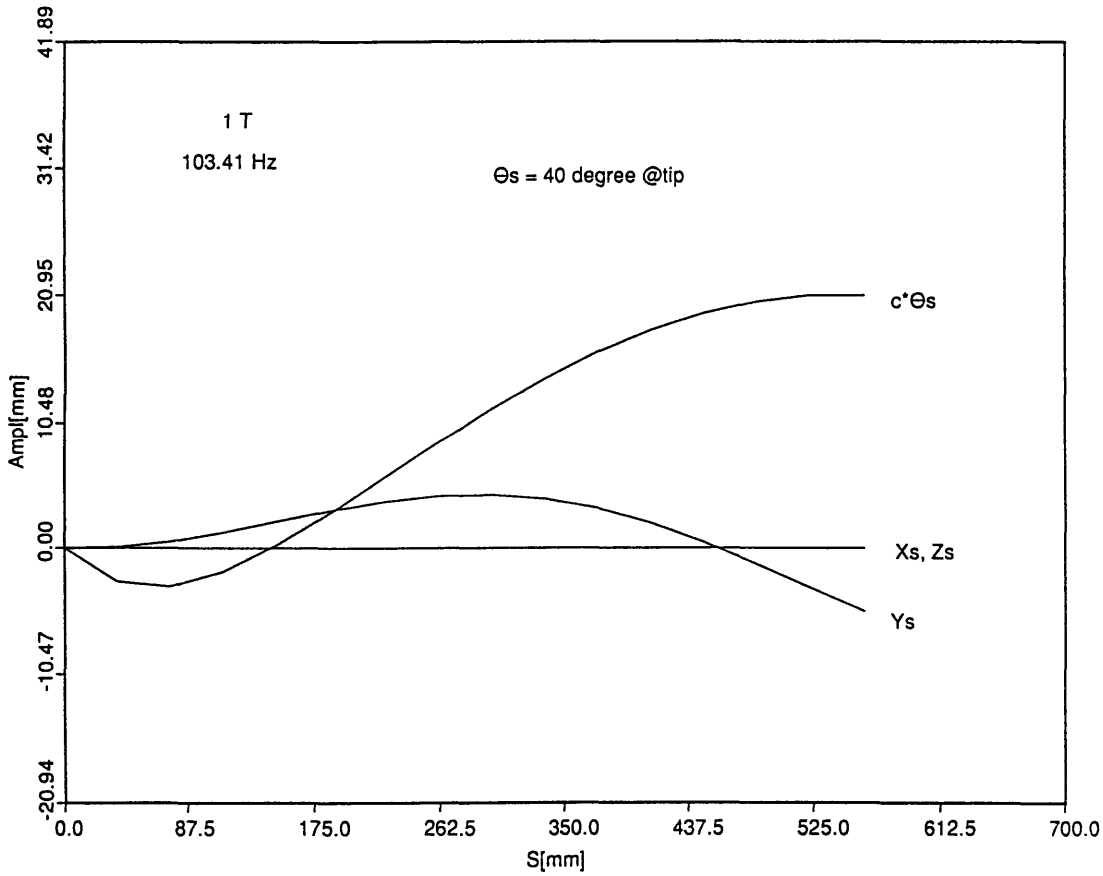

Figure 7.21: First Torsion Mode; $[0/90]_{3s}$, 210 mm tip deflection, θ_s=5, 40 deg.

Next example is the $[45/0]_s$ which, unlike the previous case, exhibit bending-twist coupling. It is mentioned that the top and bottom plies were oriented at -45 degrees around the z axis (positive coupling term E_{45}) such that positive twist would be caused when there is bending up. In an aeroelastic term, this is so called wash-out coupling. Due to the structural coupling, computer time was increased and the convergence became more sensitive. This resulted in an earlier breakdown of nonsingularity of Jacobian matrix which, in turn, resulted in a shorter range of solutions available as functions of amplitudes. Figure 7.22 through 7.26 show the frequency and centershift changes as the amplitudes of various modes increase at three different static tip deflections, 0 mm, 70 mm, and 203 mm.

Despite the existing bending-twist coupling, the two former observations (1) and (2) can again be made in these figures; a similar analogy about the relationship between frequency and centershifts can be also made. These imply that the structural couplings would not be as important as the static deflection level in determining the large amplitude trends. The effects of second harmonics on the natural frequencies of 1F modes is shown in Figure 7.27 at two different static tip deflections, 70 mm and 203 mm. No results were obtainable at lower static tip deflection levels due to numerical instabilities. Once again, for these moderate to large tip deflection levels, the presence of second harmonics is relatively weak. In particular, due to the bending-twist coupling, the middle line static position at the tip is not on the z axis initially, and the 1F motion is not symmetric about the z axis even at the zero root pitch.

Figure 7.29 through 7.40 show mode shape changes at two amplitude levels under the three different static tip deflections. Once again, the mode shapes do not change significantly from the linear modes.

Finally, it is interesting to consider what makes the Jacobian matrix singular at a certain point along the way of increasing amplitude. Except for the cases of 1B, there seem to be certain limits on the largest amplitudes that can be solved by the current algorithms. These limits were even more severe when second harmonics were

included. In section 5.1, it was suggested that one should expect deterioration in the degree of compatibility as amplitudes increase. This could be one possibility. Apart from that, other factors may attribute to the singularity of solution; the round-off errors associated with the large size of Jacobian matrix, and the interaction of several modes as amplitudes increase, with possible resulting chaotic vibration.

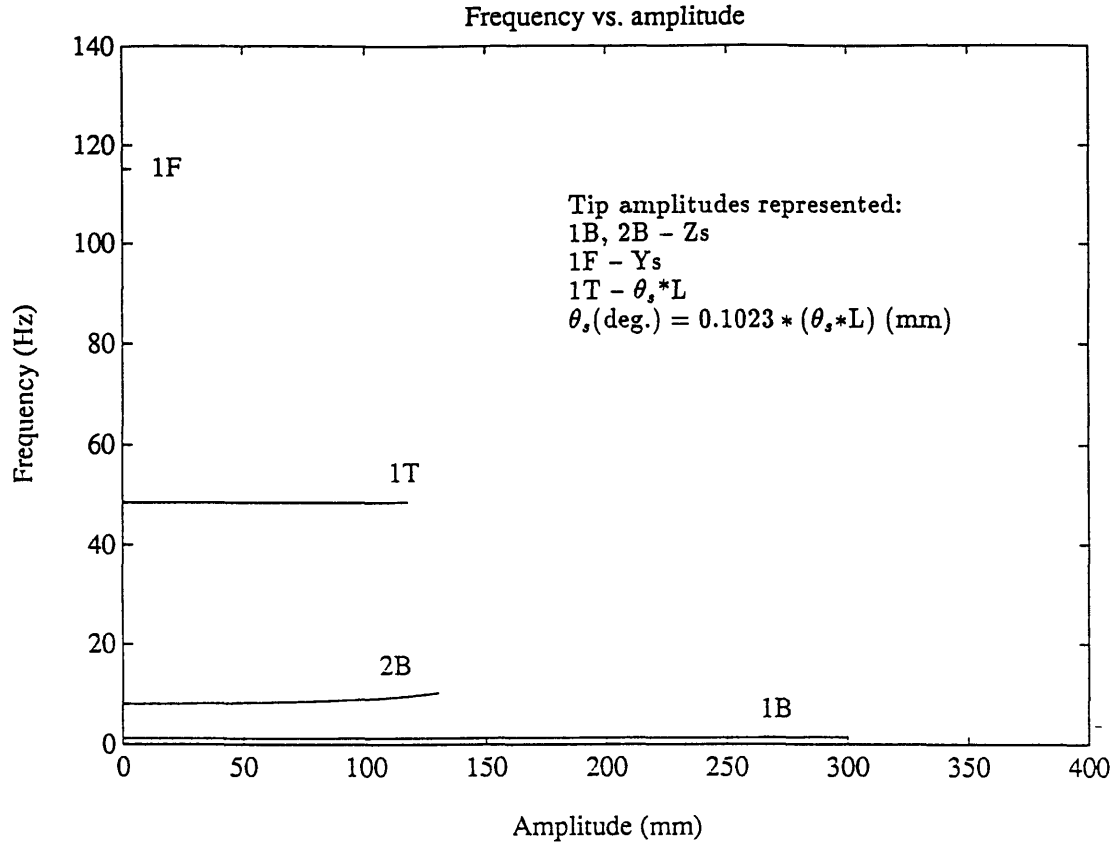

Figure 7.22: Frequency vs. amplitude; $[45/0]_s$, 0 mm tip deflection

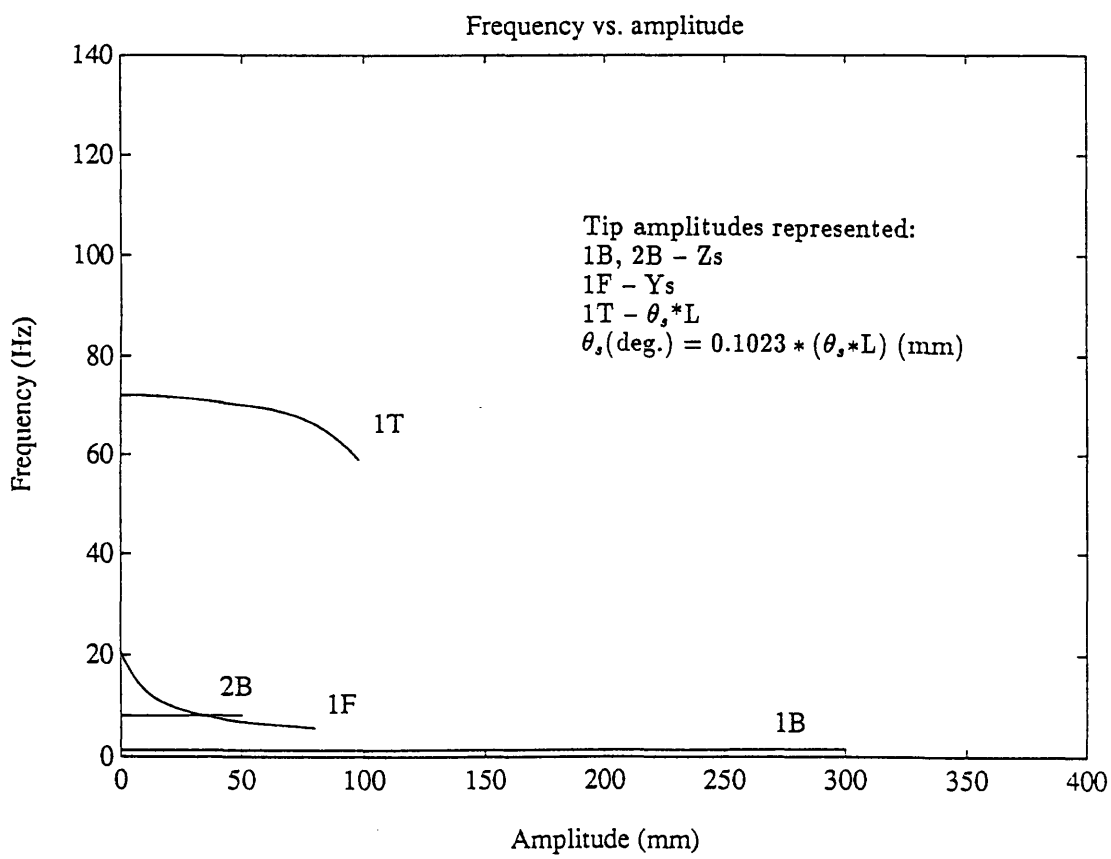

Figure 7.23: Frequency vs. amplitude; $[45/0]_s$, 70 mm tip deflection

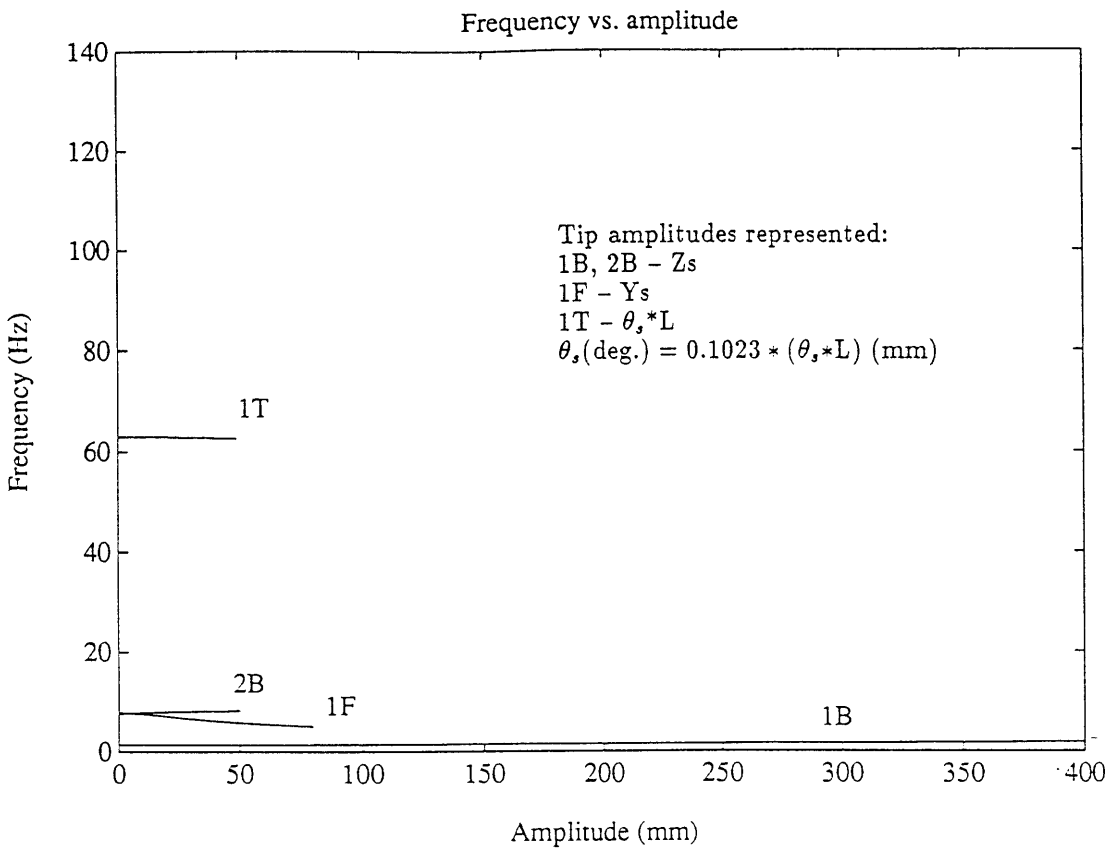

Figure 7.24: Frequency vs. amplitude; $[45/0]_s$, 203 mm tip deflection

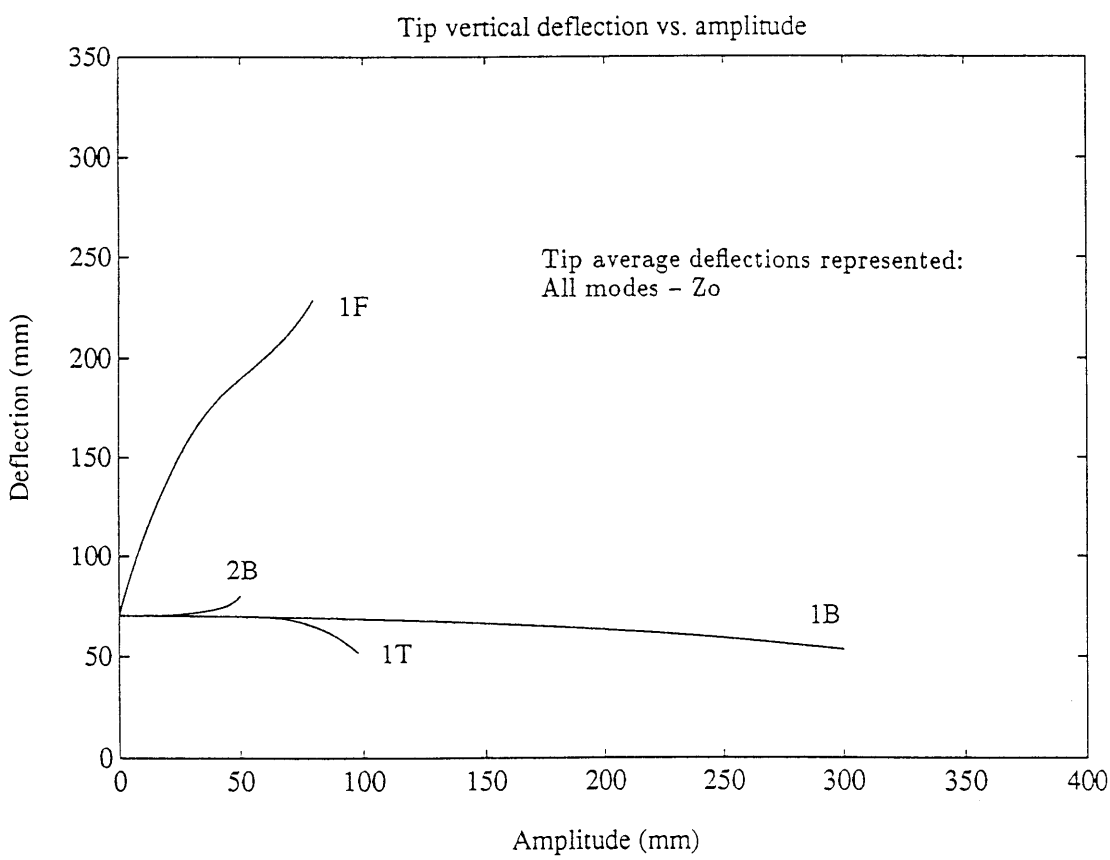

Figure 7.25: Tip average deflection vs. amplitude; $[45/0]_s$, 70 mm tip deflection

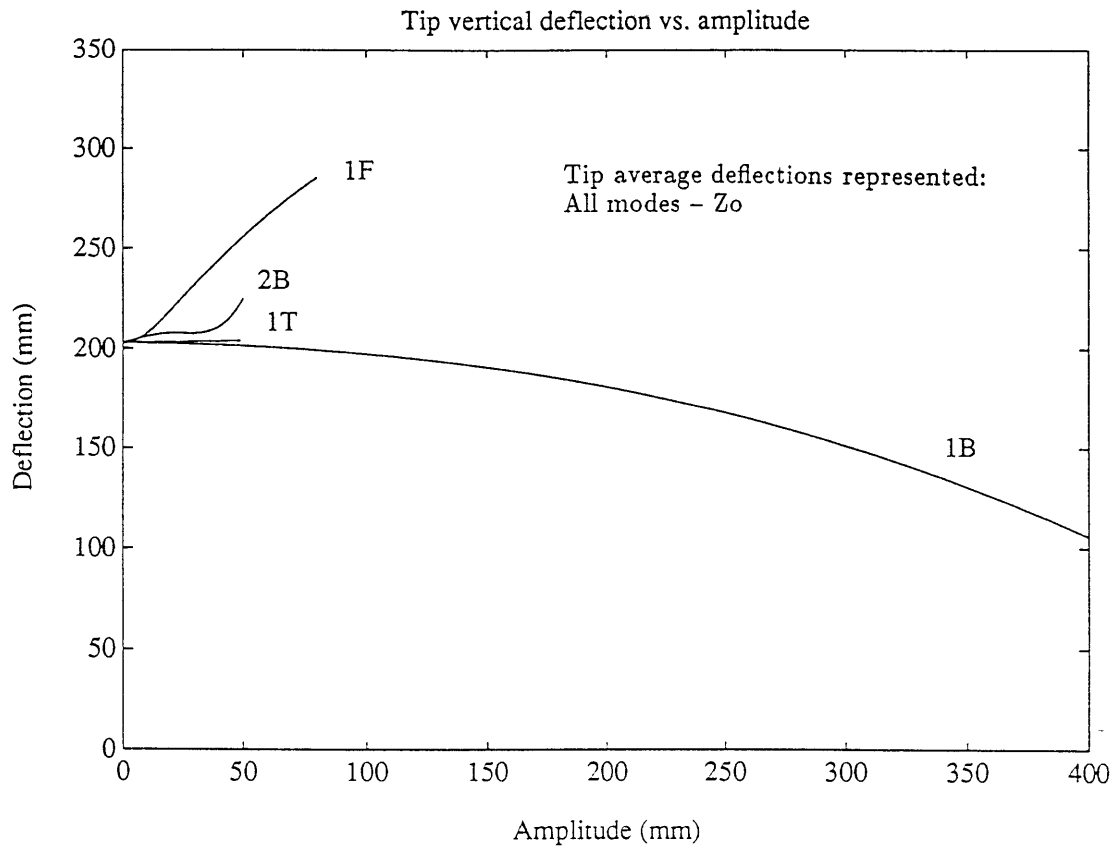

Figure 7.26: Tip average deflection vs. amplitude; $[45/0]_s$, 203 mm tip deflection

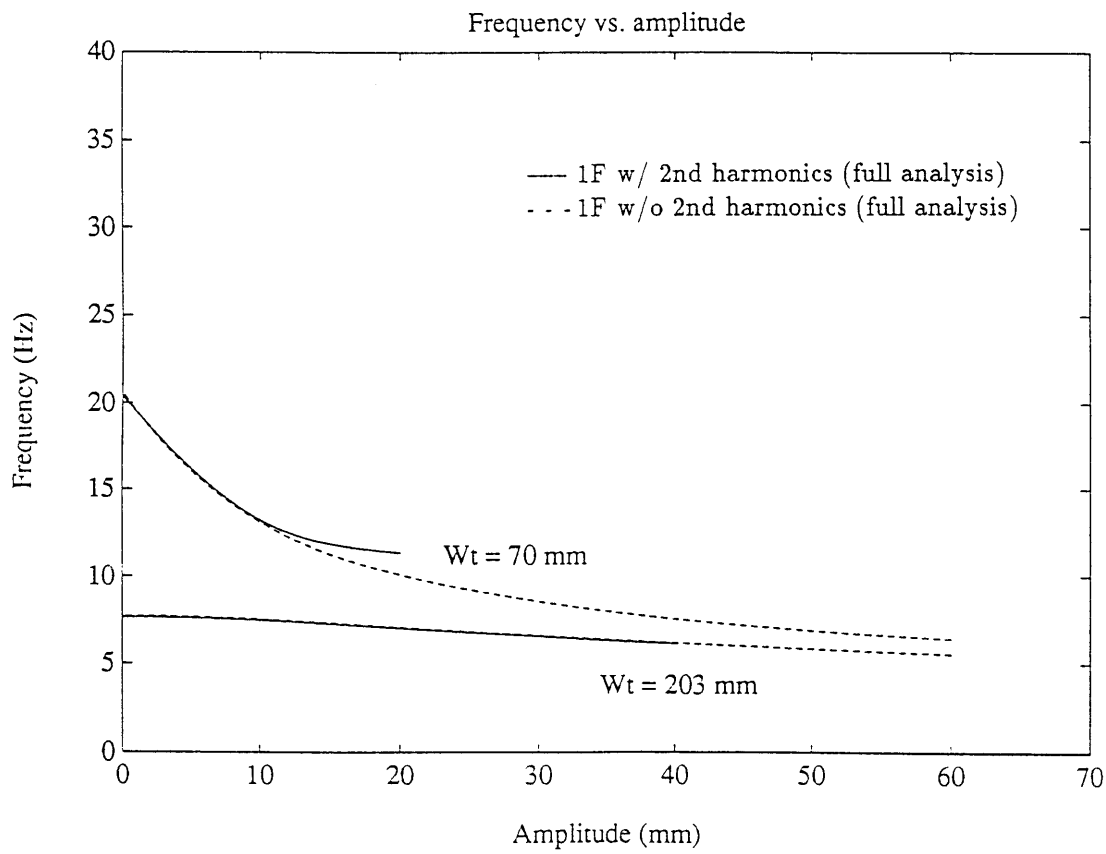

Figure 7.27: Frequency vs. amplitude w/ and w/o 2nd harmonics; $[45/0]_s$, 70 mm and 203 mm tip deflection

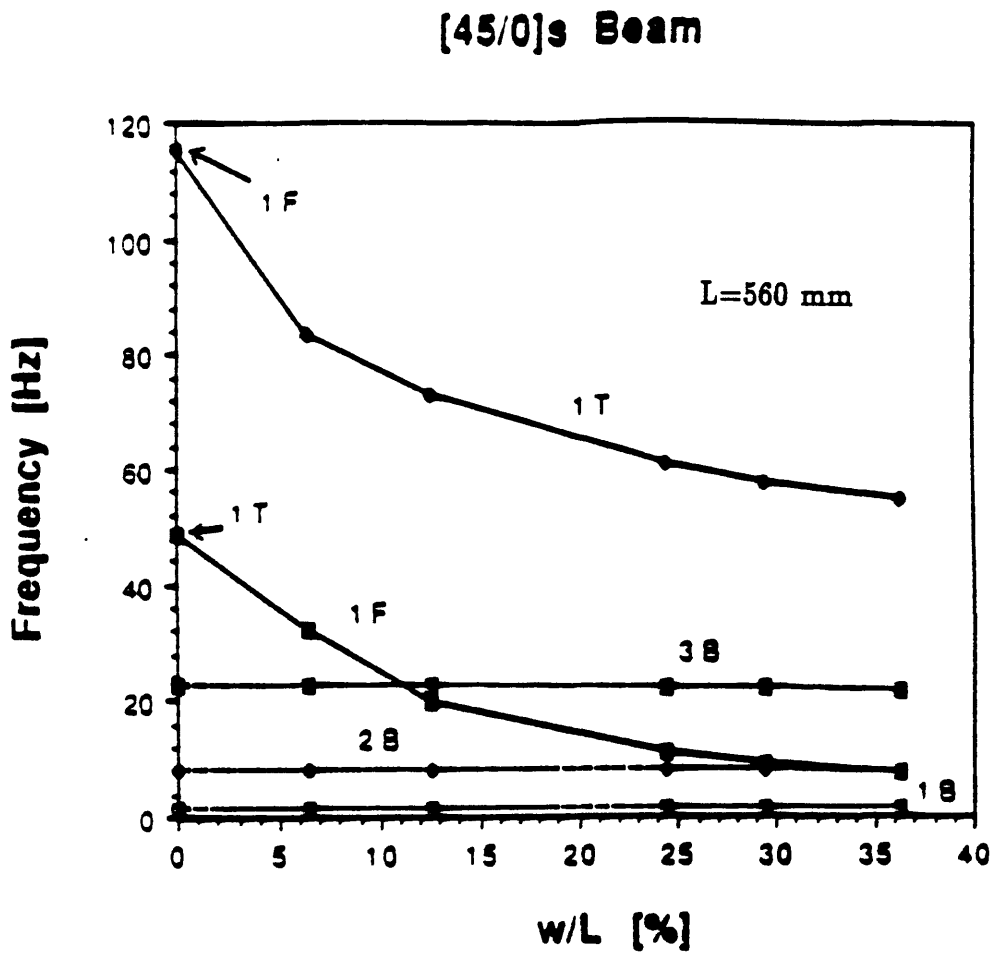

Figure 7.28: Natural frequencies of $[45/0]_s$ beam as a function of tip deflection (from Ref. 13)

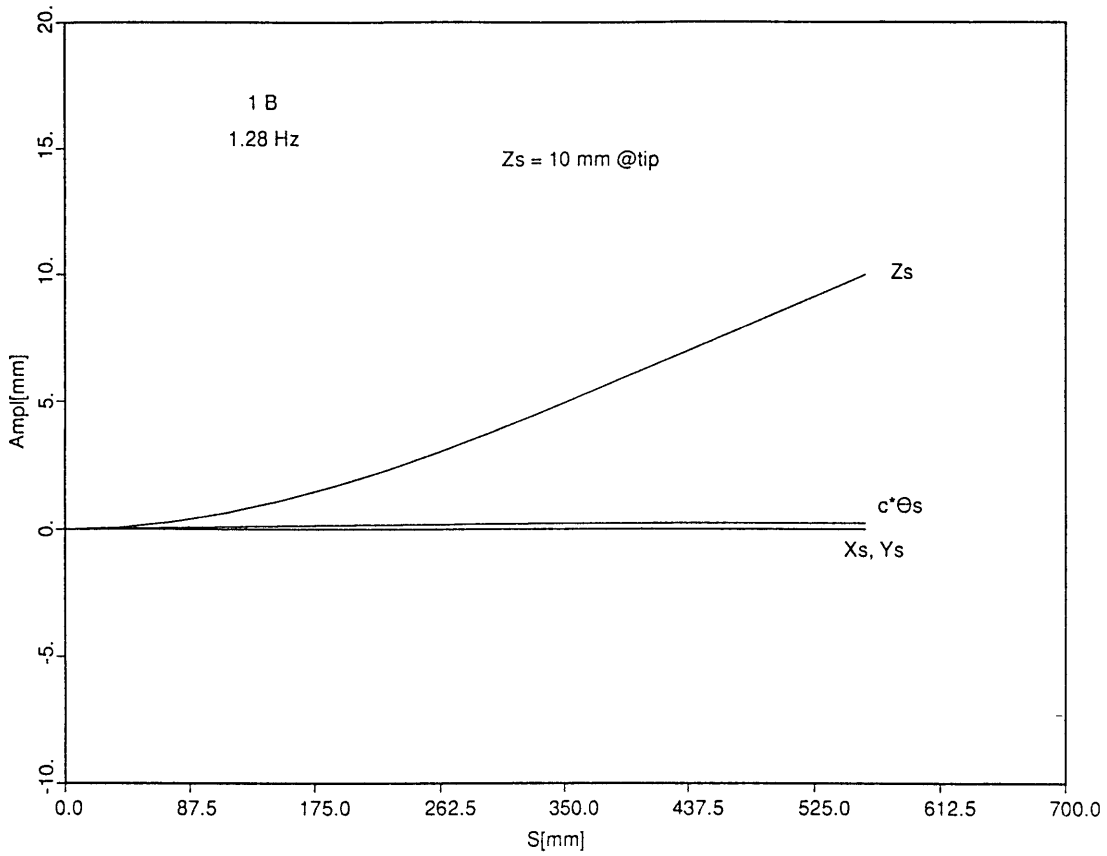

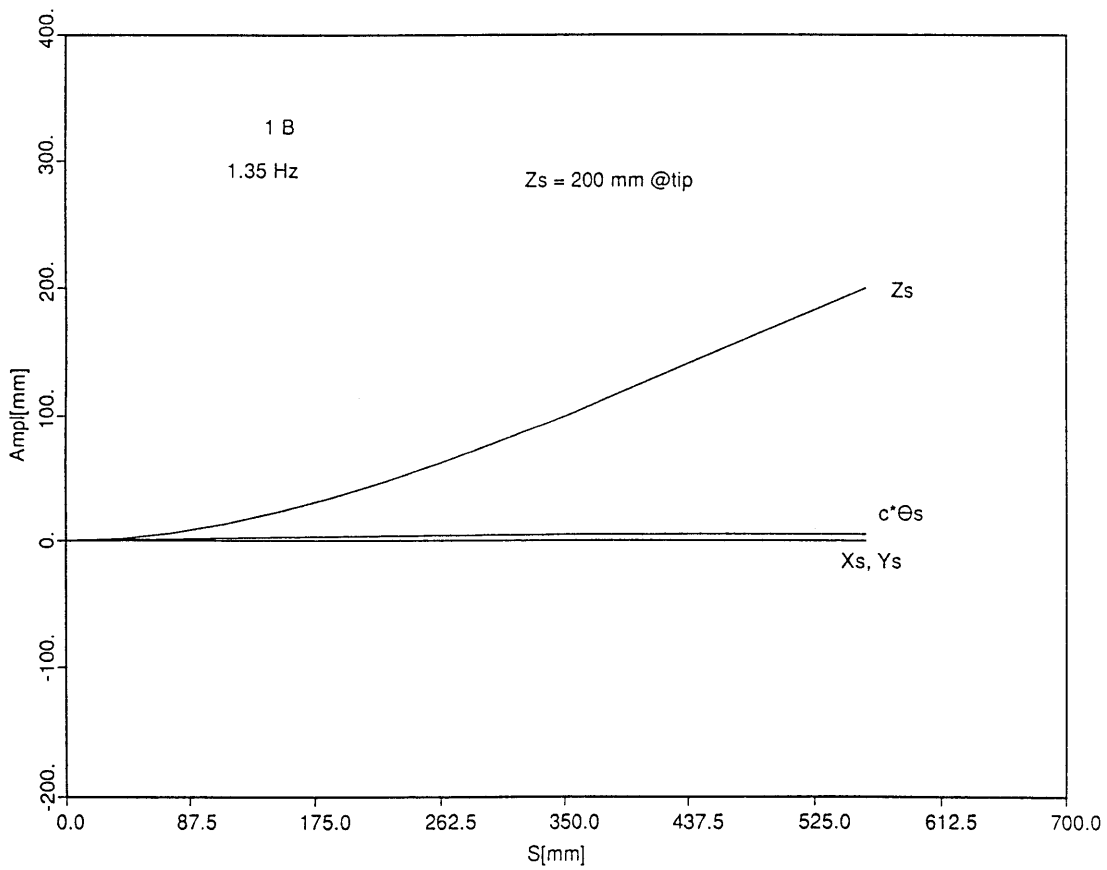

Figure 7.29: First Bending Mode; $[45/0]_s$, 0 mm tip deflection, Zs=10, 200 mm

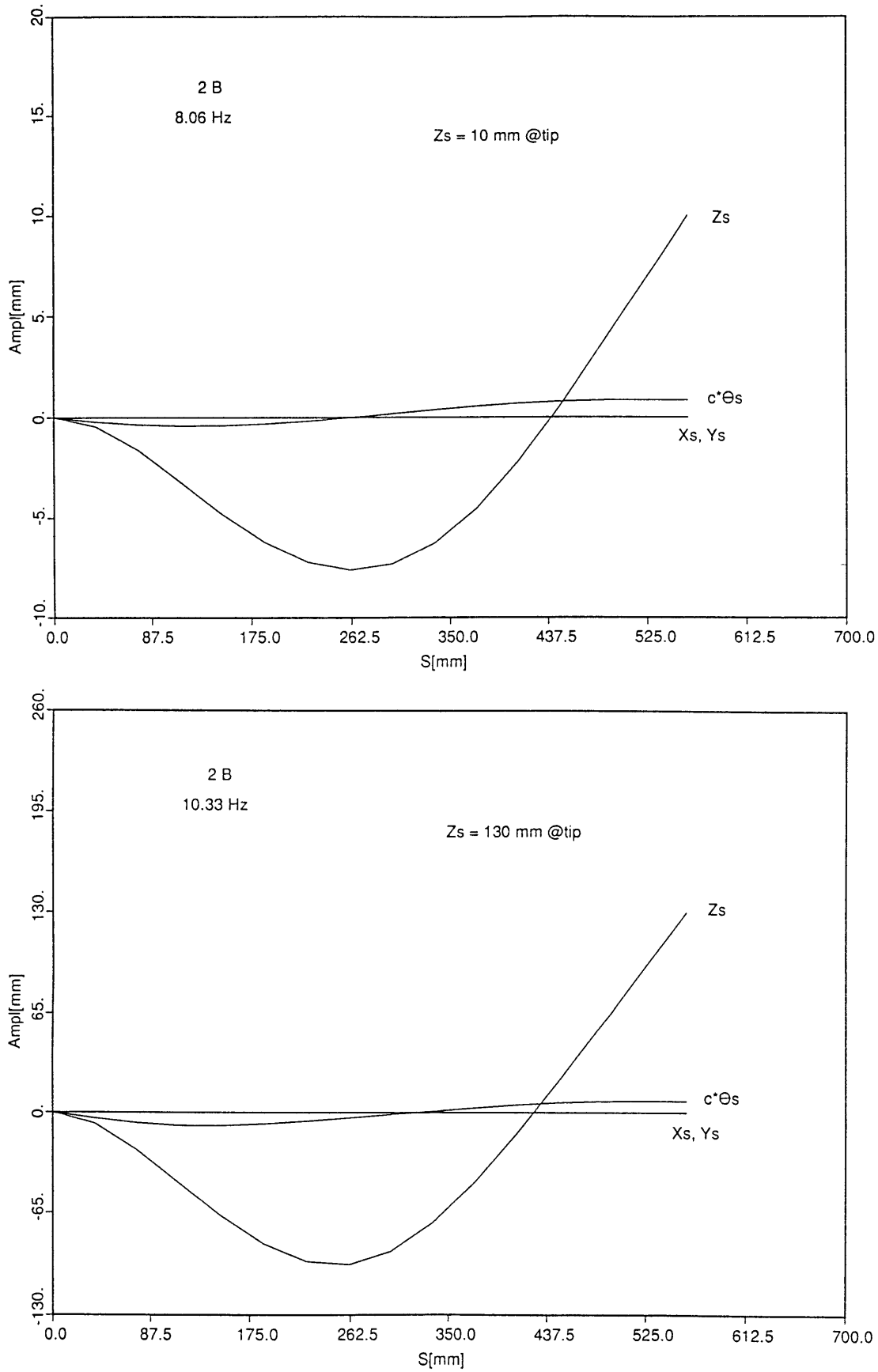

Figure 7.30: Second Bending Mode; $[45/0]_s$, 0 mm tip deflection, Zs=10, 130 mm

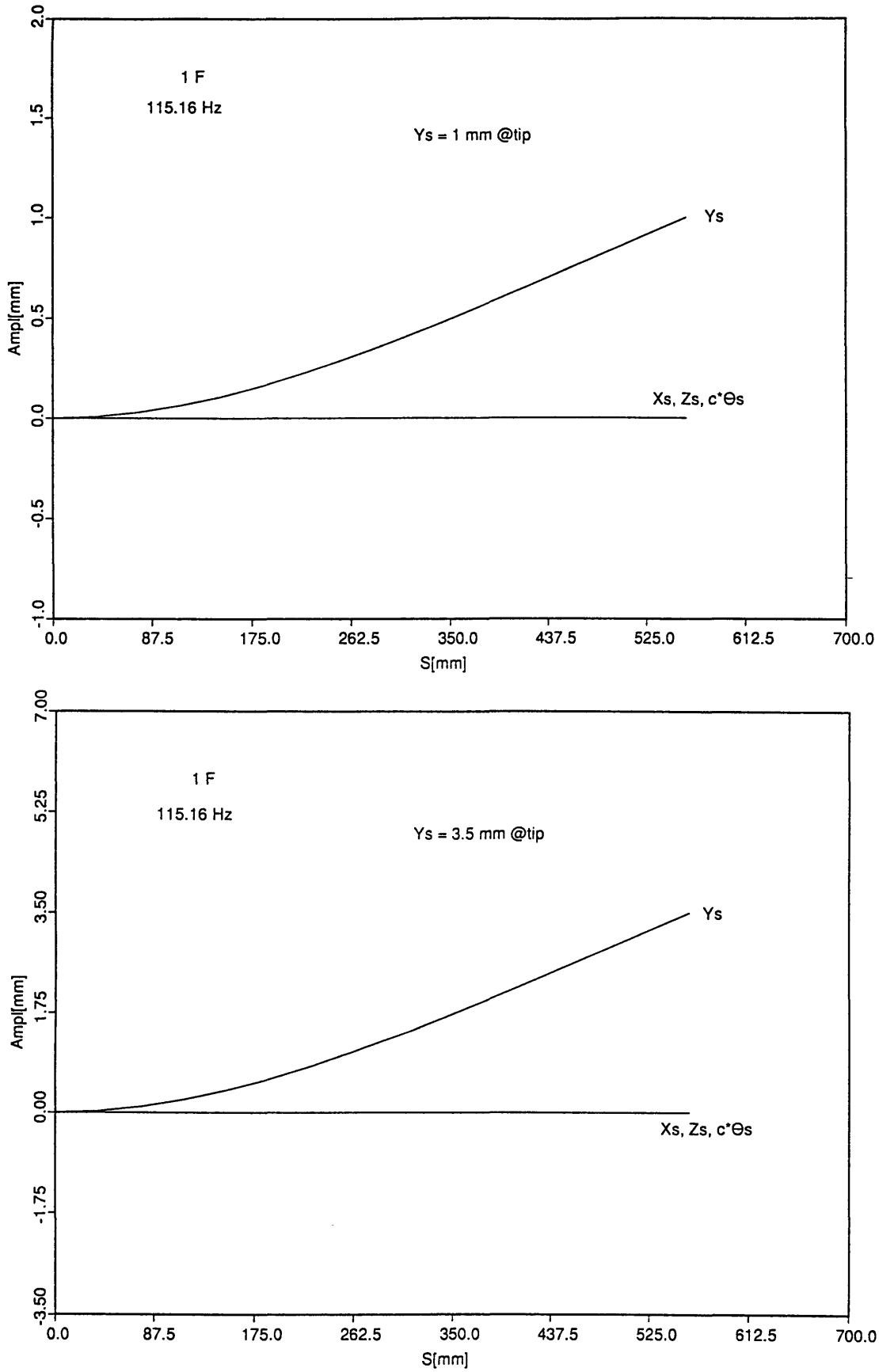

Figure 7.31: First Fore-and-Aft Mode; $[45/0]_s$, 0 mm tip deflection, Ys=1, 3.5 mm

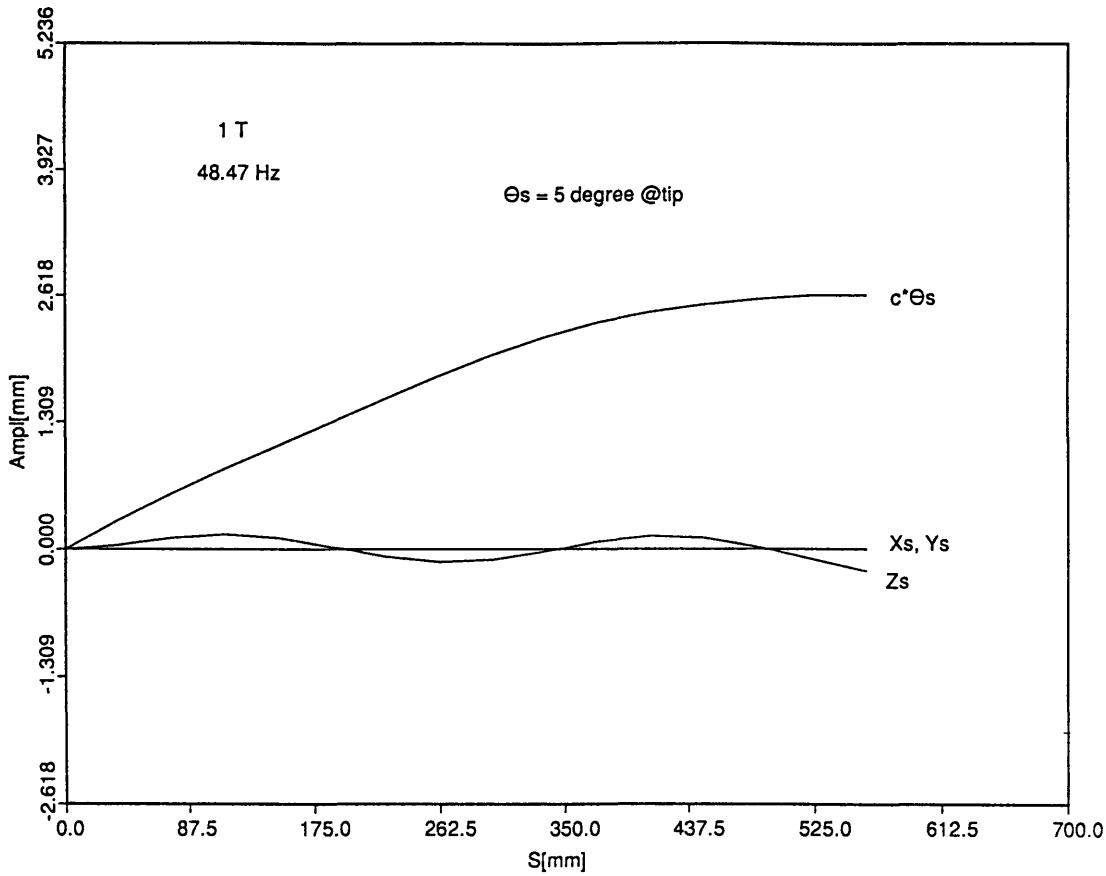

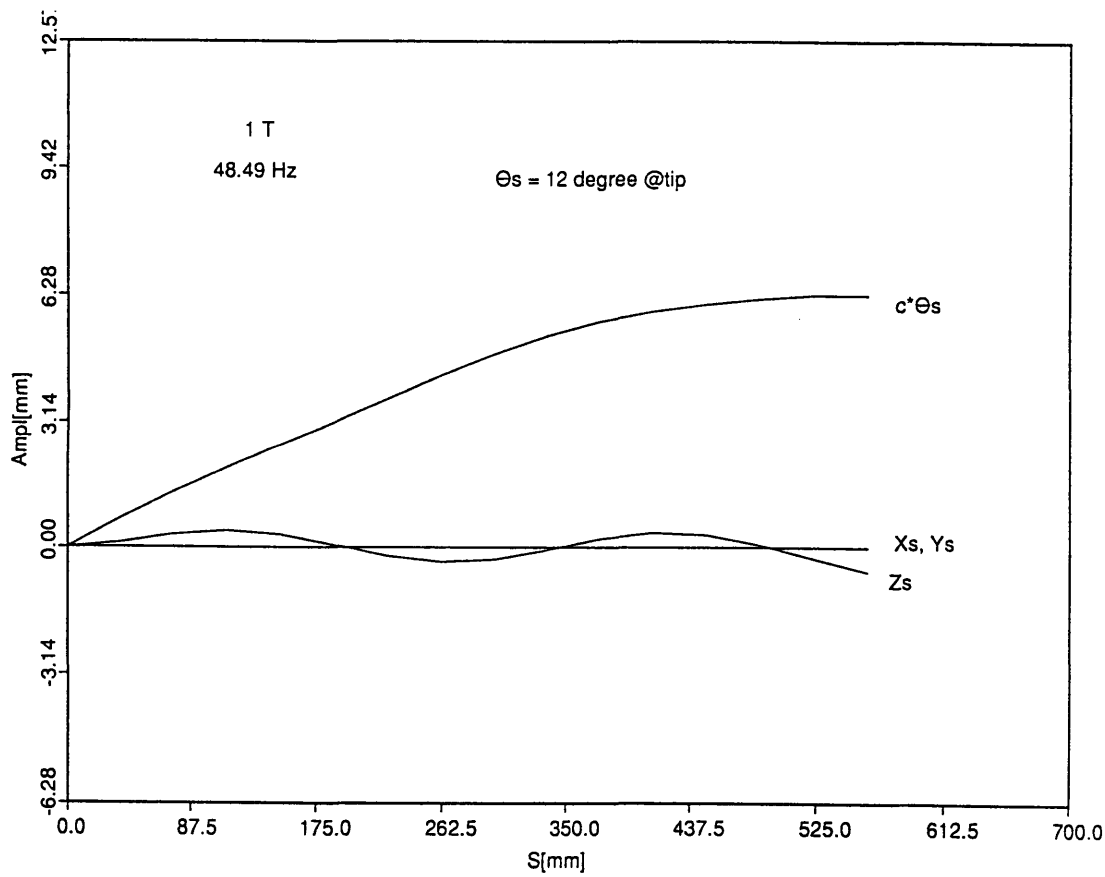

Figure 7.32: First Torsion Mode; $[45/0]_s$, 0 mm tip deflection, θ_s=5, 12 deg.

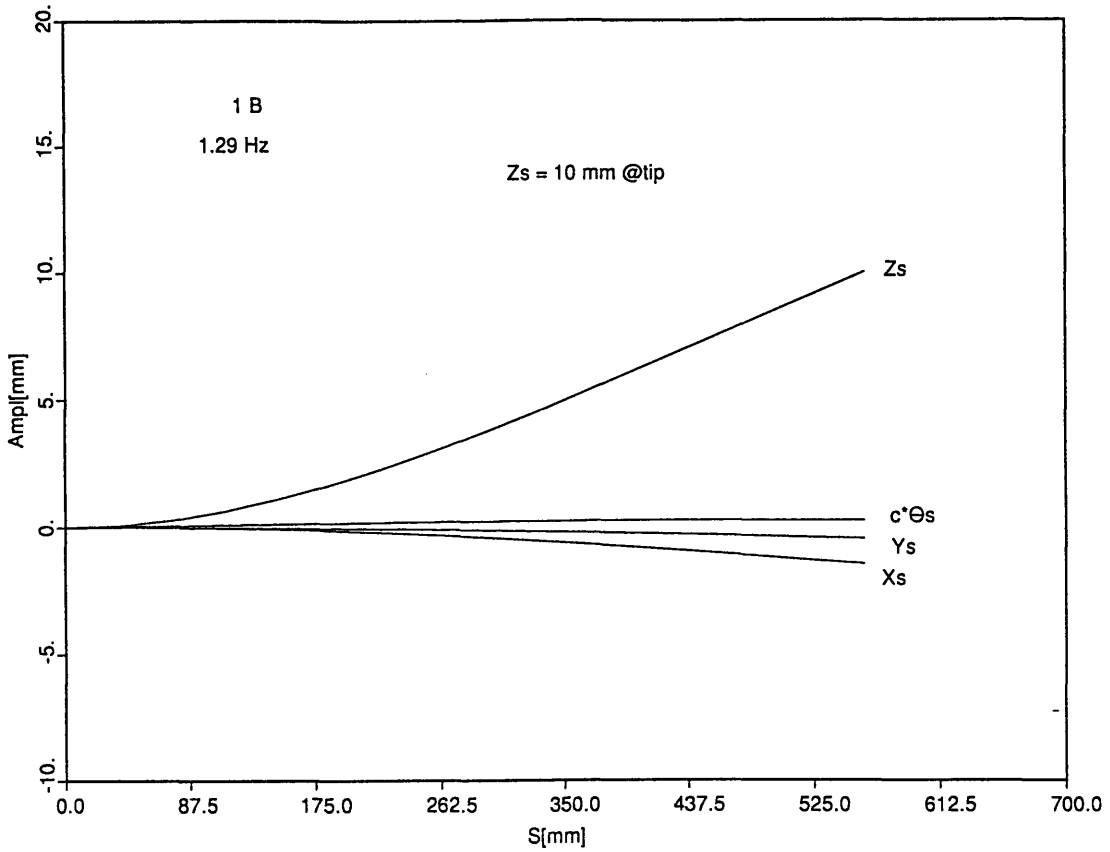

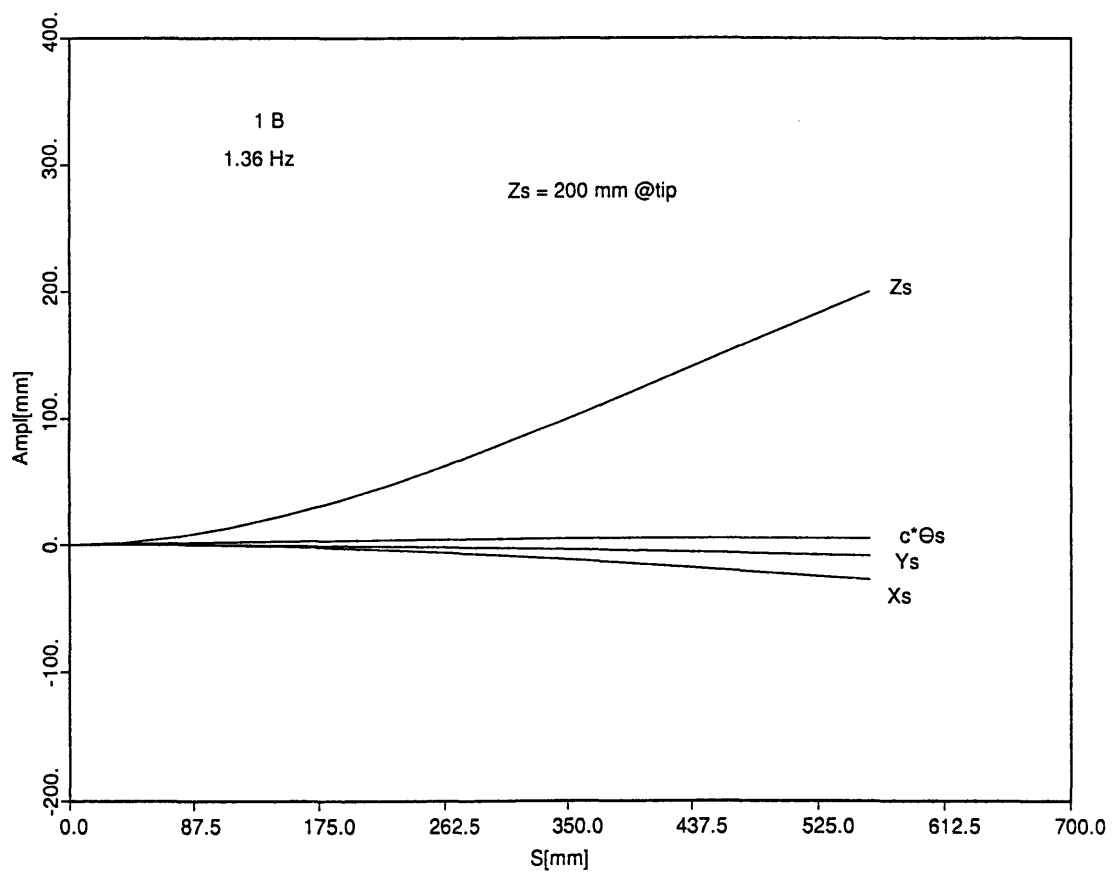

Figure 7.33: First Bending Mode; $[45/0]_s$, 70 mm tip deflection, Zs=10, 200 mm

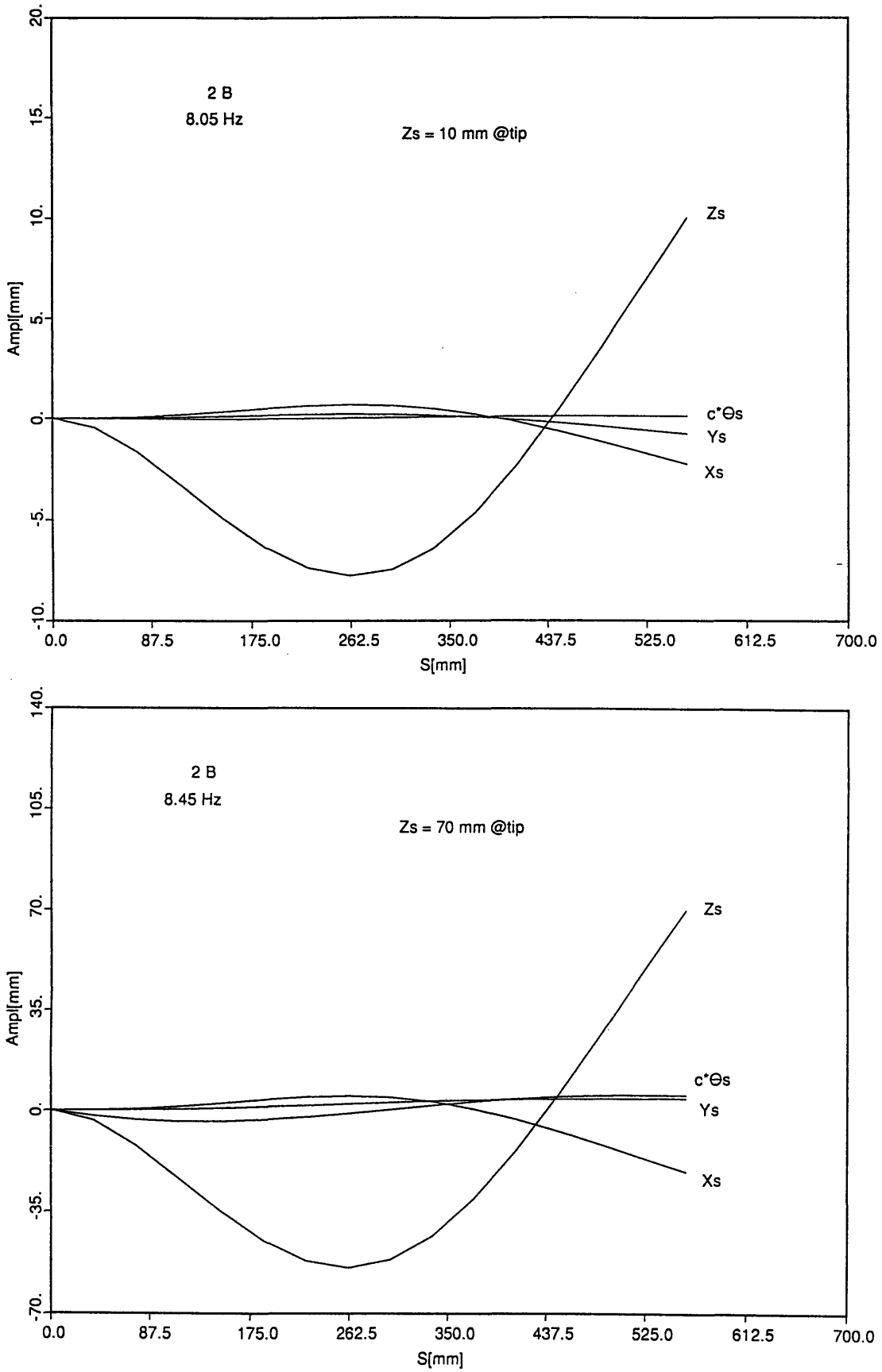

Figure 7.34: Second Bending Mode; $[45/0]_s$, 70 mm tip deflection, Zs=10, 70 mm

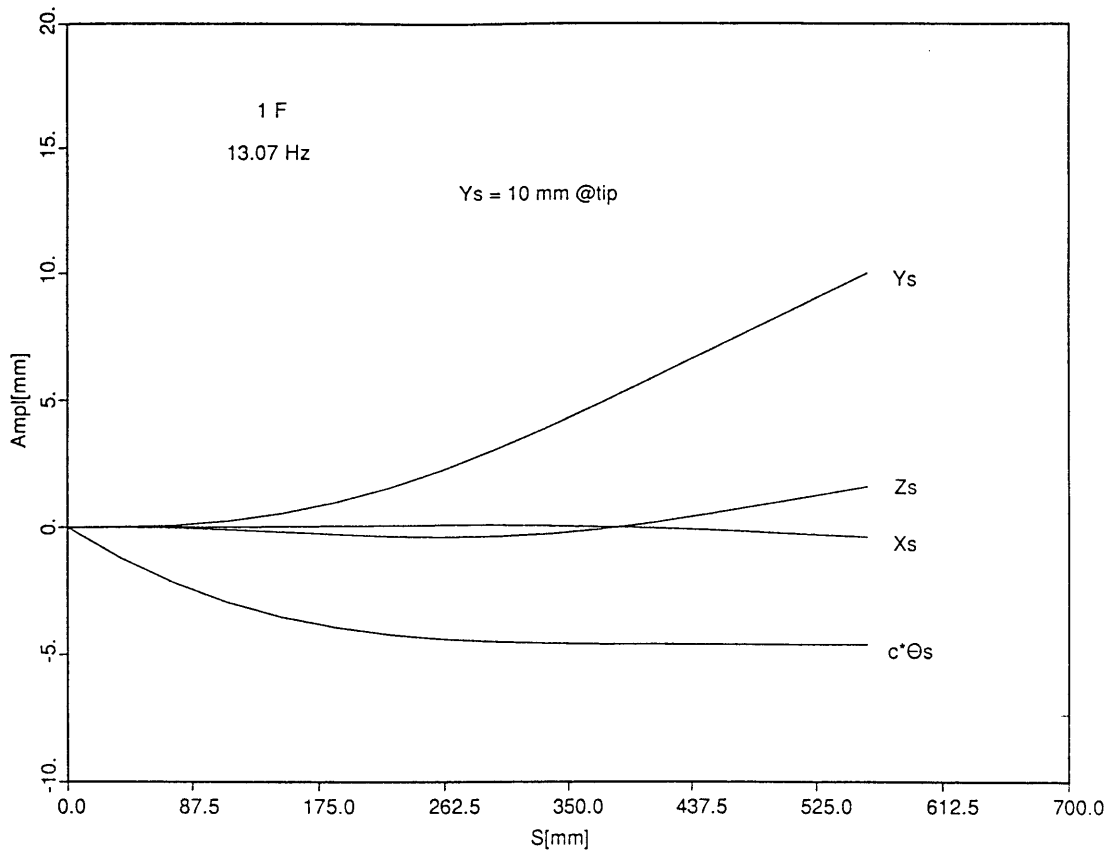

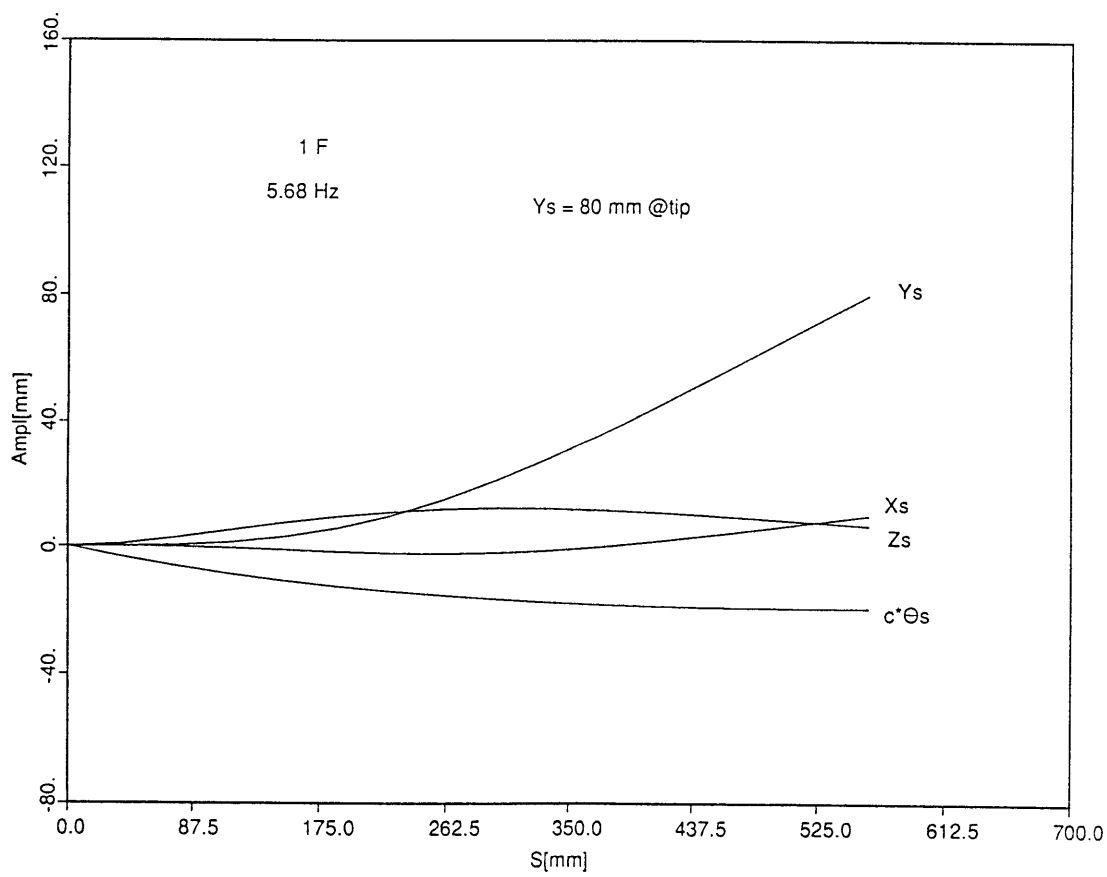

Figure 7.35: First Fore-and-Aft Mode; $[45/0]_s$, 70 mm tip deflection, Ys=10, 80 mm

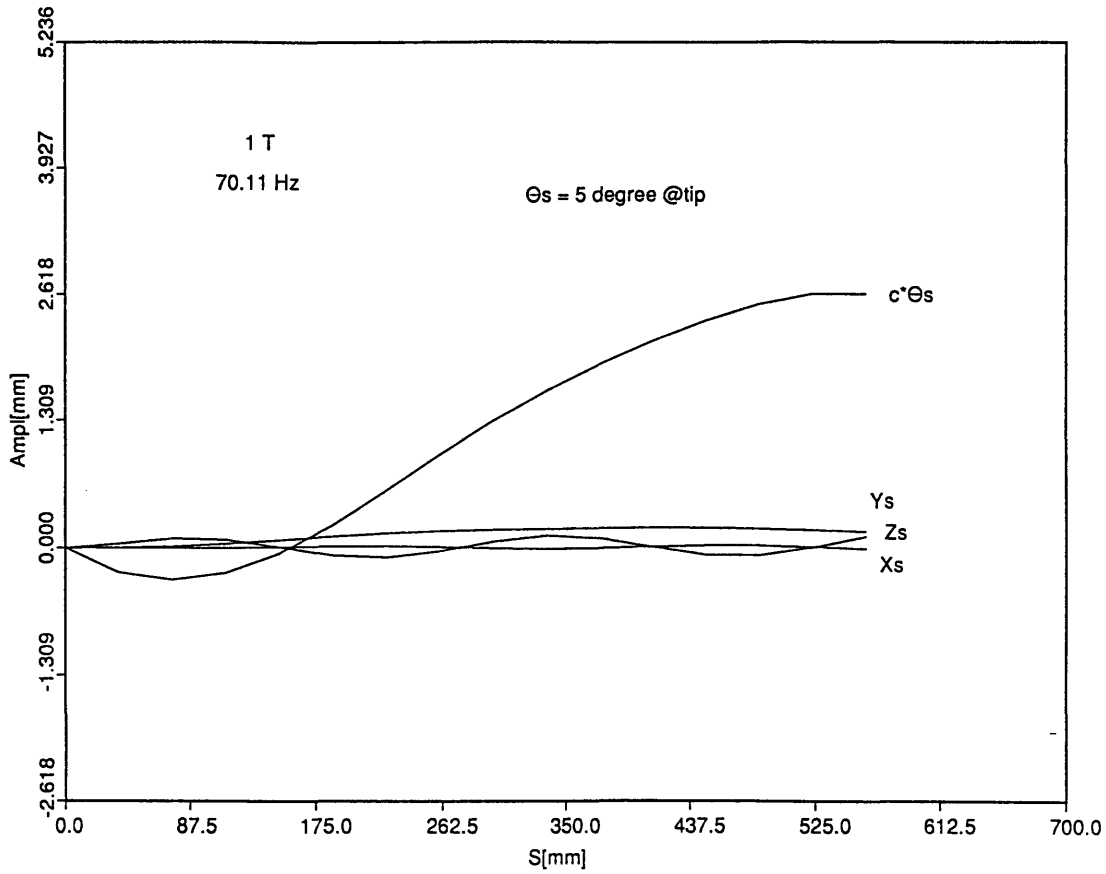

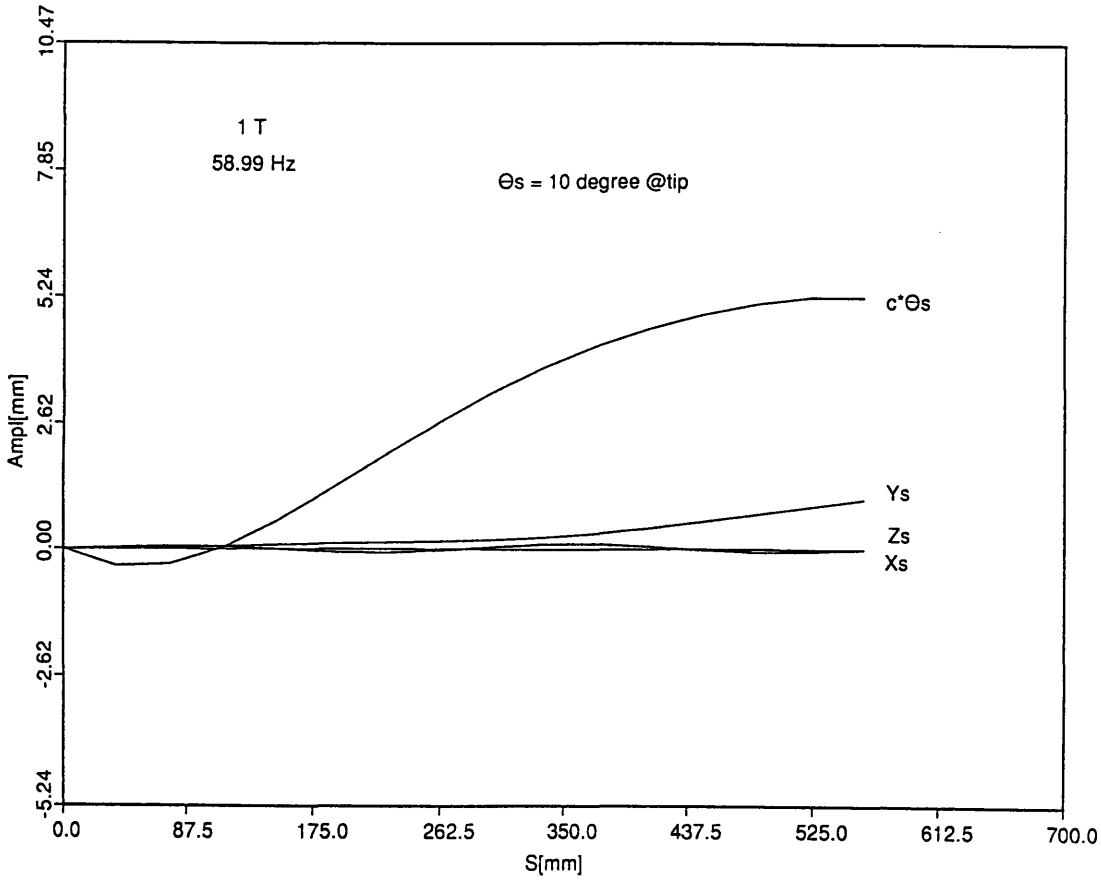

Figure 7.36: First Torsion Mode; $[45/0]_s$, 70 mm tip deflection, θ_s=5, 10 deg.

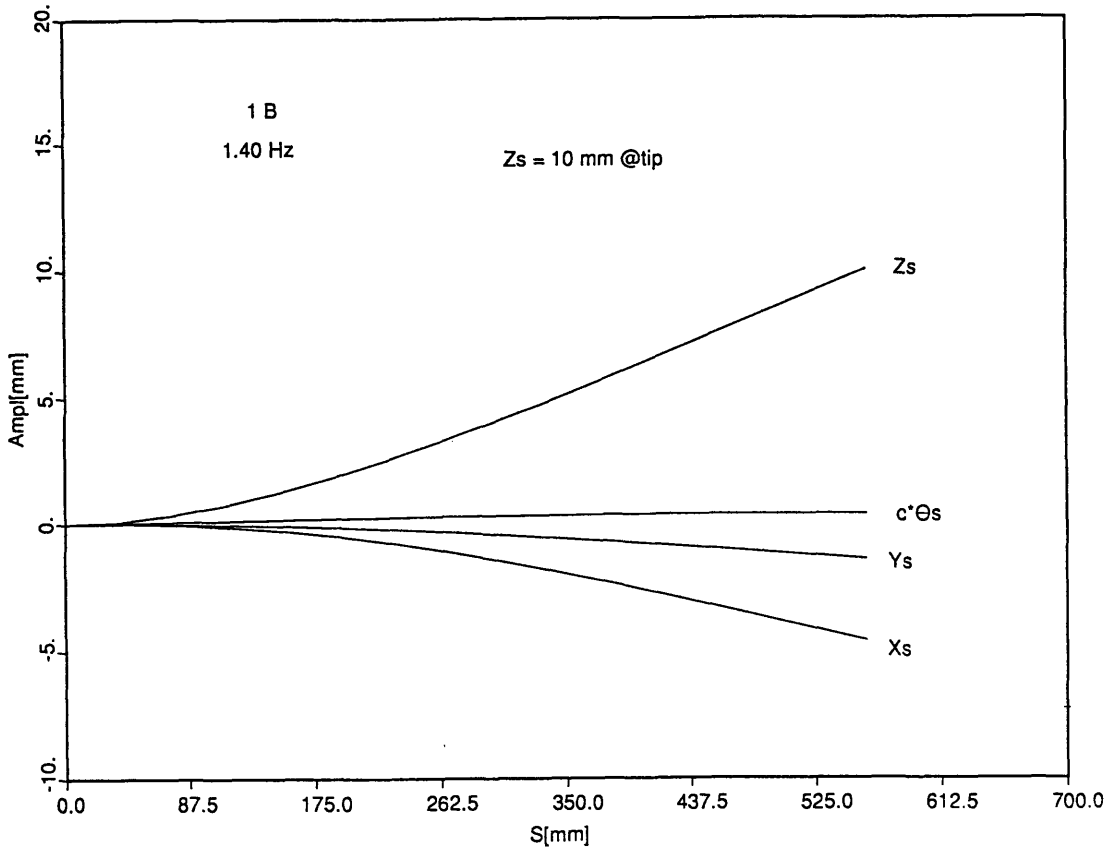

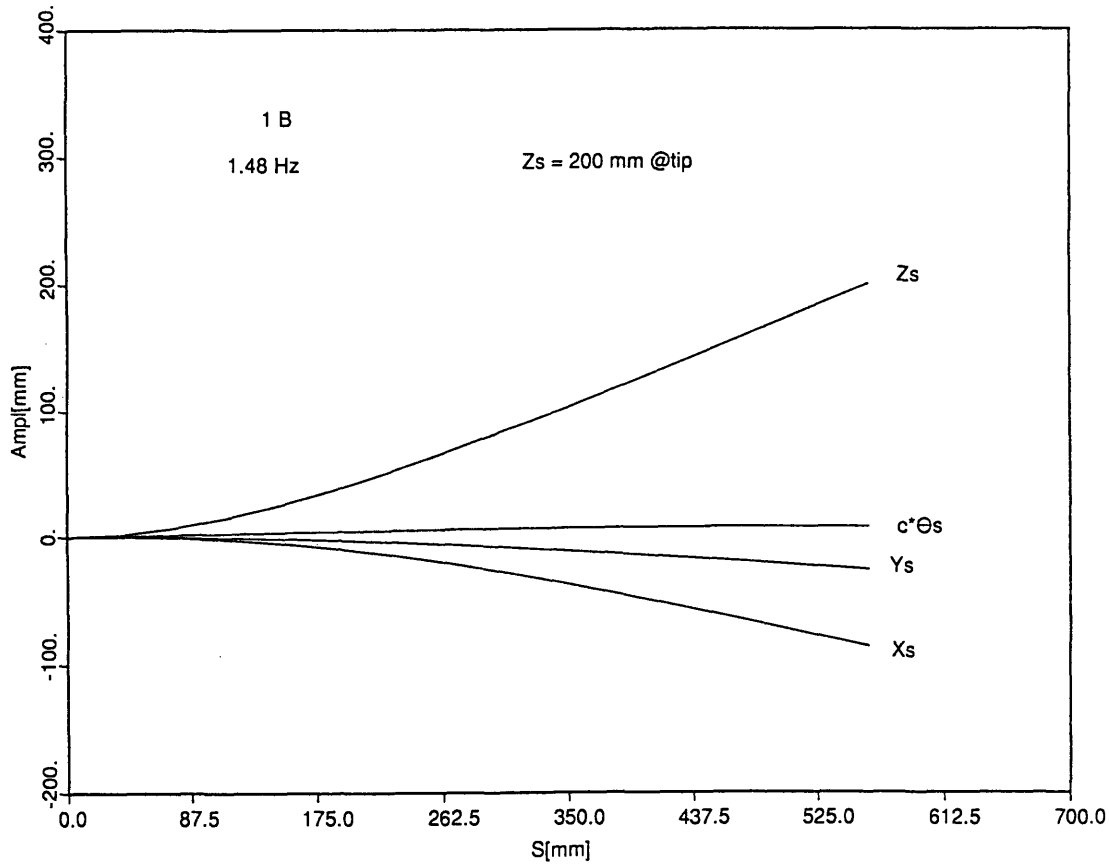

Figure 7.37: First Bending Mode; $[45/0]_s$, 203 mm tip deflection, Zs=10, 200 mm

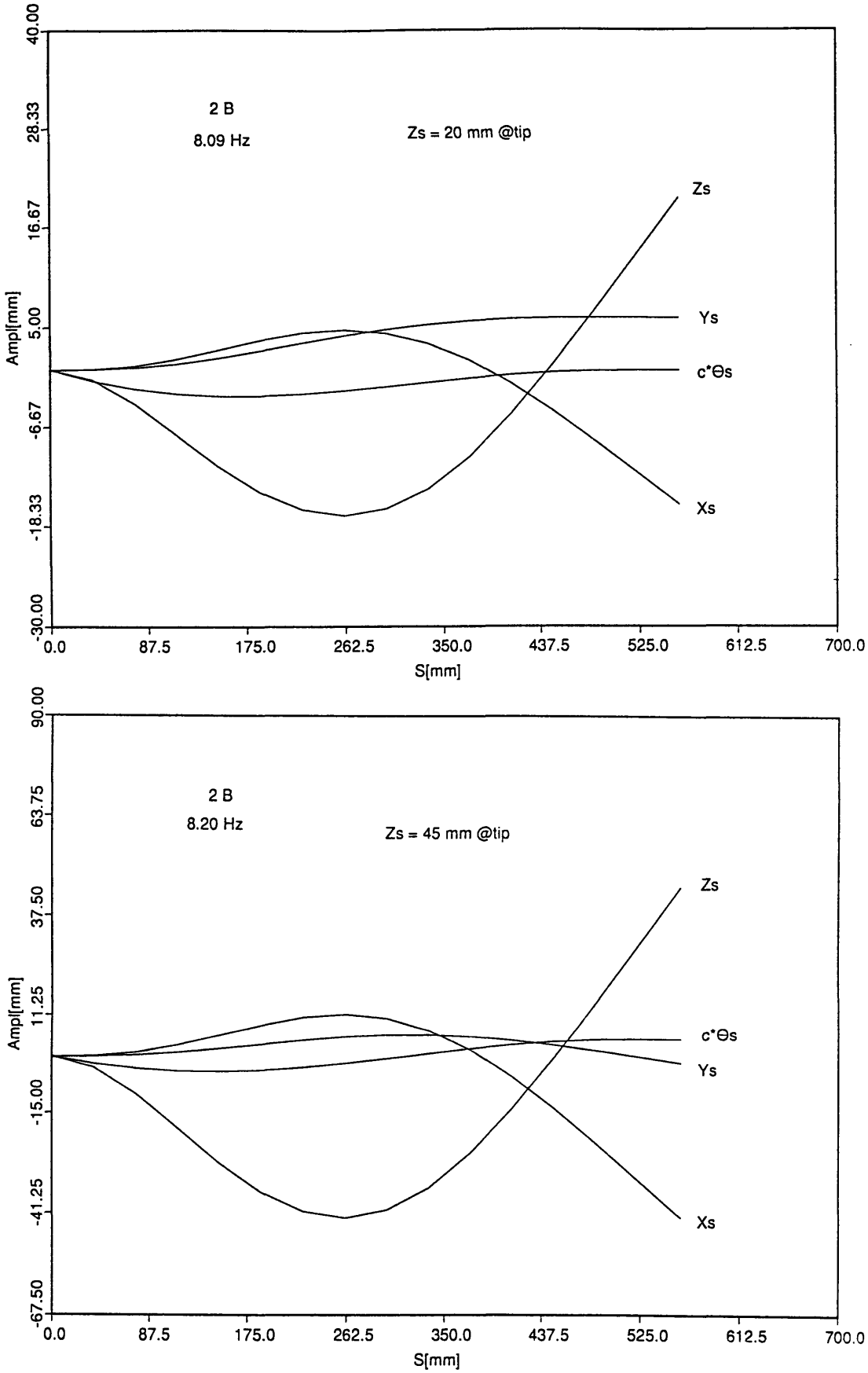

Figure 7.38: Second Bending Mode; $[45/0]_s$, 203 mm tip deflection, Zs=20, 45 mm

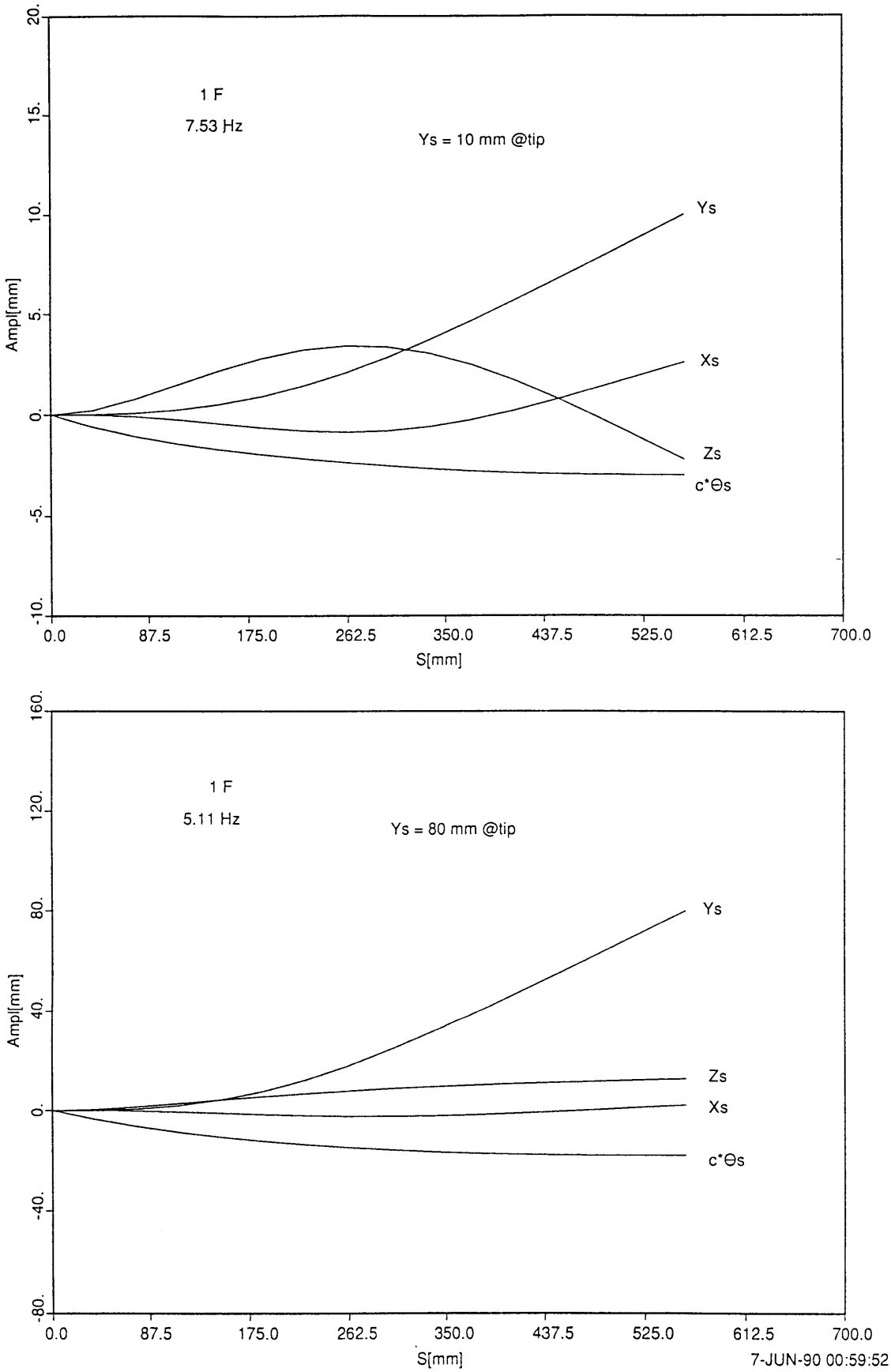

Figure 7.39: First Fore-and-Aft Mode; $[45/0]_s$, 203 mm tip deflection, Ys=10, 80 mm

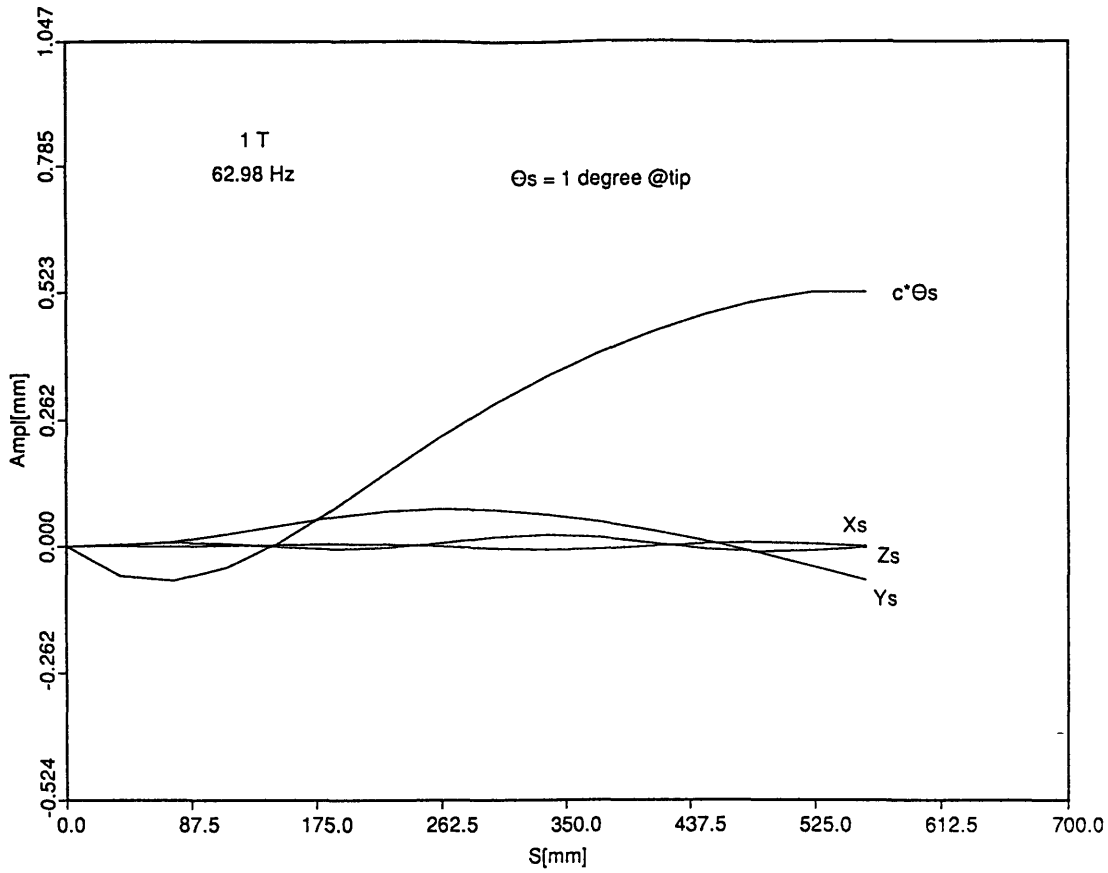

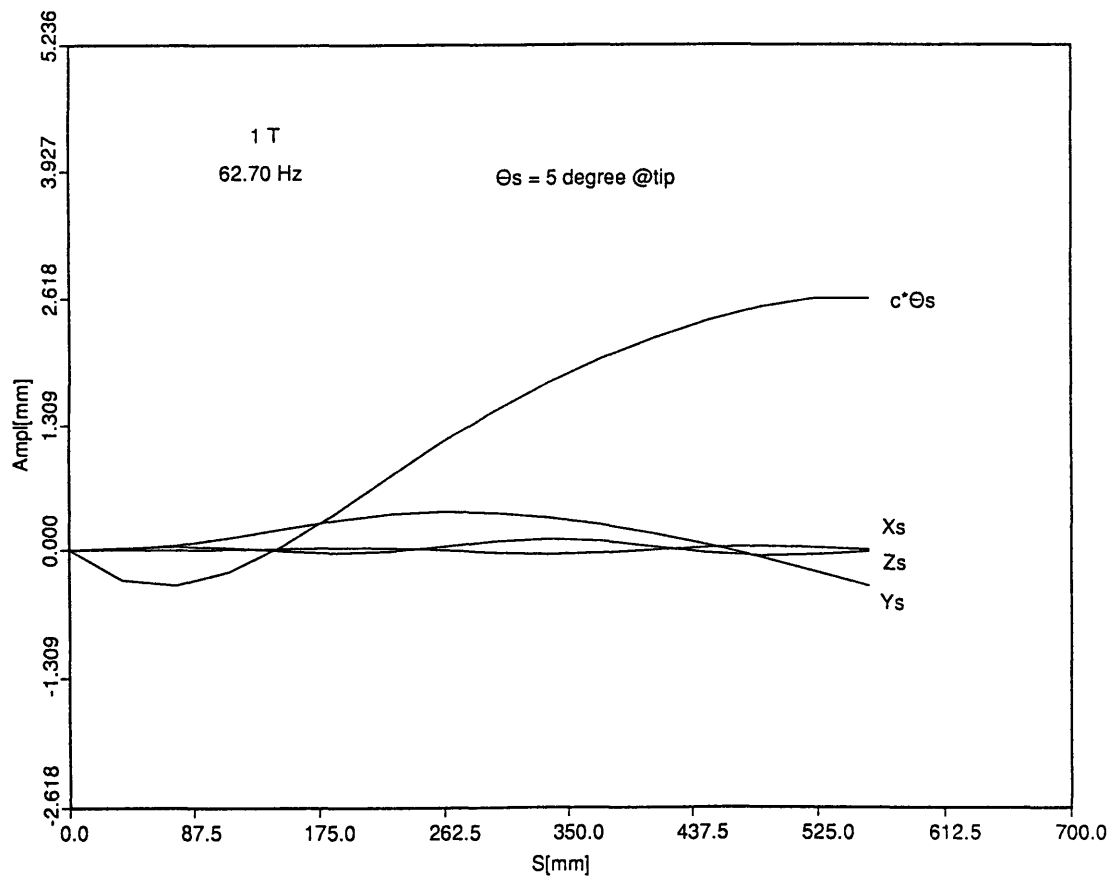

Figure 7.40: First Torsion Mode; $[45/0]_s$, 203 mm tip deflection, θ_s=1, 5 deg.

7.2 Nonrotating results using Moderate Deflection Equations

Also presented as dashed lines in the Figure 7.2 through 7.8 for the $[0/9]_{3s}$ lay-up are the results from the modal analysis using moderate deflection equations 2.47. The governing nonlinear algebraic equations along with solution procedure were described in section 6.2. Here, to stress the moderateness of the nonlinearities in the governing equations, the dashed lines are given names "moderate analysis" whereas the solid lines are defined as "full analysis" meaning that the fully nonlinear differential equations have been used. The bending and torsional modes employed in the Galerkin's method were those for straight beams without initial static deflection (Ref.47). It was found that at least 3 modes for each of v_1, θ_1 were necessary to ensure accuracy in predicting linear 1F and 1T mode shapes if initial static tip deflections are present. Total of 4 modes were used for each of w_0, v_s, θ_s in the present large amplitude analysis. As seen from the figures, the linear small amplitude predictions of all modes are good. However, as amplitudes increase, the modal results for 1F mode deviate rapidly off from the full results. In fact, except for the bending modes, all the modal results, particularly those of 1F mode, break down too early to be useful. Recall that the nonlinear couplings between w_0, v_1 and θ_1 become stronger as the ratio between the two bending stiffness EI_ζ and EI_ζ becomes higher. Incidentally, increasing the number of modes beyond 3 hardly improved the results. When a second harmonic is included in w, the moderate analysis gets improved and can yield larger amplitude motion (see Figure 7.7), but the results still deviate from the full analysis with the second harmonics, particularly at 24 mm static tip deflection. Interestingly, however, if these moderate results are compared against the full results without the second harmonics, the agreements are now seen much better (see Figure 7.8). Note also that as the level of static tip deflection increases, the error in predicting the tip average deflection accumulates (compare Figure 7.5 and 7.4). From these observations, it is believed that, to improve the modal results in large amplitude vibration of blades

with high bending stiffness ratio, either an ordering scheme higher than second order or inclusion of higher harmonics might be needed.

7.3 Rotating results using Fully Nonlinear Equations

In order to investigate the effects of rotation on the blade large amplitude free vibration, the iterative method described in section 6.3 has been employed for $[0/90]_{3s}$ lay-up blade at a particular speed of 450 rpm (7.5 Hz). The static tip deflections chosen were 59 mm and 210 mm, and generated by adjusting uniform gravity level in the presence of the rotational speed. Because of the centrifugal force effects that tend to straighten out the blade, more upward gravity than the nonrotating case was required to create the same levels of tip deflections. The purpose of maintaining the same tip deflection level by increasing the gravity, rather than maintaining the same gravity as for the nonrotating cases, is thus to simulate realistic cases where static aerodynamic force would cause initial static deformation.

Figure 7.41 and 7.42 represent the frequency changes in the basic modes as functions of tip amplitudes, and Figure 7.43 and 7.44 the changes in the tip average deflections. Figure 7.45 through 7.48 show the mode shapes at the static tip deflection of 210 mm in their $\sin \omega t$ and $\cos \omega t$ components. From Figure 7.41 and 7.42 it is seen that all modes except for the first torsion have all gained 3 to 10 percent of their original nonrotating frequencies because of centrifugal effects. On the contrary, however, the torsion mode has decreased its frequency. It is believed that the torsion mode did not have enough stiffening due to rotation, and the deformation in the middle portion of the blade was such that it actually gave rise to a softening in the twisting degree of freedom. As amplitude level increases, all modes generally follow the nonrotating trends in terms of both frequency and tip average deflection. For example, one can witnesses the softening trend in the first fore-and-aft mode as its amplitude increases. Due to the centrifugal effects, however, the centershift rise in

the tip average deflection is not as severe as the nonrotating case (See Figure 7.43, 7.44). Of particular interest is the first bending mode showing slight softening with amplitude increase accompanied by centershift rise. Recall that in the nonrotating case the first bending mode would be hardened with centershift drop as amplitude is increased. As seen from Figure 7.45, this softening trend is due to existence of significant amount of lead-lag motion that is coupled to the bending motion. This coupling is caused by Coriolis forces and would become more severe as more initial static tip deflection is introduced, as evident from Figure 7.43 and 7.44.

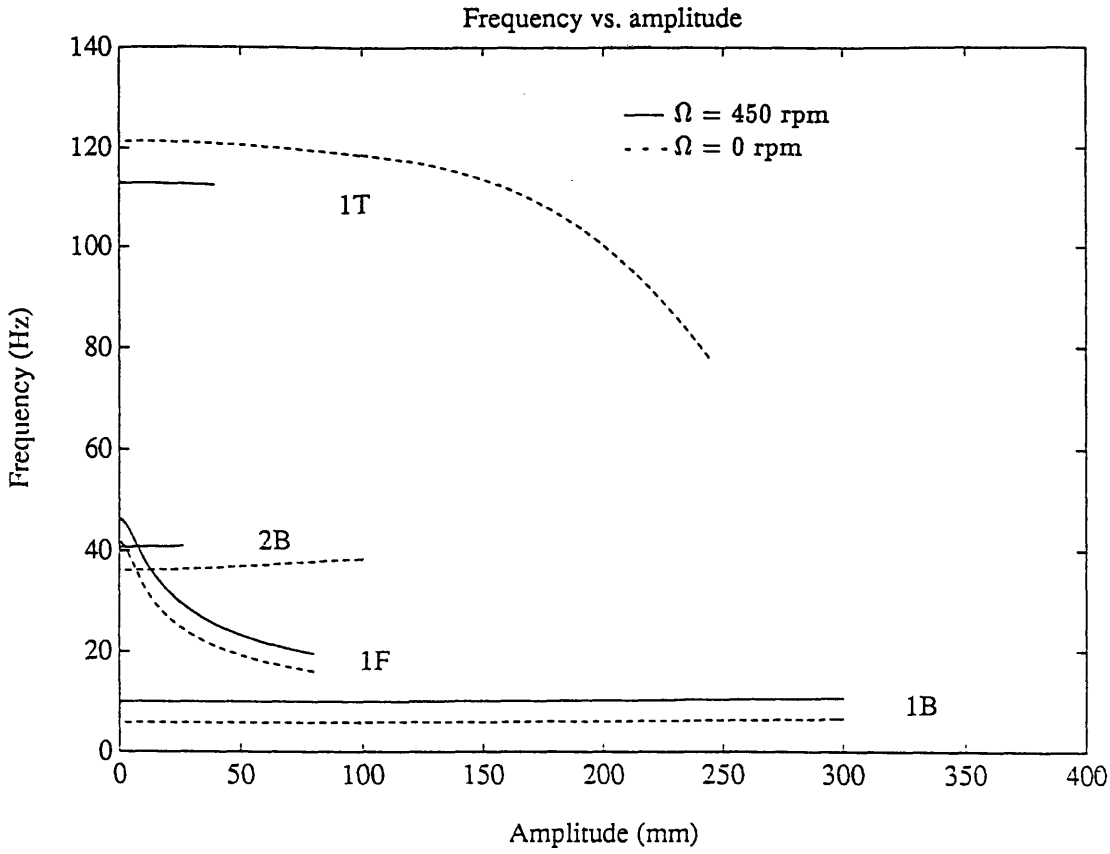

Figure 7.41: Frequency vs. amplitude; $[0/90]_{3s}$, 59 mm tip deflection, $\Omega = 450$ rpm

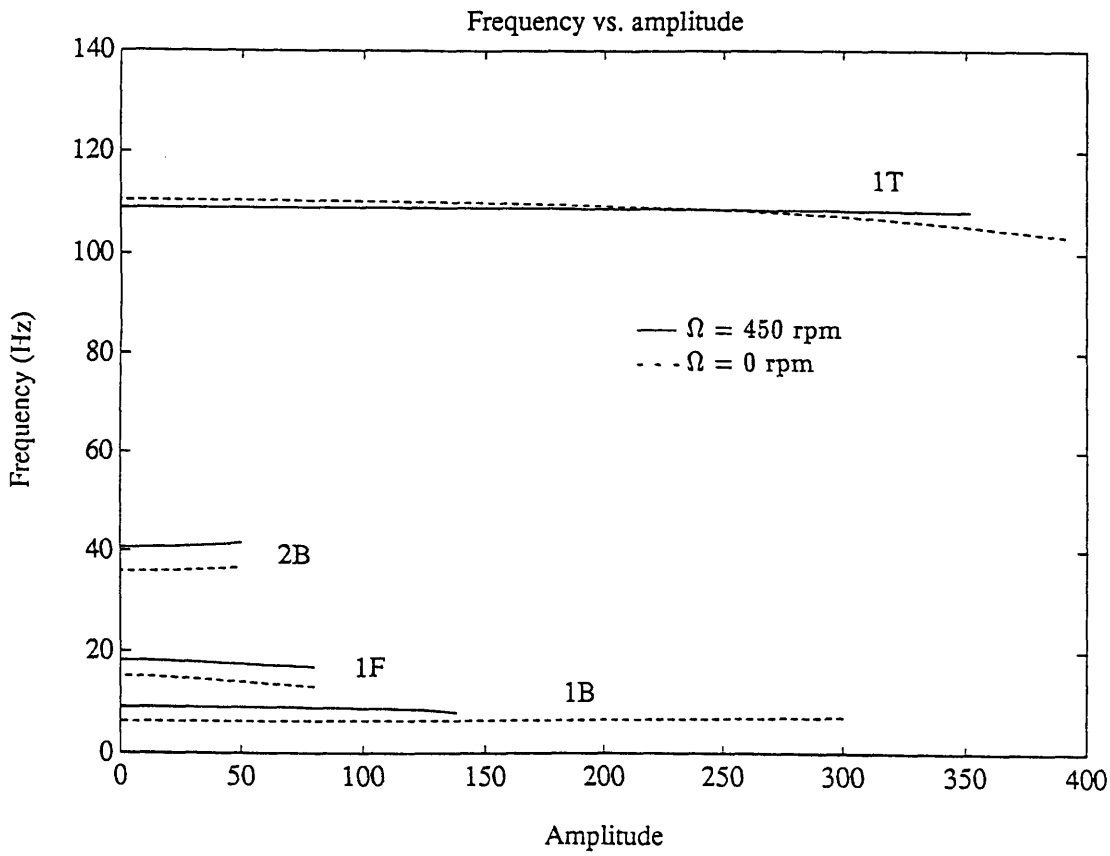

Figure 7.42: Frequency vs. amplitude; $[0/90]_{3s}$, 210 mm tip deflection, $\Omega = 450$ rpm

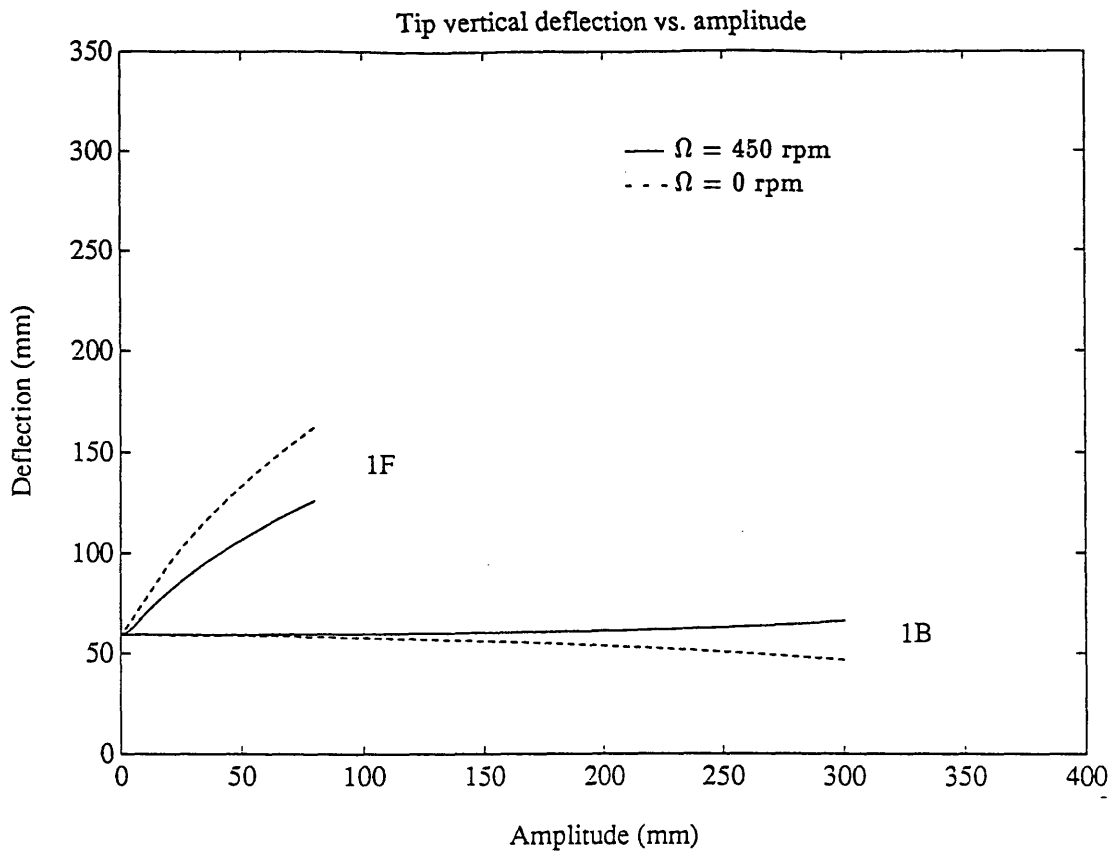

Figure 7.43: Tip average deflection vs. amplitude; $[0/90]_{3s}$, 59 mm tip deflection, $\Omega = 450$ rpm

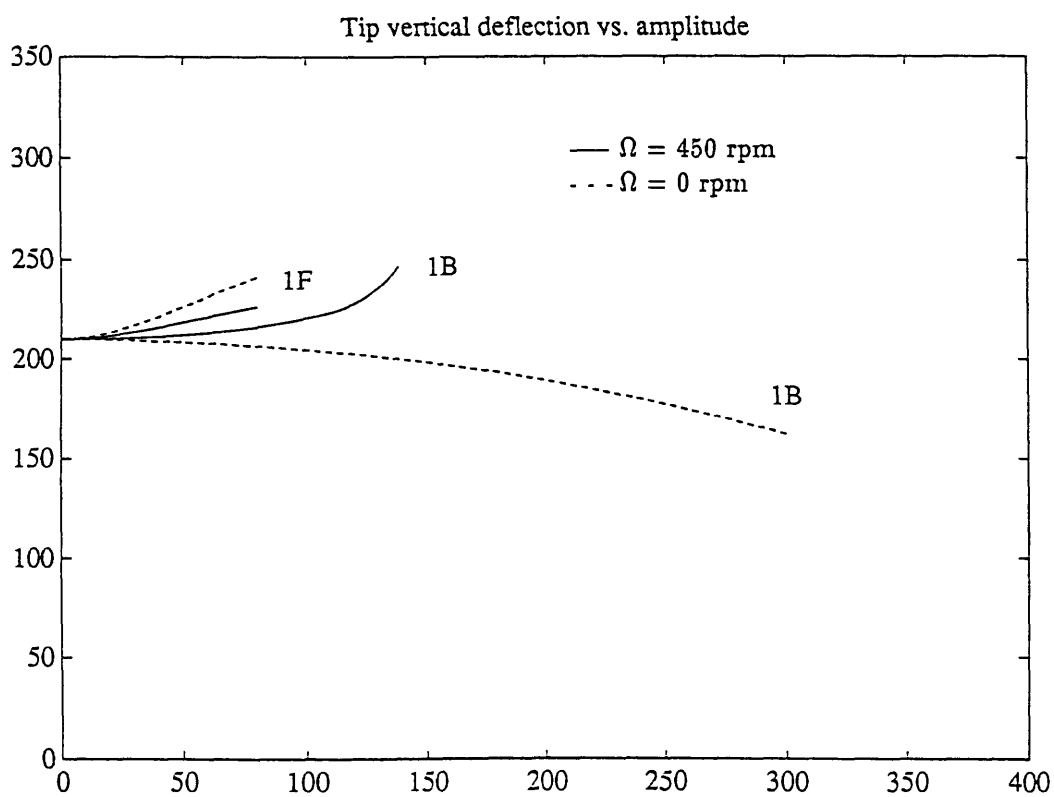

Figure 7.44: Tip average deflection vs. amplitude; $[0/90]_{3s}$, 210 mm tip deflection, $\Omega = 450$ rpm

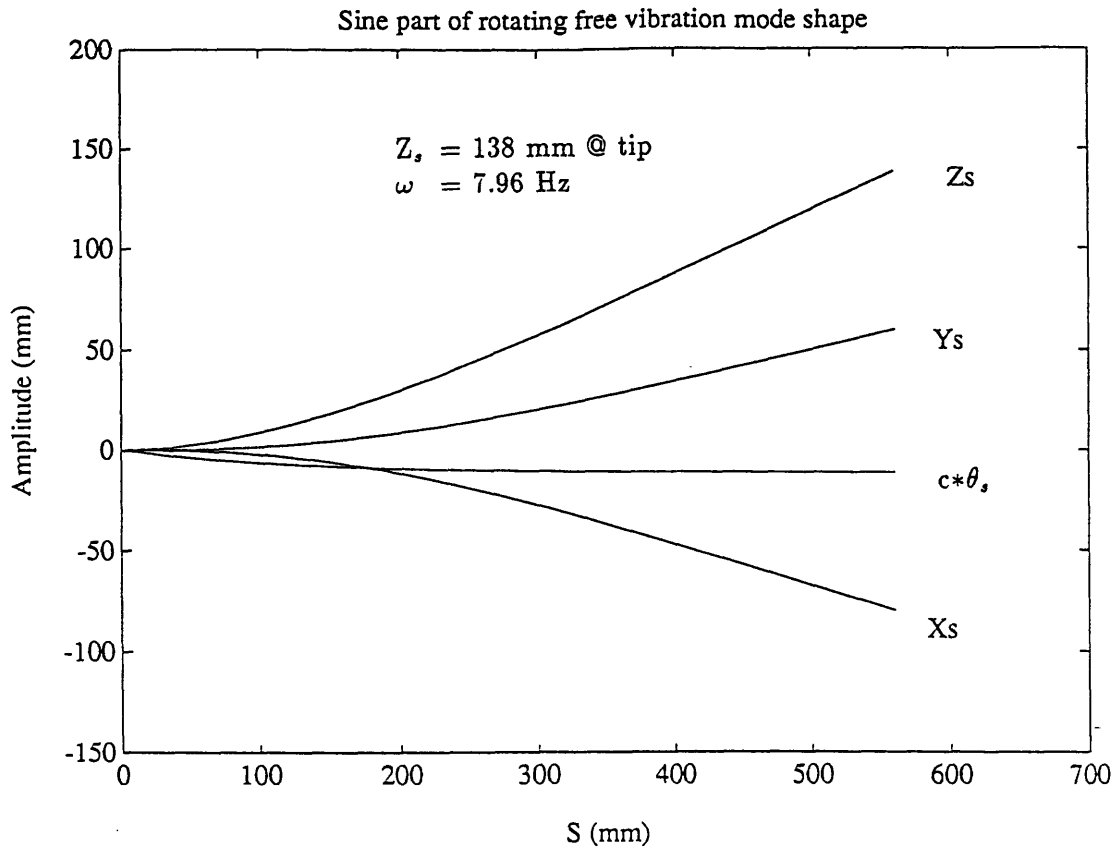

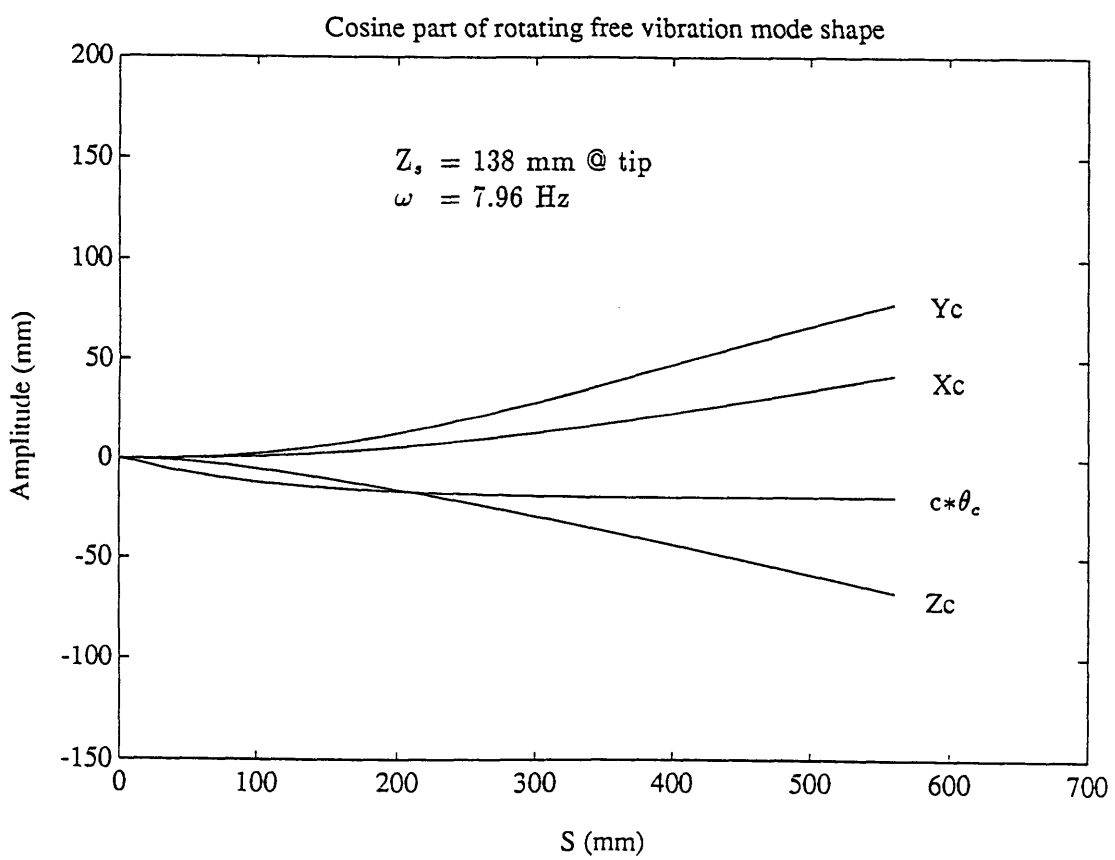

Figure 7.45: First Rotating Bending Mode; $[0/90]_{3s}$, 210 mm tip deflection, Zs=138 mm, Ω = 450 rpm

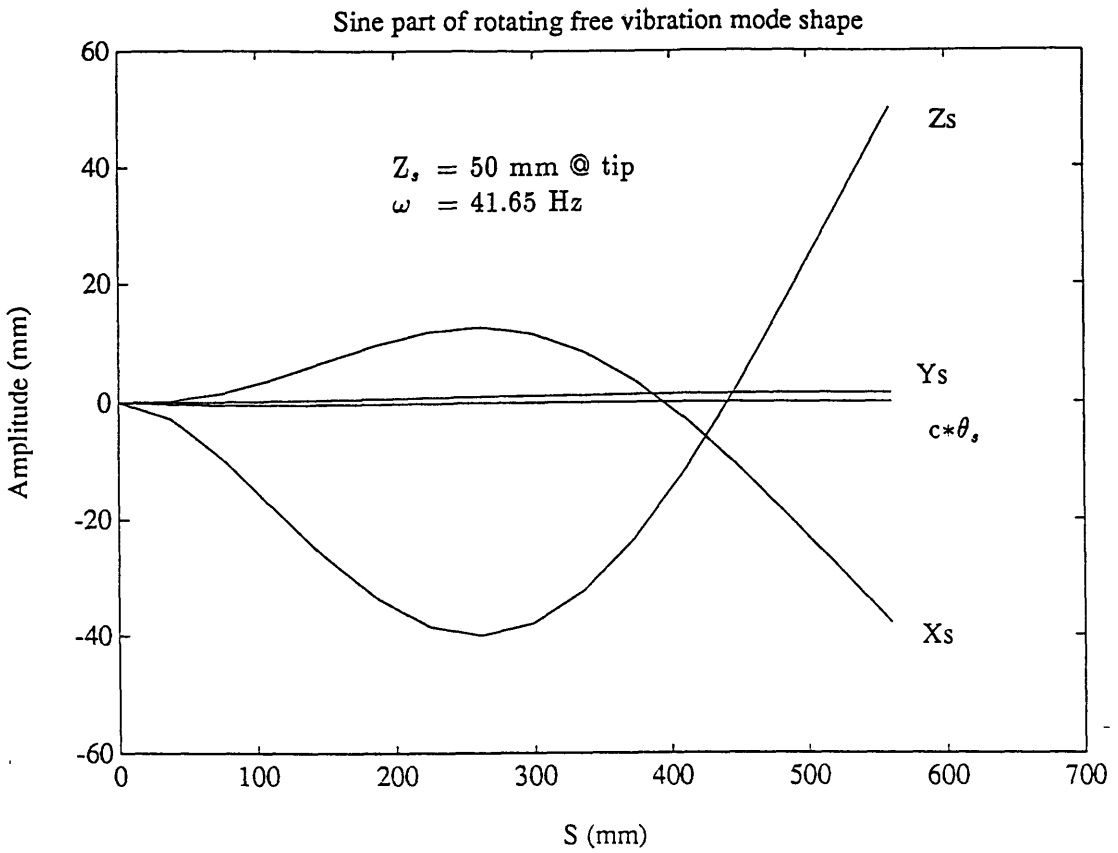

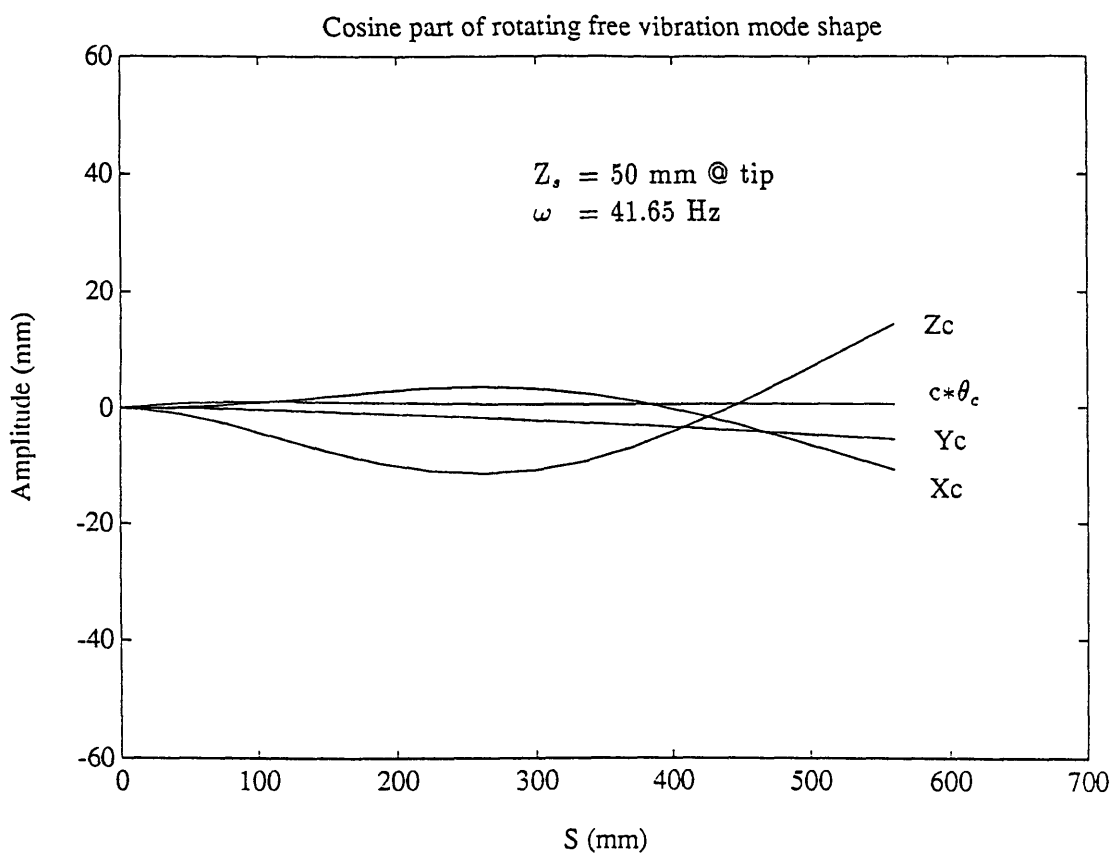

Figure 7.46: Second Rotating Bending Mode; $[0/90]_{3s}$, 210 mm tip deflection, Zs=50 mm, Ω = 450 rpm

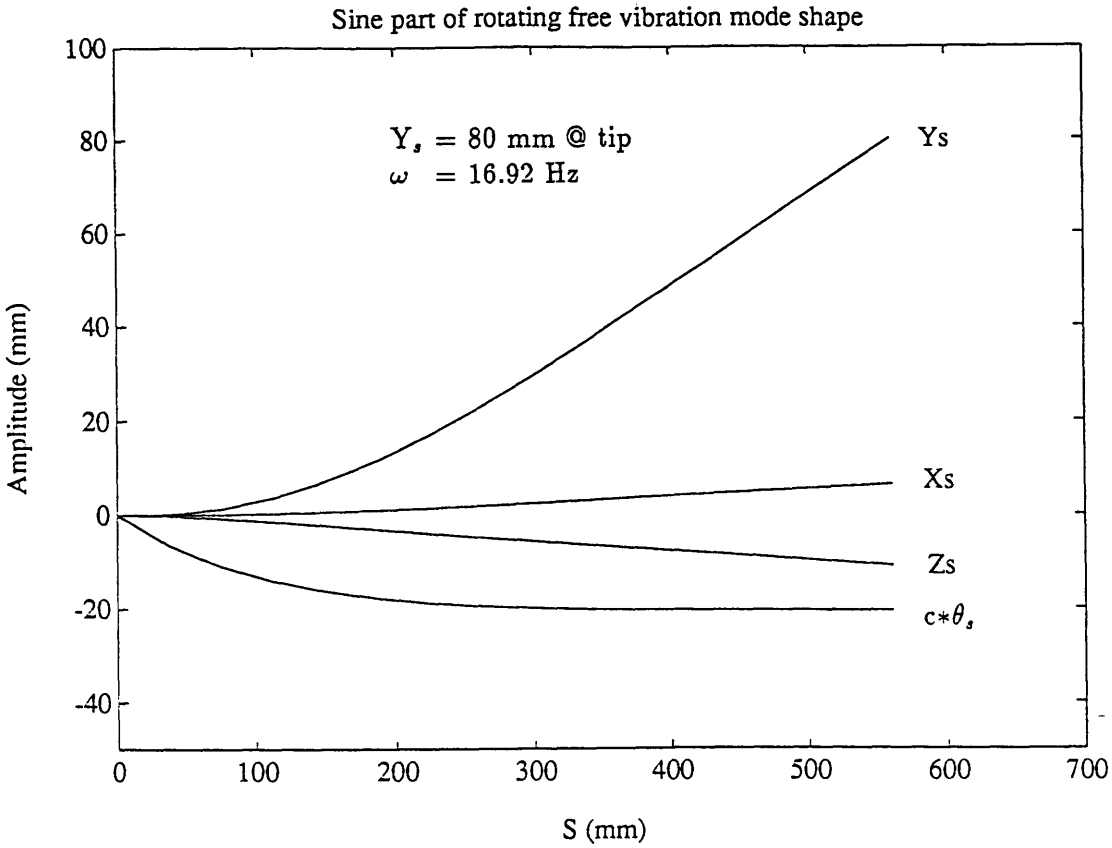

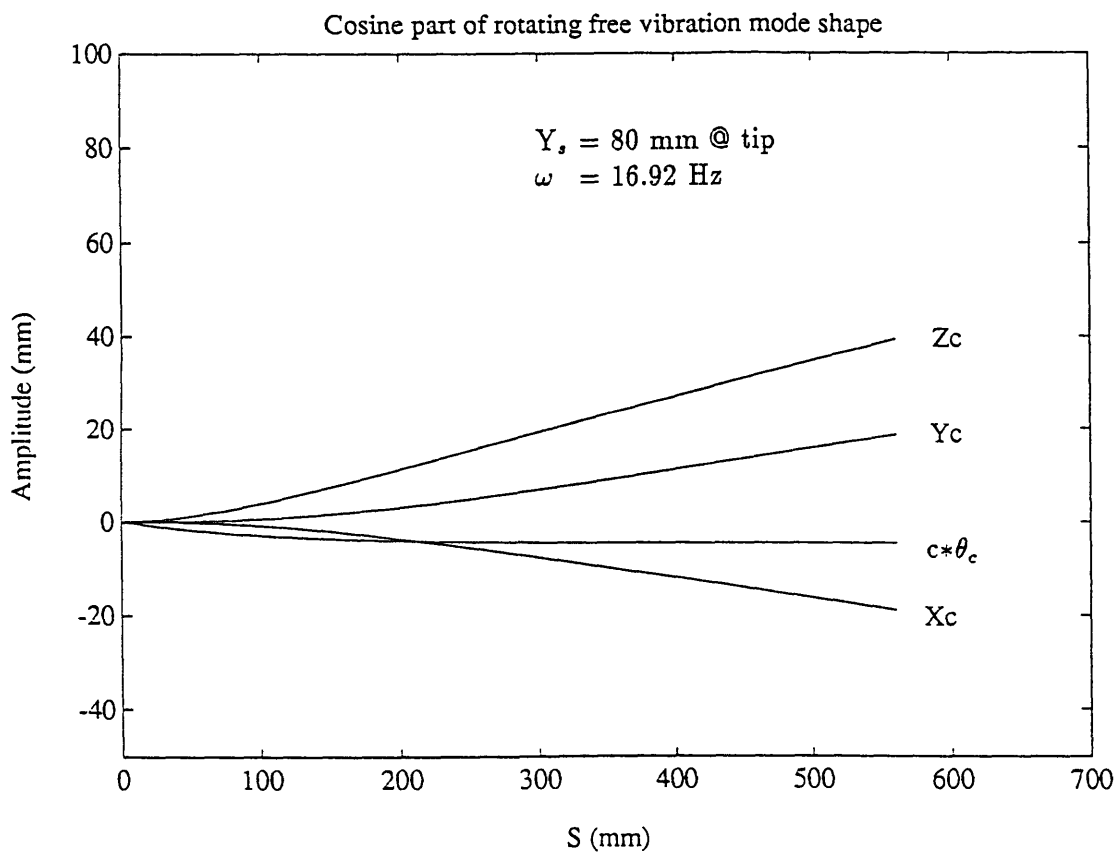

Figure 7.47: First Rotating Fore-and-Aft Mode; $[0/90]_{3s}$, 210 mm tip deflection, Ys=80 mm, Ω = 450 rpm

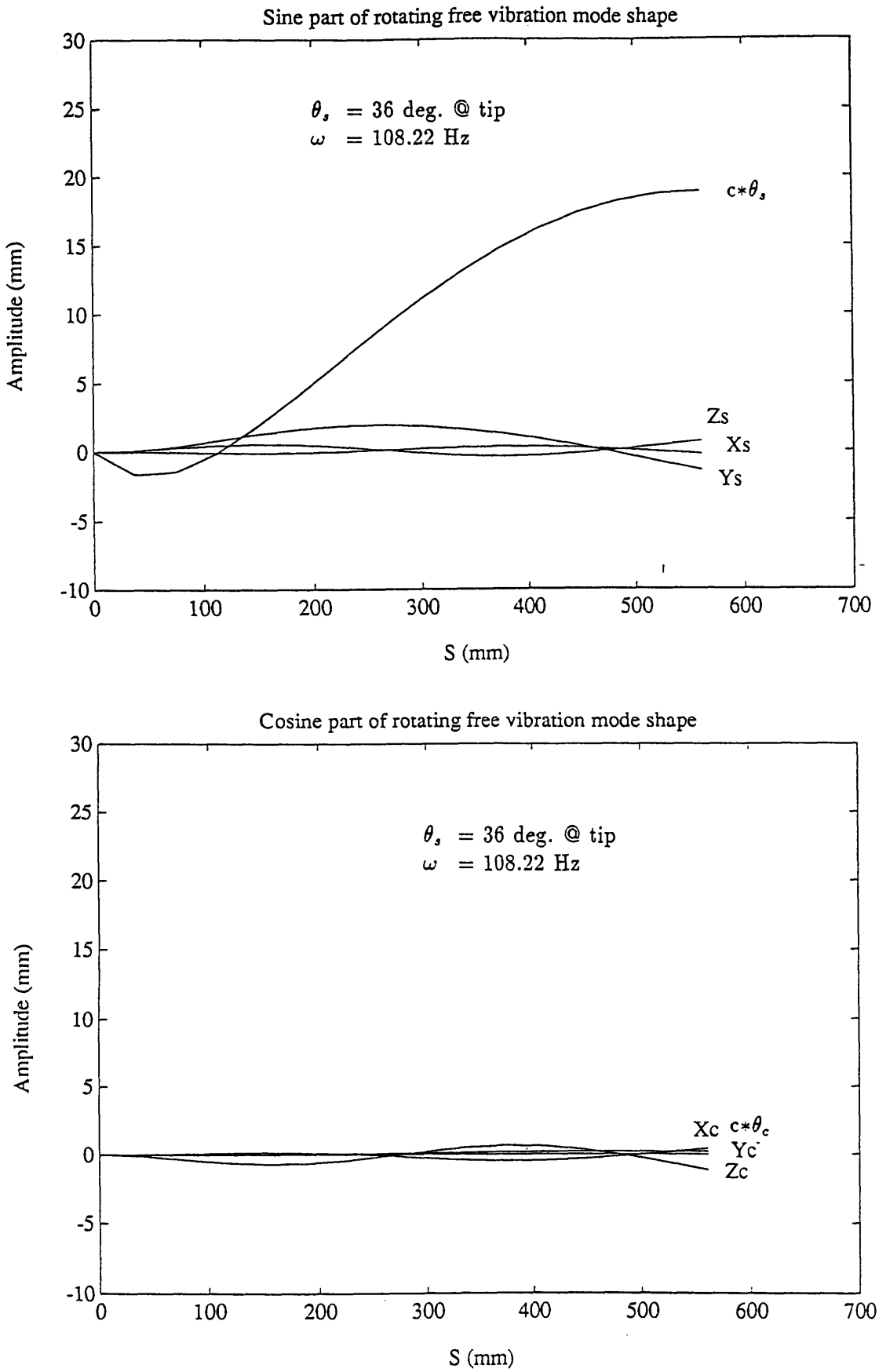

Figure 7.48: First Rotating Torsion Mode; $[0/90]_{3s}$, 210 mm tip deflection, θ_s=36 deg., Ω = 450 rpm

Chapter 8

Experiments of Nonrotating Free Vibration

8.1 Objective

A series of simple, large amplitude experiments has been performed to verify the analytic modeling of large amplitude nonrotating free vibration of composite blades. The test specimens used in these experiments consisted of several cantilever beams of various lay-up, and were all borrowed from a test site where Minguet and Dugundji (Ref. 14) set up their previous experiment. These beams were tested dynamically, first to determine their natural frequencies and mode shapes at small vibration levels, then to observe how they grow at higher vibration amplitude levels. The major goal of the vibration tests was to provide, by simple means, a set of evidence to support the analytic results rather than to give vast and comprehensive experimental survey of the nonrotating large amplitude vibrations of composite blades.

8.2 Test Specimens

Unlike the earlier experiment where Minguet and Dugundji were interested in the effects of large static deflections and various structural couplings such as bending-twist, extension-twist, on the natural frequencies and mode shapes of cantilevered blades, attention was focused on the influences of large amplitudes on the vibration

characteristics in the presence of initial static deflections. To achieve this, flat beam specimens were chosen because of their low flapwise bending stiffness which permits very large displacements to be reached without any structural failure. All of the specimens were 560 mm in length 30 mm in chord, and manufactured from Hercules AS4/3501-6 graphite/epoxy. The basic ply material properties are listed in Table 8.1. For details of how these beams were manufactured see Ref. 13. Since the initial static deflections and large amplitudes were expected to be more critical in determining the vibration characteristics than the structural couplings, most of tests were concentrated on specimens without structural couplings. Test lay-ups selected were $[0/90]_{3s}$, $[0/90/0]_s$, $[0/90]_s$, and $[45/0/45]_s$. Beam material properties of these lay-ups are listed in Table 8.2. To see how these coefficients are calculated, refer to section 2.6 of Ref. 13.

8.3 Test Set-Up

During the vibration tests, the blades were cantilevered in a test fixture shown in Figure 8.1 and 8.2, which consisted of several elements: first a stiff aluminum base was attached to a "strong-back" by two bolts. This base contains holes into which an aluminum shaft is fitted. The outer end of the shaft is flattened over a 50 mm portion where the specimen is placed. An aluminum top plate is then placed over the root of the specimen and tightened with two bolts. Using a square angle placed on the table, the vertical time-averaged midchord deflection was measured at the tip of the blade. The same method was used to record the bending amplitudes of the bending modes. To measure the amplitudes of the fore-and-aft modes, a ruler with a fine mesh was placed horizontally right underneath the blade tip along the lead-lag direction. Torsional amplitudes were assessed by measuring the height and width of the pi-shape that blade leading edge and midchord point make, and then converting them into an angular relationship geometrically. An electromagnetic shaker was placed underneath and connected to the blade with a soft spring. The shaker was connected to a variable

frequency generator through an amplifier. Two strain gage rosettes were bonded on the top and bottom face of the blade, 50 mm from its root. One of the strain gages, either an axial gage for bending modes or a 45° gage for torsion or fore-and-aft modes, was connected to an oscilloscope through a gage box. Frequently, a low-pass filter was used during the tests to remove unwanted high frequency noises. The signal from the frequency generator was also displayed on the second channel of the oscilloscope. To ensure large amplitude motions, one minute modification was added: a tiny T-shaped lever was attached on the bottom of blades near the root. The shaker was then connected to the lever horizontally via the soft spring, hence was able to excite large amplitude motion in fore-and-aft (lead-lag) and torsional modes. To excite large amplitude bending motion, this type of connection was not necessary and the shaker was directly connected to the bottom of the blades vertically via the soft spring. See Figure 8.1 and 8.2 for illustrations of the experimental set-up. Figure 8.3 is a photo of the experimental setup in the basement of TELAC laboratory.

8.4 Experimental Results

First, to identify small amplitude vibratory modes, a frequency sweep was employed starting at around 1 Hz until a resonant mode was obtained. Several ways of identification are available, for instance by noting a maximum in the amplitude of the beam or gage response. Also, at a resonance, the signals from the gage and the shaker are either exactly in phase or in opposite phase with the signal from the frequency generator. Once the fundamental mode was obtained by the frequency sweep, the amplitude of the particular mode was gradually increased by amplifying the input to the frequency generator. At each amplitude level, shaking frequency was adjusted so as to yield maximum motion, whereby a nonlinear resonance state was believed to be achieved. This peak resonance at the specific frequency simulated a large amplitude free vibration in a best possible manner. The frequency was then read and the corresponding mean vertical position (z_0) as well as the amplitude at the tip

were measured visually using methods described above. The experimental procedure described has been applied to the fundamental modes of beams, the first and second bending modes, the first fore-and-aft mode, and the first torsion mode. Figure 8.4 is a photo taken during a test of the second bending mode of $[0/90]_{3s}$ lay-up with initial static tip deflection of 39 mm (downward due to gravity). The next two figures are photos of the first fore-and-aft and torsion modes of the $[0/90]_s$ lay-up with initial static tip deflection 176 mm (downward).

All of the specimens exhibited certain amounts of initial curvatures due to residual strains. Thus, these plus gravity could be used to create initial static deflections in the cantilevered beams. The initial tip deflections of these lay-ups ranged from 39 mm to 176 mm. Table 8.3 through 8.7 show the results from the tests. For comparison, analytic results (using the differential equations with second harmonic included in the fore-and-aft motion) are shown inside parenthesis. Figure 8.7 and 8.8 show variation of the experimental frequency and the tip average deflection of the fore-and-aft modes with amplitude, for three different lay-ups $[0/90]_{3s}$, $[0/90/0]_s$, and $[0/90]_3$, with three different static tip deflections, 39 mm, 57 mm, and 176 mm, respectively. Also presented in the figures are the corresponding analytic results from the tables.

Except for first bending modes, there were always some ranges of amplitudes where it was impossible to produce pure vibrational modes due to interaction of, or parametric or combinatory resonances between several modes. Such instances are indicated as hyphens in the tables. Incidentally, the interference was most severe in 2B, 1T modes and it was virtually impossible to increase the tip amplitudes enough so as to observe any centershifts due to large amplitude motion in these modes. On the contrary, 1B and 1F modes did not have such problems in most of ranges of interest. Analytic results were not obtainable in some cases due to the singularity of solution. These are also indicated as hyphens in the tables.

As seen in the tables and the figures 8.7, 8.8, there is generally a good agreement

between analysis and experiment within the ranges of amplitudes tested. The slight decreases in the frequencies of the bending modes, which is contrary to the analytic prediction, are thought to be due to aerodynamic damping. Also, 1T modes of some blades (e.g., $[0/90]_s$ with 53 mm static tip deflection) showed a trend that is completely opposite to analysis. It is believed that in these cases, the small amount of precurvature, which might have existed but was not included in the analysis, had significant effects on 1T modes. All of the test results, except those of 2B and 1T modes, confirm well the previous analytic results. In particular, the figures show clearly the impact of both large amplitude and the large static deflections on the vibratory characteristics of rotor blades, which were well discussed in the previous chapter. That is, as the amplitude of the fore-and-aft mode increases, its frequency decreases and its tip deflection increases. Furthermore, this phenomenon is most prominent in the moderate range of static tip deflection but diminishes at very high or very low level of the static tip deflections.

From an aeroelastic point of view, it is the fore-and-aft mode that is most critical in determining stability and any nonlinear limit cycles of the blade, and the current test results are able to capture the basic aspects of large amplitudes vibration in that context.

Table 8.1: AS4/3501-6 Ply Properties
$E_l = 142$ GPa $E_t = 9.8$ GPa $G_{lt} = 6$ GPa $\nu_{lt} = 0.3$ $t_{ply} = .134$ mm $\rho = 1530$ kg/m^3

Table 8.2: Beam Material Properties (AS4/3501-6)

$[0/90]_{3s}$ Laminate	$t = 1.49 \times 10^{-3}$ m	
$m = 0.0683$ kg/m	$I_p = 5.13 \times 10^{-6}$ kg. m	
$E_{11} = 3.68 \times 10^6$ N	$E_{22} = 0.26 \times 10^6$ N	$E_{33} = 2.9 \times 10^5$ N
$E_{44} = 0.183$ N. m^2	$E_{55} = 0.707$ N. m^2	$E_{66} = 276$ N. m^2
$[0/90/0]_s$ Laminate	$t = 0.77 \times 10^{-3}$ m	
$m = 0.0327$ kg/m	$I_p = 2.402 \times 10^{-6}$ kg. m	
$E_{11} = 2.37 \times 10^6$ N	$E_{22} = 0.116 \times 10^6$ N	$E_{33} = 0.965 \times 10^5$ N
$E_{44} = 2.85 \times 10^{-2}$ N. m^2	$E_{55} = 0.128$ N. m^2	$E_{66} = 178$ N. m^2
$[0/90]_s$ Laminate	$t = 0.51 \times 10^{-3}$ m	
$m = 0.0283$ kg/m	$I_p = 1.791 \times 10^{-6}$ kg. m	
$E_{11} = 1.23 \times 10^6$ N	$E_{22} = 0.077 \times 10^6$ N	$E_{33} = 0.765 \times 10^5$ N
$E_{44} = 9.45 \times 10^{-3}$ N. m^2	$E_{55} = 4.96 \times 10^{-2}$ N. m^2	$E_{66} = 92$ N. m^2
$[45/0]_s$ Laminate	$t = 0.53 \times 10^{-3}$ m	
$m = 0.0238$ kg/m	$I_p = 1.66 \times 10^{-6}$ kg. m	
$E_{11} = 1.32 \times 10^6$ N	$E_{22} = 0.27 \times 10^6$ N	$E_{33} = 1.0 \times 10^5$ N
$E_{44} = 0.0195$ N. m^2	$E_{55} = 0.0143$ N. m^2	$E_{66} = 99.1$ N. m^2
$E_{12} = 0.9 \times 10^6$ N	$E_{45} = 0.00632$ N. m^2	
$[45/0/45]_s$ Laminate	$t = 0.78 \times 10^{-3}$ m	
$m = 0.0408$ kg/m	$I_p = 3.071 \times 10^{-6}$ kg. m	
$E_{11} = 1.49 \times 10^6$ N	$E_{22} = 0.232 \times 10^6$ N	$E_{33} = 1.014 \times 10^5$ N
$E_{44} = 0.0621$ N. m^2	$E_{55} = 0.0677$ N. m^2	$E_{66} = 112$ N. m^2
$E_{12} = 0.145 \times 10^6$ N	$E_{45} = 0.0188$ N. m^2	

Note: in more conventional terms,

$$E_{11} \simeq EA \quad E_{22} \simeq GA_\eta \quad E_{33} \simeq GA_\zeta$$

$$E_{44} \simeq GJ \quad E_{55} \simeq EI_\eta \quad E_{66} \simeq EI_\zeta$$

$E_{12} \simeq$ Extension-shear coupling

$E_{14} \simeq$ Extension-twist coupling

$E_{45} \simeq$ Bending-twist coupling

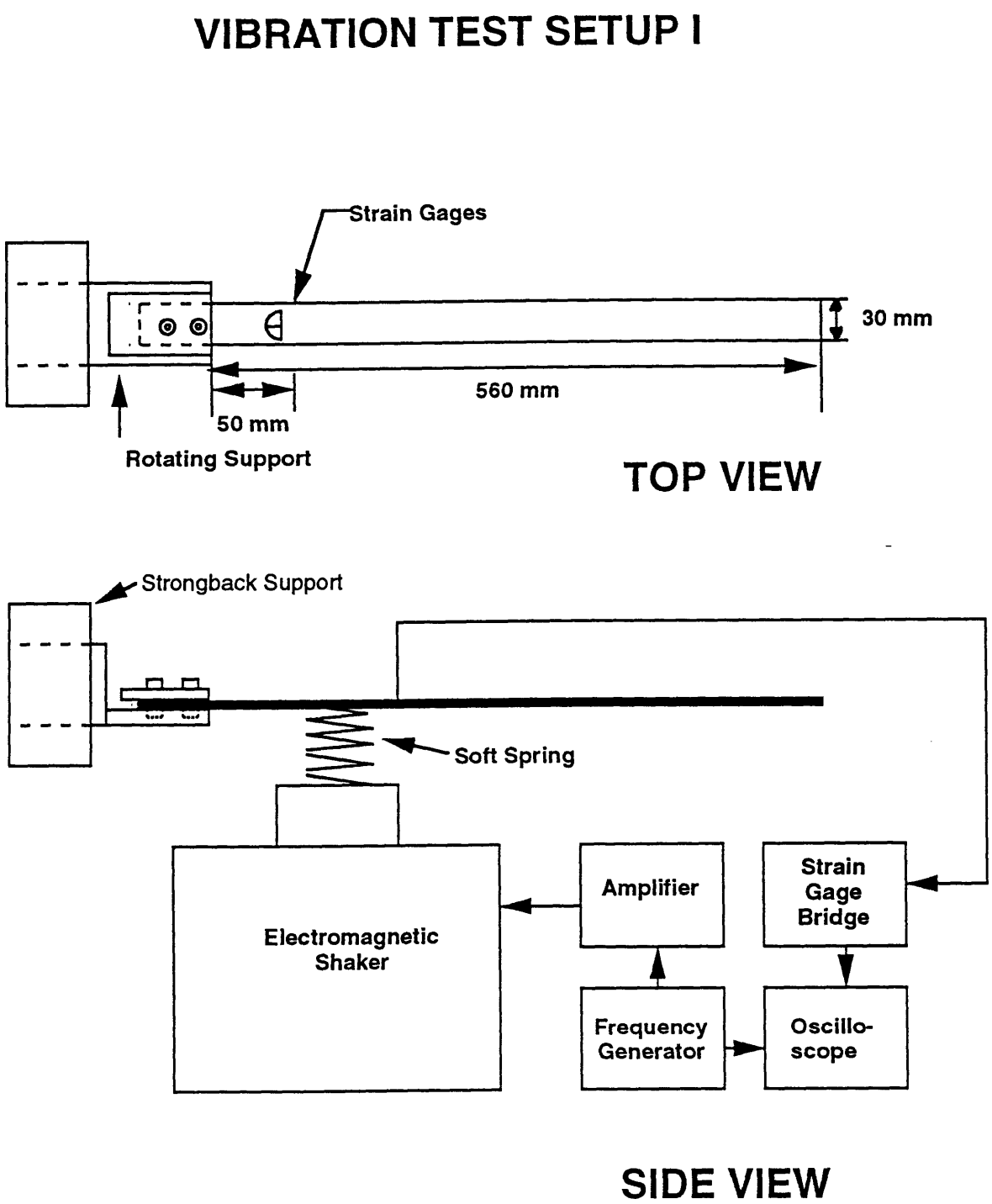

Figure 8.1: Illustration of vibration test setup for bending modes

VIBRATION TEST SETUP II

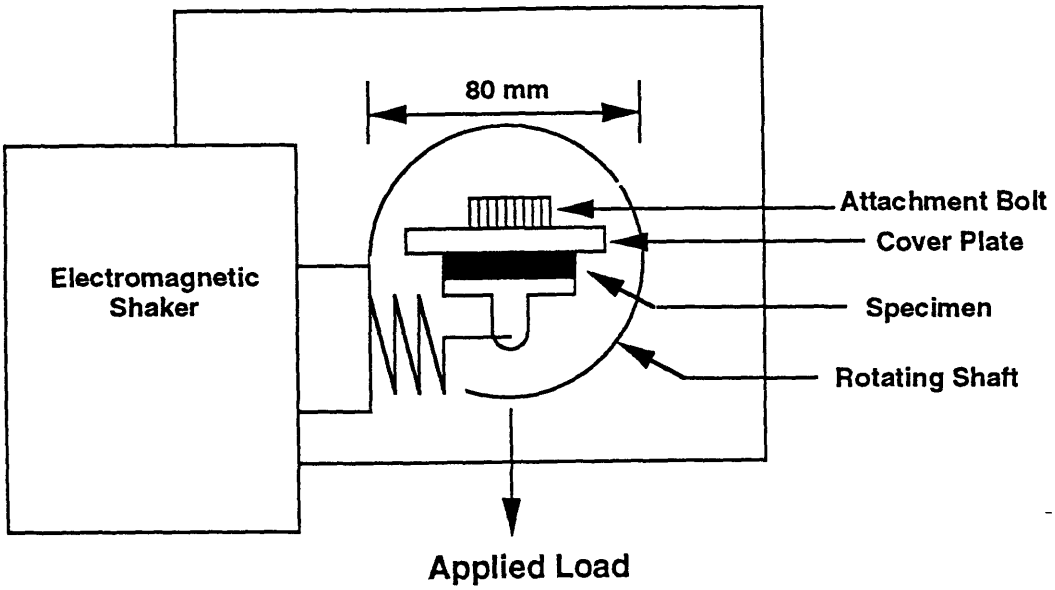

TIP VIEW

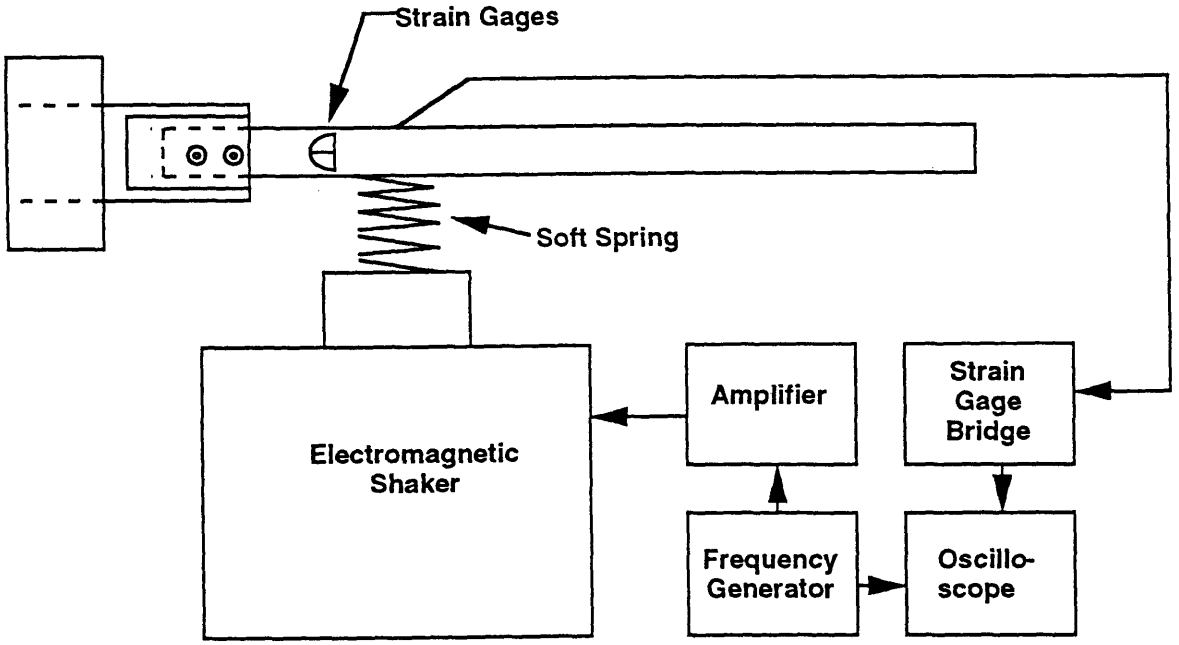

TOP VIEW

Figure 8.2: Illustration of vibration test setup for fore-and-aft and torsion modes

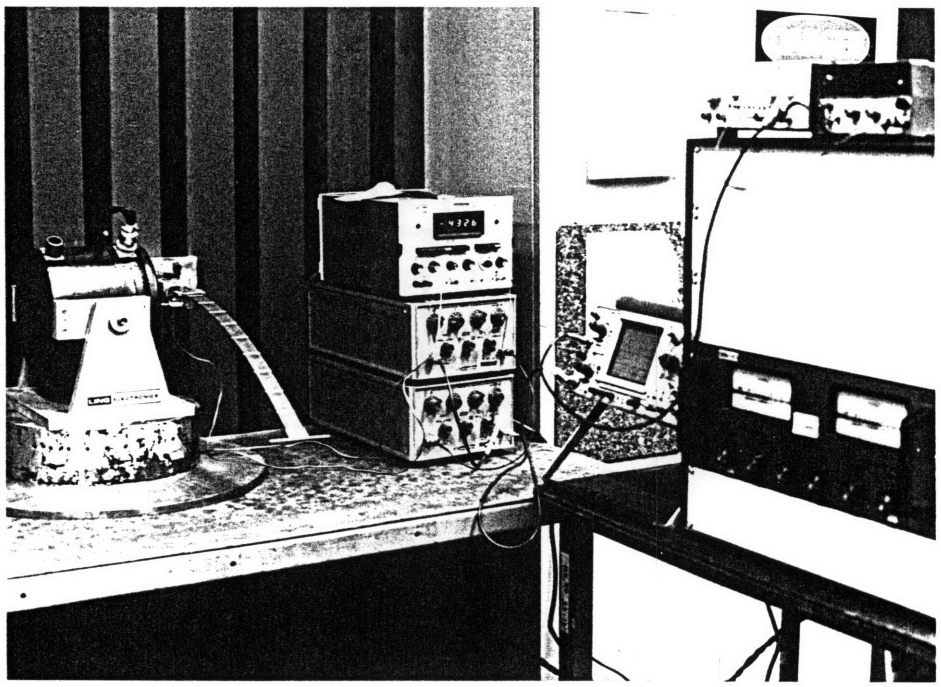

Figure 8.3: Photograph of vibration test setup site

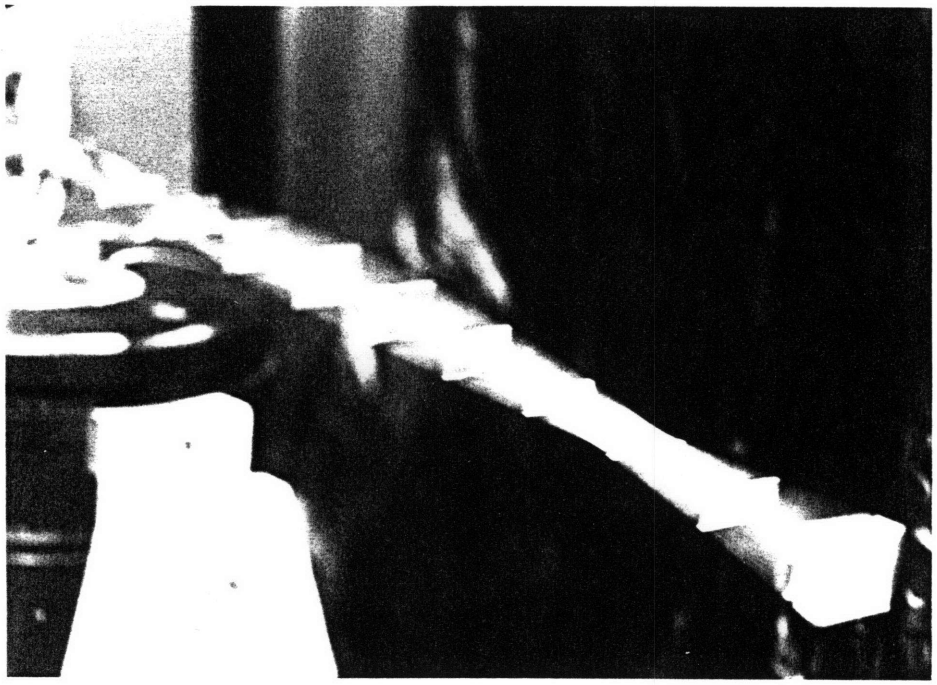

Figure 8.4: Photograph of a second bending mode; $[0/90]_{3s}$ with 39 mm tip deflection

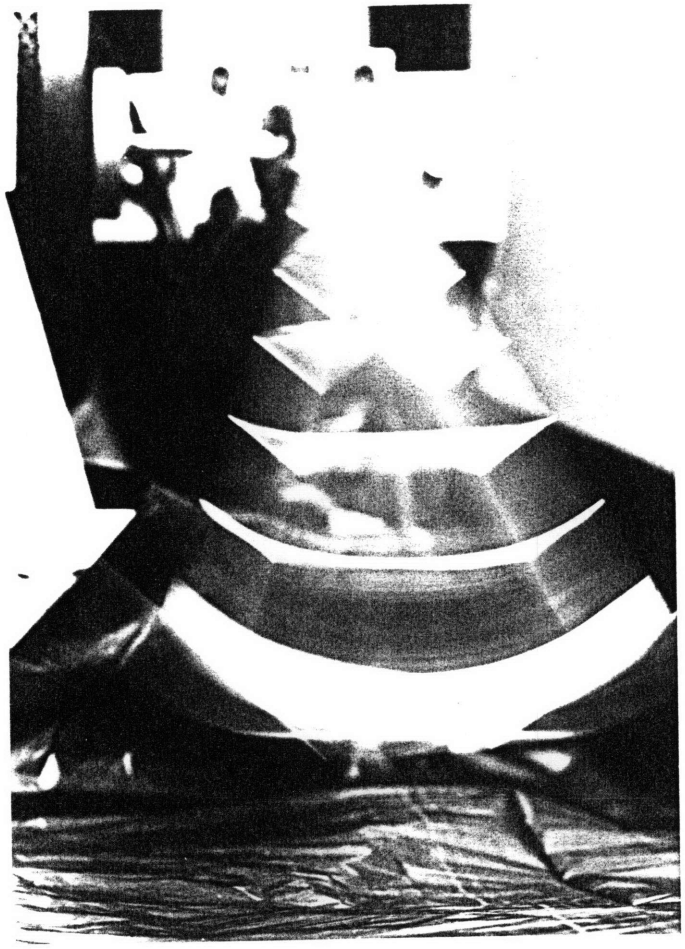

Figure 8.5: Photograph of a first fore-and-aft mode; $[0/90]_s$ with 176 mm tip deflection

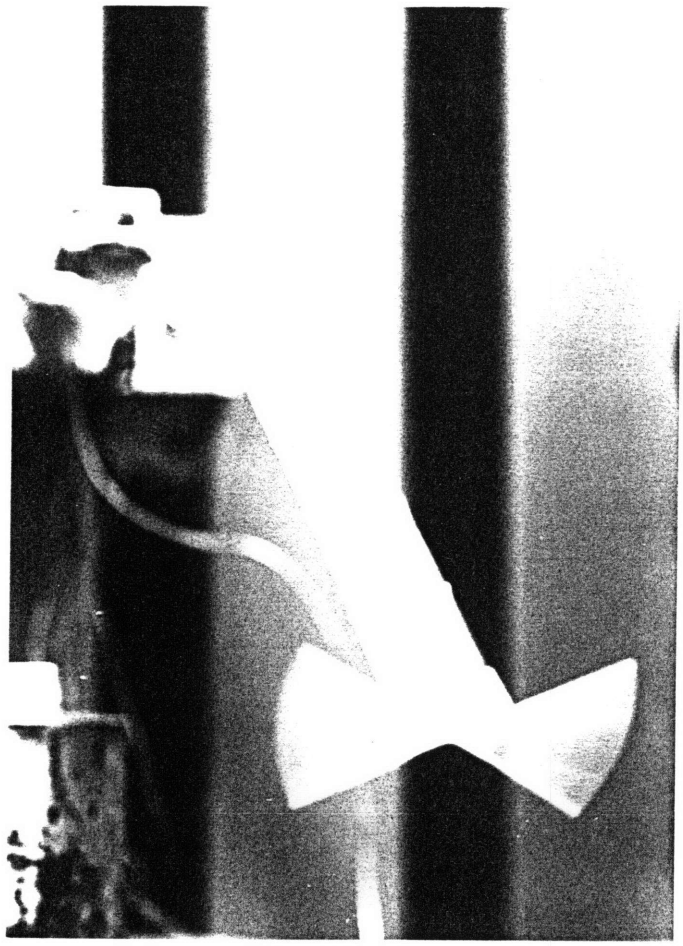

Figure 8.6: Photograph of a first torsion mode; $[0/90]_s$ with 176 mm tip deflection

Table 8.3: Experimental frequency and tip average deflection vs. amplitude; $[0/90]_{3s}$, 39 mm tip deflection

$[0/90]_{3s}$: 1B Mode					
Ampl.(mm)	linear	16	44	80	120
Freq. (Hz)	5.6 (5.8)	5.5 (5.8)	5.5 (5.8)	5.5 (5.8)	5.5 (5.9)
Z_0 (mm)	39 (39)	38 (39)	36 (39)	36 (39)	34 (38)

$[0/90]_{3s}$: 2B Mode						
Ampl.(mm)	linear	6	12	19	25	-
Freq. (Hz)	35 (36)	35 (36)	35 (36)	34 (36)	34 (36)	-
Z_0 (mm)	39 (39)	38 (39)	37 (39)	36 (40)	36 (40)	-

$[0/90]_{3s}$: 1F Mode						
Ampl.(mm)	linear	-	17	24	39	-
Freq. (Hz)	54 (55)	-	34 (30)	30 (26)	25 (22)	-
Z_0 (mm)	39 (39)	-	78 (79)	92 (92)	122 (123)	-

Experiment - solid

Analysis - ( )

Table 8.4: Experimental frequency and tip average deflection vs. amplitude; $[0/90/0]_{3s}$, 57 mm tip deflection

$[0/90/0]_s$: 1B Mode					
Ampl.(mm)	linear	21	50	73	110
Freq. (Hz)	3.0 (3.6)	3.0 (3.6)	3.0 (3.6)	2.9 (3.6)	2.9 (3.6)
Z_0 (mm)	57 (57)	60 (57)	58 (57)	59 (56)	54 (56)

$[0/90/0]_s$: 2B Mode						
Ampl.(mm)	linear	6	13	19	23	-
Freq. (Hz)	19 (22)	19 (22)	19 (22)	18 (22)	18 (22)	-
Z_0 (mm)	57 (57)	59 (57)	59 (57)	59 (57)	58 (58)	-

$[0/90/0]_s$: 1F Mode							
Ampl.(mm)	linear	8	-	22	32	65	-
Freq. (Hz)	25 (26)	22 (21)	-	17 (15)	15 (13)	12 (-)	-
Z_0 (mm)	57 (57)	66 (71)	-	94 (97)	115 (116)	179 (-)	-

$[0/90/0]_s$: 1T Mode					
Ampl.(deg.)	linear	6.5	10	15	20
Freq. (Hz)	83 (75)	83 (74)	- (73)	- (70)	- (65)
Z_0 (mm)	57 (57)	57 (57)	- (57)	- (56)	- (49)

Experiment - solid

Analysis - ( )

Table 8.5: Experimental frequency and tip average deflection vs. amplitude; $[0/90]_s$, 53 mm tip deflection

$[0/90]_s$: 1B Mode				
Ampl.(mm)	linear	35	72	100
Freq. (Hz)	2.2 (2.6)	2.1 (2.6)	2.2 (2.6)	2.1 (2.6)
Z_0 (mm)	53 (53)	55 (53)	53 (52)	62 (52)

$[0/90]_s$: 2B Mode				
Ampl.(mm)	linear	7	10	-
Freq. (Hz)	13.4 (16.1)	13.4 (16.1)	13.4 (16.1)	-
Z_0 (mm)	53 (53)	53 (53)	53 (53)	-

$[0/90]_s$: 1F Mode						
Ampl.(mm)	linear	11	28	49	65	-
Freq. (Hz)	11.8 (18.5)	11.5 (13.5)	10.3 (9.9)	9.1 (8.6)	8.7 (8.4)	-
Z_0 (mm)	53 (53)	57 (72)	81 (105)	118 (161)	151 (167)	-

$[0/90]_s$: 1T Mode					
Ampl.(deg.)	linear	10	20	25	-
Freq. (Hz)	52 (51)	53 (49)	54 (45)	54 (30)	-
Z_0 (mm)	53 (53)	54 (53)	62 (48)	68 (27)	-

Experiment - solid

Analysis - ( )

Table 8.6: Experimental frequency and tip average deflection vs. amplitude; $[0/90]_s$, 176 mm tip deflection

$[0/90]_s$: 1B Mode				
Ampl.(mm)	linear	35	73	100
Freq. (Hz)	2.2 (2.7)	2.2 (2.7)	2.2 (2.8)	2.1 (2.8)
Z_0 (mm)	176 (176)	178 (175)	168 (174)	163 (172)

$[0/90]_s$: 2B Mode				
Ampl.(mm)	linear	7	10	-
Freq. (Hz)	13.0 (16.0)	12.9 (16.0)	12.8 (16.0)	-
Z_0 (mm)	176 (176)	176 (176)	176 (176)	-

$[0/90]_s$: 1F Mode					
Ampl.(mm)	linear	14	48	55	68
Freq. (Hz)	7.6 (6.9)	7.3 (6.7)	7.4 (6.0)	7.4 (5.8)	7.2 (5.6)
Z_0 (mm)	176 (176)	183 (178)	210 (193)	216 (197)	226 (203)

$[0/90]_s$: 1T Mode						
Ampl.(deg.)	linear	14	25	29	33	-
Freq. (Hz)	43 (44)	43 (44)	44 (44)	44 (44)	44 (44)	-
Z_0 (mm)	176 (176)	178 (177)	185 (179)	189 (180)	197 (181)	-

Experiment - solid

Analysis - ( )

Table 8.7: Experimental frequency and tip average deflection vs. amplitude; $[45/0/45]_s$, 93 mm tip deflection

$[45/0/45]_s$: 1B Mode					
Ampl.(mm)	linear	43	79	110	141
Freq. (Hz)	2.3 (2.2)	2.3 (2.2)	2.3 (2.3)	2.2 (2.3)	2.2 (2.3)
Z_0 (mm)	93 (93)	92 (93)	87 (92)	93 (90)	82 (89)

$[45/0/45]_s$: 2B Mode					
Ampl.(deg.)	linear	9	18	26	-
Freq. (Hz)	13.8 (13.7)	13.6 (13.8)	13.9 (13.8)	13.2 (13.8)	-
Z_0 (mm)	93 (93)	95 (93)	96 (94)	96 (95)	-

$[45/0/45]_s$: 1F Mode					
Ampl.(mm)	linear	6	12	16	-
Freq. (Hz)	23 (22)	20 (20)	18 (19)	17 (-)	-
Z_0 (mm)	93 (93)	103 (105)	117 (133)	127 (-)	-

$[45/0/45]_s$: 1T Mode					
Ampl.(deg.)	linear	6.5	10	18	-
Freq. (Hz)	91 (91)	91 (90)	90 (89)	88 (-)	-
Z_0 (mm)	93 (93)	95 (93)	96 (91)	96 (-)	-

Experiment - solid

Analysis - ( )

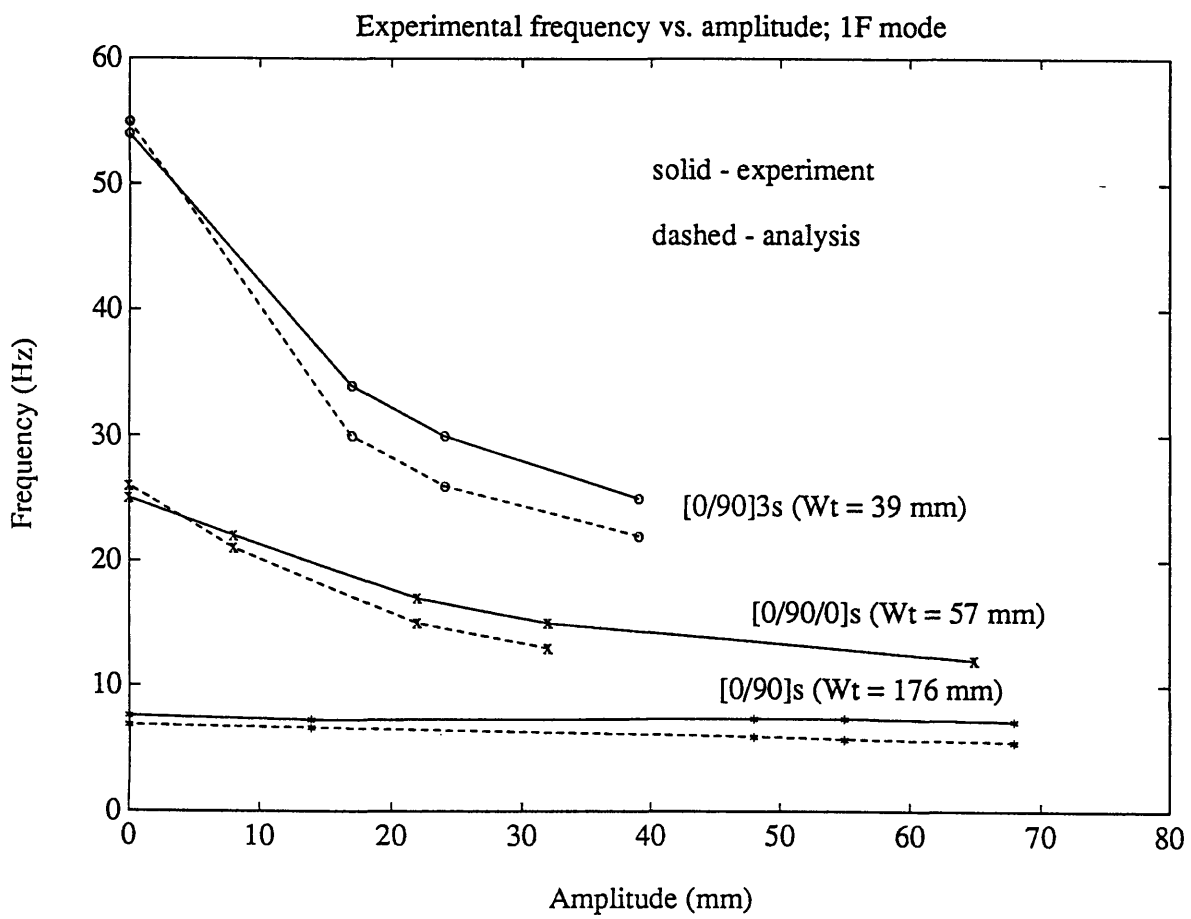

Figure 8.7: Experimental frequency vs. amplitude; Fore-and-aft modes

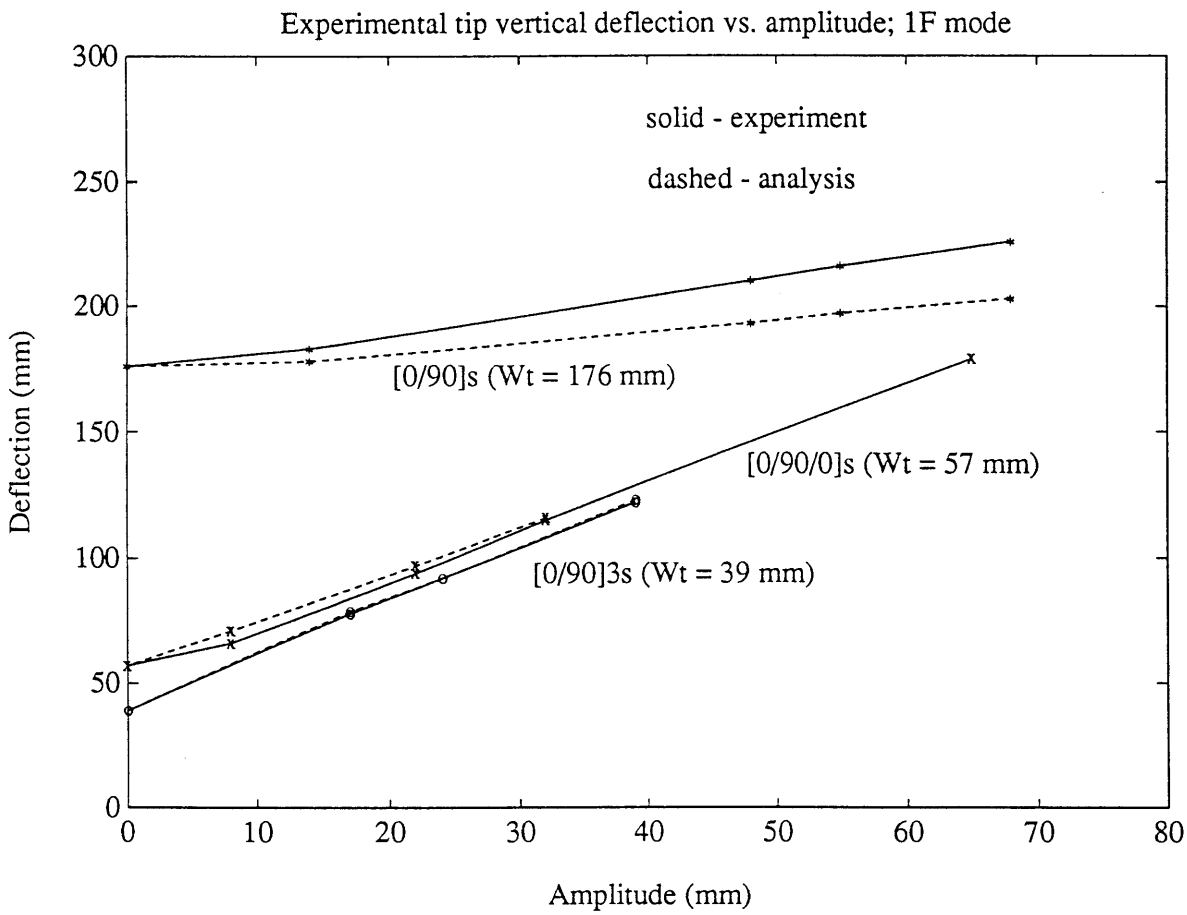

Figure 8.8: Experimental tip average deflection vs. amplitude; Fore-and-aft modes

Chapter 9

Results of Large Amplitude Aeroelastic Limit Cycles

9.1 Hingeless Blade Examples

The proposed solution techniques in section 6.4, 6.5, 6.6 have been employed to explore the nonlinear large amplitude aeroelastic behavior of hingeless rotor blades. To be continuous and consistent with the previous results, two of the blade examples chosen were $[0/90]_{3s}$ and $[45/0]_s$ graphite/epoxy laminates (560 mm in span, 30 mm in chord). The nonrotating characteristics of these lay-ups have been well investigated in the previous two chapters. For simplicity, the blades were assumed to be two-blade models with zero preconing angle and zero hinge-offset. These blades exhibit typical rotating lag and torsional frequencies ranging from 4 to 6 and from 7 to 10 per rev. respectively, therefore can be categorized as so called hard-inplane blades (blades whose rotating lag frequencies are higher than one per rev.). As before, the warping and transverse shear were not included in all of the calculations. A total of only 8 node points were used along the blades to save computing time. Occasionally, convergence was checked by using 16 node points instead. All the runs were made on an IBM RSAIX 6000 computer with typical number of iterations from 10 to 20 for convergence. With the speed of the IBM computer, each iteration took less than a few seconds of CPU time.

In order to appreciate the individual effects of the nonlinear structure and aero-

dynamic stall as fully as possible, three different modeling philosophies have been embedded in the programming. They are, (a) the full analysis employing all the nonlinearities (designated as $NS + NA$), (b) an analysis combining linearized structure (linearized about static position with the large amplitude structural effects eliminated) and the dynamic stall (designated as $S + NA$), (c) an analysis combining the nonlinear structure and the linear aerodynamics excluding the stall effects (designated as $NS + A$). Note that the analysis (b) still retains full structural nonlinearities in the static terms. This analysis is equivalent to eliminating all the higher order dynamic terms in the series expansions of the transformation matrix given in the Appendix A. Thus, according to the analysis, the structure will behave as if the amplitudes were very small, but its static position can be arbitrarily large commensurate with the static outputs of the aerodynamics which contains the nonlinear stall effects. On the contrary, in the analysis (c), there are no stall effects both statically and dynamically, and the aerodynamic part will behave as if the amplitudes were small. Although these different combinations can not separate influences of the nonlinear structure from the nonlinear aerodynamics completely (principle of superposition can not be applied in nonlinear problems), they should nevertheless reveal relative importance of the two different kinds of nonlinearities.

A typical search for a limit cycle solution includes all of the aeroelastic analyses mentioned in chapter 6 and proceeds as follows. First, given a root pitch angle and a rotational speed, a static deformation of the blade is obtained. The rotational speed is initially given a low value and then later increased in a sweeping fashion. Second, for the static solution just obtained, the linearized equations of motion are used to look for a linear flutter solution using the transfer matrix method described in section 6.5. If no flutter is found, then a higher value is assigned for the rotational speed and a new static position is calculated about which a new flutter investigation is performed. These steps are repeated as many times as required until the flutter solution is obtained. Lastly, once a flutter point is found, the nonlinear large amplitude solutions

that evolve from the linear flutter solution, are sought by means described in section 6.6 using the eigen mode solution from the linear analysis as an initial guess. Usually, any part of tip amplitudes can be fixed at the blade tip, but the torsional amplitude was fixed in all of the current calculations, i.e., θ_{ts} =given, $\theta_{tc} = 0$ at the tip.

The first of the blade models, the $[0/90]_{3s}$ laminate, is illustrated in Figure 9.1 through 9.23. The first group of these figures, Figure 9.1 through 9.5, contain the following information corresponding to three different root pitch angles, 3, 6, and 8 degrees within each plot: (a) the variation of tip torsional amplitude θ_{ts} (with θ_{tc} set equal to zero) with rotational speed Ω; (b) the variation of flutter frequency with Ω; (c) the variation of time-averaged midchord tip deflection z_{t0} with Ω; (d) the variation of time-averaged total tip angle θ_{t0} with Ω; (e) the variation of time-averaged total thrust level with Ω. Also shown in (c), (d), (e) as dashed lines are static curves when no flutter limit cycles are present. Thus, all of the limit cycle results start at linear flutter points where dashed and solid curves meet, and the analysis continues with each increasing torsion amplitude level. The next group of figures, Figure 9.6 through 9.11 show the flutter mode shapes represented in their $\sin \omega t$ and $\cos \omega t$ parts at two extreme amplitude levels. All of these first two groups of figures were obtained by the fully nonlinear analysis combining both nonlinear structure and nonlinear aerodynamics. After these figures, the final group, Figure 9.12 through 9.23 contain the above information (a), (c), (d), and (e) again, but this time for the three different analyses described above ($NS + NA$, $S + NA$, $NS + A$) with solid line, circle marks, and x marks, respectively.

Referring to the first group of figures, Figure 9.1 through 9.5, the first case with 3 degrees of root pitch is initially in the unstalled region (average angle of attack at the tip, α_{t0} is about 3.5°) beginning at 15.03 Hz of rotational speed, and then enters into the stall region at approximately 5 degrees of the tip torsional amplitude. This is indicated by the sharp turn at $\theta_{ts} = 5^o$ after a straight vertical branch in the amplitude vs. Ω plot, and initial sharp decreases in the corresponding average tip deflection, tip

angle, and the thrust level. Along this vertical branch, the aerodynamics is essentially unchanged as given by Greenberg's theorem, and the structure doesn't seem to show any significant large amplitude effects. Also, the average tip deformations do not change much from their values at the onset of flutter. The sharp turn at the beginning of dynamic stall could be termed as "hardening', i.e., increase in rotational speed will result in increase in the amplitude. The sudden drops in the average deformations at the start of this hardening, are caused by loss of static lift and moment associated with the initiation of dynamic stall. It is mentioned that the average tip angle of attack was always within the linear region for the entire range of amplitudes investigated. Therefore, the loss in the static aerodynamic loads is a result of unsteady angle of attack whose average value is well below stall angle but peak value enters into the stalled region, thus smearing the dynamic stall effects over one cycle. Once the stall occurs, however, beginning at about $\theta_{ts} = 12^0$, the time averaged deformations and the thrust seem to increase continuously even though the thrust eventually drops at higher amplitudes. Next cases with 6 and 8 degrees of root pitch are initially in stalled region ($\alpha_{t0} = 8.1^o, 8.4^o$, respectively), and hence an outboard blade portion near the tip is stalled statically before flutter begins. Here, the flutter starts at rotational speeds of 13.56 Hz and 11.11 Hz, respectively, indicating that statically stalled blade has flutter speed lower than unstalled one. This is attributed to destabilizing effects of the unsteady aerodynamic coefficients for small amplitude motion about a stalled angle of attack. This, however, would not be true if the amplitude were substantially large as will be seen later. As seen from the Figure 9.1, both softening and hardening trends could occur in the amplitude vs. critical speed characteristics depending on root pitch and amplitude level. In particular, as mentioned above, there is strong hardening at low root pitch (3°) and high root pitch (8°) in the amplitude region after the blade stalls. There seems to be initial hardening for 6° root pitch case also, but it soon disappears as soon as the amplitude starts to increase. At moderate amplitude levels, the softening trend occurs in all three cases, but at even higher amplitude

levels, the hardening is seen to recover. However, in view of the discussion given in section 5.3 regarding aerodynamic hysteresis generated by the ONERA Model, all the results at high amplitude levels may have to be accepted with caution. Accordingly, any asymptotic aeroelastic behavior found in high amplitude range might be viewed as a breakdown of the ONERA Model, rather than as a result. The flutter frequencies for all three cases, initially increase with amplitude, but eventually drops with further increase in the amplitude. This is consistent with the hardening-softening trends in Figure 9.1, and also with the findings in Figure 9.3, 9.4 that the tip average deflection initially drops but picks up later at higher amplitude levels. The question regarding how much of the nonlinearities, i.e., the hardening or softening, is due to structure and dynamic stall has to be postponed until the results from the $NS + NA$, $S + NA$, and $NS + A$ analyses are fully discussed.

Figure 9.6 through 9.11 show flutter mode shapes at two extreme tip torsional amplitudes, one at very small, the other at very large level. Whether stalled or not, most of the flutter modes, except at low amplitude for 3° root pitch, have strong couplings between all fundamental modes, i.e., torsion, lag, and flap bending. In particular, the coupling between torsion and lag, and its vibration frequencies suggest proximity of the flutter mode shape to the first fore-and-aft (lag) mode shape whose large amplitude characteristics were investigated in the previous chapter. At this point, it is recalled that when tip amplitude increases above a certain level in the presence of moderate amount of static tip deflection, the lag mode could undergo a significant increase in its average tip deflection z_{t0} and a decrease in its frequency. It is interesting to see that the 3 degrees root pitch case initially does not contain much motion in the lag direction (Figure 9.6), but later on picks up much component in y_s (Figure 9.7). This phenomenon should be the source of the dramatic aeroelastic softening in the moderate range of amplitudes found in Figure 9.1. Also, the bending motion z_s and z_c components in all of the mode shapes for the entire range of amplitudes are the second bending modes.

The final group, figures 9.12 through 9.23 show the relative effects of the structural nonlinearity and the aerodynamic nonlinearity upon the flutter characteristics of the blade. At 6 and 8 degrees of root pitch where the blade was initially stalled, the linear aerodynamics with Greenberg's theorems (x marks) overpredicts the onset of flutter, yielding higher critical Ω than the nonlinear aerodynamics would predict. Thus, all of the tip static deformations as well as static thrust level predicted by the linear aerodynamics alone extend well beyond the points of flutter onset predicted by the dynamic stall theorem. At any rate, it appears that the initial hardening phenomenon which are found in all of the three root pitch cases is mainly attributed to the aerodynamic part; here, the linearized structure with dynamic stall seems accurate enough to capture the hardening effect whereas the linear aerodynamics completely misses it. This initial hardening is mainly due to increases in "effective" aerodynamic damping coefficients in both the plunging and pitching motion, associated with the lift and moment hysteresis loops at high amplitude levels. In other words, contrary to the small amplitude motion around a statically stalled large angle of attack, the large amplitude motion that crosses between the unstalled and stalled regions generally yields increase in the overall aerodynamic damping as the amplitude increases, and, thereby results in stabilizing (hardening) effects. However, a part of this hardening could be a structural hardening which results from the drop in the tip deflection as a result of the stall initiation. The initial hardening trend becomes severe at high root pitch angles or when the blade is initially stalled. Compare $S + NA$ curves in Figure 9.16 and 9.20 with that of Figure 9.12.

As the amplitude level is increased further, the coupling between the static and dynamic parts of the structure emerges and the dynamic stall alone can not capture the opposite softening trend in the moderate to high amplitude region; curiously, the nonlinear structure with linear aerodynamic theory is able to predict this softening to a certain extent. At high root pitch angle or when the blade is initially stalled, the structural softening effect becomes more dominant and seems to pervade into the

low amplitude region. This can be seen in the flutter mode shapes, Figure 9.6, 9.8, and 9.10; the lag component y_s in Figure 9.8 and 9.10 is more prominent than that in Figure 9.6.

From the structural point of view, it is not surprising that the nonlinear structure with linear aerodynamics in the entire amplitude region merely yields softening results accompanied by centershift rises, due to the flutter mode being close to the first fore-and-aft mode shape of free vibration. On the other hand, the linearized structure with dynamic stall analysis seems to yield merely hardening results in most of amplitude range, and hardly regain z_{t0} once the stall starts as a result of lift and moment loss associated with the dynamic stall.

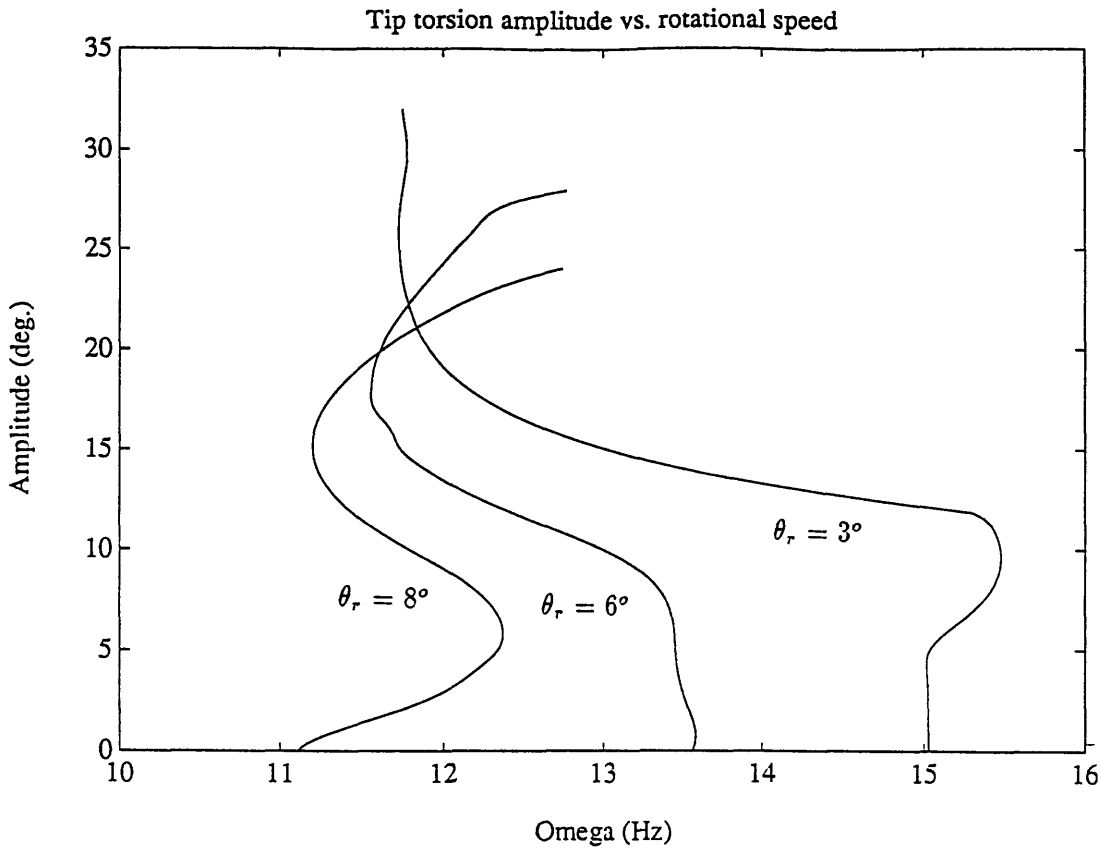

Figure 9.1: Torsional amplitude vs. rotational speed; $[0/90]_{3s}$, $\theta_r = 3, 6, 8$ deg.

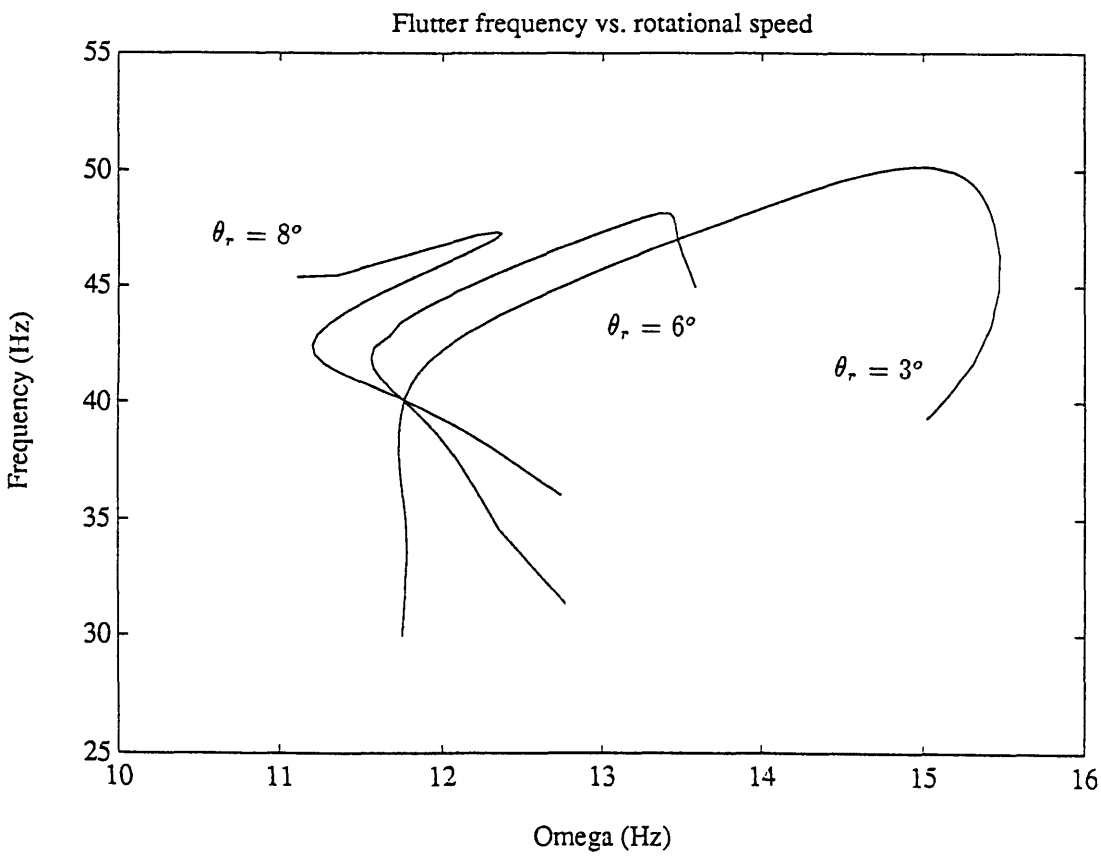

Figure 9.2: Flutter frequency vs. rotational speed; $[0/90]_{3s}$, $\theta_r = 3, 6, 8$ deg.

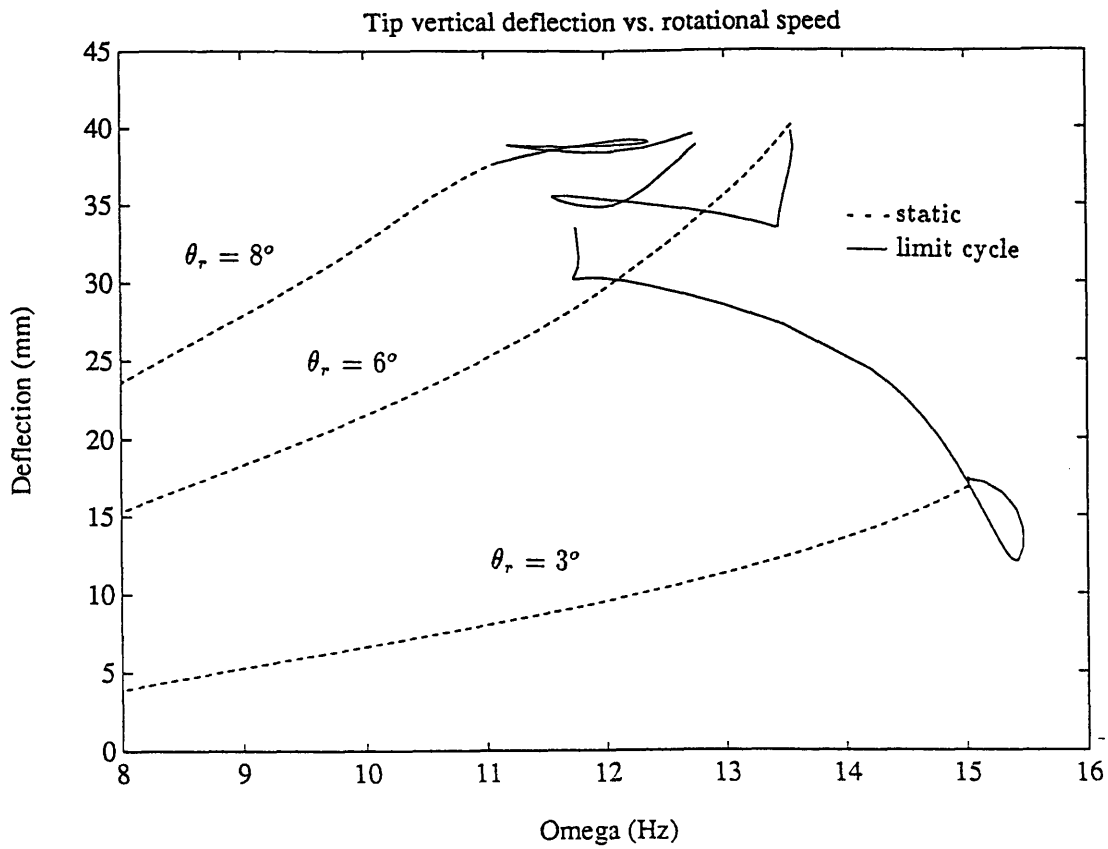

Figure 9.3: Tip average deflection vs. rotational speed; $[0/90]_{3s}$, $\theta_r = 3$, 6, 8 deg.

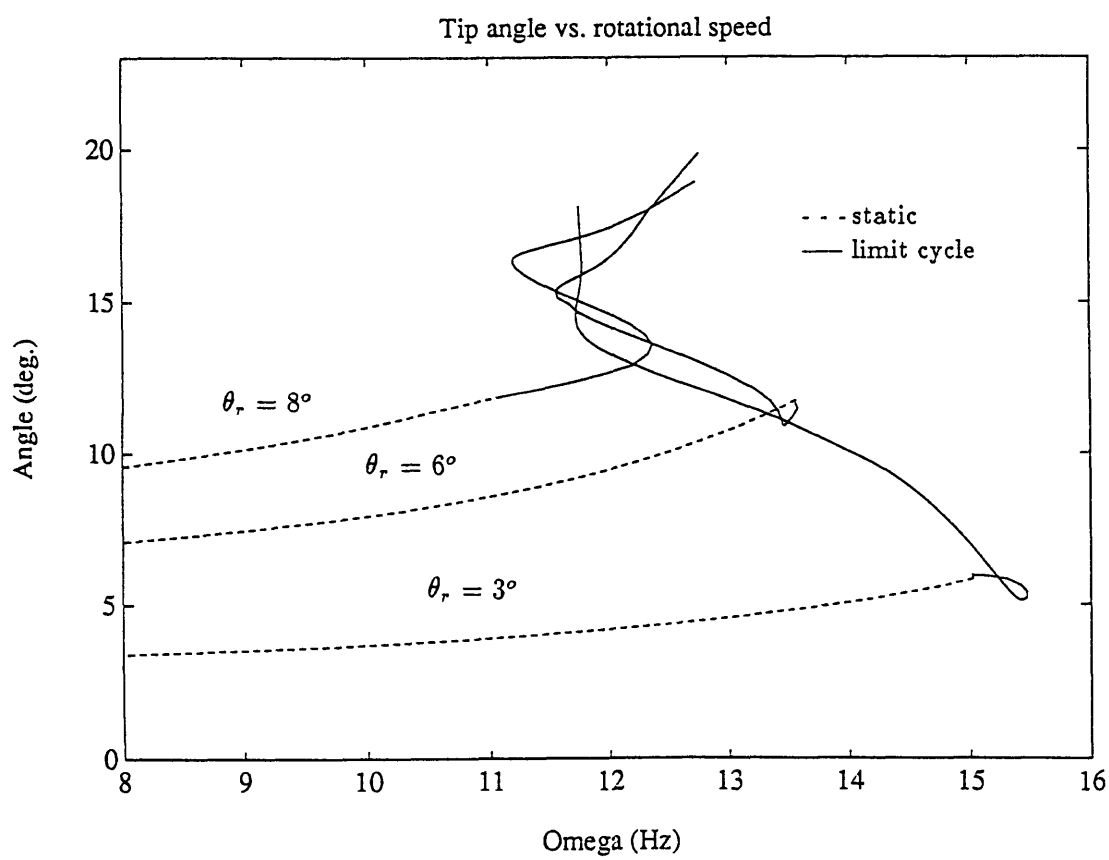

Figure 9.4: Tip average angle vs. rotational speed; $[0/90]_{3s}$, $\theta_r = 3$, 6, 8 deg.

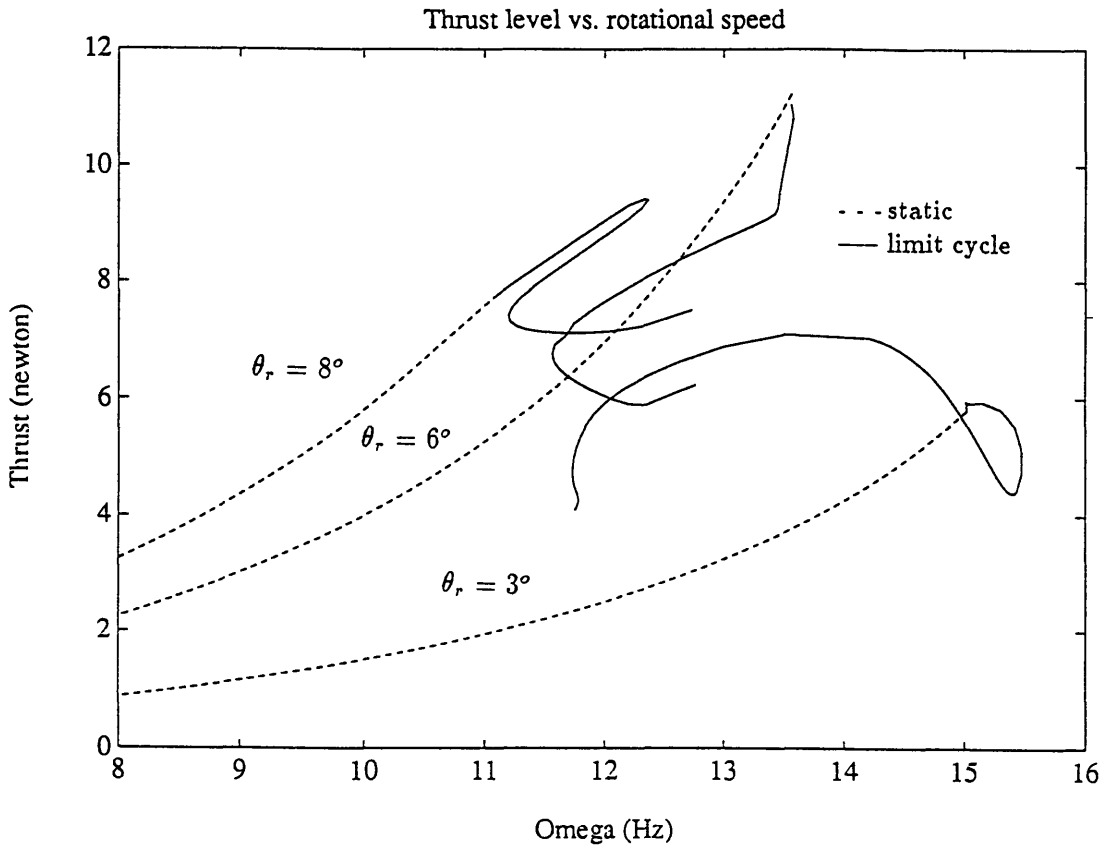

Figure 9.5: Average thrust level vs. rotational speed; $[0/90]_{3s}$, $\theta_r = 3$, 6, 8 deg.

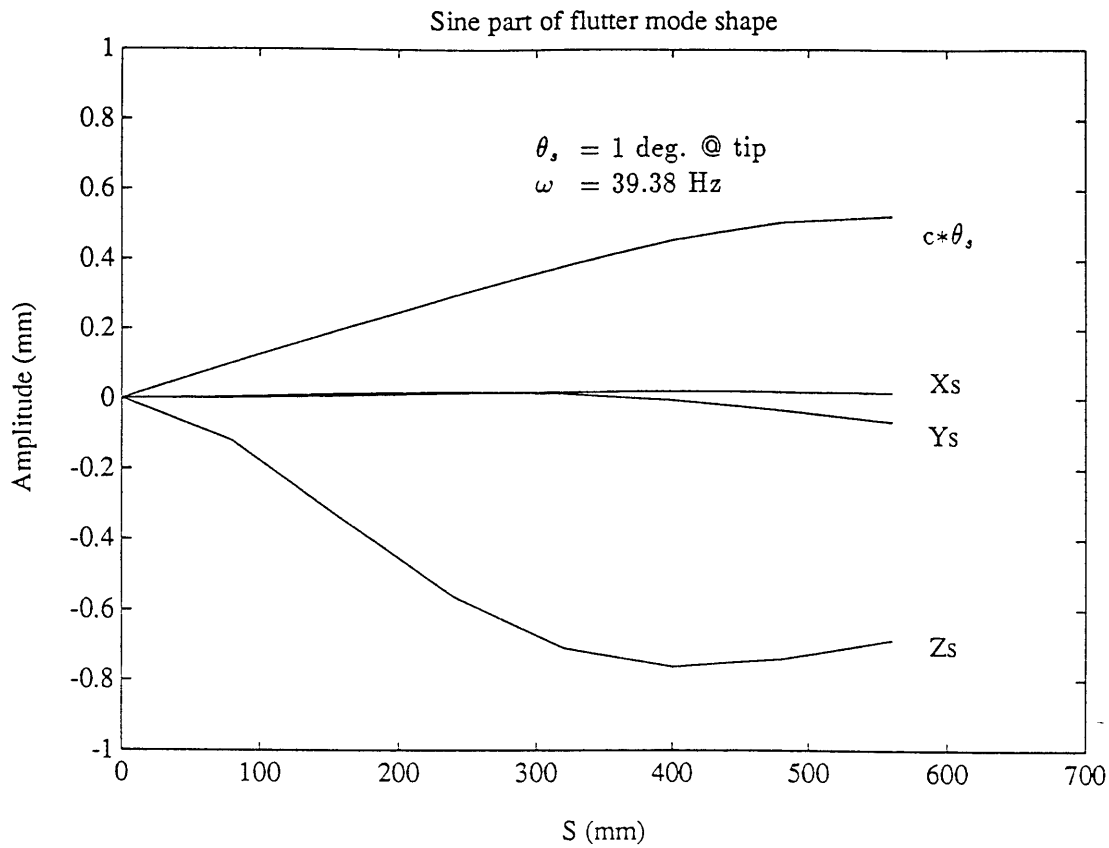

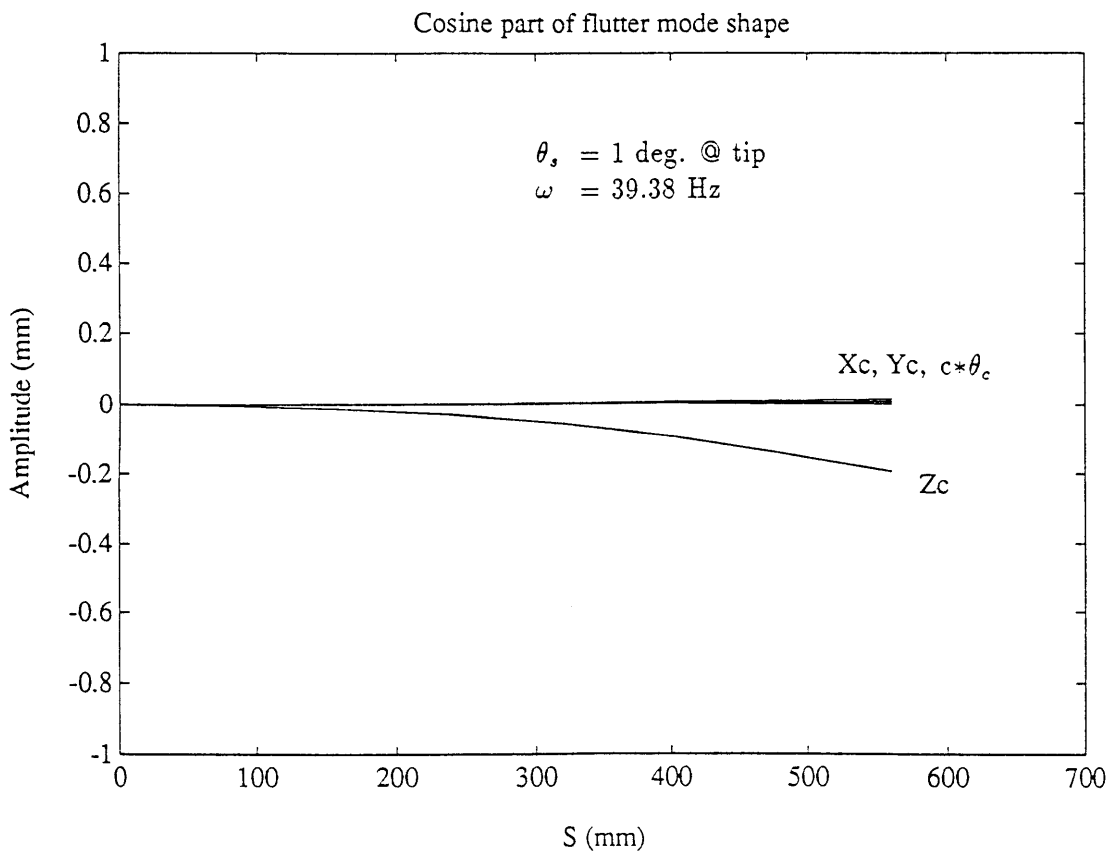

Figure 9.6: Flutter mode shape; $[0/90]_{3s}$, $\theta_r = 3$ deg., $\Omega = 15.03$ Hz

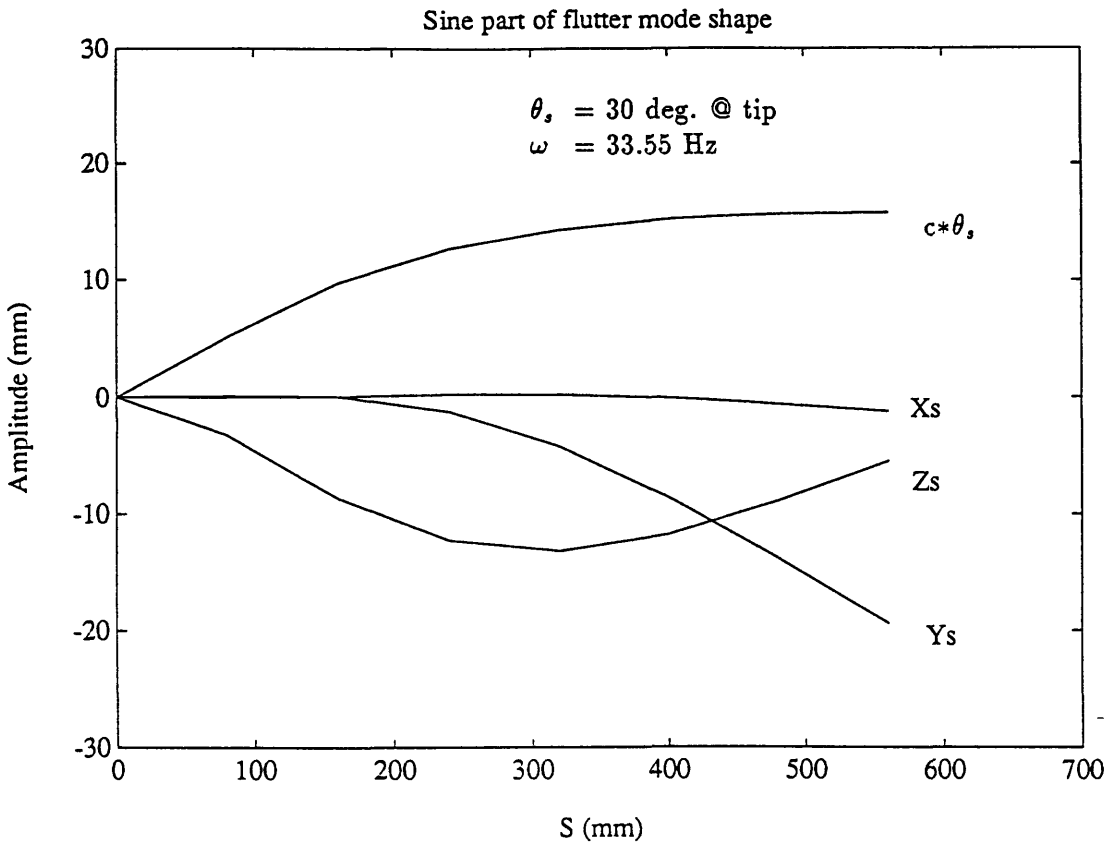

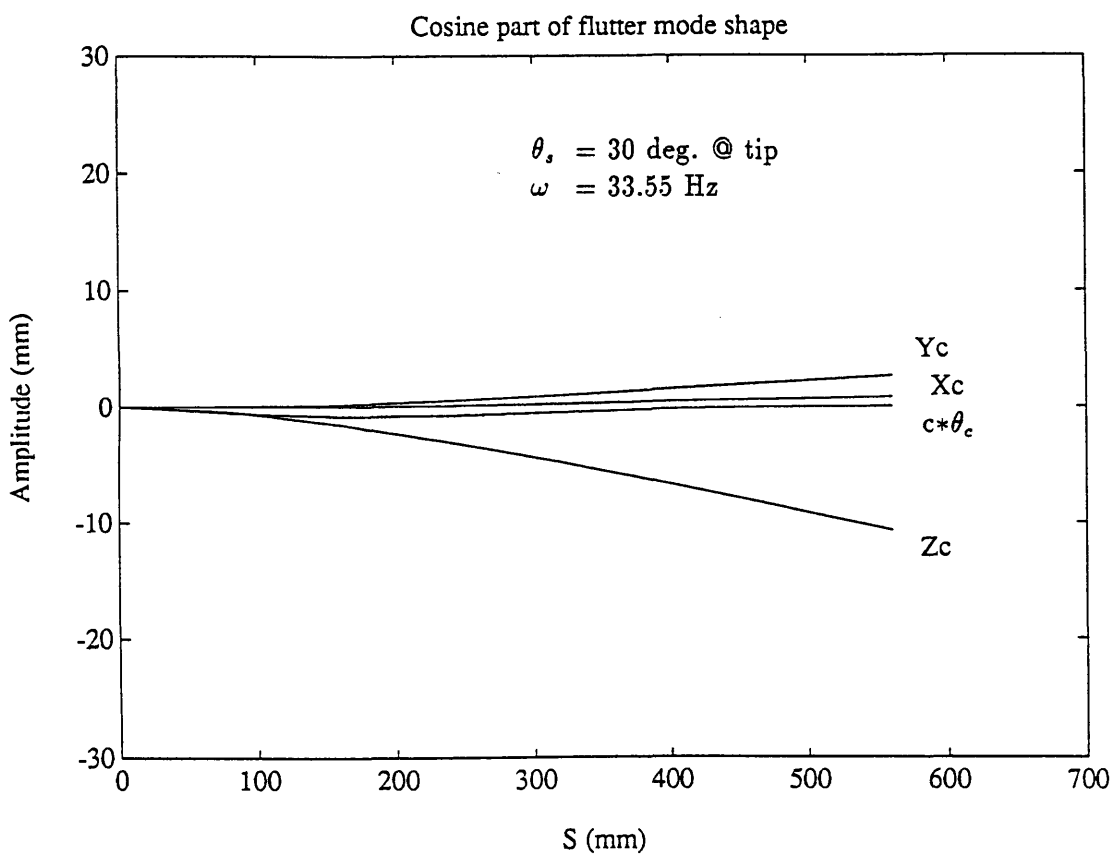

Figure 9.7: Flutter mode shape; $[0/90]_{3s}$, $\theta_r = 3$ deg., $\Omega = 11.78$ Hz

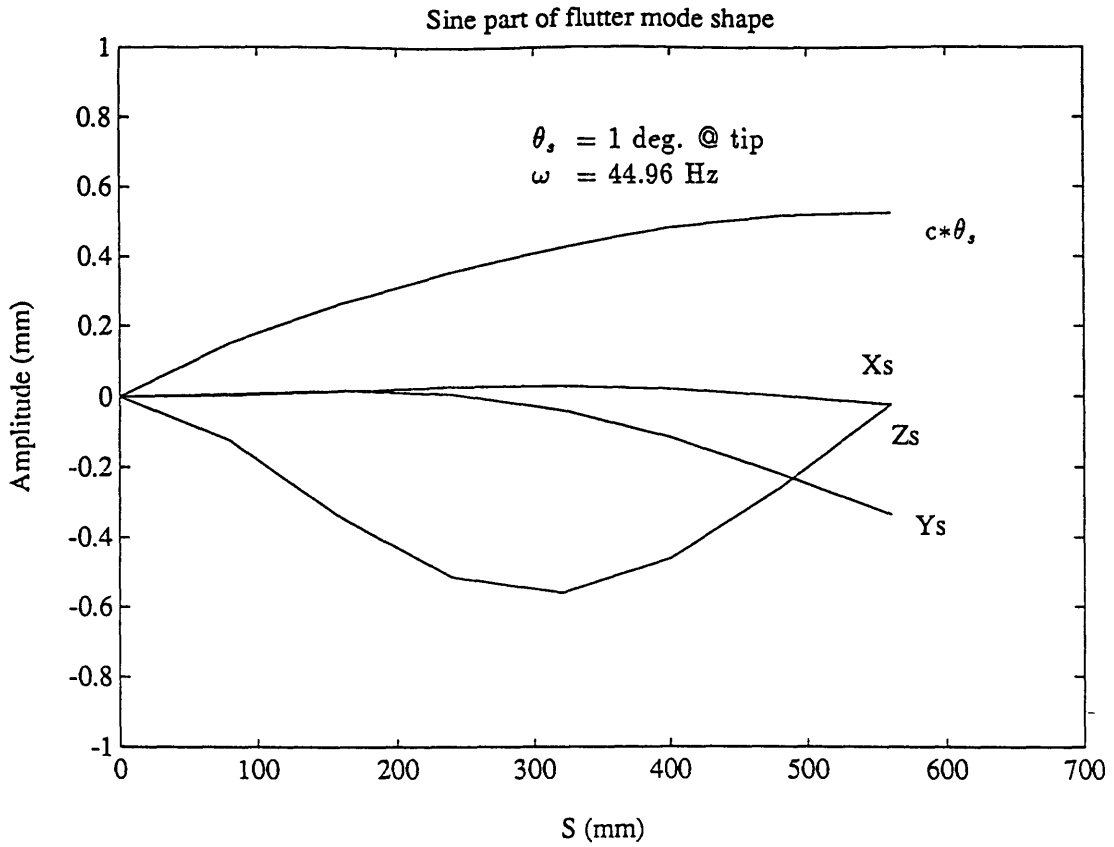

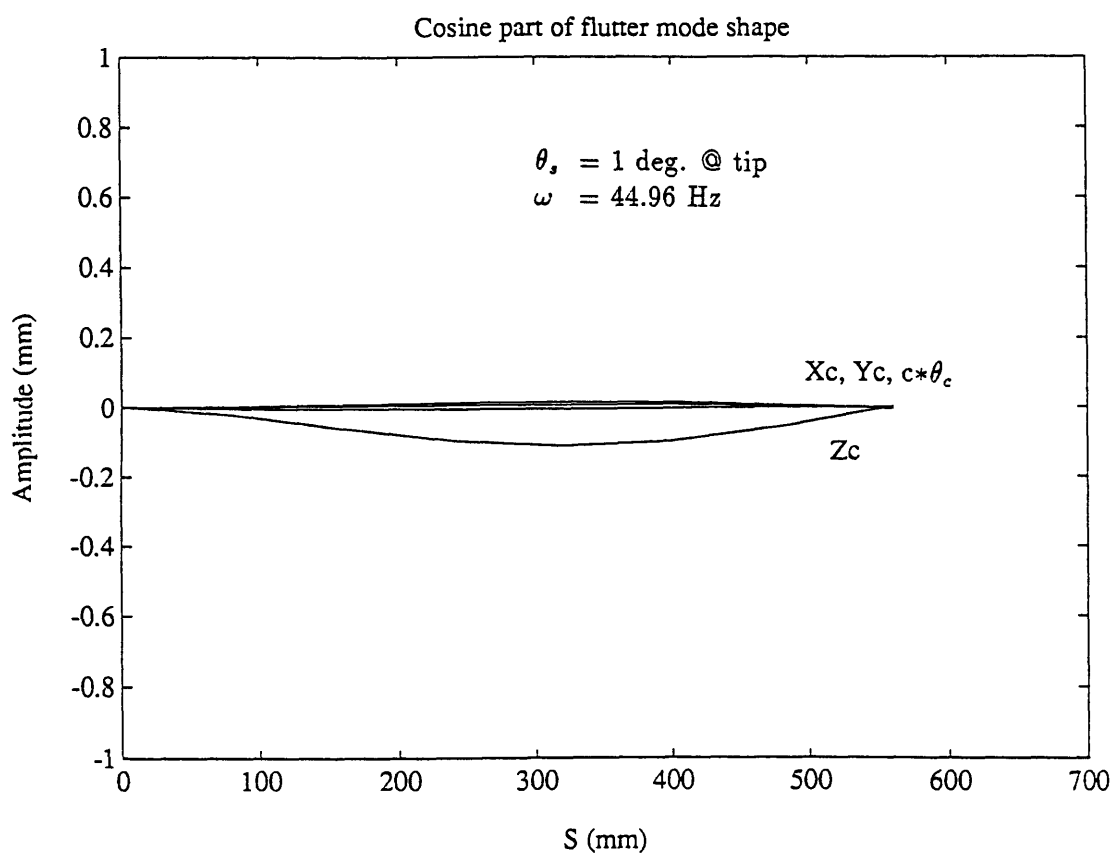

Figure 9.8: Flutter mode shape; $[0/90]_{3s}$, $\theta_r = 6$ deg., $\Omega = 13.56$ Hz

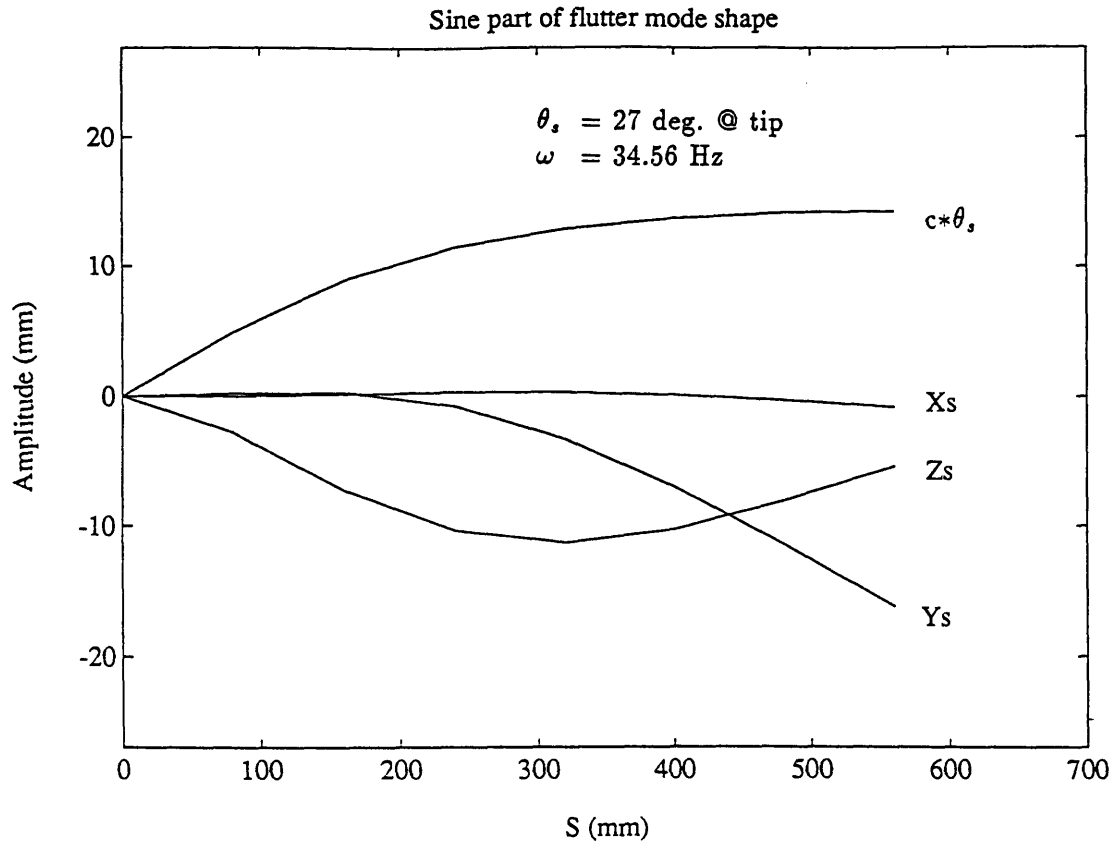

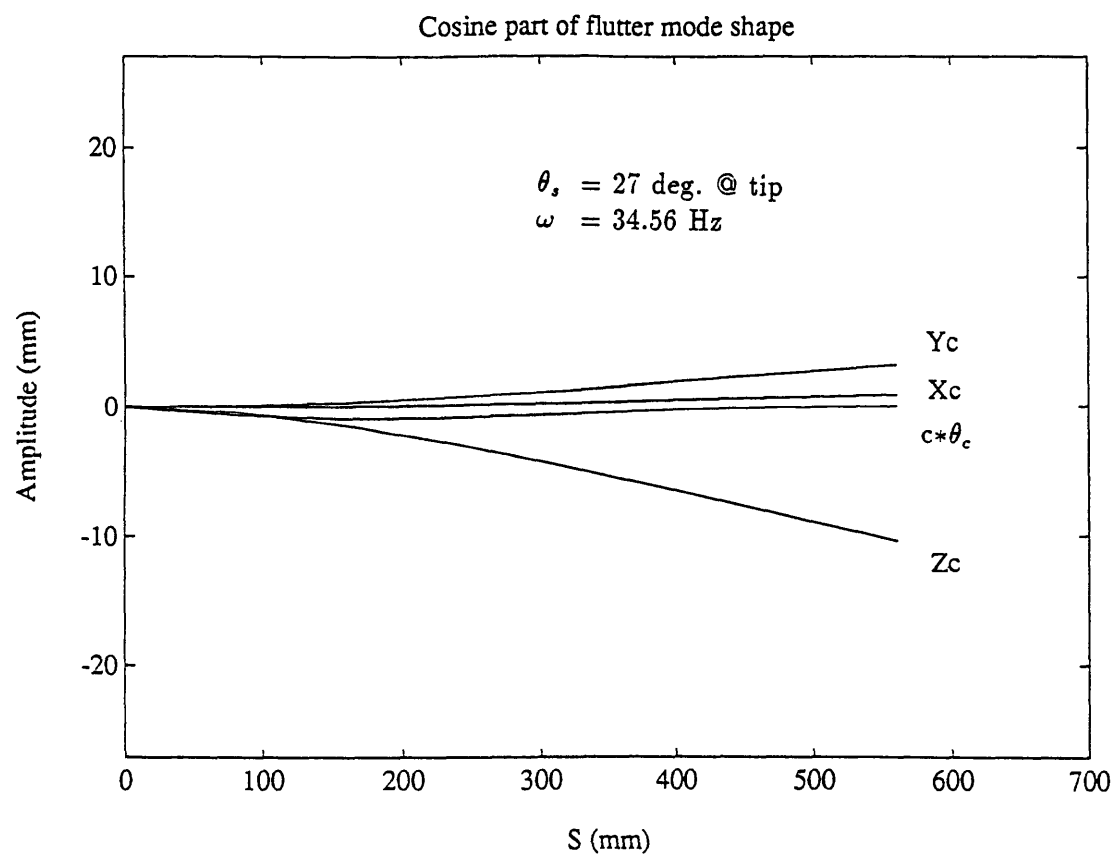

Figure 9.9: Flutter mode shape; $[0/90]_{3s}$, $\theta_r = 6$ deg., $\Omega = 12.35$ Hz

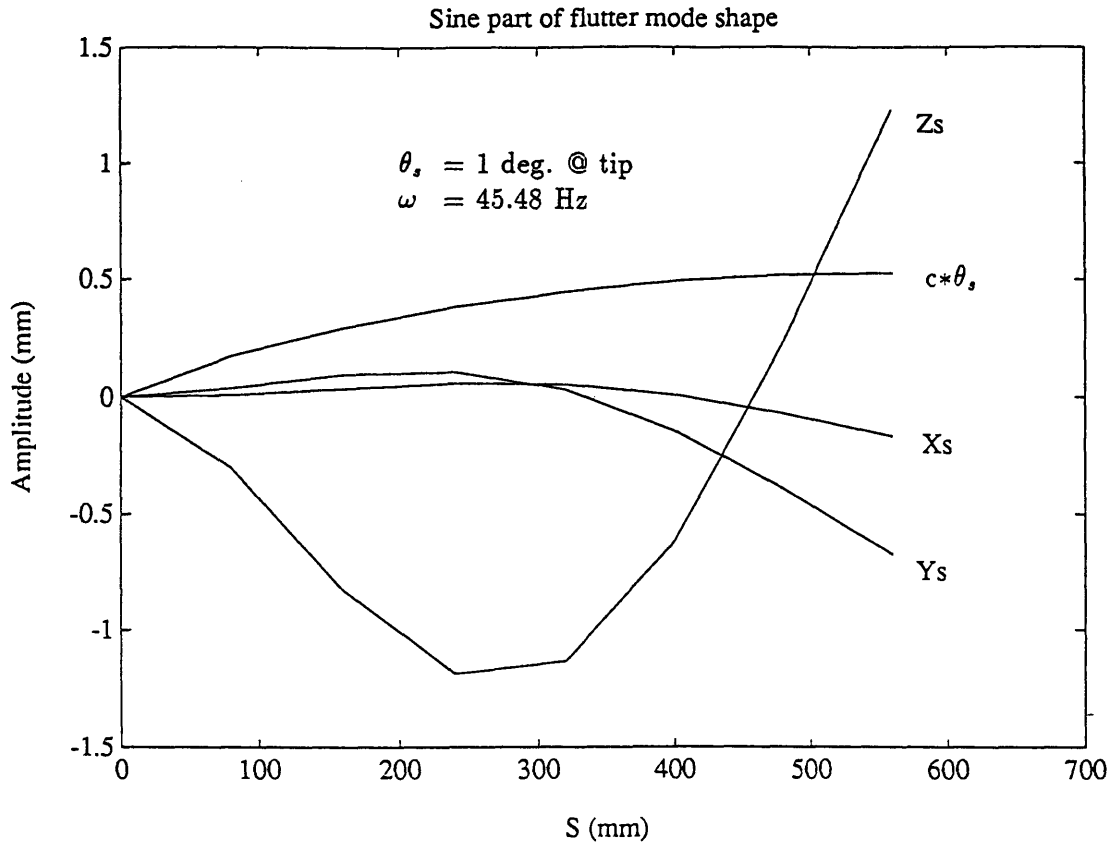

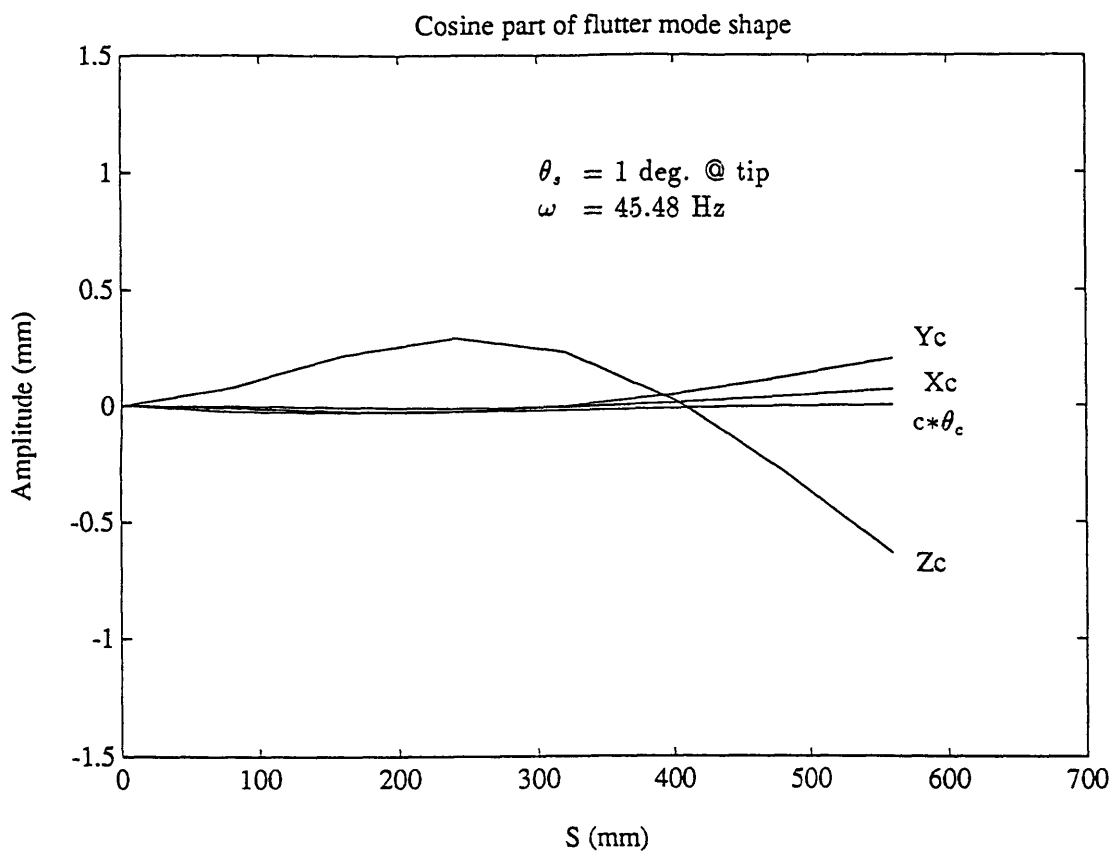

Figure 9.10: Flutter mode shape; $[0/90]_{3s}$, $\theta_r = 8$ deg., $\Omega = 11.11$ Hz

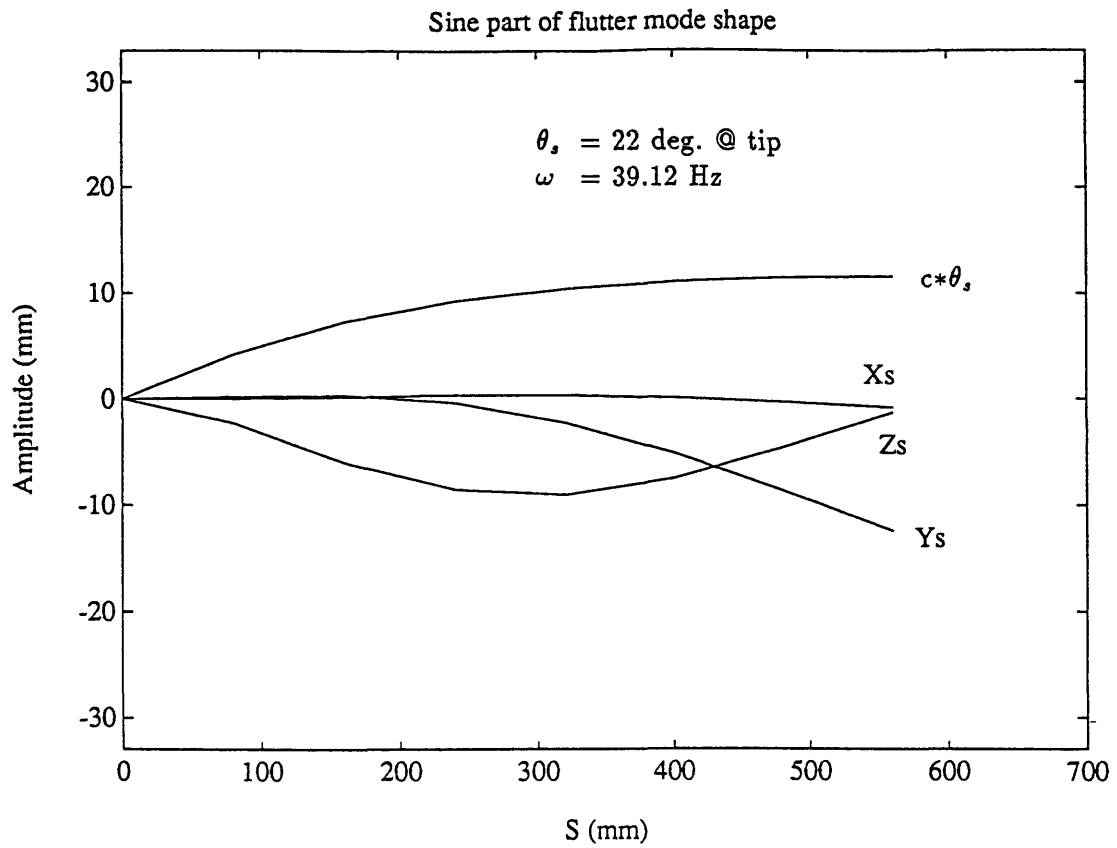

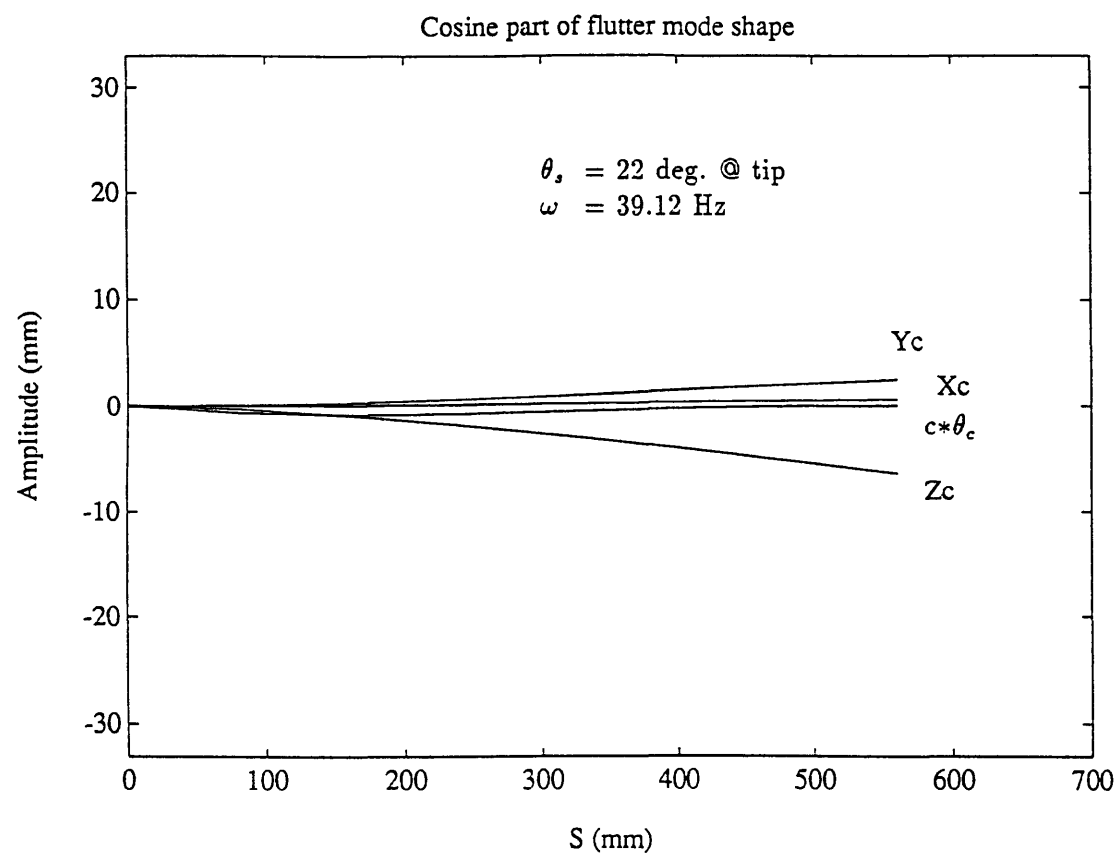

Figure 9.11: Flutter mode shape; $[0/90]_{3s}$, $\theta_r = 8$ deg., $\Omega = 12.04$ Hz

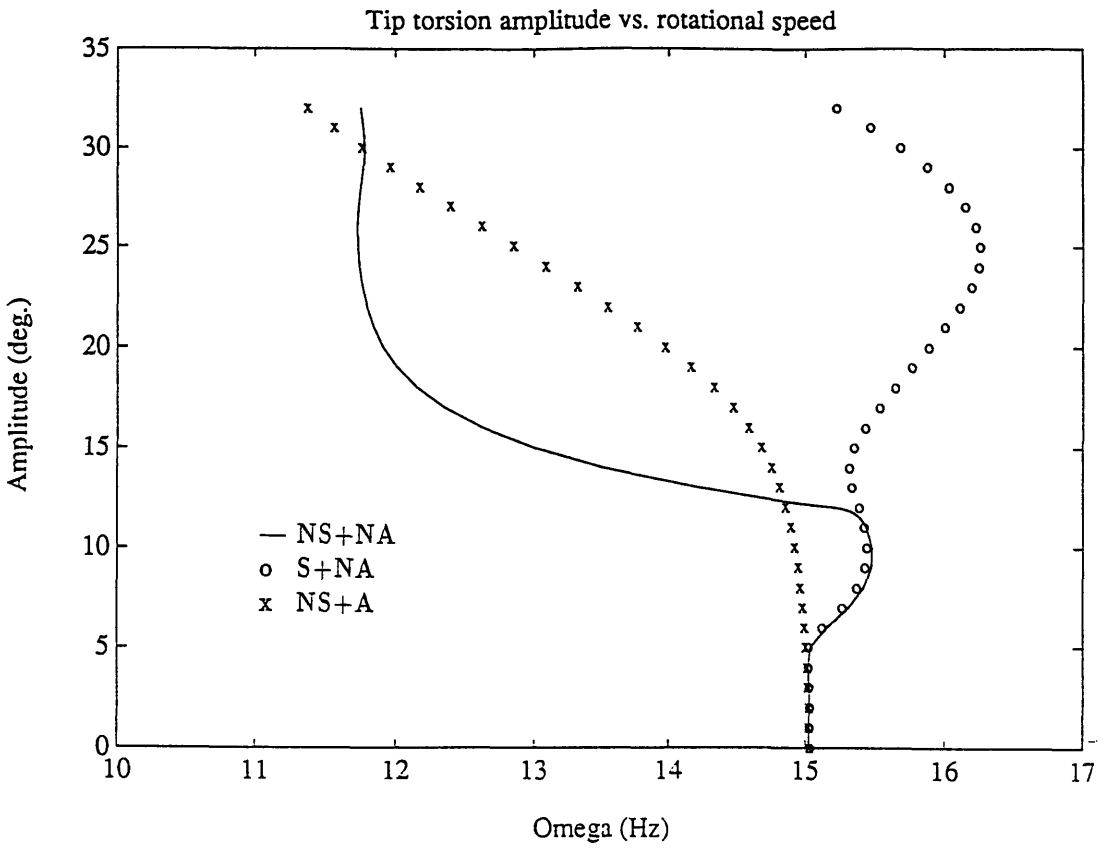

Figure 9.12: Torsional amplitude vs. rotational speed; $[0/90]_{3s}$, $\theta_r = 3$ deg.

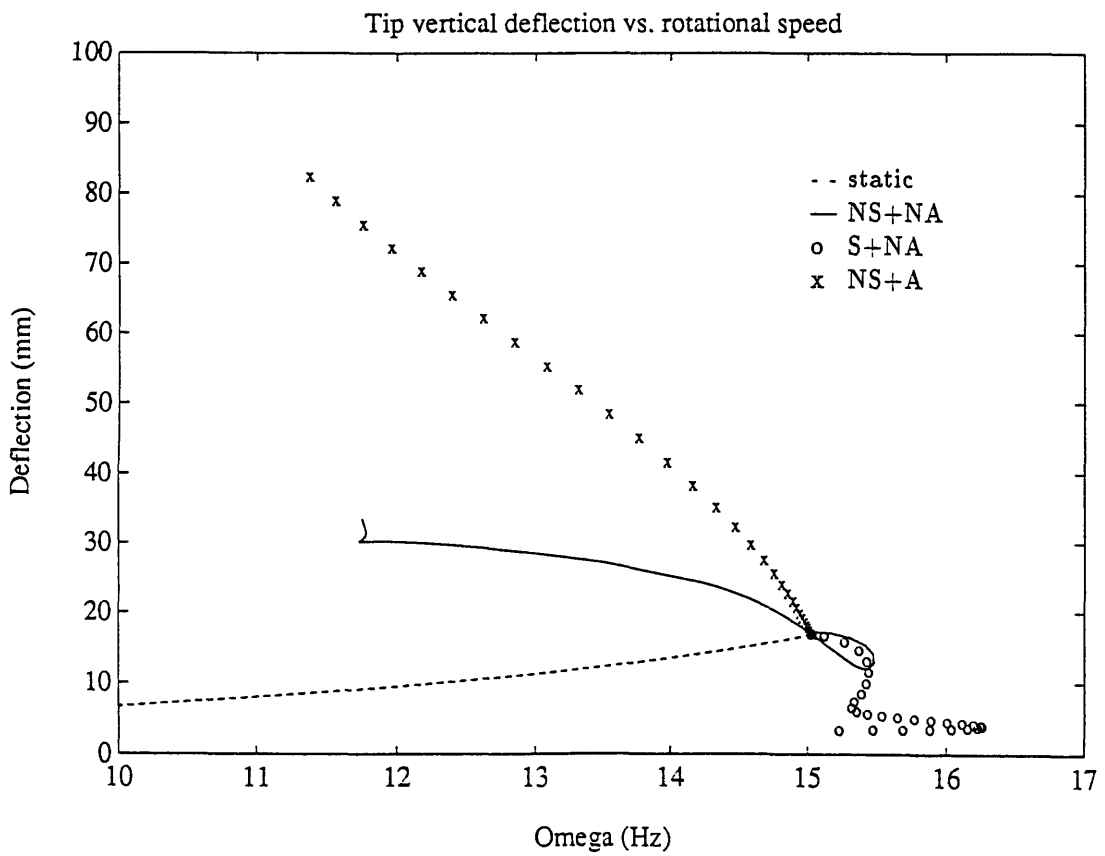

Figure 9.13: Tip average deflection vs. rotational speed; $[0/90]_{3s}$, $\theta_r = 3$ deg.

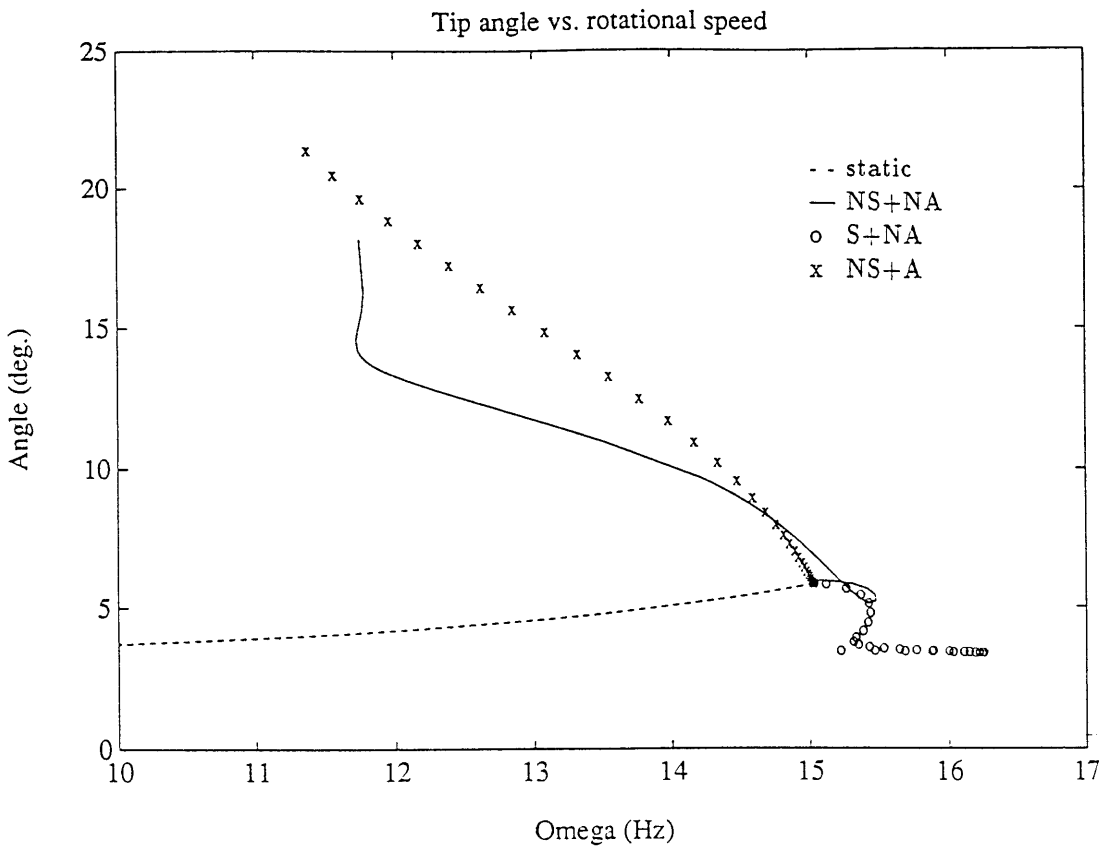

Figure 9.14: Tip average angle vs. rotational speed; $[0/90]_{3s}$, $\theta_r = 3$ deg.

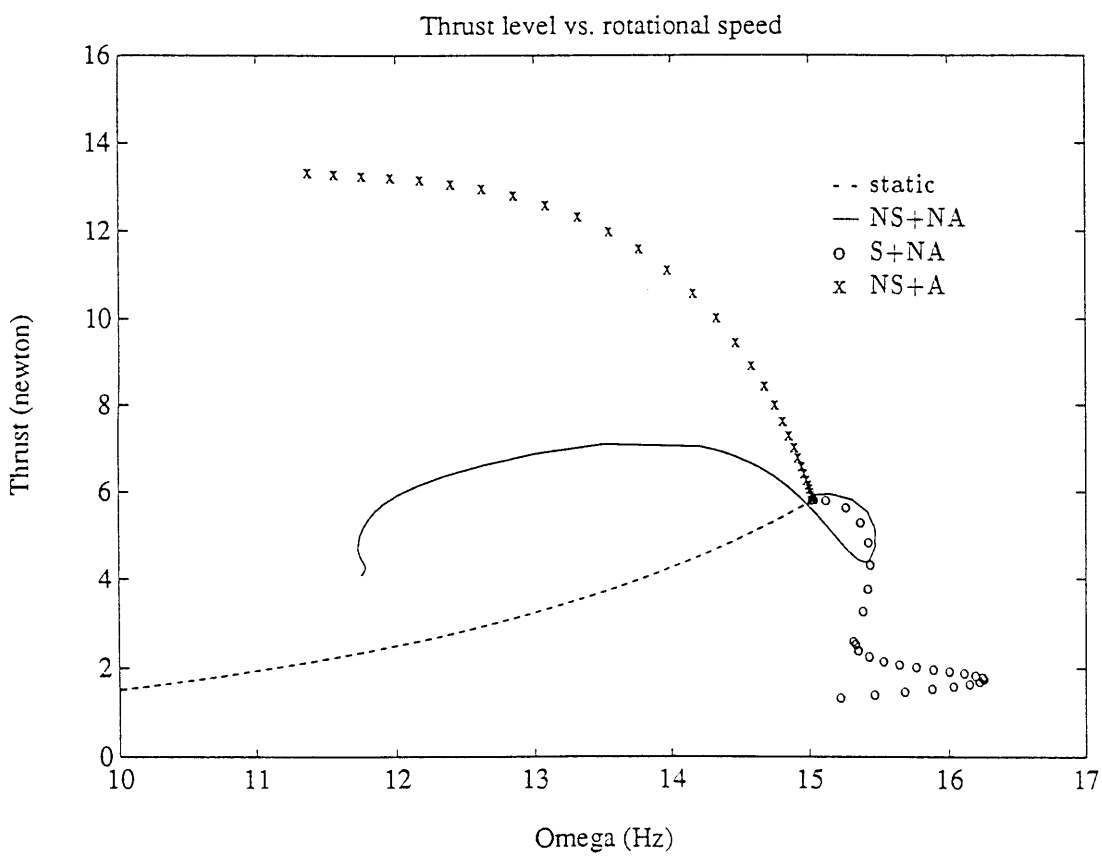

Figure 9.15: Average thrust level vs. rotational speed; $[0/90]_{3s}$, $\theta_r = 3$ deg.

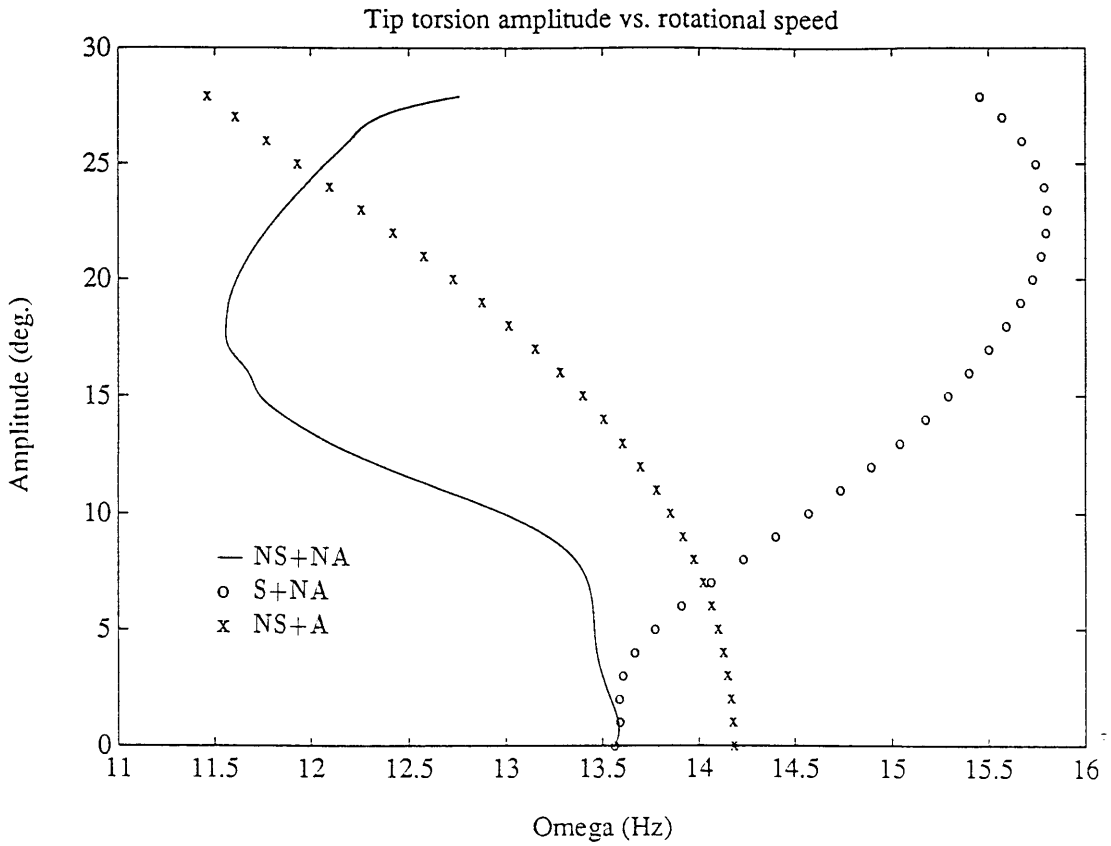

Figure 9.16: Torsional amplitude vs. rotational speed; $[0/90]_{3s}$, $\theta_r = 6$ deg.

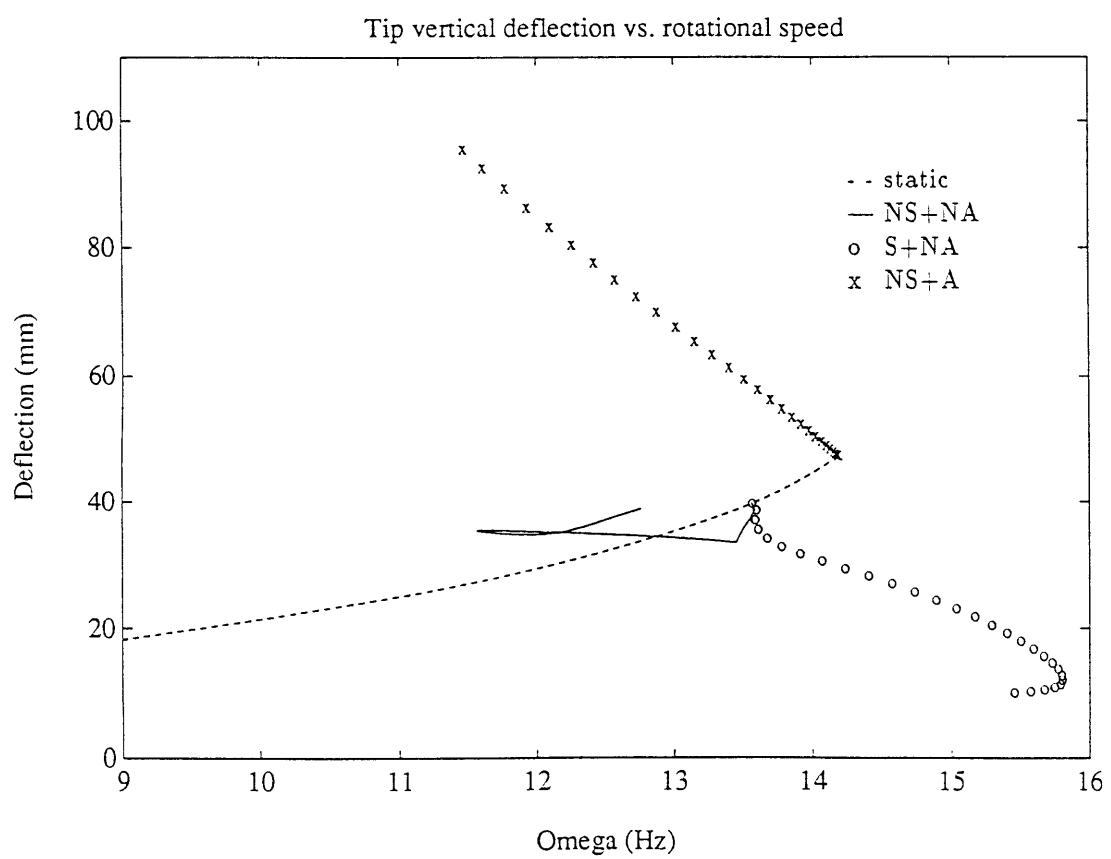

Figure 9.17: Tip average deflection vs. rotational speed; $[0/90]_{3s}$, $\theta_r = 6$ deg.

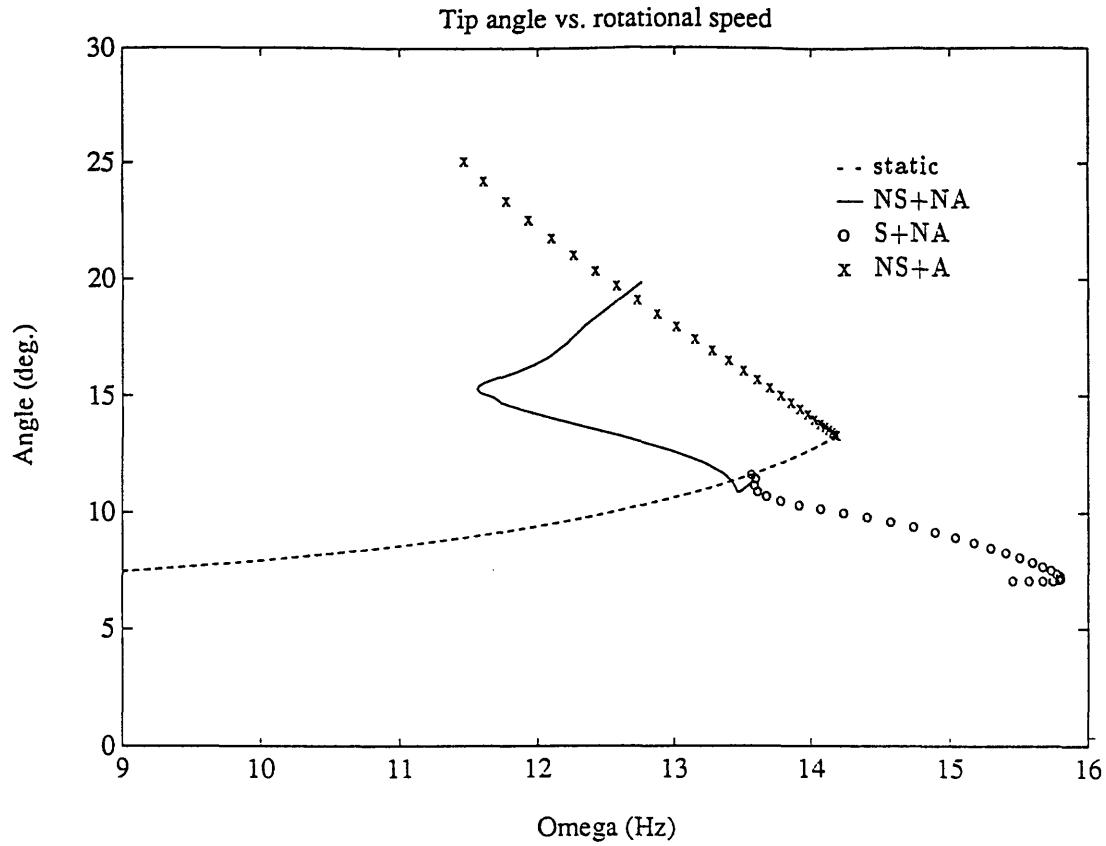

Figure 9.18: Tip average angle vs. rotational speed; $[0/90]_{3s}$, $\theta_r = 6$ deg.

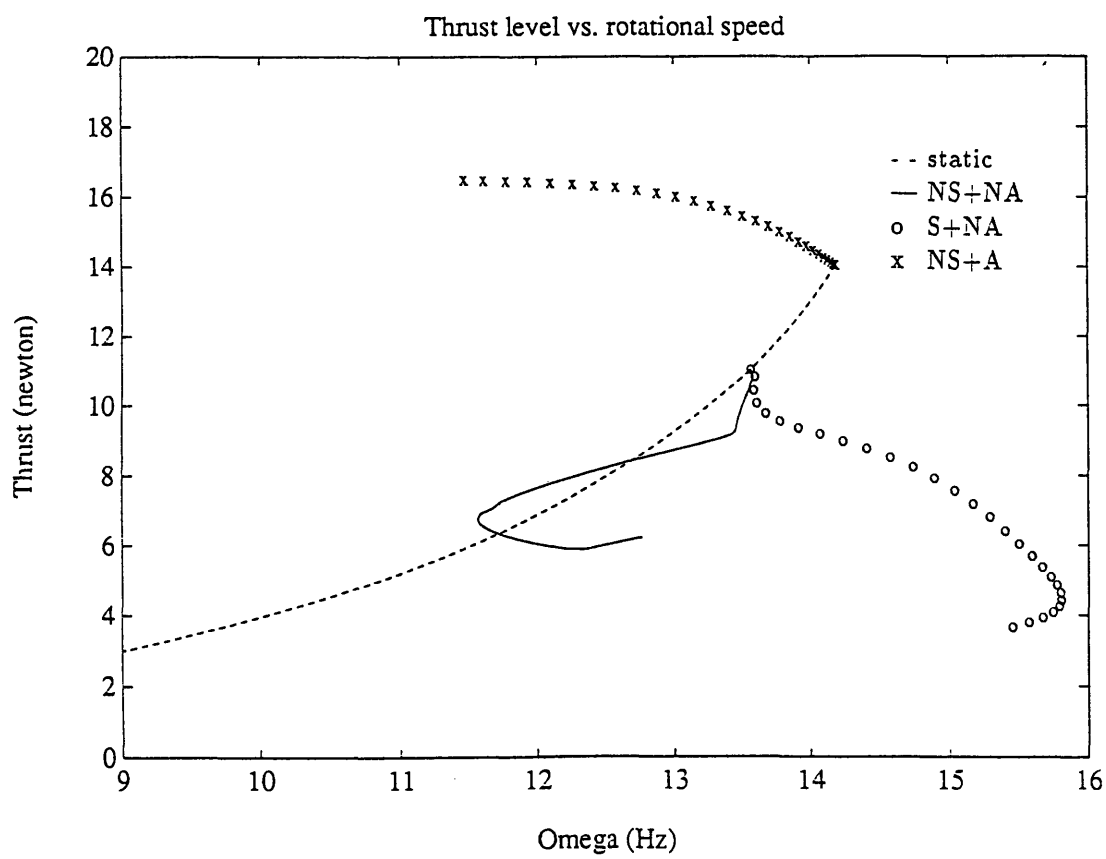

Figure 9.19: Average thrust level vs. rotational speed; $[0/90]_{3s}$, $\theta_r = 6$ deg.

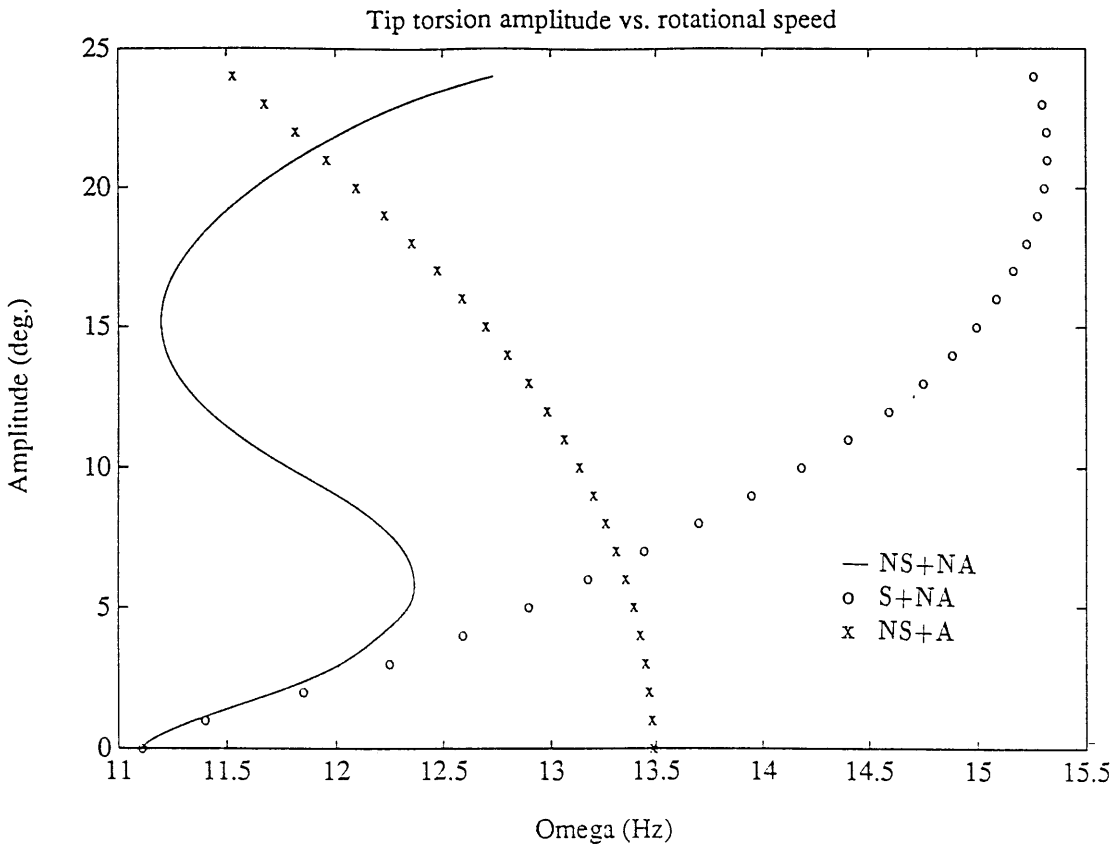

Figure 9.20: Torsional amplitude vs. rotational speed; $[0/90]_{3s}$, $\theta_r = 8$ deg.

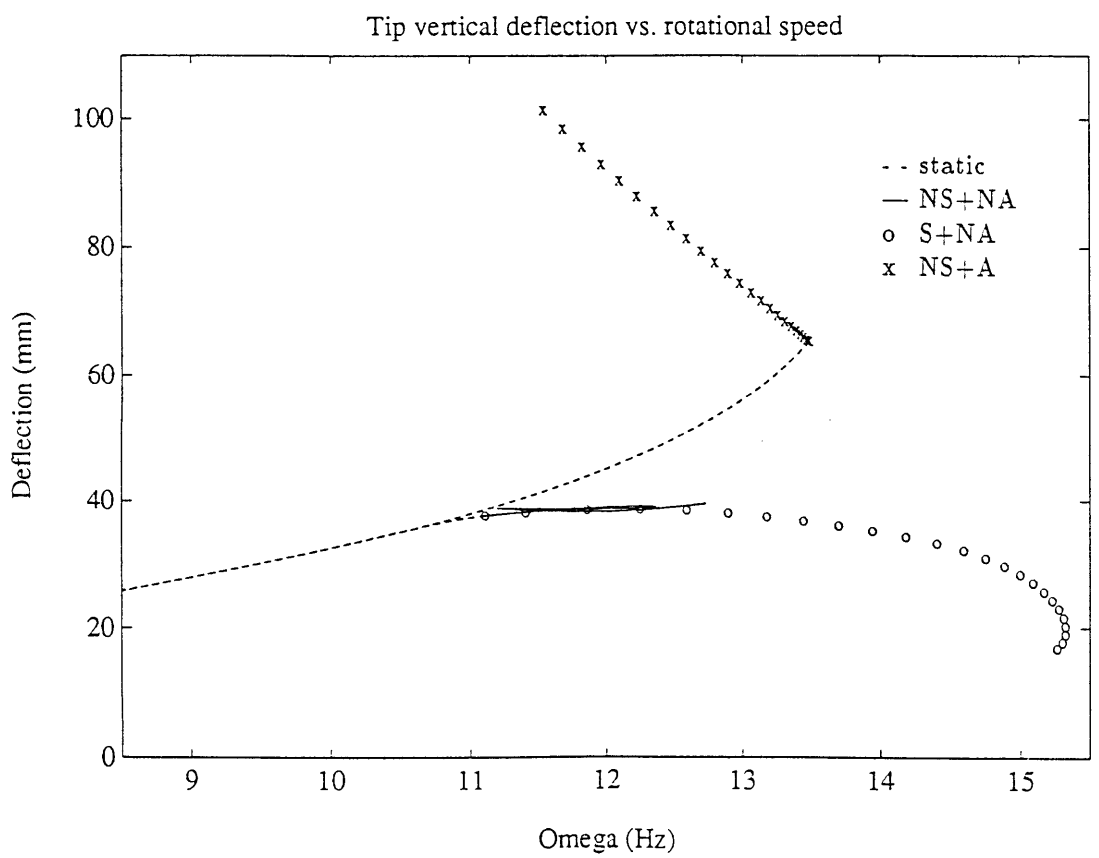

Figure 9.21: Tip average deflection vs. rotational speed; $[0/90]_{3s}$, $\theta_r = 8$ deg.

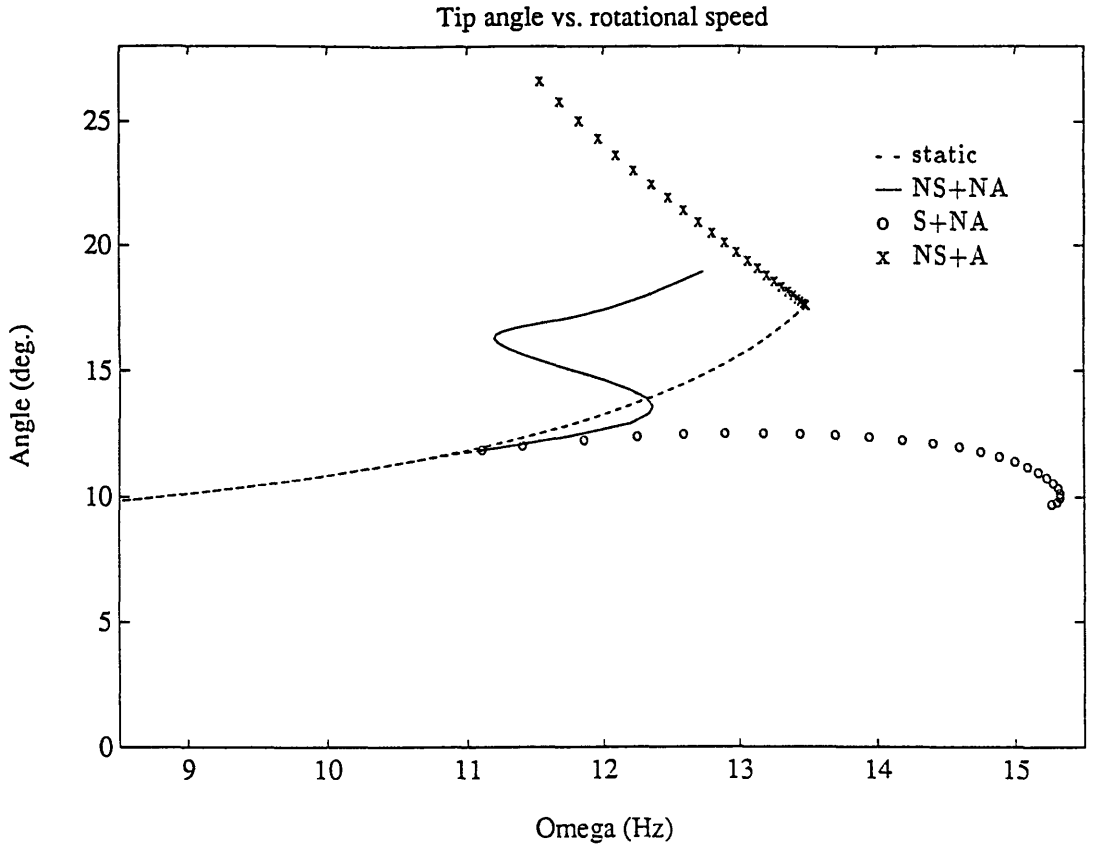

Figure 9.22: Tip average angle vs. rotational speed; $[0/90]_{3s}$, $\theta_r = 8$ deg.

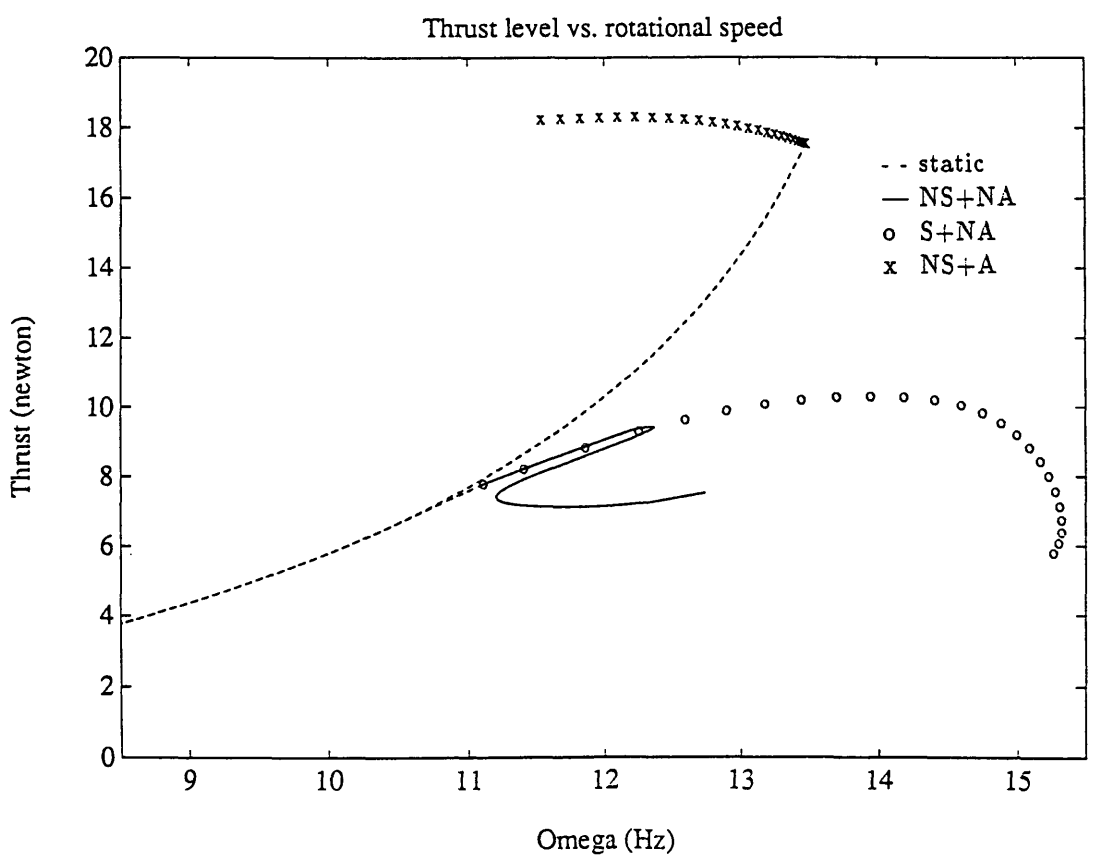

Figure 9.23: Average thrust level vs. rotational speed; $[0/90]_{3s}$, $\theta_r = 8$ deg.

The next two-bladed model, $[45/0]_s$ laminate case is illustrated in Figure 9.24 through 9.46 in the same order of information as before for the $[0/90]_{3s}$ case. It is mentioned that unlike analysis in the free vibrations, the top and bottom plies here were oriented at $+45^o$ around the z axis (negative coupling term E_{45}) such that negative twist would be caused when there is bending up. This is so called wash-in coupling, and normally serves as an aeroelastic tailoring tool to raise the critical flutter speed or suppress the flutter. Since the blade now has the beneficial bending-twist coupling in the structure, the blade is expected to behave better aeroelastically, and this is indeed seen in the figures.

The first group of figures, Figure 9.24 through 9.28, as before, show the information in (a), (b), (c), (d), (e) at the root pitch angles 3, 6, and 8 degrees. Basically similar trends to the $[0/90]_{3s}$ blade case are seen in these figures, but the range of critical rotational speed involved is relatively short compared to the previous case. Initially, all of the cases were found in linear aerodynamic range. Hence, there are initially vertical straight branches in the amplitude vs. critical rotational speed plot Figure 9.24. Unlike the case of $[0/90]_{3s}$ blade, the flutter frequencies continuously increase until very high level of amplitudes, and the corresponding tip average deformations as well as average thrust decrease monotonically until the very last stage of amplitude.

Looking at the next figures, Figure 9.29 through 9.34, one can find lack of fore-and-aft motion y_s and y_c in all of the flutter mode shapes for entire range of amplitudes. Instead, there is always a second bending type motion in z_c at low amplitudes, and a third bending motion in z_c at high amplitudes. This is not surprising since the high pitch motion should be always coupled with bending motion due to the wash-in coupling. The lack of any dramatic softening trend in the aeroelastic behavior apparent in Figure 9.24 may then be attributed to this phenomenon of lack of lag mode and existence of high bending modes in the flutter mode shapes.

In the final group of figures, Figure 9.36 through 9.46, the individual effects of nonlinear structure and the dynamic stall are seen very different from those of $[0/90]_{3s}$.

Most striking are curves of $NS + A$ which exhibit completely opposite trend, i.e., continuous hardening phenomenon (see Figure 9.35, 9.39, 9.43). As matter of fact, no convergence was obtained on $NS+A$ curves in higher range of amplitudes, and this implies there could exist an asymptote that reaches to the far right side of the solution plane. As a result, it is the dynamic stall effect, not the nonlinear structure, that allows limit cycle solutions in the moderate range of amplitudes. At high amplitude levels, however, the dynamic stall also exhibits very strong hardening trend, forming another asymptote which full solutions will eventually approach. Once again, in view of the discussion given in section 5.3, the asymptotic hardening behavior in the high amplitude range might represent a breakdown of the ONERA Model.

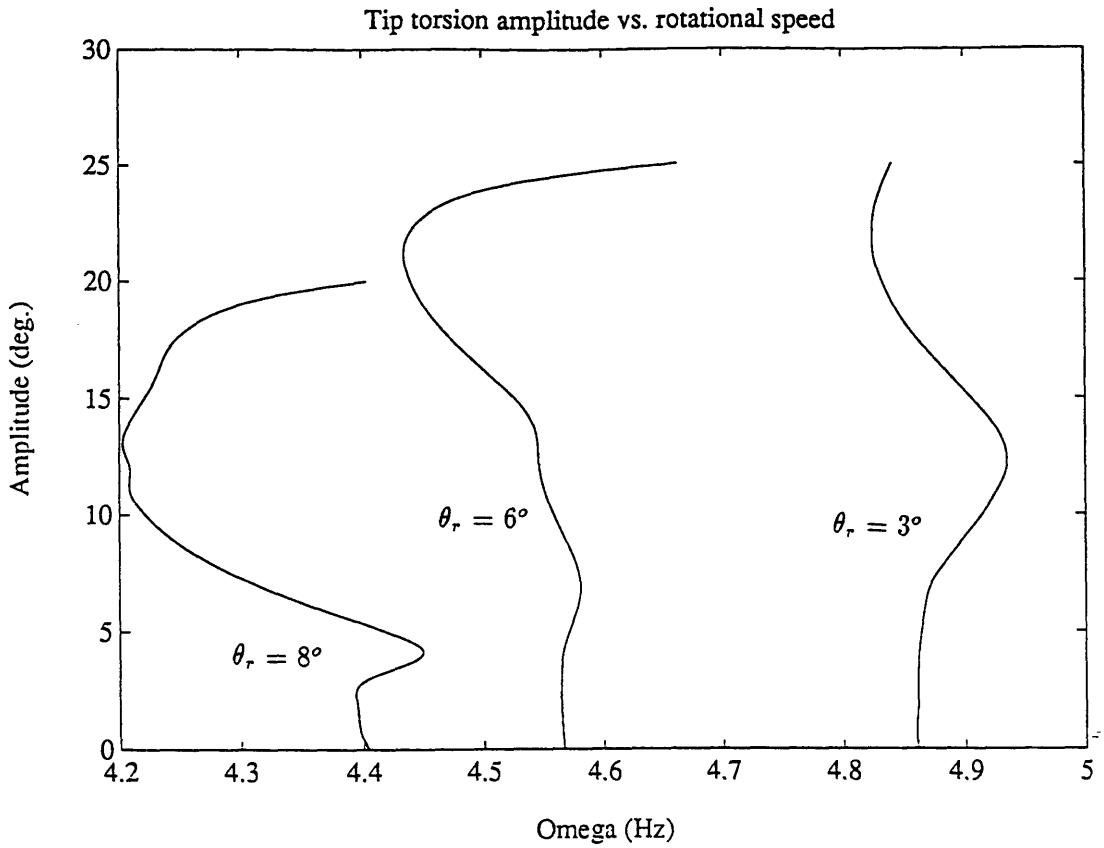

Figure 9.24: Torsional amplitude vs. rotational speed; $[45/0]_s$, $\theta_r = 3, 6, 8$ deg.

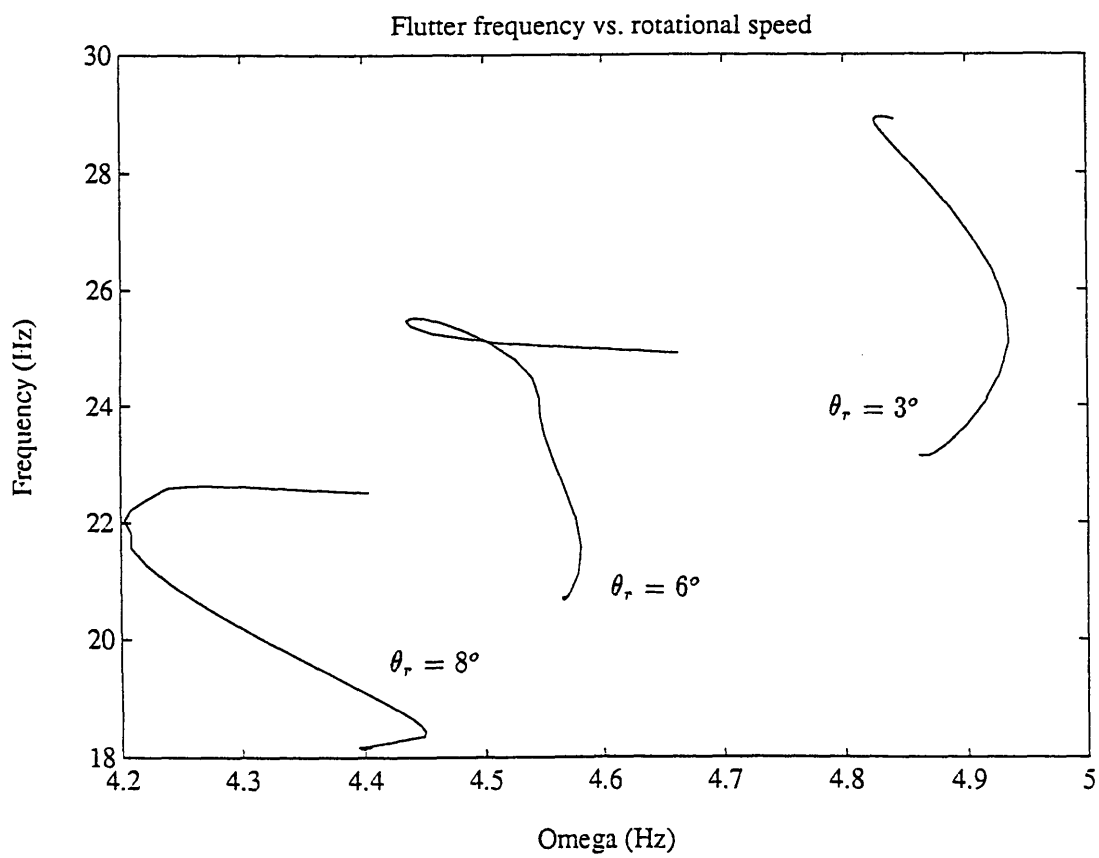

Figure 9.25: Flutter frequency vs. rotational speed; $[45/0]_s$, $\theta_r = 3, 6, 8$ deg.

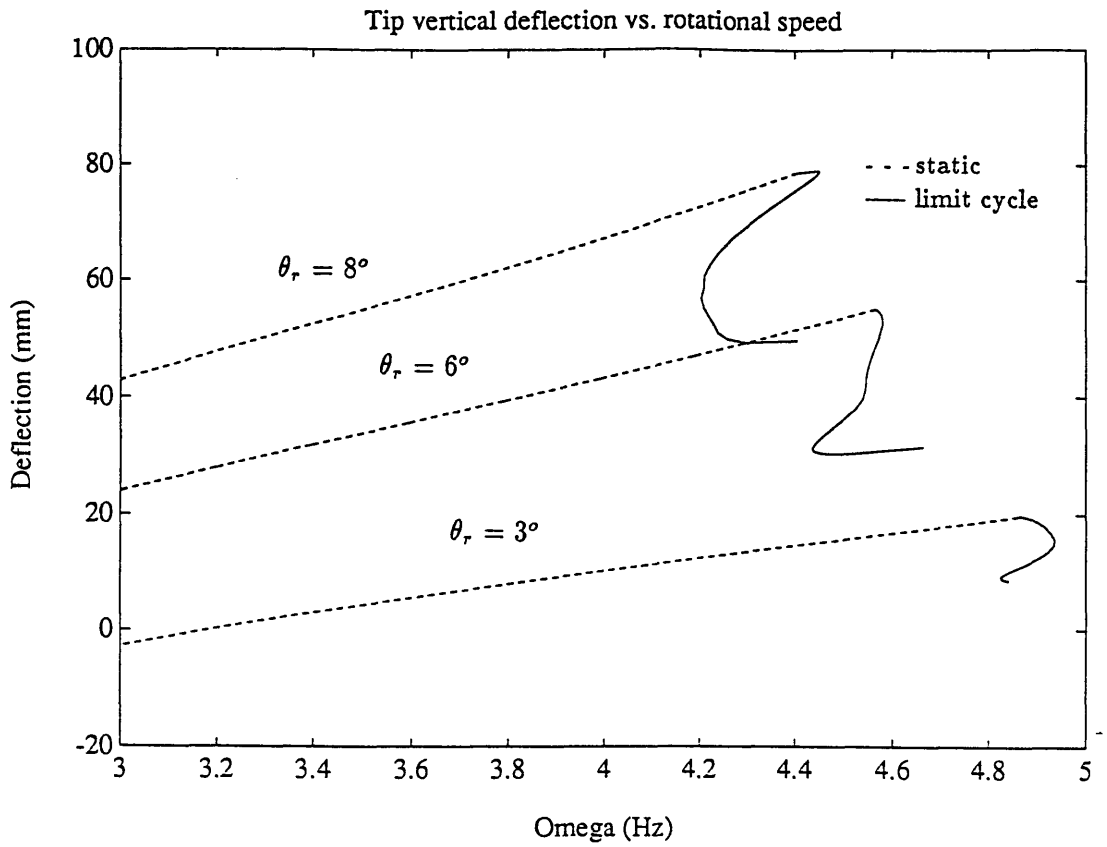

Figure 9.26: Tip average deflection vs. rotational speed; $[45/0]_s$, $\theta_r = 3, 6, 8$ deg.

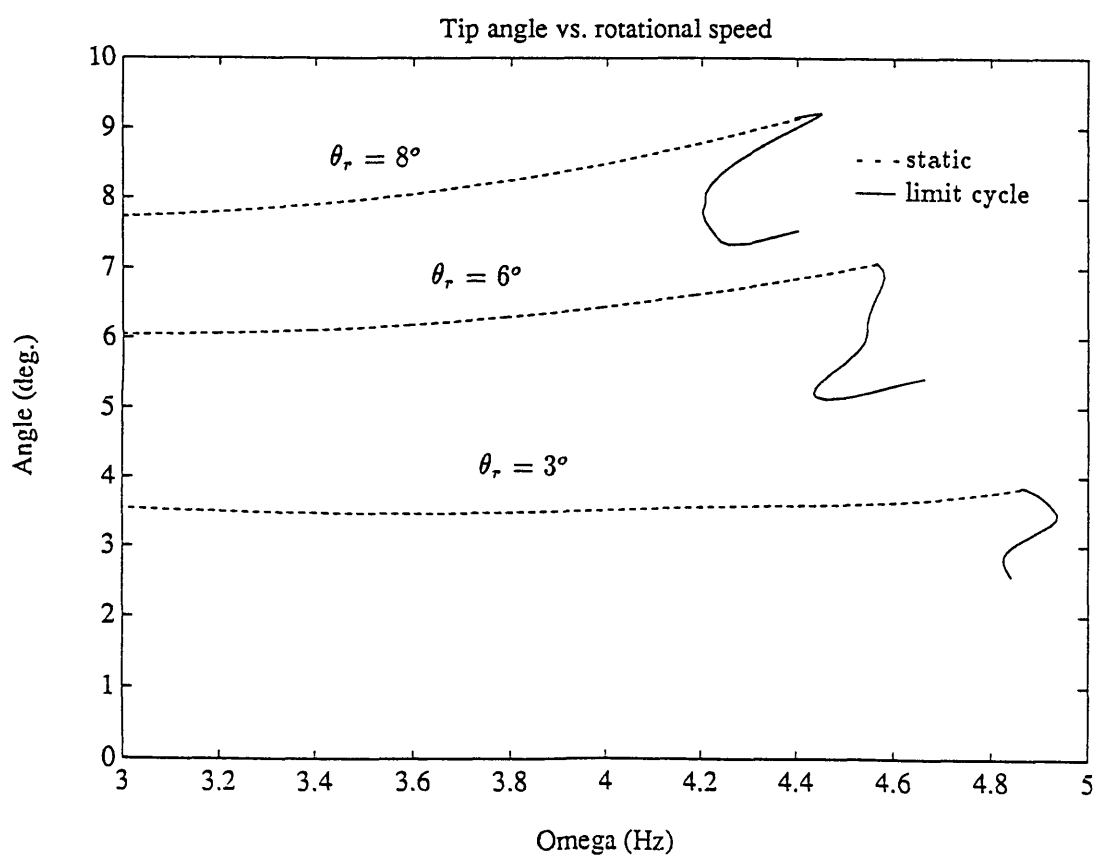

Figure 9.27: Tip average angle vs. rotational speed; $[45/0]_s$, $\theta_r = 3, 6, 8$ deg.

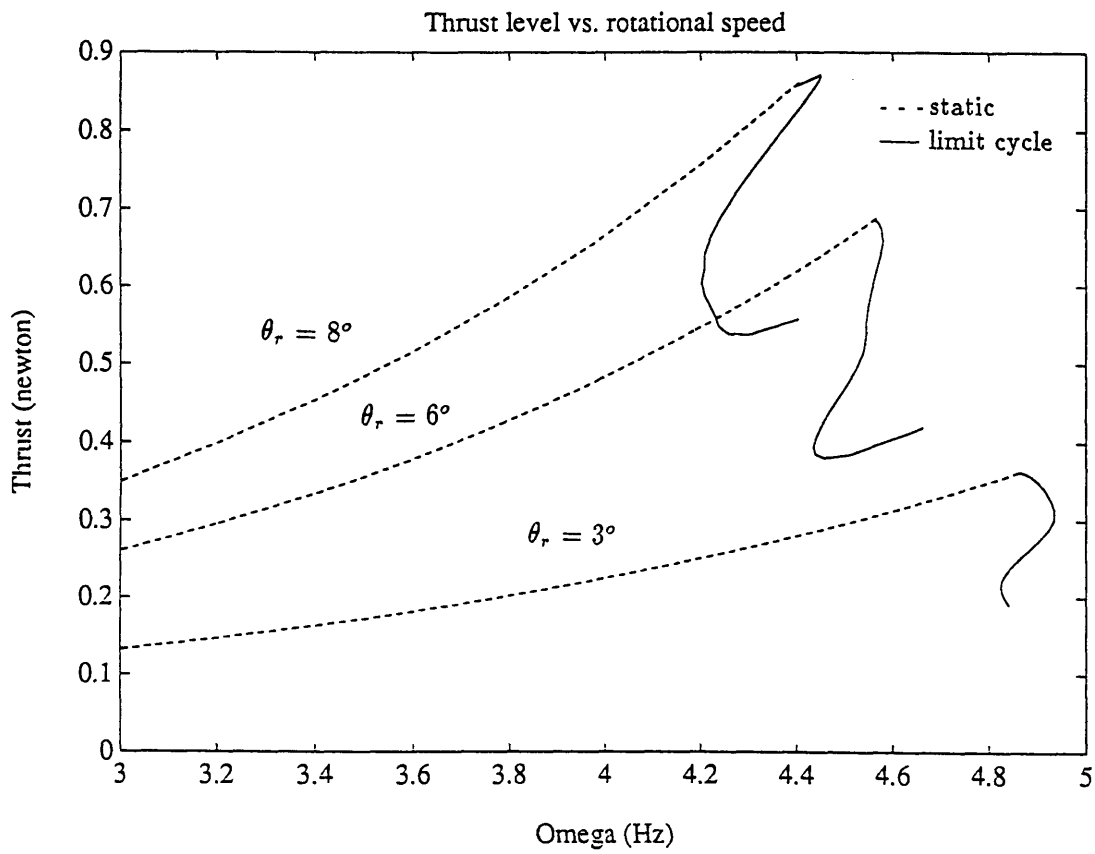

Figure 9.28: Average thrust level vs. rotational speed; $[45/0]_s$, $\theta_r = 3, 6, 8$ deg.

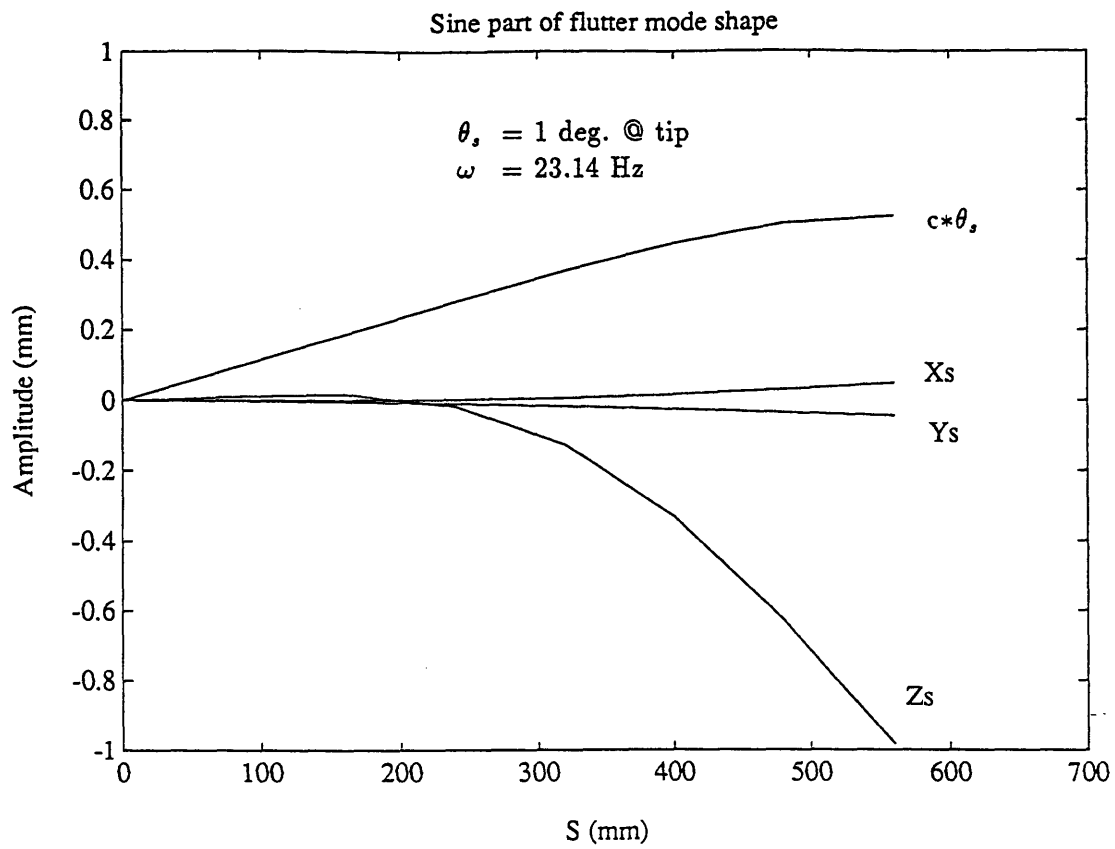

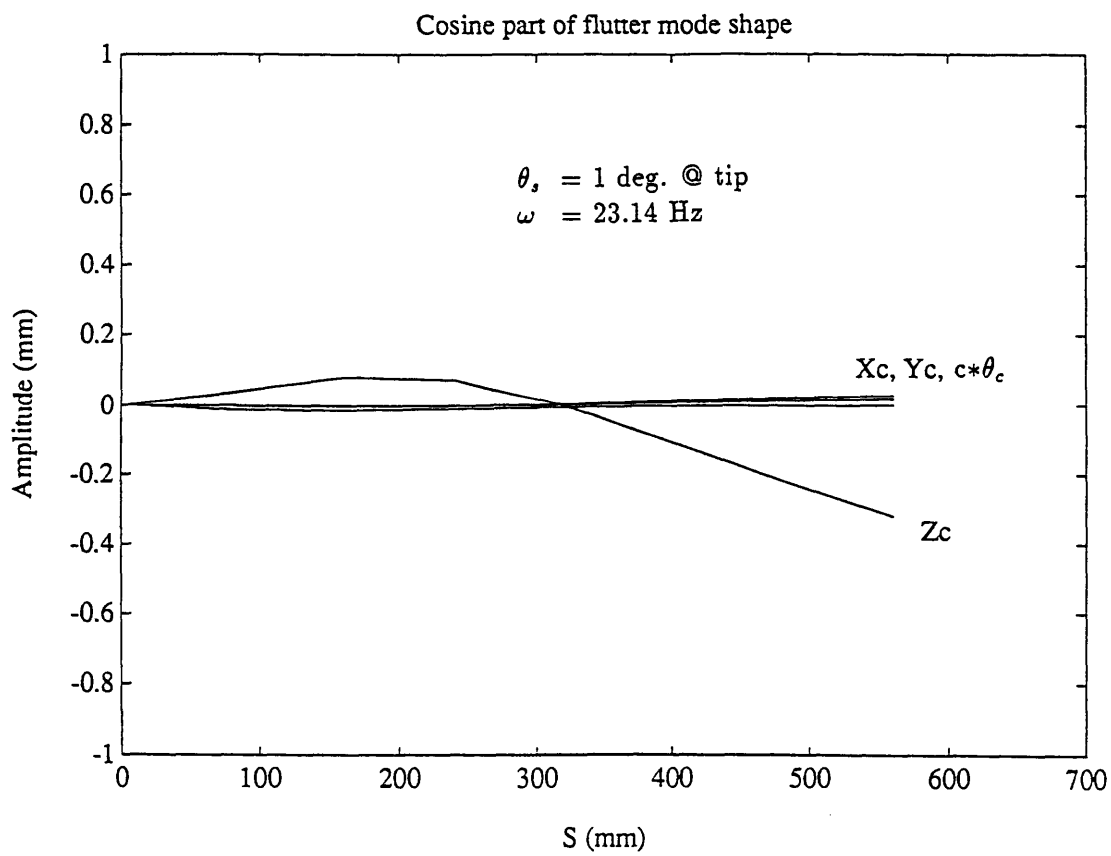

Figure 9.29: Flutter mode shape; $[45/0]_s$, $\theta_r = 3$ deg., $\Omega = 4.86$ Hz

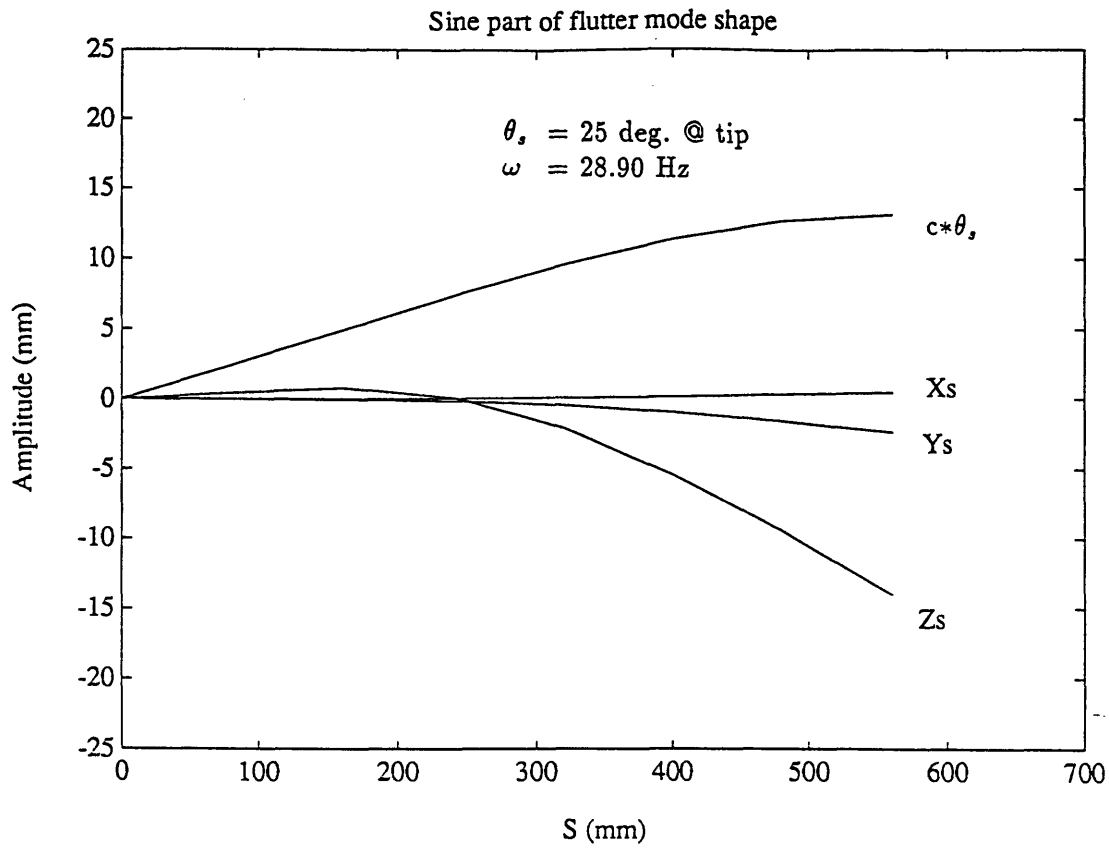

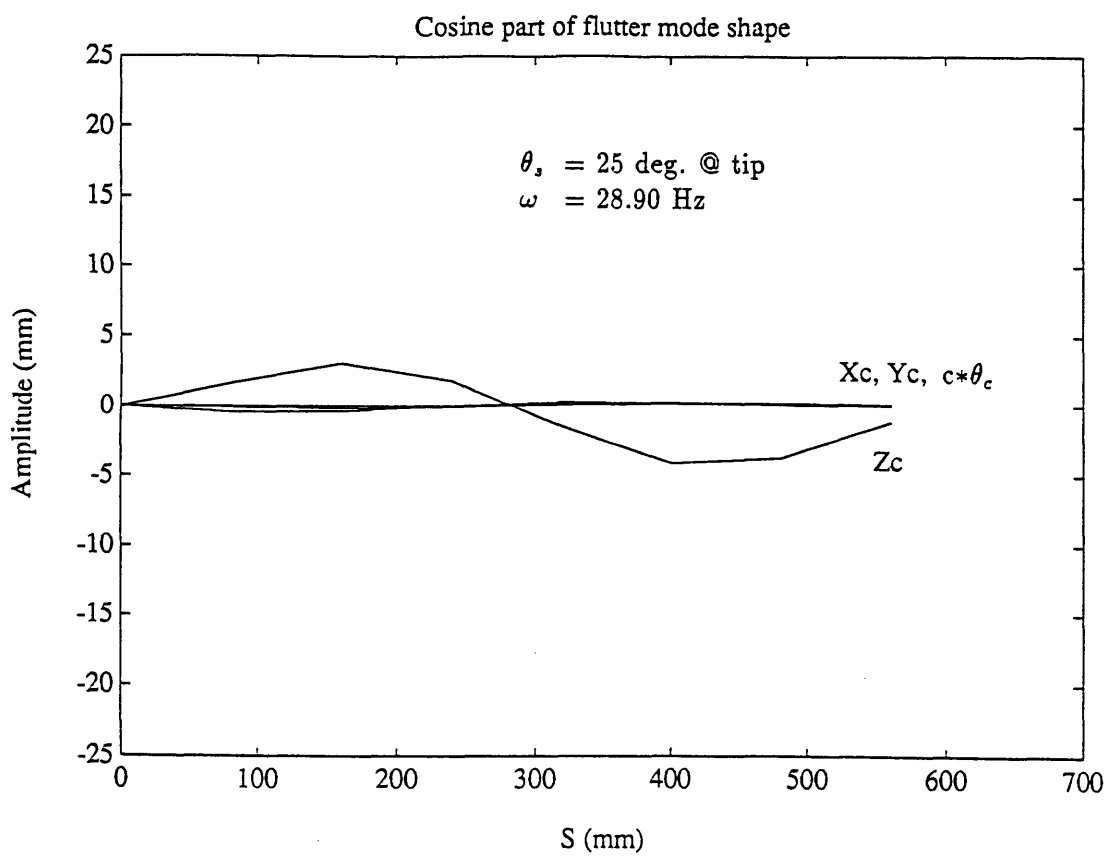

Figure 9.30: Flutter mode shape; $[45/0]_s$, $\theta_r = 3$ deg., $\Omega = 4.84$ Hz

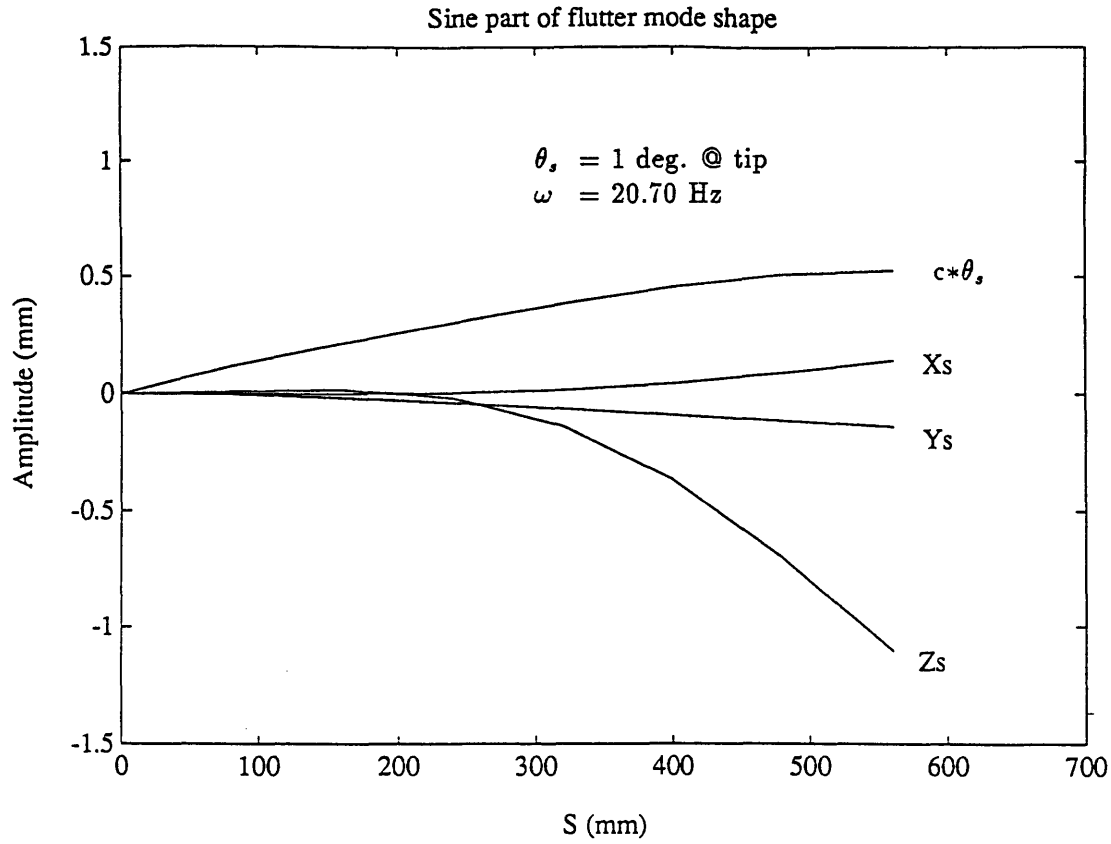

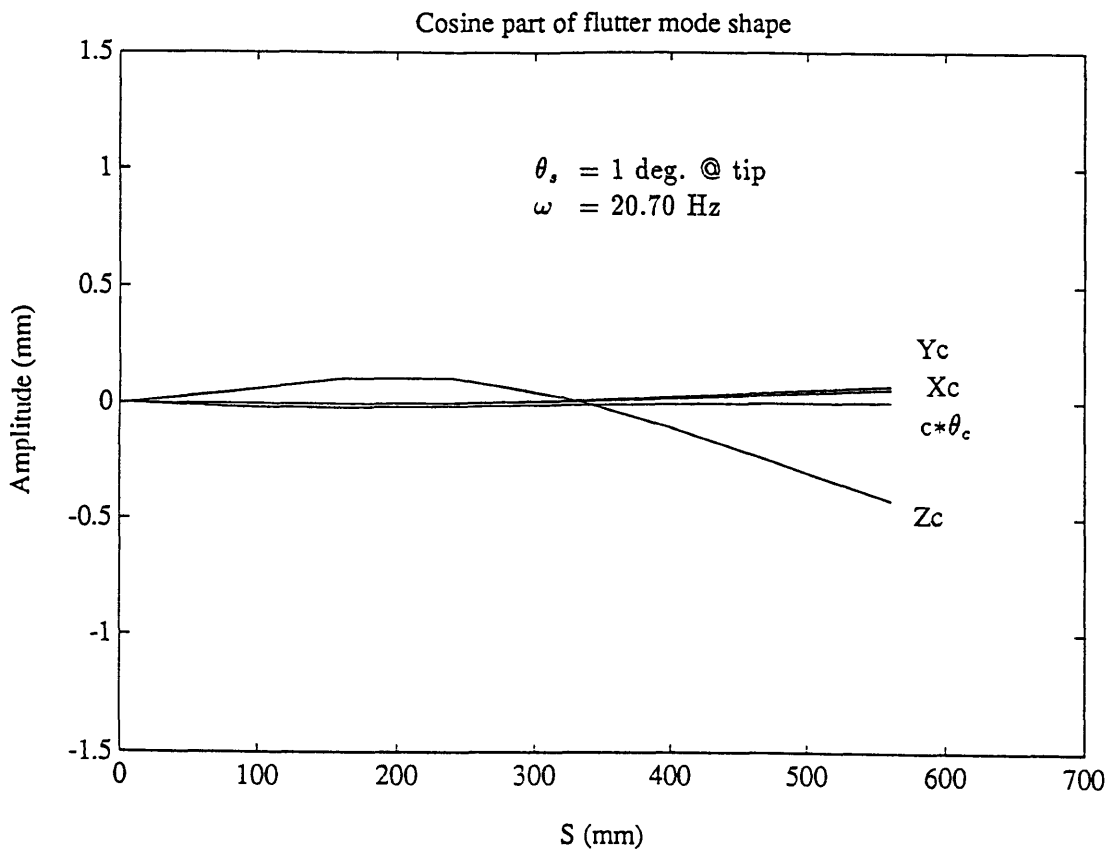

Figure 9.31: Flutter mode shape; $[45/0]_s$, $\theta_r = 6$ deg., $\Omega = 4.56$ Hz

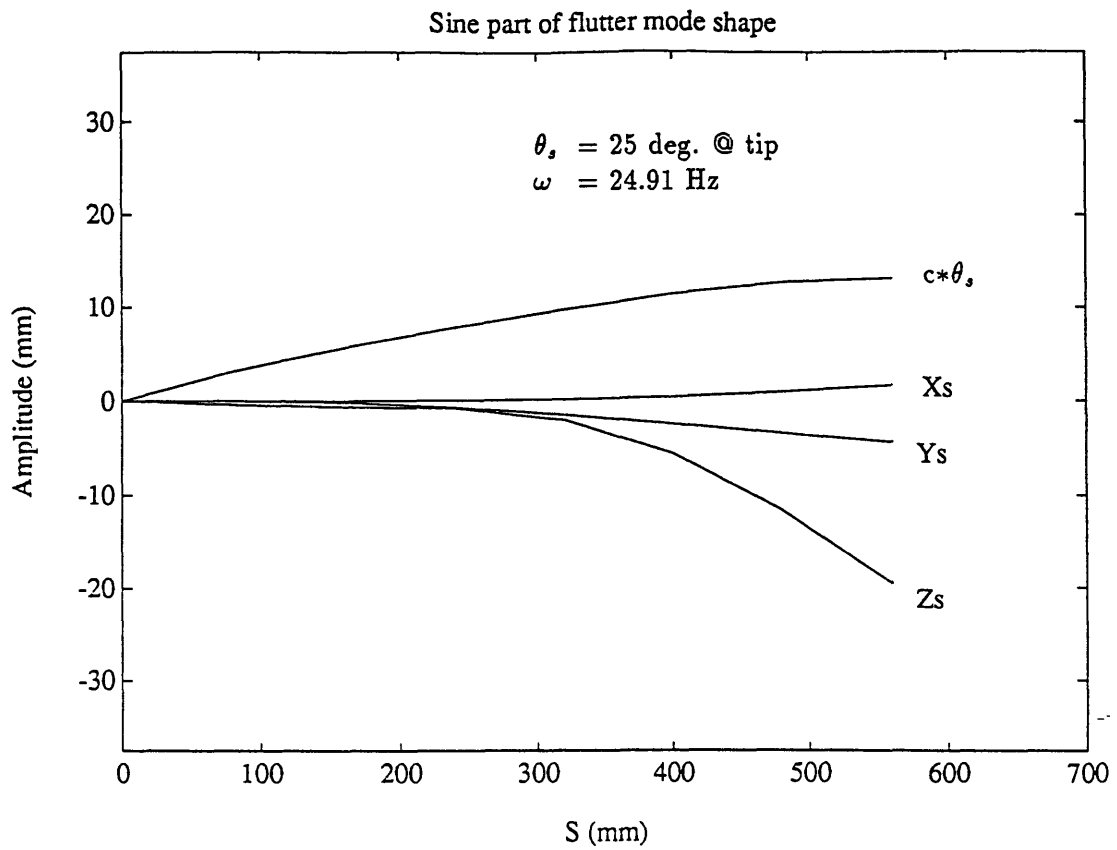

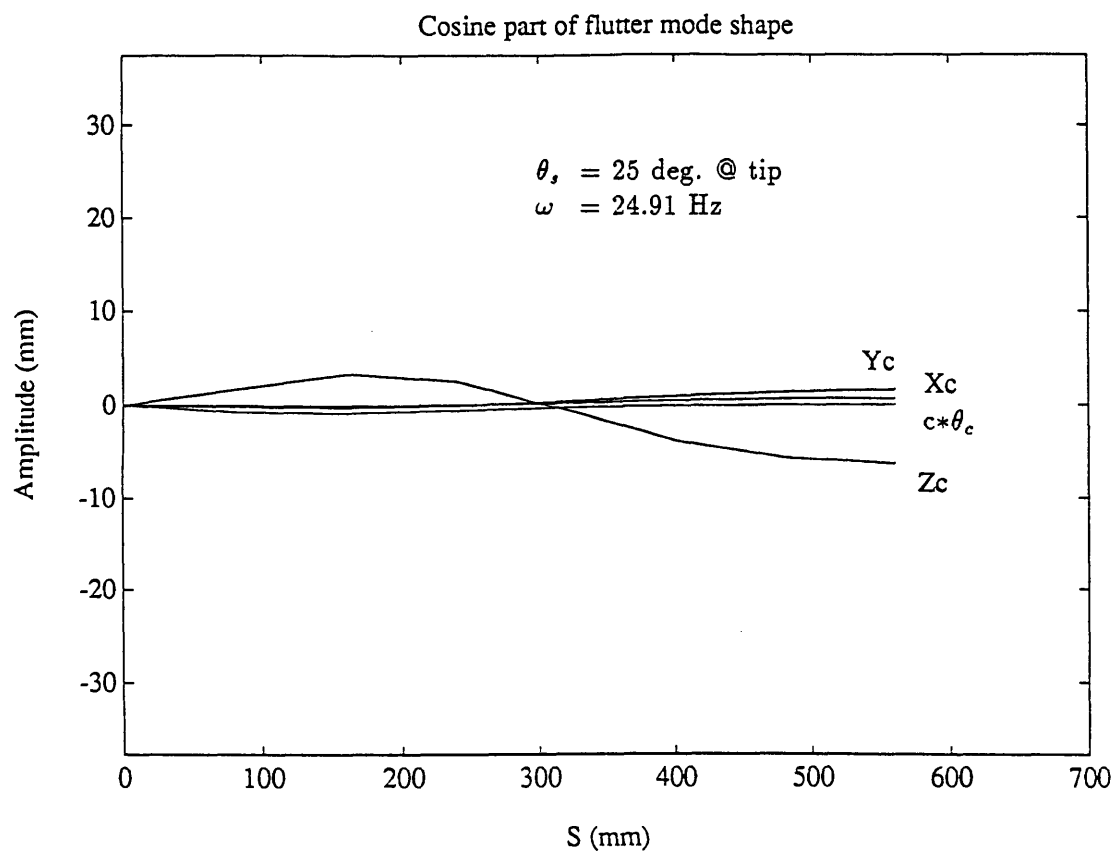

Figure 9.32: Flutter mode shape; $[45/0]_s$, $\theta_r = 6$ deg., $\Omega = 4.66$ Hz

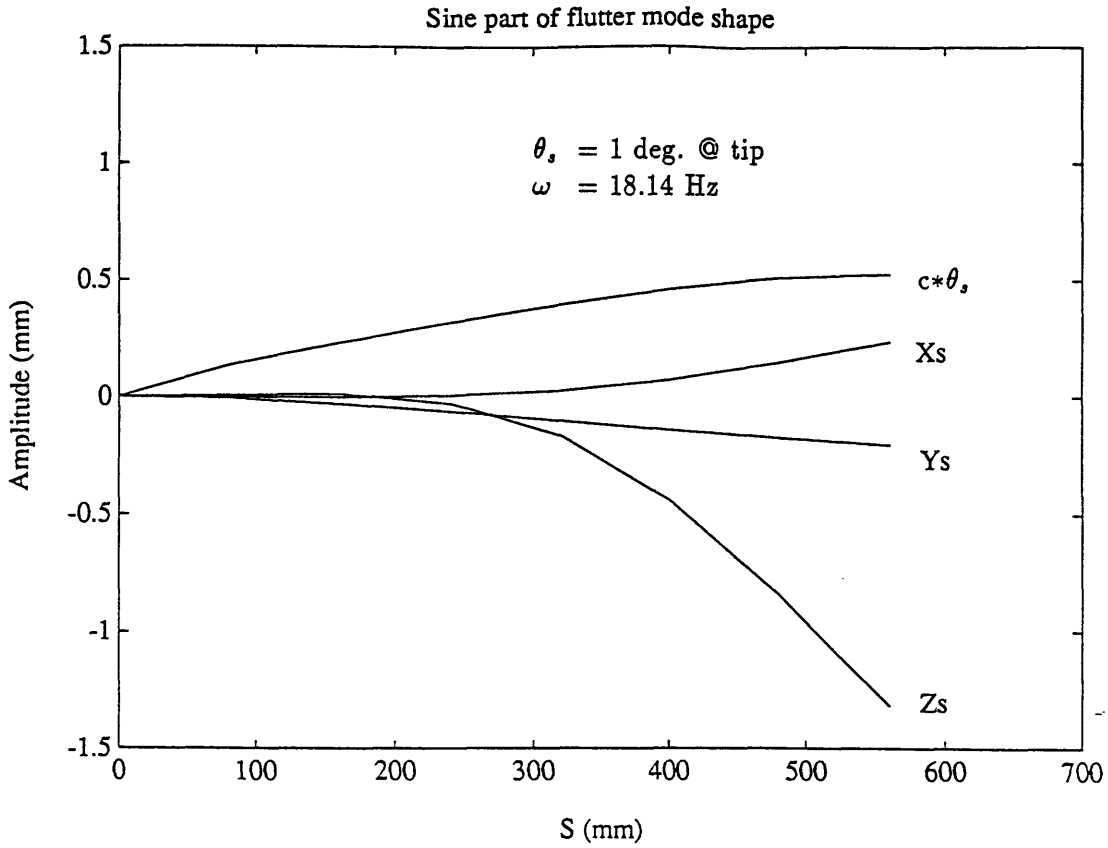

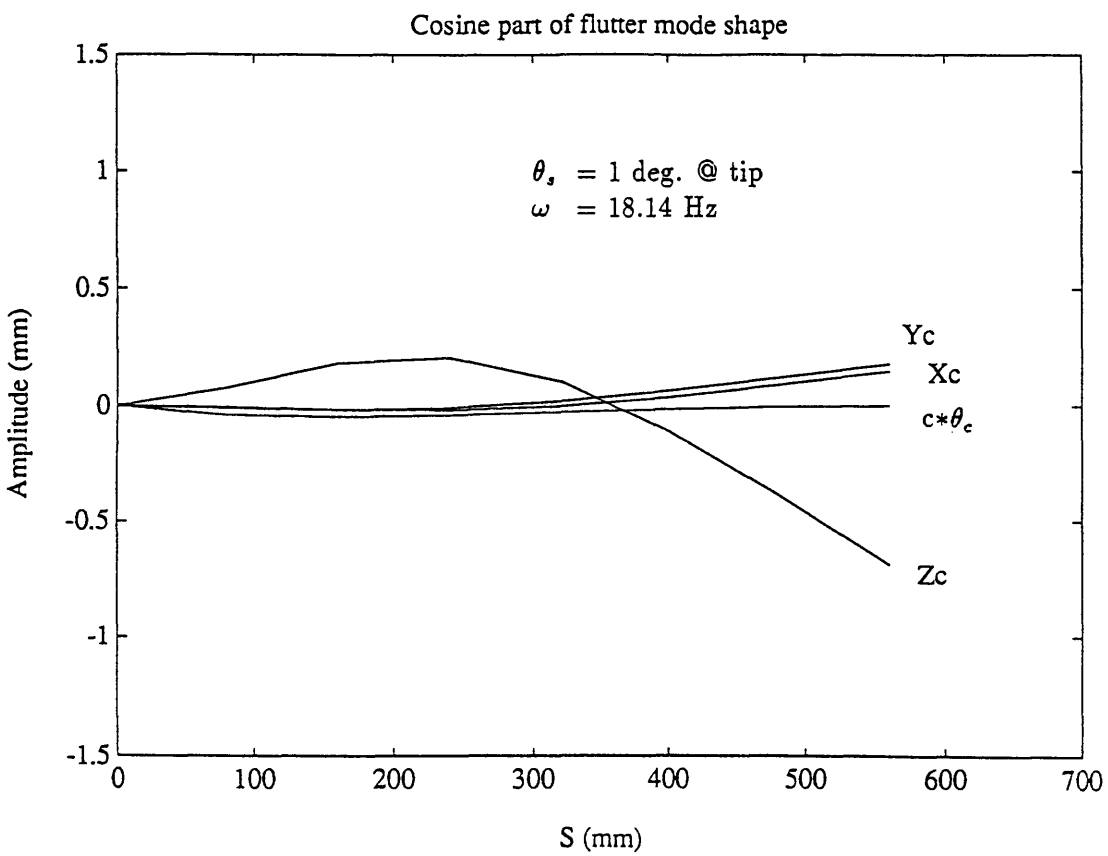

Figure 9.33: Flutter mode shape; $[45/0]_s$, $\theta_r = 8$ deg., $\Omega = 4.40$ Hz

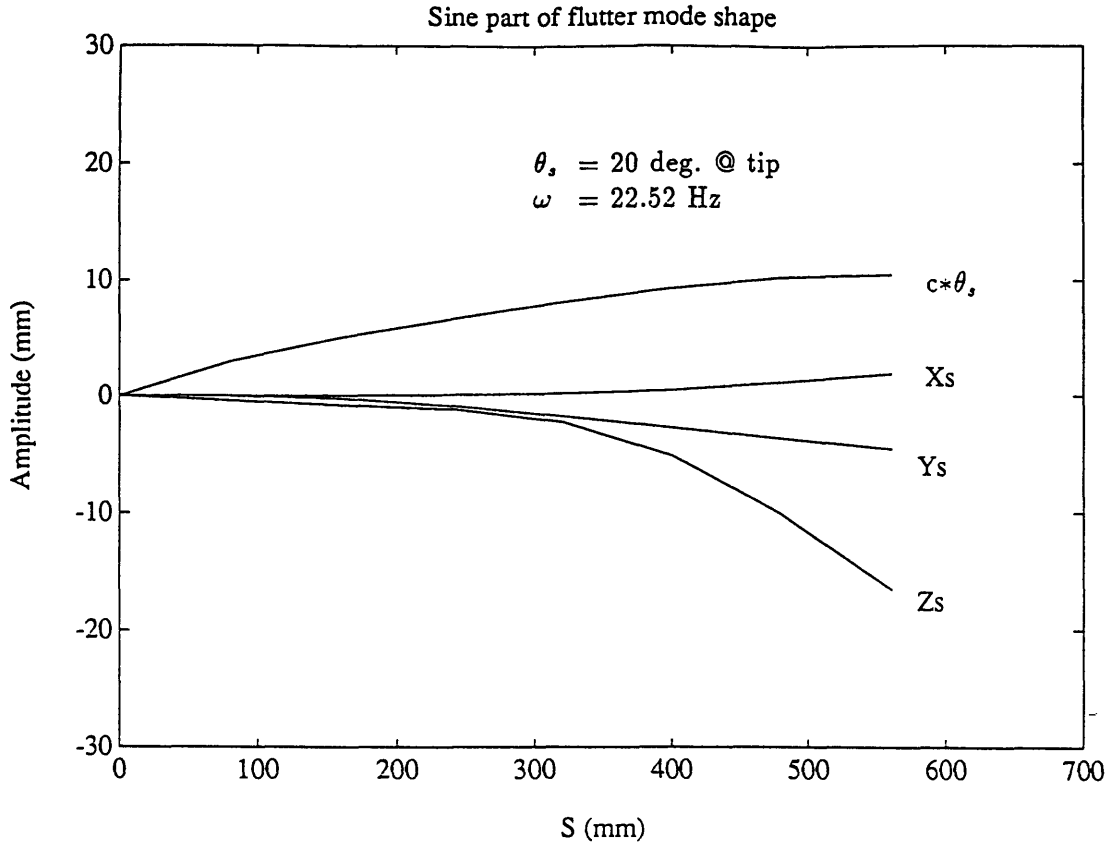

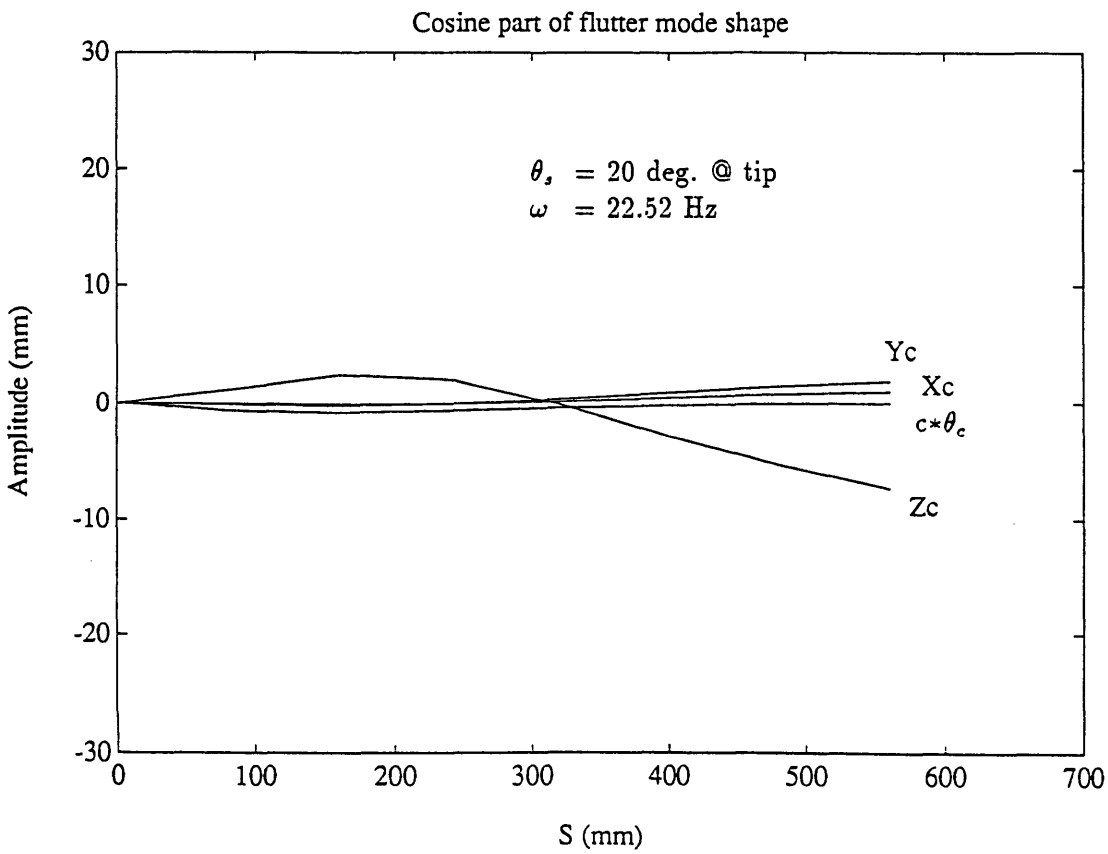

Figure 9.34: Flutter mode shape; $[45/0]_s$, $\theta_r = 8$ deg., $\Omega = 4.40$ Hz

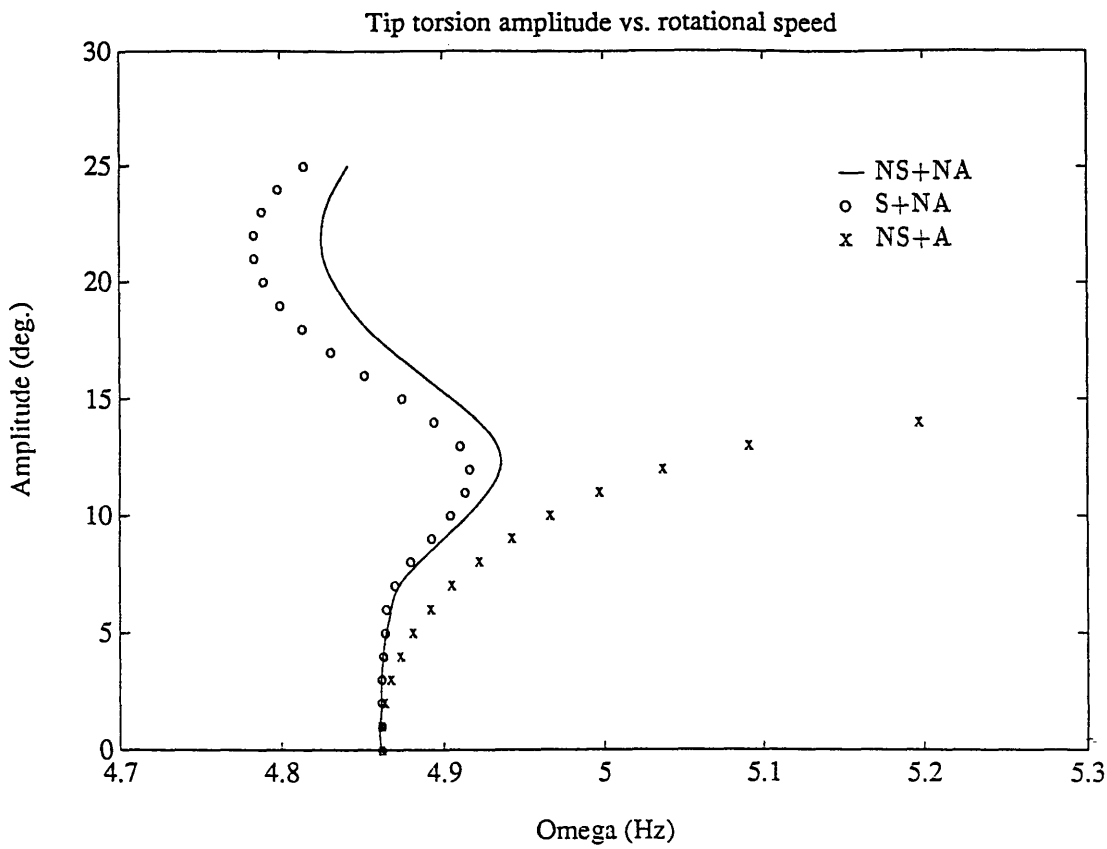

Figure 9.35: Torsional amplitude vs. rotational speed; $[45/0]_s$, $\theta_r = 3$ deg.

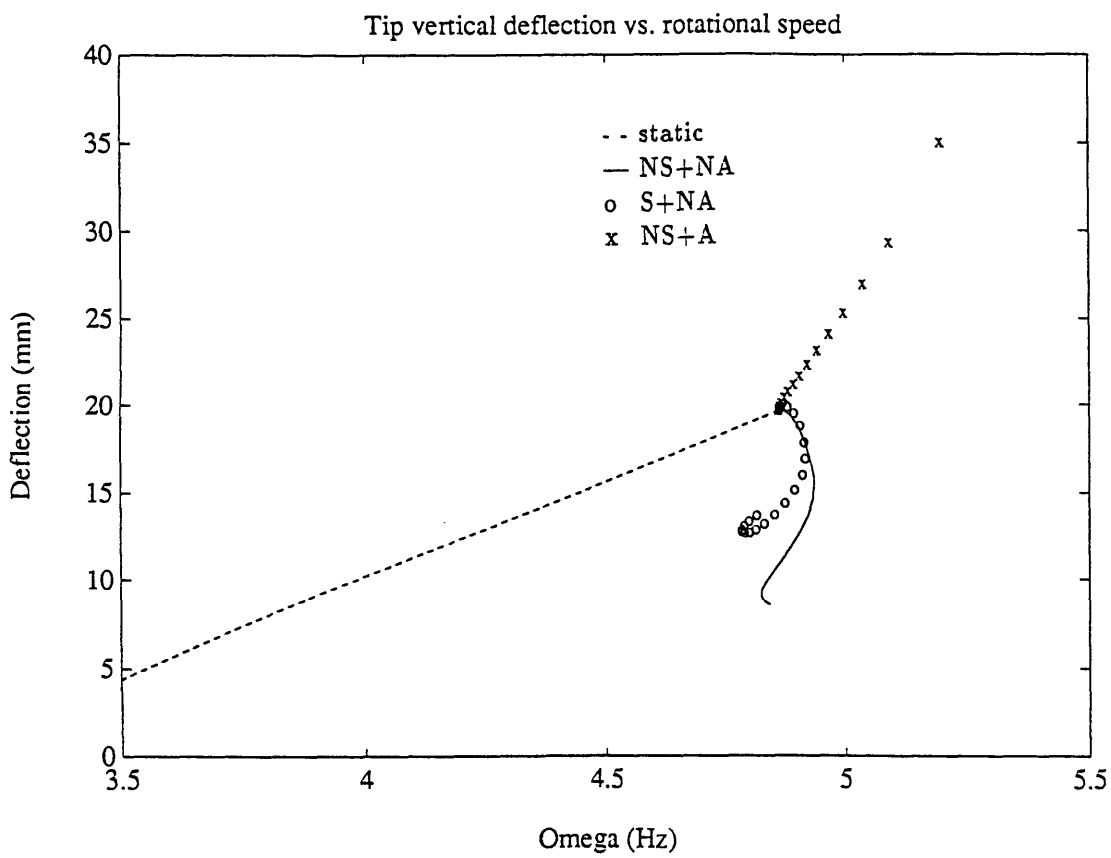

Figure 9.36: Tip average deflection vs. rotational speed; $[45/0]_s$, $\theta_r = 3$ deg.

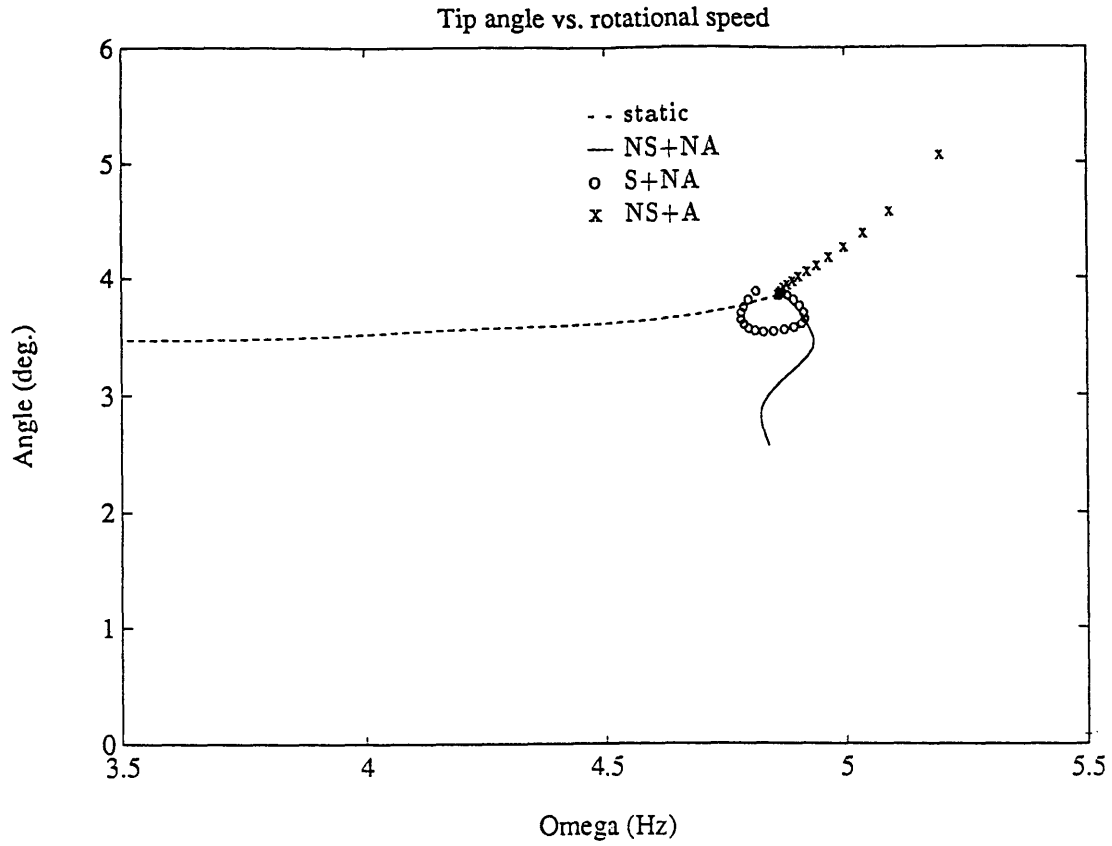

Figure 9.37: Tip average angle vs. rotational speed; $[45/0]_s$, $\theta_r = 3$ deg.

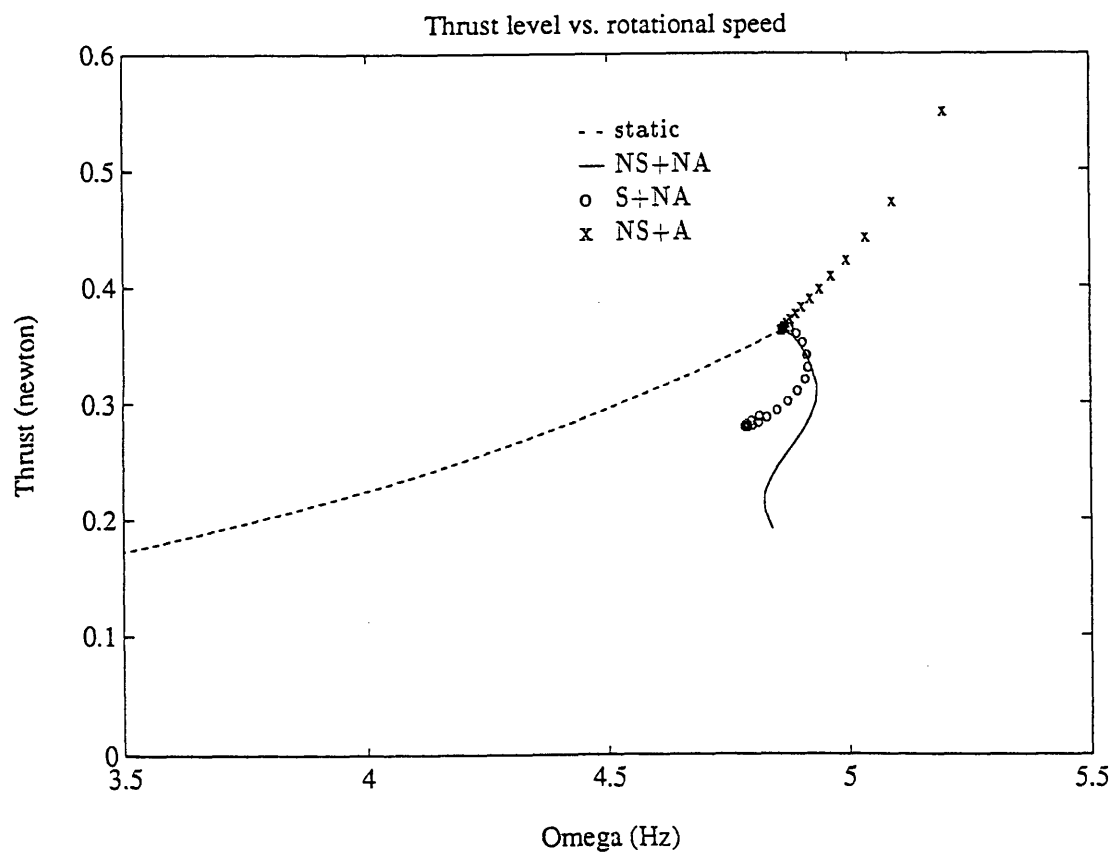

Figure 9.38: Average thrust level vs. rotational speed; $[45/0]_s$, $\theta_r = 3$ deg.

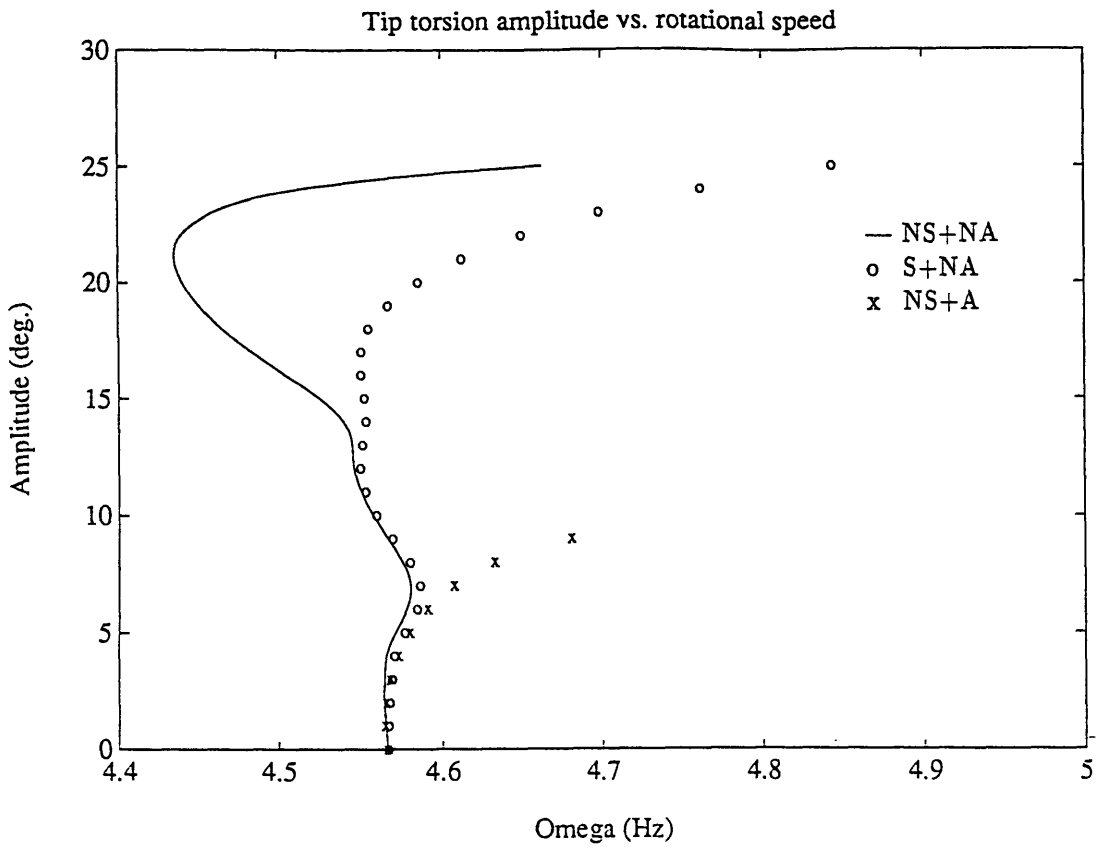

Figure 9.39: Torsional amplitude vs. rotational speed; $[45/0]_s$, $\theta_r = 6$ deg.

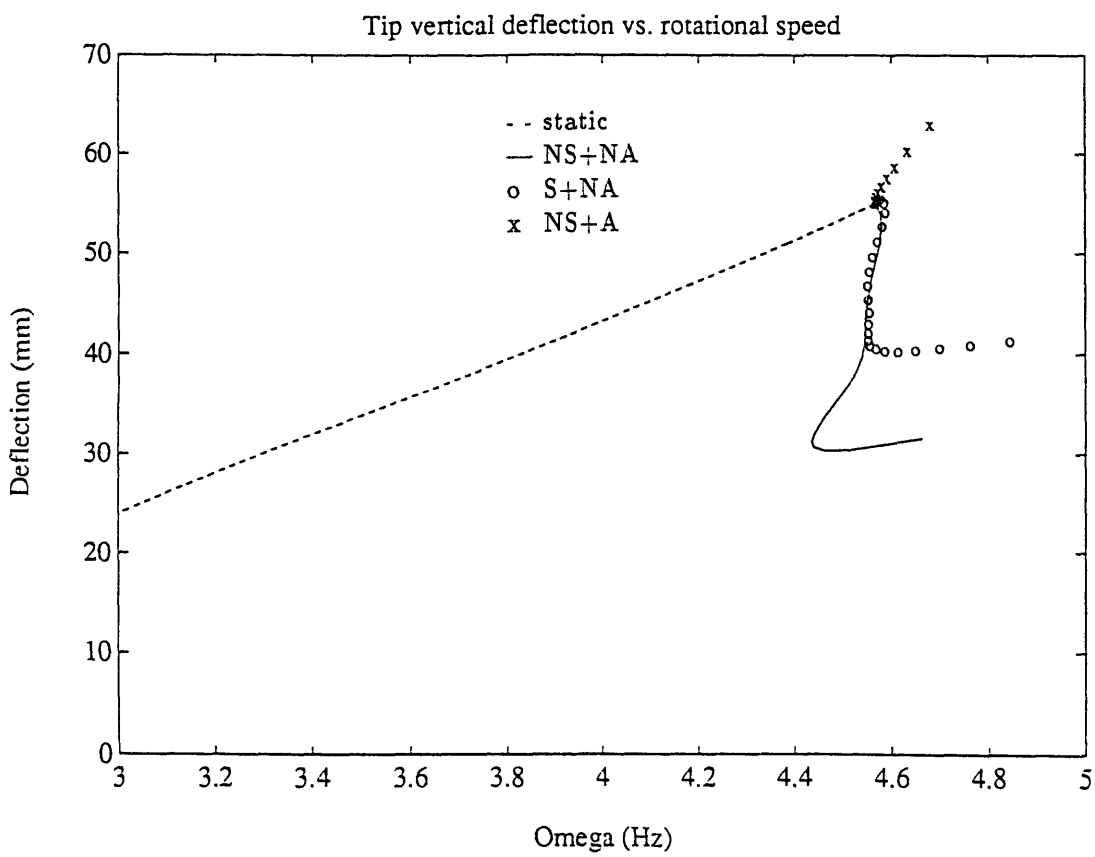

Figure 9.40: Tip average deflection vs. rotational speed; $[45/0]_s$, $\theta_r = 6$ deg.

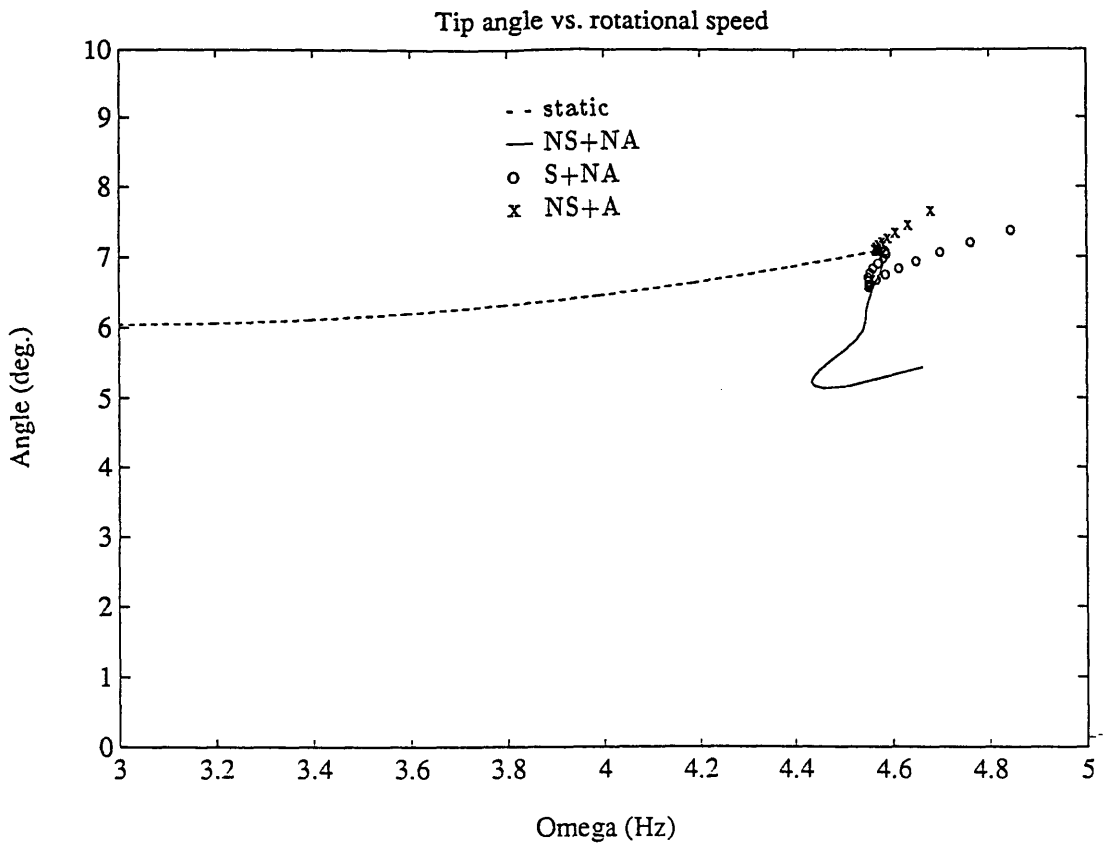

Figure 9.41: Tip average angle vs. rotational speed; $[45/0]_s$, $\theta_r = 6$ deg.

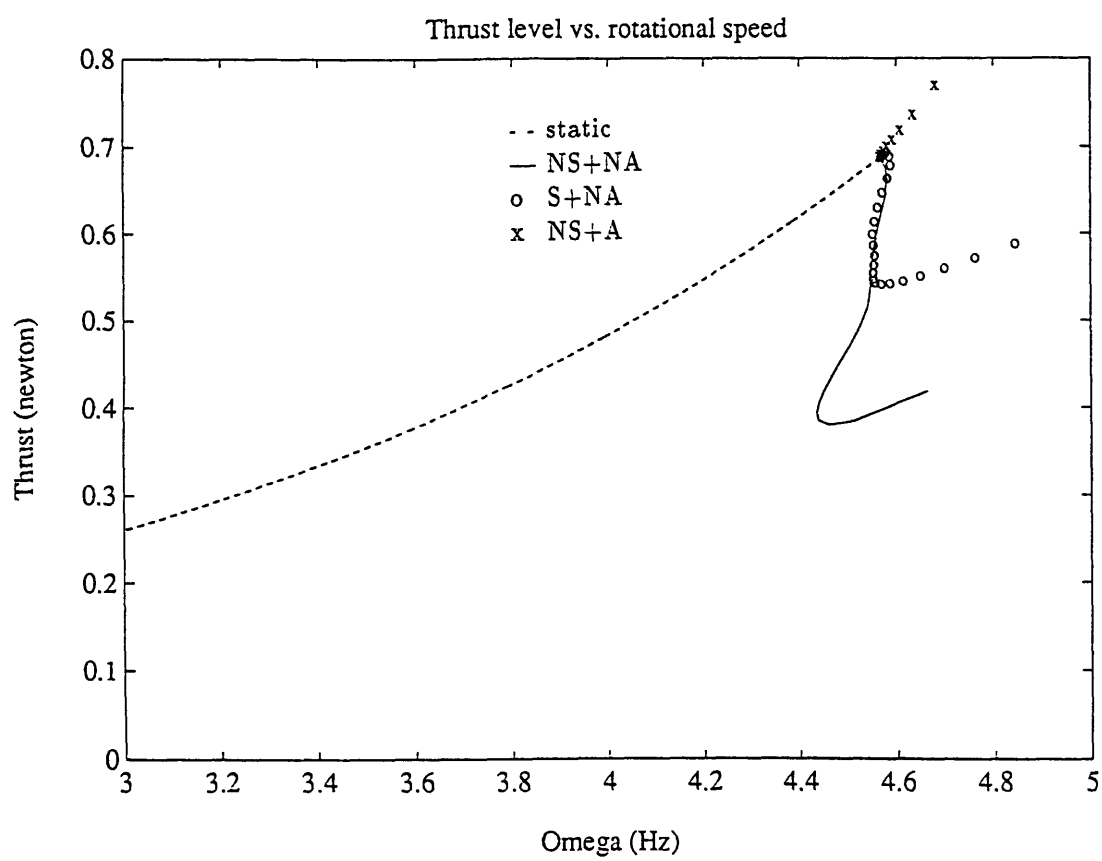

Figure 9.42: Average thrust level vs. rotational speed; $[45/0]_s$, $\theta_r = 6$ deg.

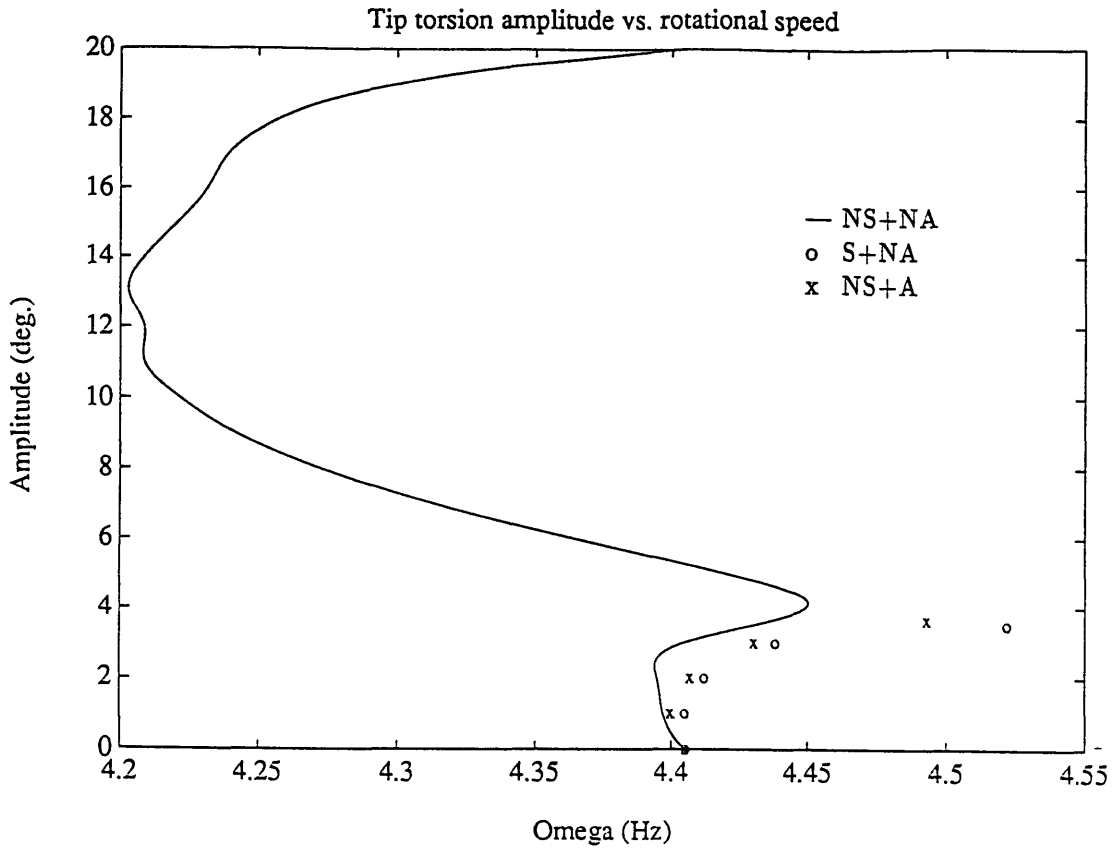

Figure 9.43: Torsional amplitude vs. rotational speed; $[45/0]_s$, $\theta_r = 8$ deg.

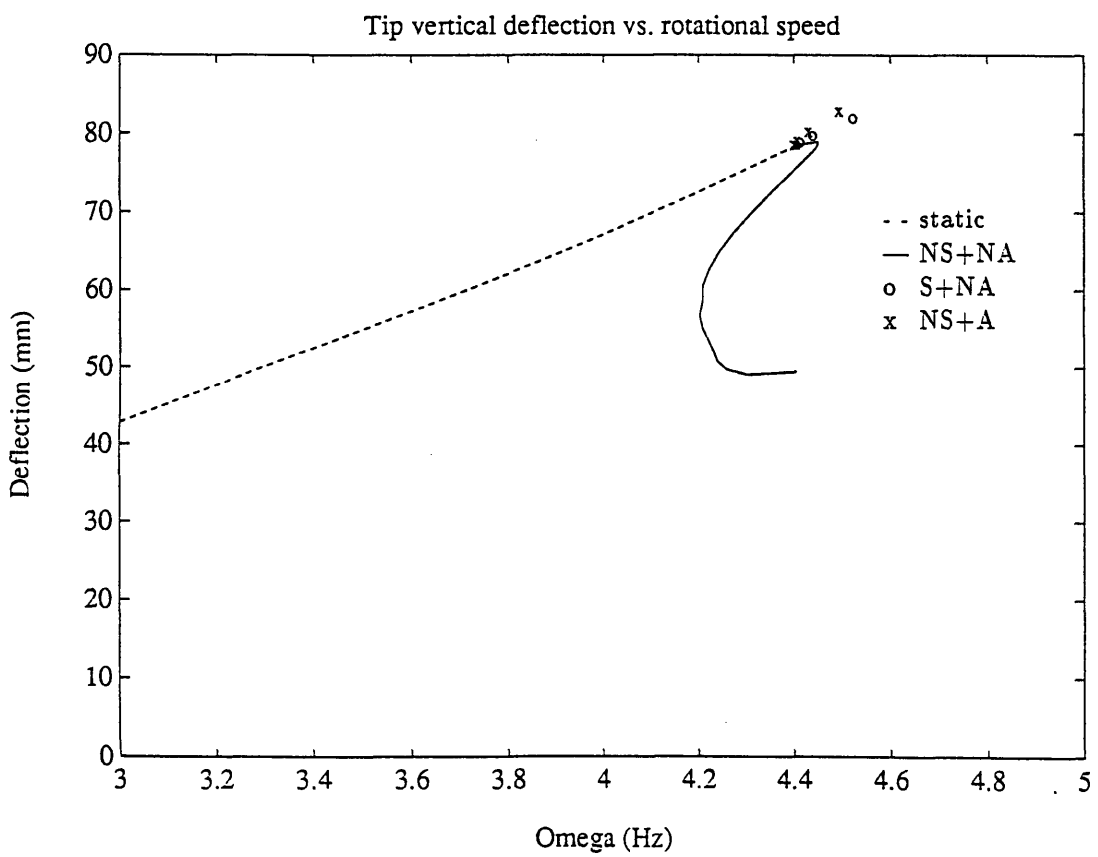

Figure 9.44: Tip average deflection vs. rotational speed; $[45/0]_s$, $\theta_r = 8$ deg.

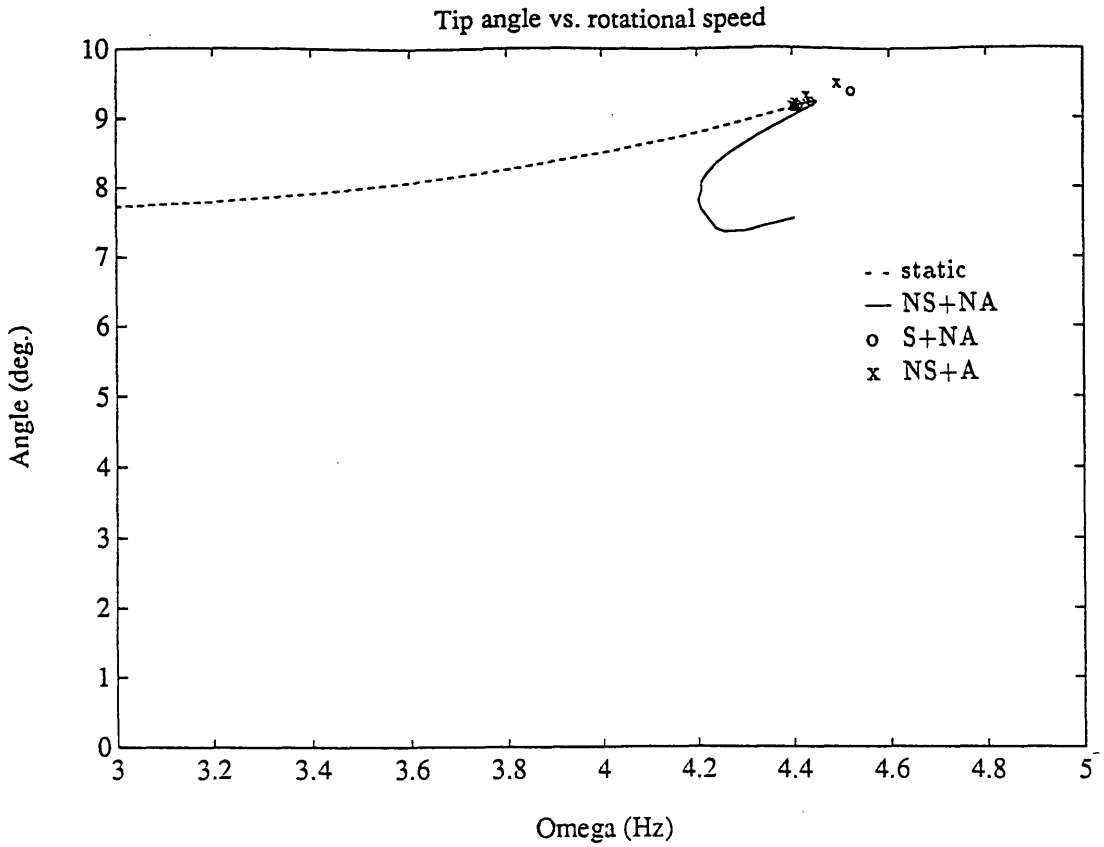

Figure 9.45: Tip average angle vs. rotational speed; $[45/0]_s$, $\theta_r = 8$ deg.

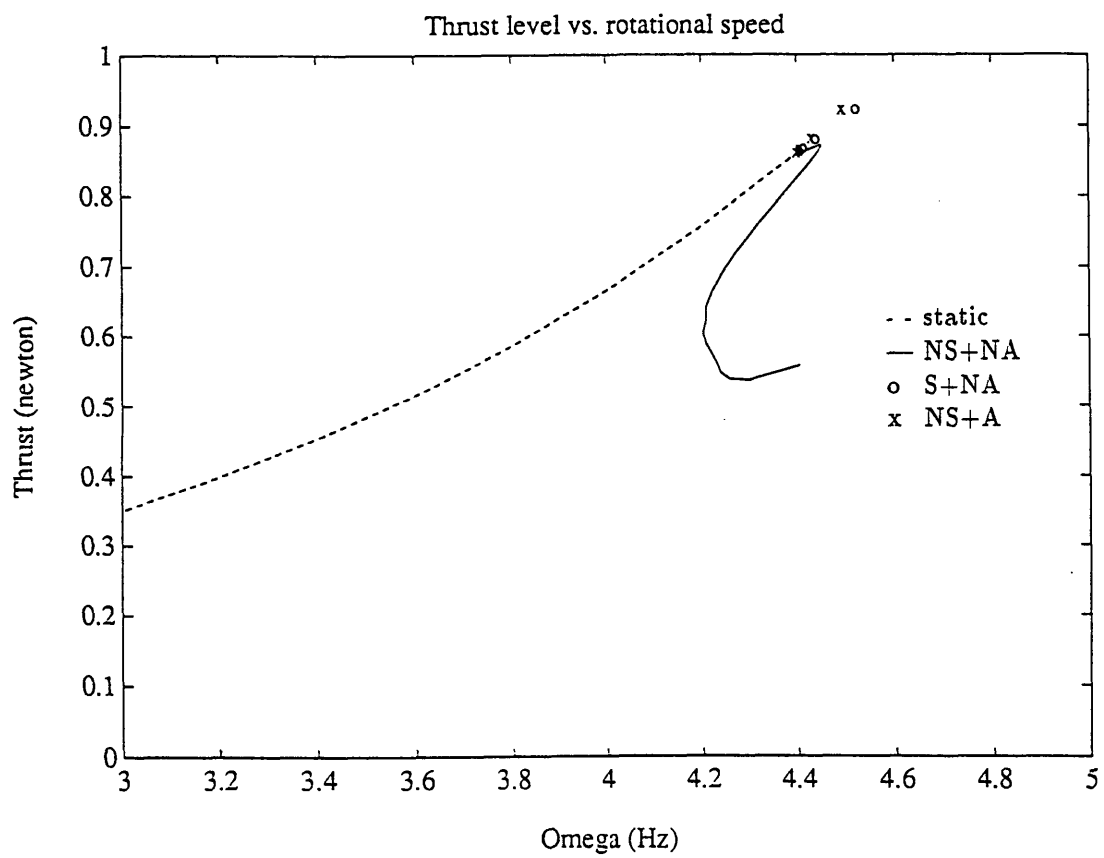

Figure 9.46: Average thrust level vs. rotational speed; $[45/0]_s$, $\theta_r = 8$ deg.

9.2 Lag-hinged Blade Examples

In this section, an example of lag-hinged blade made of $[0/90]_{3s}$ with a lag spring is considered as an example. The lag spring constant K_ψ was fixed at 120 newton-meter/rad, and a new set of boundary condition, the third one in section 2.2, has been introduced. The root pitch chosen was 3 degrees. The lag-hinge-spring construction will yield very low effective lag bending stiffness and, consequently, a low chordwise to flapwise bending stiffness ratio. Therefore, no strong softening effects were expected from the lag motion. The major components in the flutter modes are now bending and lag which is almost a rigid mode. This flap-lag coupled mode is a typical of the so-called soft in-plane rotor blades (where rotating free vibration frequencies are below one per. rev.). There is still, as Figure 9.47 suggests, a strong structural softening trend accompanied by monotonically decreasing tip average deflection, when the nonlinear structure is combined with linear aerodynamics. This is believed to be due to the softening in the torsion components still existent in the flutter modes. It is recalled from Figure 7.2 and 7.4 that there are drops in both the frequency and centershift in the first torsion mode when the static tip deflection is within moderate range. Nevertheless, as a whole, the full analysis yields mostly hardening trend because of the nonlinear dynamic stall effects.

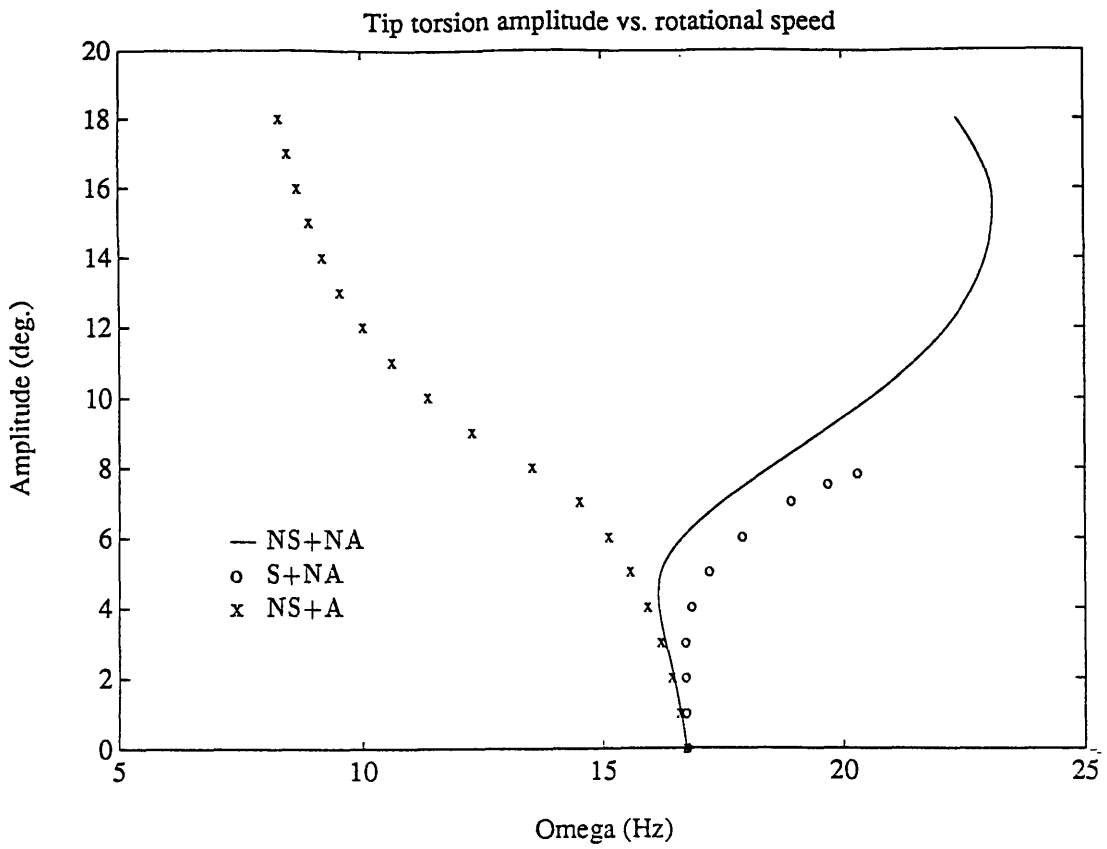

Figure 9.47: Torsional amplitude vs. rotational speed; lag-hinged $[0/90]_{3s}$, $\theta_r = 3$ deg.

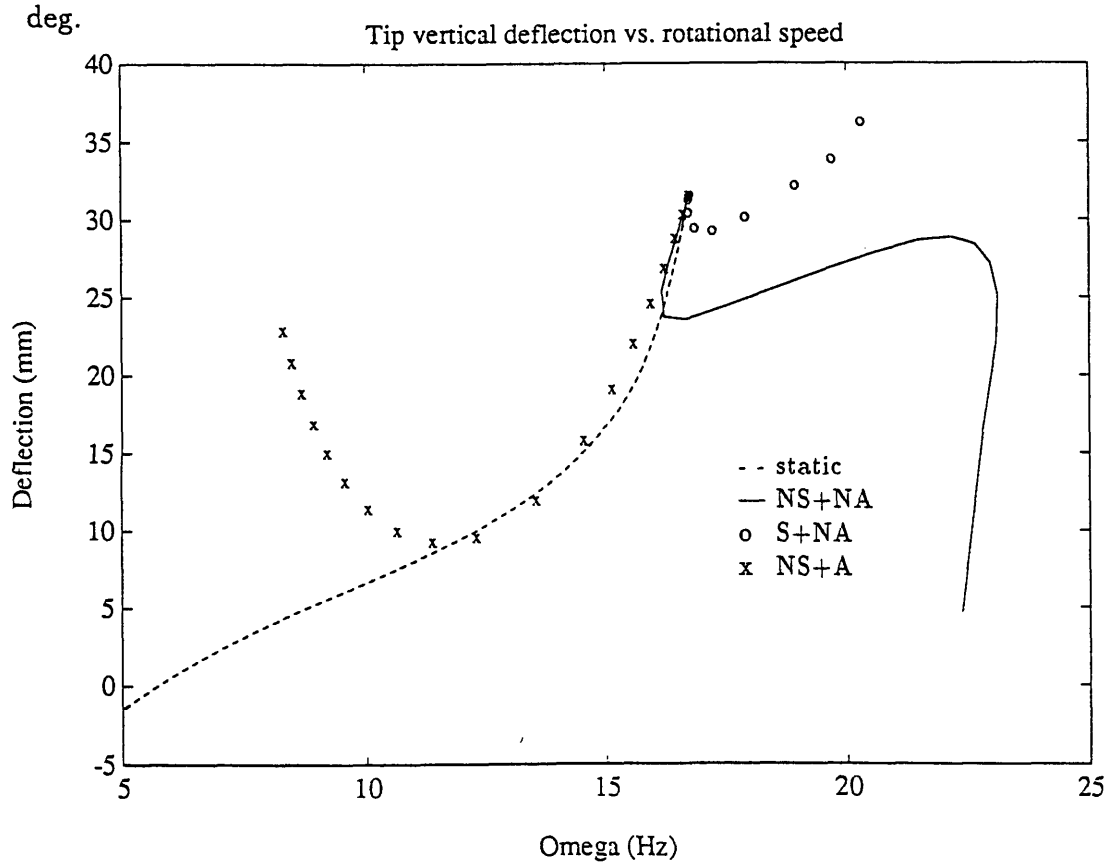

Figure 9.48: Tip average deflection vs. rotational speed; lag-hinged $[0/90]_{3s}$, $\theta_r = 3$ deg.

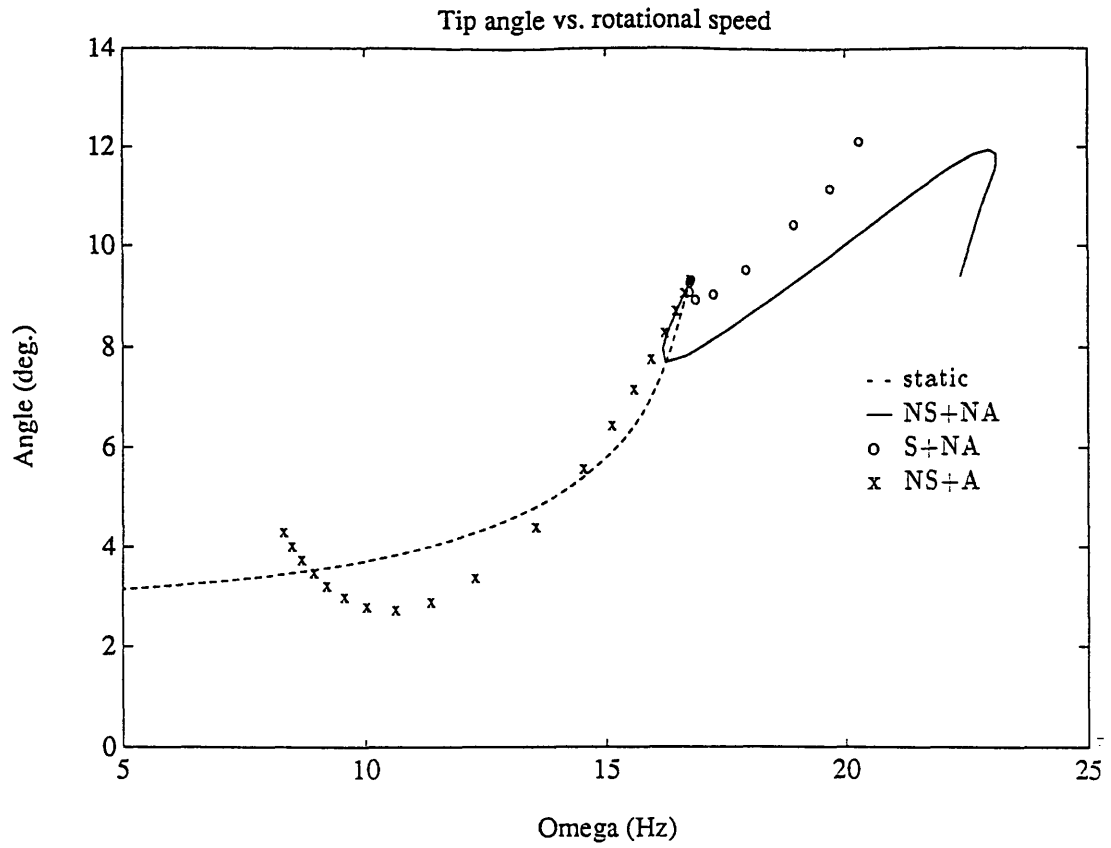

Figure 9.49: Tip average angle vs. rotational speed; lag-hinged $[0/90]_{3s}$, $\theta_r = 3$ deg.

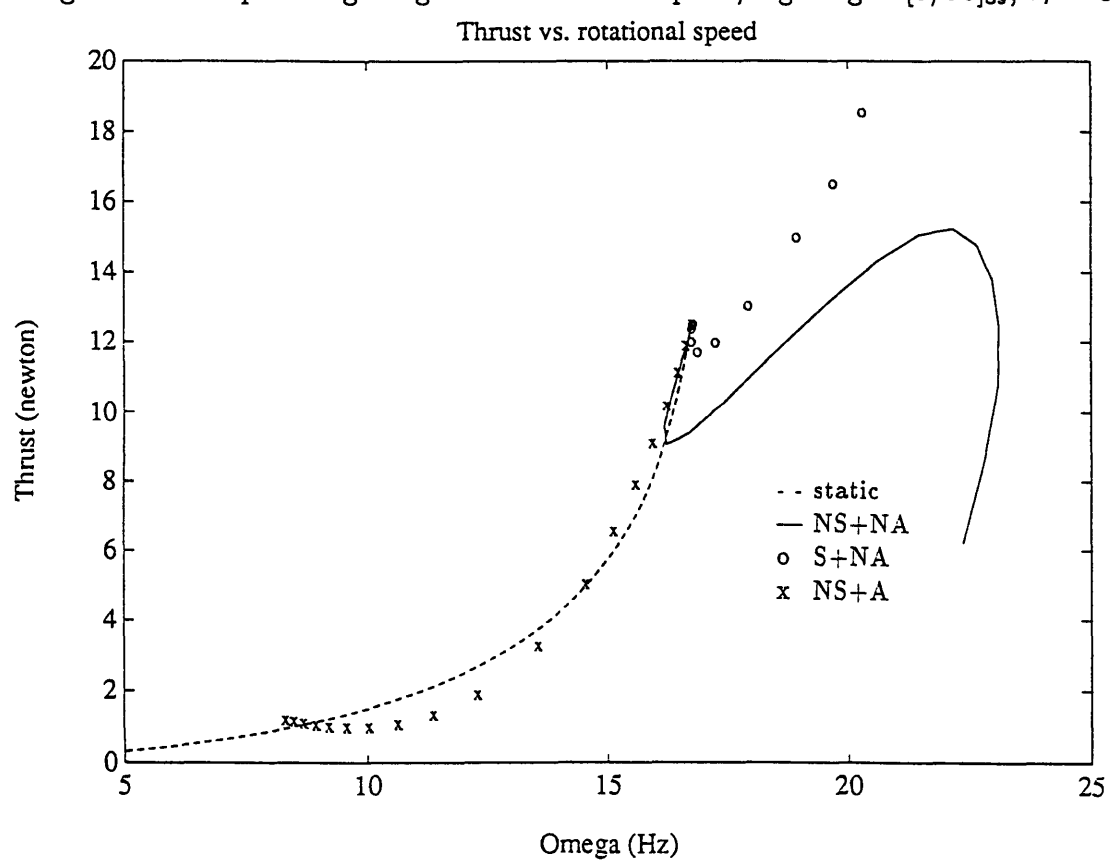

Figure 9.50: Average thrust level vs. rotational speed; lag-hinged $[0/90]_{3s}$, $\theta_r = 3$ deg.

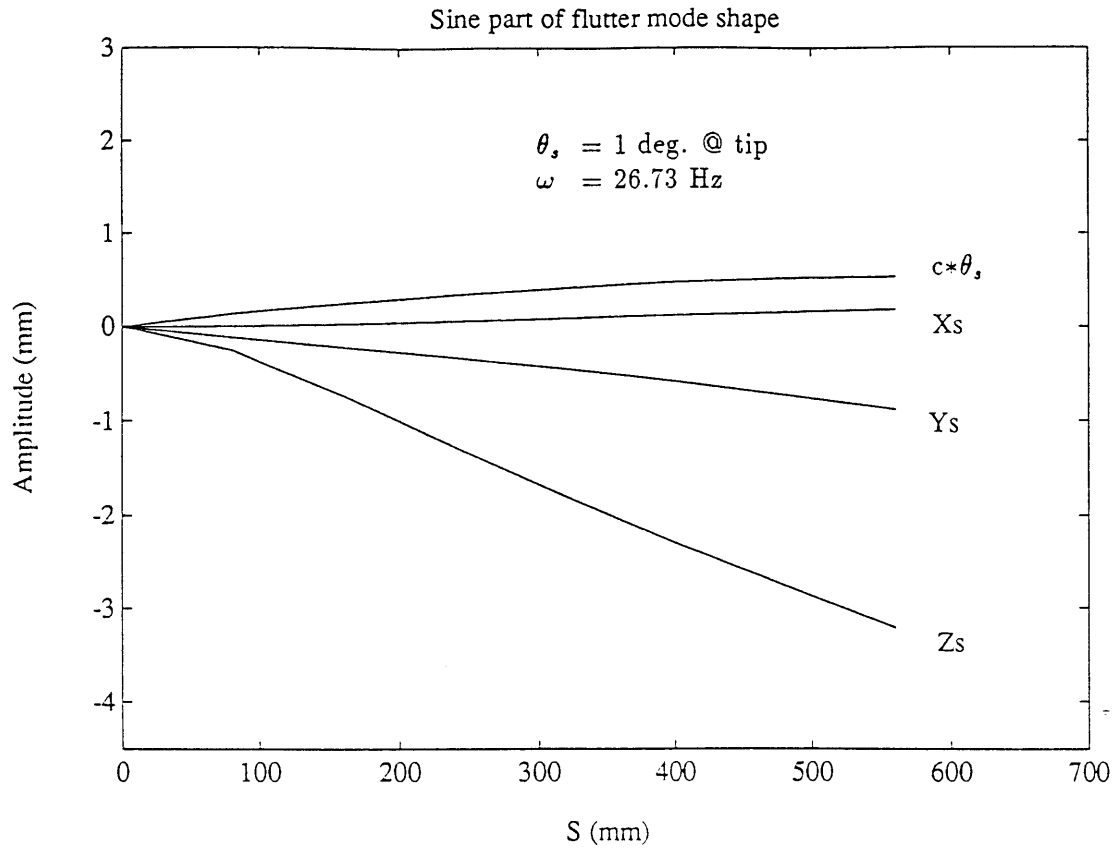

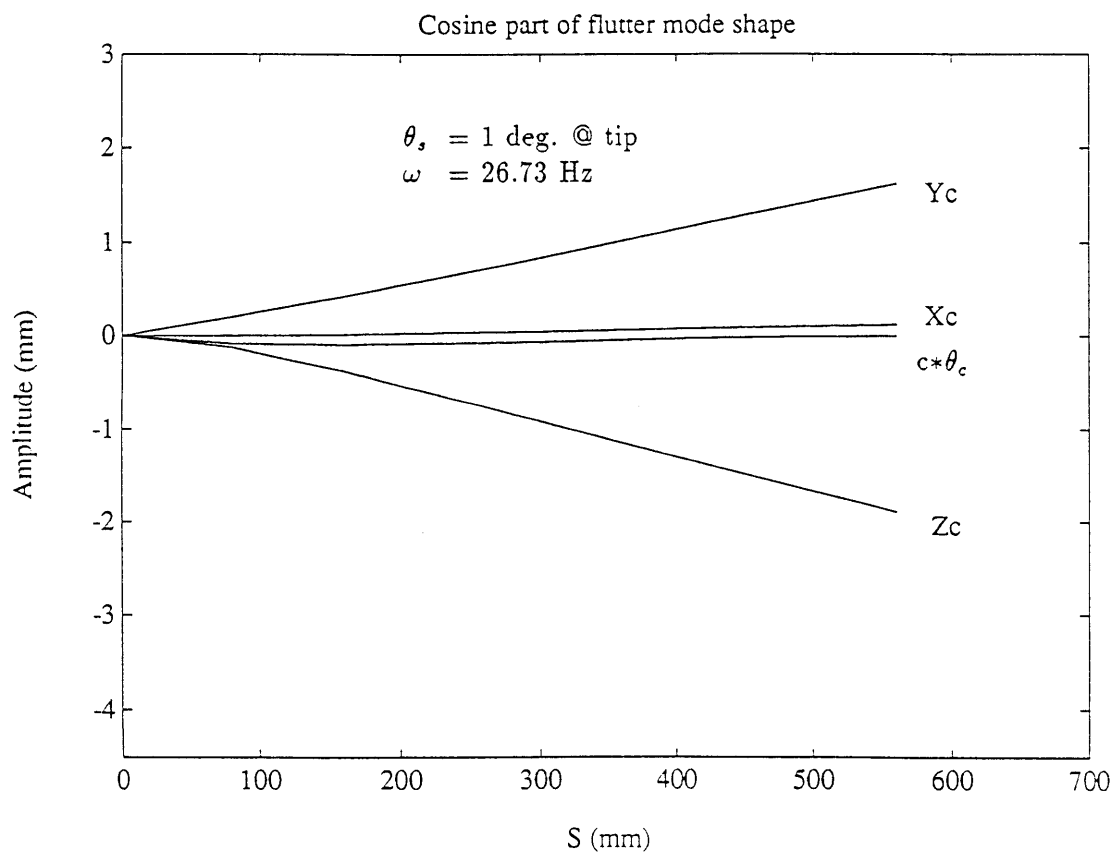

Figure 9.51: Flutter mode shape; lag-hinged $[0/90]_{3s}$, $\theta_r = 3$ deg., $\Omega = 16.64$ Hz

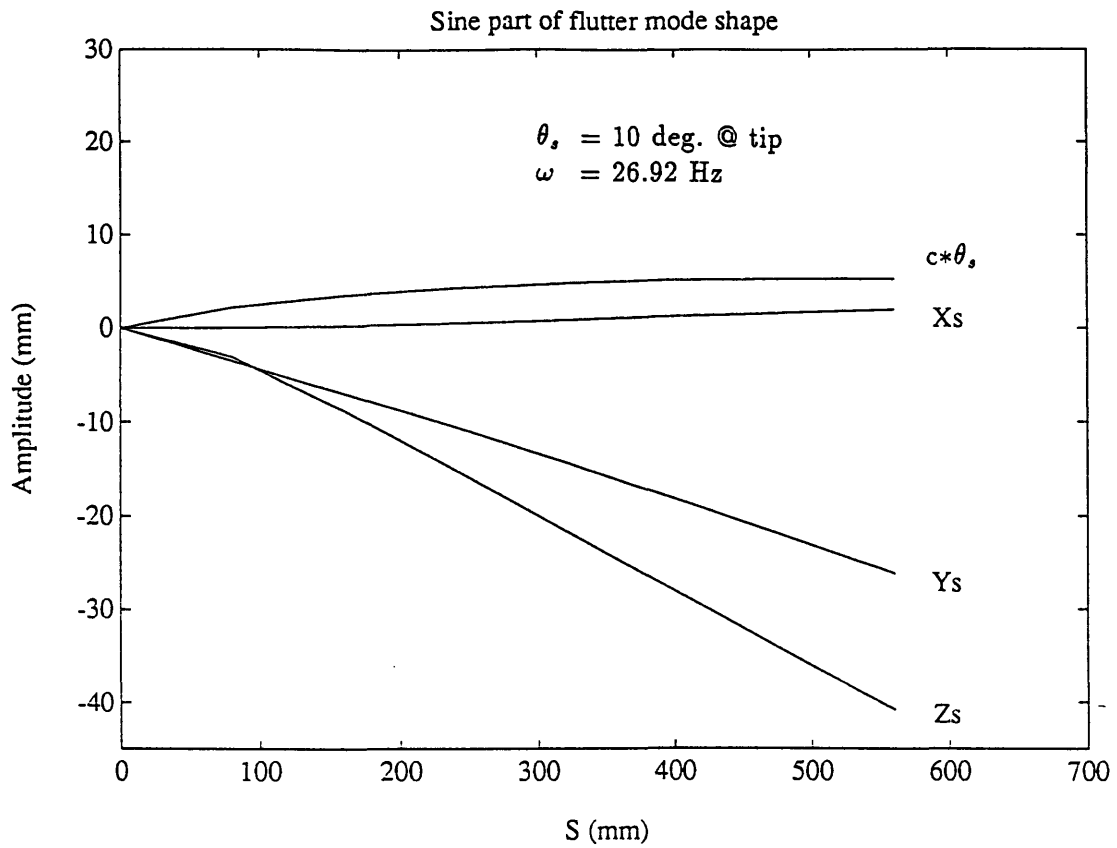

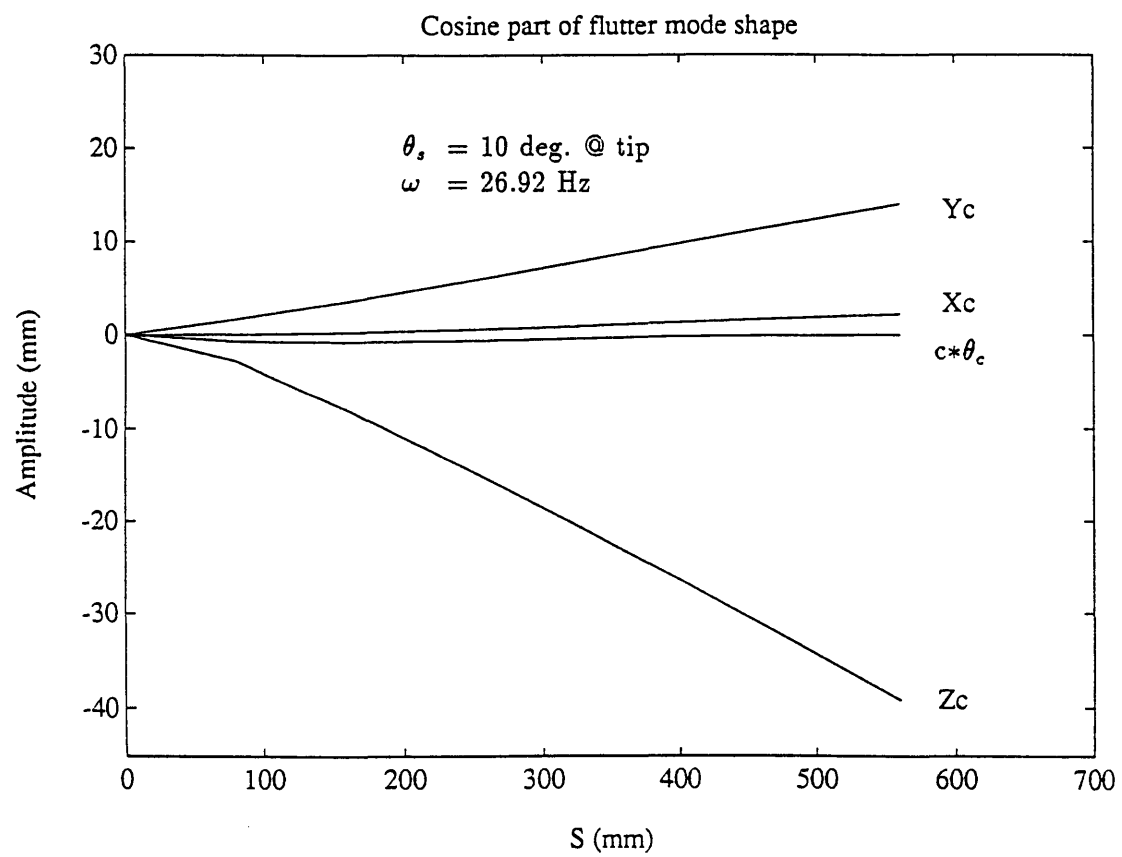

Figure 9.52: Flutter mode shape; lag-hinged $[0/90]_{3s}$, $\theta_r = 3$ deg., $\Omega = 20.58$ Hz

Chapter 10

Conclusions

In this final chapter, the most important and interesting findings of this research will be summarized, along with recommendations regarding some extension of the present work in the future.

Throughout the present research, it has been demonstrated that the new nonlinear analysis based on the differential equations derived by Minguet and Dugundji, and iterative methods based on harmonic balance and numerical integration of the basic equations is efficient for large amplitude structural and aeroelastic problems of composite rotor blades. These include the nonlinear, large amplitude nonrotating and rotating free vibration problems, nonlinear large static deformation and nonlinear, large amplitude aeroelastic limit cycle problems with dynamic stall in hover. The new nonlinear, large amplitude phenomena found in both the free vibration and the aeroelastic system have never been issues in the literature, and should now shed some insights into the complex nonlinear structural and aerodynamic interactions occurring in composite, aeroelastically tailored helicopter blades.

First, investigation of nonlinear large amplitude free vibration behavior of nonrotating and rotating blades has been performed on hingeless blades of two different lay-ups $[0/90]_{3s}$ and $[45/0]_s$ of graphite/epoxy composite beams under various static deflections. It has been analytically and experimentally shown, for the nonrotating case, that both large static deflection and large amplitude can affect significantly the fore-and-aft modes and torsion modes, but not much the bending modes. It was also

found that modal analysis based on use of moderate deflection equations developed by Hodges and Dowell may not yield accurate results for the nonlinear, large amplitude vibration problems of the rotor blade, particularly in the large amplitude ranges. The numerical results for rotating free vibration indicate a hardening phenomenon due to centrifugal forces in all modes except the torsional modes. More specific conclusions as for the large amplitude nonrotating and rotating free vibrations are as follows.

(1) Increasing amplitude level has slight stiffening effects in bending modes whereas it has significant softening effects in 1F, 1T modes, particularly for moderate range of static tip deflections. As a result, the natural frequencies of bending modes rise slightly while those of 1F and 1T modes always drop.

(2) Increasing amplitude level of a particular mode also results in changes in static deformations that are small for the bending modes but significant for the 1F and 1T modes, particularly for moderate static tip deflections. The 1F centershift seems to increase considerably with amplitude level.

(3) The $[90/0]_{3s}$ or any isotropic blade with zero root angle has significant second harmonic contents in the 1F mode for small static tip deflections. These appear mostly in the bending amplitude z_s. If the root angle is not zero, or there is bending-torsion coupling however, the second harmonics may not be as strong.

(4) It is shown that modal analysis based on a traditional second ordering scheme does not model the large amplitude vibration adequately. A set of equations based upon higher ordering scheme and/or inclusion of higher harmonic terms may be needed.

(5) All of the basic modes except torsional modes become slightly stiffened if the blade is in rotation.

(6) Experiments on large amplitude nonrotating blade vibrations confirm the general trends of the analysis, particularly for the fore-and-aft modes.

Next, investigation of nonlinear large amplitude aeroelastic behavior of rotating blades in hover has been performed on hingeless blades of two lay-ups, $[0/90]_{3s}$ and

$[45/0]_s$. Also, a $[0/90]_{3s}$ lag-hinged blade with lag spring constraint has been briefly considered. The linear flutter solutions were first obtained by transfer matrix method, and large amplitude solutions that evolve from these linear solutions were sought. More specific conclusions regarding the nonlinear large amplitude stall flutter of the composite rotor blades are as follows.

(1) The $[0/90]_{3s}$ blade yields results that show dominant hardening trend in the moderate range of amplitudes, but equally strong softening trend in the higher range of amplitudes.

(2) The initial hardening in the $[0/90]_{3s}$ blade is due to the dynamic stall effects, while the later softening is mainly due to the large amplitude effects in the nonlinear structure.

(3) The effects of both the nonlinear structure and the dynamic stall on the large amplitude aeroelastic behavior become significant when the root pitch is large or when stall occurs initially.

(4) The structural softening effect in the $[0/90]_{3s}$ blade is attributted to the proximity of the flutter mode shapes to the fore-and-aft mode of free vibration.

(5) The $[45/0]_s$ blade with a wash-in bending-twist coupling has strong hardening effects due to nonlinear structure, but seems stable in most range of amplitudes.

(6) The structural hardening effect in the $[45/0]_s$ blade may be due to lack of lag motion and existence of high bending motion in the flutter mode shapes as a result of the bending-twist coupling.

(7) The lag-hinged $[0/90]_{3s}$ blade has different flutter modes than the hingeless blades, but it can still have softening effects due to nonlinear structure.

As for possible future work, first, stability of the nonlinear aeroelastic limit cycle solutions can be checked by perturbing the coefficients in the basic harmonic expression, and, second, more research can be performed on other types of blades, with more realistic blade specifications, and more reliable dynamic stall characteristics. Third, it would be interesting to include higher harmonic terms and see the effects of

the higher harmonics on the stalled limit cycles. Lastly, a series of hovering tests can be performed on the same blade models to verify the analytic findings of the present research on the nonlinear aeroelastic stall flutter of the composite blades.

Bibliography

[1] Ormiston, R.A., "Investigation of Hingeless Rotor Stability", Vertica, Vol. 7, No. 2, March 1983.

[2] Friedmann, P.P., "Recent Developments in Rotary-Wing Aeroelasticity", Journal of Aircraft, Vol. 14, November 1977, pp. 1027-1041.

[3] Yuan, I., and Friedmann, P.P., "A New Aeroelastic Model for Composite Rotor Blades with Straight and Swept Tips", paper presented at 33rd AIAA/ASME/ASCE/AHS/ASC Structures, Structural Dynamics and Materials Conference, April 1991, Dallas, TX.

[4] Nixon, M.W., "Improvement to Tilt Rotor Performance Trough Passive Blade Twist Control", NASA TM 100583, April 1988.

[5] Lake, R.C., and Nixon, M.W., "A preliminary Investigation of Finite Element Modeling for Composite Rotor Blades", NASA TM 100559, January 1988.

[6] Nixon, M.W., "Preliminary Structural Design of Composite Main Rotor Blades for Minimum Weight", NASA TP 2730, July 1987.

[7] Hodges, and R.V., Nixon, M.W., "Comparison of Composite Rotor Blade Models: a Coupled-Beam and an MSC-NASTRAN Finite-Element Model", NASA TM 89024, March 1987.

[8] Hong, C.H, and Chopra, I., "Aeroelastic Stability Analysis of a Composite Rotor Blade", J. Amer. Helicopter Society, Vol. 26, 57-67, 1985.

[9] Panda, B., and Chopra, I., "Dynamics of Composite Rotor Blades in Forward Flight", Vertica, Vol. 11, No. 1/2, 1987, pp. 187-209.

[10] Hodges, D.H., and Dowell, E.H., "Nonlinear Equations of Motion for the Elastic Bending and Torsion of Twisted Non-uniform Rotor Blades", NASA TN D-7818, December 1974.

[11] Boyd, W.N., "Effect of Chordwise Forces and Deformations and Deformations due to Steady Lift on Wing Flutter", SUDAAR No. 508, Department of Aeronautics and Astronautics, Stanford University, Stanford, California, December 1977.

[12] Hodges, D.H., Hopkins, A.S., Kunz, D.L., and Hinant, H.E., "Introduction to GRASP-General Rotorcraft Aeromechanical Stability Program. A Modern Approach to Rotorcraft Modeling", J. Amer. Helicopter Society, Vol. 32, April 1987, pp.78-90.

[13] Minguet, P.J., "Static and Dynamic Behavior of Composite Helicopter Rotor blades under Large deflection", TELAC Report 89-7A, Department of Aeronautics and Astronautics, M.I.T., Cambridge, Massachusetts, May 1989.

[14] Minguet, P.J., and Dugundji, J.,"Experiments and Analysis for Composite Blades Under Large Deflections. Part 1: Static Behavior, Part 2: Dynamic Behavior", AIAA Journal, Vol. 28, September 1990, pp. 1573-1588.

[15] Chung, Y., and Hodges, D.H., "Discrete Transfer Matrix Method for Rotary Beams", paper presented at 33rd AIAA/ASME/ASCE/AHS/ASC Structures, Structural Dynamics and Materials Conference, April 1991, Dallas, TX.

[16] Crespo da Silva, M.R.M., "Flap-Lag-Torsional Dynamics of Rotor Blades By a Direct, "Transfer Matrix", Method", 23rd Workshop on Dynamics and Aeroelasticity Stability Modeling of Rotorcraft Systems, Duke University, Durham, North Caroliana, March 1990.

[17] Theodorsen, T., "General Theory of Aerodynamic Instability and the Mechanism of Flutter", NACA Rep. No. 496, 1935

[18] Von Karman, T., and Sears, W.R., "Airfoil Theory for Non-Uniform Motion", Journal of the Aeronautical Sciences, Vol. 5, No. 10, August 1938, pp. 379-390.

[19] Greenberg, J.M., "Airfoil in Sinusoidal Motion in a Pulsating Stream", NACA TN No. 1326, 1947.

[20] Loewy, R.G., "A Two-dimensional Approximation to the Unsteady Aerodynamics of Rotary Wings", Journal of the Aeronautical Sciences, Vol. 24, No. 144, 1957, pp. 81-92.

[21] Ham, N.D., "An Experimental Investigation of Stall Flutter", J. Amer. Helicopter Society, Vol. 7, January, 1962, pp. 3-16.

[22] Ham, N.D., "Torsional Oscillation of Helicopter Blades Due to Stall", Journal of Aircraft, Vol. 3, No. 3, May-June 1966, pp. 218-224.

[23] McCroskey, W.J., "The Phenomenon of Dynamic Stall", NASA TM 81264, 1981.

[24] Mehta, U.B., "Dynamic Stall of an Oscillating Airfoil", AGARD Paper No. 23, 1977.

[25] Tran, C.T., and Petot, D., "Semi-Empirical Model for the Dynamic Stall of Airfoils in View of their Application to the Calculation of Responses of a Helicopter Rotor in Forward Flight," Vertica, Vol. 5, No. 1, 1981, pp. 35-53.

[26] Friedmann, P.P., 212z"Helicopter Rotor Dynamics and Aeroelasticity: Some Key Ideas and Insights", Vertica, Vol. 14, No. 1, 1990, pp. 101-121.

[27] Bergh, H., and Van der Wekken, J.P., "Comparison Between Measured and Calculated Stall-Flutter Behaviour of a One-Bladed Model Rotor", Vertica, Vol. 11, No. 3, 1987, pp. 447-456.

[28] Chopra, I., and Dugundji, J., "Non-linear Dynamic Response of a Wind Turbin Blade", Journal of Sound and Vibration, Vol. 63, 1979, pp. 265-286.

[29] Dunn, P.E., and Dugundji, J., "Nonlinear Stall Flutter and Divergence Analysis of Cantilevered Graphite/Epoxy Wings", AIAA Journal, Vol. 30, No. 1, January 1992, pp. 153-162.

[30] Tang, D., and Dowell, E., "Experimental and Theoretical Study for Nonlinear Aeroelastic Behavior of a Flexible Rotor Blades", paper presented at 33rd AIAA/ASME/ASCE/AHS/ASC Structures, Structural Dynamics and Materials Conference, April 1991, Dallas, TX.

[31] Reissner, E., and Stein, M., "Torsion and Transverse Bending of Cantilever Plates", NACA TN 2369, 1951.

[32] Crawley, E.F., and Dugundji, J., "Frequency Determination and Non-Dimensionalization for Composite Cantilever Plates", Journal of Sound and Vibration, Vol. 72, No. 1, 1980, pp. 1-10.

[33] Dinyavari, M.A.H., and Friedmann, P.P., "Application of Time-Domain Unsteady Aerodynamics to Rotary-Wing Aeroelasticity", AIAA Journal, Vol. 24, No. 9, 1986, pp. 1424-1432,

[34] Venkatesan, C., and Friedmann, P.P., "Finite State Modeling of Unsteady Aerodynamics and Its Application to a Rotor Dynamic Problem", Proceedings of the 11th European Rotorcraft Forum, London, Paper No. 72, 1985.

[35] Peters, D.A., and HaQuang, Ninh, "Dynamic Inflow for Practical Applications", Journal of the American Helicopter Society, Vol. 33, No. 4, October 1988, pp. 64-68.

[36] Peters, D.A., Boyd, D.D., and He, C.H., "Finite State Induced-Flow Model for Rotor in Hover and Forward Flight", Journal of the American Helicopter Society, Vol. 34, No. 4, 1989, pp. 5-17.

[37] Tran, C.T., and Falchero, D., "Application of the ONERA Dynamic Stall Model to a Helicopter Blade in Forward Flight", Vertica, Vol. 6, 1982, pp. 219-239.

[38] Rogers, J.P., "Application of an Analytic Stall Model to Time History and Eigenvalue Analysis of Rotor Blades", Journal of the American Helicopter Society, Vol. 29, No. 1, 1984, pp. 25-33.

[39] Peters, D.A., "Toward a Unified Lift Model for Use in Rotor Blade Stability Analysis", Journal of the American Helicopter Society, Vol. 30, No. 3, 1985, pp. 32-42.

[40] Petot, D., and Dat, R., "Unsteady Aerodynamic Loads on an Oscillating Airfoil with Unsteady Stall", 2nd Workshop on Dynamics and Aeroelasticity Stability Modeling of Rotorcraft Systems, Florida Atlantic University, Boca Raton, Florida, November 1987.

[41] Barwey, D., Gaonkar, G.H., and Ormiston R.A., "Investigation of Dynamic Stall Effects on Isolated Rotor Flap-Lag Stability with Experimental Correction", Journal of the American Helicopter Society, Vol. 36, No. 4, 1991, pp. 12-24.

[42] Jacobs, E.N., and Sherman, A., "Airfoil Section Characteristics as Affected by Variations of the Reynolds Number", NACA Report No. 586, 1937.

[43] Bisplinghoff, R.L., Ashley, H., and Halfman, R.L., Aeroelasticity, Addison-Wesley, Co., 1955.

[44] McAllister, K.W., Pucci, S.L., and McCroskey, W.J., Carr, L.W., "An experimental Study of Dynamic Stall on Advanced Airfoil Section", NATM-84245.

[45] Brown, K.M., and Dennis, J.E., "Derivative Free Analogues of the Levenberg-Marquardt and Gauss Algorithms for Nonlinear Least Squares Approximation", Numerische Mathematik, 18, pp 289-297, 1972.

[46] Isakson, G., and Eisley, J.G., "Natural Frequencies in Coupled Bending and Torsion of Twisted Rotating and Nonrotating Blades", NASA CR-65, July 1964.

[47] Meirovitch, L., Elements of Vibration Analysis, McGraw-Hill, Inc., 1975.

Appendix A

Calculation of Coefficients of Harmonic Quantities

In section 5.1 it was suggested that for large amplitude motion, every variable be expressed as

$$X(\Omega,\omega,t) \;=\; X_0(\Omega,\omega) + X_s(\Omega,\omega)\sin\omega t + X_c(\Omega,\omega)\cos\omega t$$

where X_0, and X_s, X_c represent the static and dynamic components of a particular variable. Consequently, all of the quantities in the original twelve governing equations will take the above form immediately. Recall, however, that many of the terms in the equations involve trigonometric functions and their arguments are the three Euler angles ψ,β,θ. Then, one can not apply harmonic balance method with the Euler angles expressed as above and themselves inside the trigonometric functions. Therefore, it is useful to rely on series expansion versions of these trigonometric functions. Let x represent any of the three Euler angles, and let $X(x)$ be any trigonometric function, i. e. $\cos x$, $\sin x$, $\tan x$, or $1/\cos x$. Then substituting

$$x \;=\; x_0 + x_s\sin\omega t + x_c\cos\omega t$$

into the function X and expanding in a Taylor series about x_0 yields

$$
\begin{aligned}
X(x) &= X(x_0) + \frac{dX}{ds}(x_0)\, x_s \sin\omega t + \frac{dX}{ds}(x_0)\, x_c \cos\omega t \\
&\quad + 1/2\, \frac{d^2X}{dx^2}(x_0)\, x_s^2 \sin^2\omega t + 1/2\, \frac{d^2X}{dx^2}(x_0)\, x_c^2 \cos^2\omega t \\
&\quad + \frac{d^2X}{dx^2}(x_0)\, x_s x_c \sin\omega t \cos\omega t + 1/6\, \frac{d^3X}{dx^3}(x_0)\, x_s^3 \sin^3\omega t \\
&\quad + 1/6\, \frac{d^3X}{dx^3}(x_0)\, x_c^3 \cos^3\omega t + 1/2\, \frac{d^3X}{dx^3}(x_0)\, x_s^2 x_c \sin^2\omega t \cos\omega t \\
&\quad + 1/2\, \frac{d^3X}{dx^3}(x_0)\, x_s x_c^2 \sin\omega t \cos^2\omega t + \text{H. O. T.} \\
&= X_0 + X_s \sin\omega t + X_c \cos\omega t + X_{s2} \sin^2\omega t \\
&\quad + X_{c2} \cos^2\omega t + X_{sc} \sin\omega t \cos\omega t + X_{s3} \sin^3\omega t \\
&\quad + X_{c3} \cos^3\omega t + X_{s2c} \sin^2\omega t \cos\omega t + X_{sc2} \sin\omega t \cos^2\omega t \\
&\quad + \text{H. O. T.}
\end{aligned} \tag{A.1}
$$

where

$$
\begin{aligned}
X_0 &\equiv X(x_0) \\
X_s &\equiv \frac{dX}{dx}(x_0)\, x_s \\
X_c &\equiv \frac{dX}{dx}(x_0)\, x_c \\
X_{s2} &\equiv 1/2\, \frac{d^2X}{dx^2}(x_0)\, x_s^2 \\
X_{c2} &\equiv 1/2\, \frac{d^2X}{dx^2}(x_0)\, x_c^2 \\
X_{sc} &\equiv \frac{d^2X}{dx^2}(x_0)\, x_s x_c \\
X_{s3} &\equiv 1/6\, \frac{d^3X}{dx^3}(x_0)\, x_s^3 \\
X_{c3} &\equiv 1/6\, \frac{d^3X}{dx^3}(x_0)\, x_c^3 \\
X_{s2c} &\equiv 1/2\, \frac{d^3X}{dx^3}(x_0)\, x_s^2 x_c \\
X_{sc2} &\equiv 1/2\, \frac{d^3X}{dx^3}(x_0)\, x_s x_c^2
\end{aligned} \tag{A.2}
$$

Here according to our ordering scheme only terms up to third order are kept in

the expansion (see section 5.1). Then, when applying harmonic balance methods, the $\sin^2 \omega t$, $\sin^3 \omega t$, and $\cos^2 \omega t$, $\cos^3 \omega t$ can be expanded into constant, $\sin \omega t$, and $\cos \omega t$ type terms after multiplication with other harmonic quantities, as shown in Appendices B and C.

In the current analysis four different trigonometric functions are encountered. They are $\cos x$, $\sin x$, $\tan x$, and $1/\cos x$. According to above expansion rules then each trigonometric function can be expressed, up to third order, as

$$\begin{aligned}
\cos x \;=\; & \cos x_0 - (\sin x_0)\, x_s \sin \omega t - (\sin x_0)\, x_c \cos \omega t \\
& - 1/2\,(\cos x_0)\, x_s^2 \sin^2 \omega t - 1/2\,(\cos x_0)\, x_c^2 \cos^2 \omega t \\
& + 1/6\,(\sin x_0)\, x_s^3 \sin^3 \omega t + 1/6\,(\sin x_0)\, x_c^3 \cos^3 \omega t \\
& + 1/2\,(\sin x_0)\, x_s^2 x_c \sin^2 \omega t \cos \omega t \\
& + 1/2\,(\sin x_0)\, x_s x_c^2 \sin \omega t \cos^2 \omega t
\end{aligned} \tag{A.3}$$

$$\begin{aligned}
\sin x \;=\; & \sin x_0 + (\cos x_0)\, x_s \sin \omega t + (\cos x_0)\, x_c \cos \omega t \\
& - 1/2\,(\sin x_0)\, x_s^2 \sin^2 \omega t - 1/2\,(\sin x_0)\, x_c^2 \cos^2 \omega t \\
& - 1/6\,(\cos x_0)\, x_s^3 \sin^3 \omega t - 1/6\,(\cos x_0)\, x_c^3 \cos^3 \omega t \\
& - 1/2\,(\cos x_0)\, x_s^2 x_c \sin^2 \omega t \cos \omega t \\
& - 1/2\,(\cos x_0)\, x_s x_c^2 \sin \omega t \cos^2 \omega t
\end{aligned} \tag{A.4}$$

$$\begin{aligned}
\tan x \;=\; & \tan x_0 + (1/\cos^2 x_0)\, x_s \sin \omega t + (1/\cos^2 x_0)\, x_c \cos \omega t \\
& + (\tan x_0/\cos^2 x_0)\, x_s^2 \sin^2 \omega t + (\tan x_0/\cos^2 x_0)\, x_c^2 \cos^2 \omega t \\
& + 2\,(\tan x_0/\cos^2 x_0)\, x_s x_c \sin \omega t \cos \omega t \\
& + 1/3\,\{(2\tan^2 x_0 + 1/\cos^2 x_0)\,/\cos^2 x_0\} x_s^3 \sin^3 \omega t \\
& + 1/3\,\{(2\tan^2 x_0 + 1/\cos^2 x_0)\,/\cos^2 x_0\} x_c^3 \cos^3 \omega t \\
& + \{(2\tan^2 x_0 + 1/\cos^2 x_0)\,/\cos^2 x_0\} x_s^2 x_c \sin^2 \omega t \cos \omega t
\end{aligned}$$

$$+\{(2\tan^2 x_0 + 1/\cos^2 x_0)/\cos^2 x_0\} x_s x_c^2 \sin\omega t \cos^2\omega t \qquad \text{(A.5)}$$

$$\begin{aligned}
1/\cos x \;=\; & 1/\cos x_0 + (\tan x_0/\cos x_0)\, x_s \sin\omega t + (\tan x_0/\cos x_0)\, x_c \cos\omega t \\
& + 1/2\,(1/cos^3 x_0 + \tan^2 x_0/\cos x_0)\, x_s^2 \sin^2\omega t \\
& + 1/2\,(1/cos^3 x_0 + \tan^2 x_0/\cos x_0) \\
& .\, x_c^2 \cos^2\omega t + (1/cos^3 x_0 + \tan^2 x_0/\cos x_0)\, x_s x_c \sin\omega t \cos\omega t \\
& + 1/6\,(5\tan x_0/\cos^3 x_0 + \tan^3 x_0/\cos x_0)\, x_s^3 \sin^3\omega t \\
& + 1/6\,(5\tan x_0/\cos^3 x_0 + \tan^3 x_0/\cos x_0)\, x_c^3 \cos^3\omega t \\
& + 1/2\,(5\tan x_0/\cos^3 x_0 + \tan^3 x_0/\cos x_0)\, x_s^2 x_c \sin^2\omega t \cos\omega t \\
& + 1/2\,(5\tan x_0/\cos^3 x_0 + \tan^3 x_0/\cos x_0)\, x_s x_c^2 \sin\omega t \cos\omega t \qquad \text{(A.6)}
\end{aligned}$$

Appendix B

Multiplication of Two Harmonic Quantities

In Appendix A it was seen that any harmonic quantity can be expressed, up to third order, as

$$\begin{aligned} X &= X_0 + X_s \sin\omega t + X_c \cos\omega t + X_{s2} \sin^2\omega t + X_{c2} \cos^2\omega t \\ &\quad + X_{sc} \sin\omega t \cos\omega t + X_{s3} \sin^3\omega t + X_{c3} \cos^3\omega t \\ &\quad + X_{s2c} \sin^2\omega t \cos\omega t + X_{sc2} \sin\omega t \cos^2\omega t \end{aligned} \tag{B.1}$$

where X_0, X_s, X_c, X_{s2}, etc. are determined by the formula A.2. $X(x)$ could be either a harmonic variable itself (e.g. F,M,x,... etc.) or a trigonometric function. If it is a harmonic variable all of the coefficients after X_c are identically zero. Also, if one is dealing with nonrotating free vibration problem, then all of the coefficients that are multiplied by $\sin\omega t$ are zero. Now let's consider a product of two quantities, X and Y which are expressed as above. It can be shown that

$$\begin{aligned} XY &= (X_0 + X_s \sin\omega t + X_c \cos\omega t + X_{s2} \sin^2\omega t + X_{c2} \cos^2\omega t \\ &\quad + X_{sc} \sin\omega t \cos\omega t + X_{s3} \sin^3\omega t + X_{c3} \cos^3\omega t \\ &\quad + X_{s2c} \sin^2\omega t \cos\omega t + X_{sc2} \sin\omega t \cos^2\omega t) \\ &\quad .(Y_0 + Y_s \sin\omega t + Y_c \cos\omega t + Y_{s2} \sin^2\omega t + Y_{c2} \cos^2\omega t \\ &\quad + Y_{sc} \sin\omega t \cos\omega t + Y_{s3} \sin^3\omega t + Y_{c3} \cos^3\omega t \end{aligned}$$

$$
\begin{aligned}
& + Y_{s2c} \sin^2 \omega t \cos \omega t + Y_{sc2} \sin \omega t \cos^2 \omega t) \\
= \; & (XY)_0 + (XY)_s \sin \omega t + (XY)_c \cos \omega t + (XY)_{s2} \sin^2 \omega t \\
& + (XY)_{c2} \cos^2 \omega t + (XY)_{sc} \sin \omega t \cos \omega t + (XY)_{s3} \sin^3 \omega t \\
& + (XY)_{c3} \cos^3 \omega t + (XY)_{s2c} \sin^2 \omega t \cos \omega t \\
& + (XY)_{sc2} \sin \omega t \cos^2 \omega t
\end{aligned} \tag{B.2}
$$

where

$$
\begin{aligned}
(XY)_0 &\equiv X_0 Y_0 \\
(XY)_s &\equiv X_0 Y_s + X_s Y_0 \\
(XY)_c &\equiv X_0 Y_c + X_c Y_0 \\
(XY)_{s2} &\equiv X_0 Y_{s2} + X_s Y_s + X_{s2} Y_0 \\
(XY)_{c2} &\equiv X_0 Y_{c2} + X_c Y_c + X_{c2} Y_0 \\
(XY)_{sc} &\equiv X_0 Y_{sc} + X_s Y_c + X_c Y_s + X_{sc} Y_0 \\
(XY)_{s3} &\equiv X_0 Y_{s3} + X_s Y_{s2} + X_{s2} Y_s + X_{s3} Y_0 \\
(XY)_{c3} &\equiv X_0 Y_{c3} + X_c Y_{c2} + X_{c2} Y_c + X_{c3} Y_0 \\
(XY)_{s2c} &\equiv X_0 Y_{s2c} + X_s Y_{sc} + X_{s2} Y_c + X_c Y_{s2} \\
&\quad + X_{sc} Y_s + X_{s2c} Y_0 \\
(XY)_{sc2} &\equiv X_0 Y_{sc2} + X_s Y_{c2} + X_c Y_{sc} + X_{sc} Y_c \\
&\quad + X_{c2} Y_s + X_{sc2} Y_0
\end{aligned}
$$

When applying harmonic balance method only the static and the first harmonic terms are retained. For this purpose note that

$$
\begin{aligned}
\sin^2 \omega t &= 1/2 - 1/2 \cos 2\omega t \\
\cos^2 \omega t &= 1/2 + 1/2 \cos 2\omega t \\
\sin \omega t \cos \omega t &= 1/2 \sin 2\omega t \\
\sin^3 \omega t &= 3/4 \sin \omega t - 1/4 \sin 3\omega t
\end{aligned}
$$

$$
\begin{aligned}
\cos^3 \omega t &= 3/4 \cos \omega t + 1/4 \cos 3\omega t \\
\sin^2 \omega t \cos \omega t &= 1/4 \cos \omega t - 1/4 \cos 3\omega t \\
\sin \omega t \cos^2 \omega t &= 1/4 \sin \omega t + 1/4 \sin 3\omega t
\end{aligned}
$$

So after neglecting higher harmonics one gets

$$
\begin{aligned}
XY = & [(XY)_0 + 1/2\{(XY)_{s2} + (XY)_{c2}\}] + [(XY)_s + 3/4(XY)_{s3} \\
& + 1/4(XY)_{sc2}] \sin \omega t + [(XY)_c + 3/4(XY)_{c3} \\
& + 1/4(XY)_{s2c}] \cos \omega t
\end{aligned} \tag{B.3}
$$

Appendix C

Multiplication of Three Harmonic Quantities

Some of the governing equations such as equation 2.7, and some of the transformation matrix elements contain products of three harmonic quantities. Multiplication of three harmonics X,Y,Z can then be performed as a series of two multiplications involving two harmonic quantities as follows.

$$
\begin{aligned}
XYZ &= (XY)Z \\
&= [(XY)_0 + (XY)_s \sin\omega t + (XY)_c \cos\omega t + (XY)_{s2} \sin^2\omega t \\
&\quad + (XY)_{c2} \cos^2\omega t + (XY)_{sc} \sin\omega t \cos\omega t + (XY)_{s3} \sin^3\omega t \\
&\quad + (XY)_{c3} \cos^3\omega t + (XY)_{s2c} \sin^2\omega t \cos\omega t + (XY)_{sc2} \sin\omega t \cos^2\omega t) \\
&\quad .(Z_0 + Z_s \sin\omega t + Z_c \cos\omega t + Z_{s2} \sin^2\omega t + Z_{c2} \cos^2\omega t \\
&\quad + Z_{sc} \sin\omega t \cos\omega t + Z_{s3} \sin^3\omega t + Z_{c3} \cos^3\omega t \\
&\quad + Z_{s2c} \sin^2\omega t \cos\omega t + Z_{sc2} \sin\omega t \cos^2\omega t) \\
&= (XYZ)_0 + (XYZ)_s \sin\omega t + (XYZ)_c \cos\omega t + (XYZ)_{s2} \sin^2\omega t \\
&\quad + (XYZ)_{c2} \cos^2\omega t + (XYZ)_{sc} \sin\omega t \cos\omega t + (XYZ)_{s3} \sin^3\omega t \\
&\quad + (XYZ)_{c3} \cos^3\omega t + (XYZ)_{s2c} \sin^2\omega t \cos\omega t \\
&\quad + (XYZ)_{sc2} \sin\omega t \cos^2\omega t
\end{aligned}
\tag{C.1}
$$

where

$$
\begin{aligned}
(XYZ)_0 &\equiv (XY)_0 Z_0 \\
(XYZ)_s &\equiv (XY)_0 Z_s + (XY)_s Z_0 \\
(XYZ)_c &\equiv (XY)_0 Z_c + (XY)_c Z_0 \\
(XYZ)_{s2} &\equiv (XY)_0 Z_{s2} + (XY)_s Z_s + (XY)_{s2} Z_0 \\
(XYZ)_{c2} &\equiv (XY)_0 Z_{c2} + (XY)_c Z_c + (XY)_{c2} Z_0 \\
(XYZ)_{sc} &\equiv (XY)_0 Z_{sc} + (XY)_s Z_c + (XY)_c Z_s + (XY)_{sc} Z_0 \\
(XYZ)_{s3} &\equiv (XY)_0 Z_{s3} + (XY)_s Z_{s2} + (XY)_{s2} Z_s + (XY)_{s3} Z_0 \\
(XYZ)_{c3} &\equiv (XY)_0 Z_{c3} + (XY)_c Z_{c2} + (XY)_{c2} Z_c + (XY)_{c3} Z_0 \\
(XYZ)_{s2c} &\equiv (XY)_0 Z_{s2c} + (XY)_s Zsc + (XY)_{s2} Z_c + (XY)_c Z_{s2} \\
&\quad + (XY)_{sc} Z_s + (XY)_{s2c} Z_0 \\
(XYZ)_{sc2} &\equiv (XY)_0 Z_{sc2} + (XY)_s Z_{c2} + (XY)_c Z_{sc} + (XY)_{sc} Z_c \\
&\quad + (XY)_{c2} Z_s + (XY)_{sc2} Z_0
\end{aligned}
$$

and $(XY)_0$, $(XY)_s$, $(XY)_c$, ... etc. are defined in the Appendix B. Once again, neglecting higher harmonics one gets

$$
\begin{aligned}
XYZ \;=\; & [(XYZ)_0 + 1/2\{(XYZ)_{s2} + (XYZ)_{c2}\}] + [(XYZ)_s + 3/4(XYZ)_{s3} \\
& + 1/4(XYZ)_{sc2}] \sin\omega t + [(XYZ)_c + 3/4(XYZ)_{c3} \\
& + 1/4(XYZ)_{s2c}] \cos\omega t
\end{aligned}
\tag{C.2}
$$

Appendix D

Fourier Analysis of Airforce Deviations

Fourier analysis of lift, moment and drag deviations are given. First, ΔC_z's are approximated by two straight line fits of low Reynolds number static curves of NACA 0012 airfoil.

$$\begin{aligned}
\Delta C_z &= 0 && \text{if } \alpha \leq \alpha_\Delta \\
\Delta C_z &= a_{z1}(\alpha - \alpha_\Delta) && \text{if } \alpha_\Delta < \alpha \leq \alpha_{\Delta 1} \\
\Delta C_z &= a_{z1}(\alpha - \alpha_\Delta) + a_{z2}(\alpha - \alpha_{\Delta 1}) \\
& && \text{if } \alpha > \alpha_{\Delta 1}
\end{aligned} \tag{D.1}$$

where

$$a_{L1} = 6.32284, \quad a_{L2} = -0.42284$$

$$a_{M1} = 0.65317, \quad a_{M2} = -0.48128$$

$$\alpha_\Delta = 8 \text{ degrees}, \quad \alpha_{\Delta 1} = 18 \text{ degrees}$$

For the drag deviation ΔC_D, the following cubic form was assumed.

$$\Delta C_D = -a_{D1}\,\alpha - a_{D2}\,\alpha^2 - a_{D3}\,\alpha^3 \tag{D.2}$$

where

$$a_{D1} = 0.042, \quad a_{D2} = 0.1473, \quad a_{D3} = 4.923$$

In the remainder of section, a single break point model with positive stall part is used for an illustration of the harmonic analysis of the lift and moment deviations. Fourier results of the drag deviation is also given using the full expression D.2. A stall delay of 10 units in the non-dimensional time τ is introduced by taking an initial portion corresponding to duration $10k$ in the non-dimensional time φ out of the Fourier integrals. The results can be extended to any model with more than a single line approximation by repeating within each disrete region, and then summing over the whole range of angle of attack according to equation 5.7.

For a single break point model of lift and moment deviations, let's assume

$$\begin{aligned} \Delta C_z &= a_{11z}(\alpha - \alpha_\Delta) \text{ for } \alpha \geq \alpha_\Delta \\ \Delta C_z &= 0 \quad \text{for } \alpha \leq \alpha_\Delta \end{aligned} \tag{D.3}$$

With the stall delay introduced, the Fourier integrals 5.6 are devided into two parts

$$\begin{aligned} \Delta C_{z0} &= \frac{1}{\pi}\int_{\varphi_\Delta}^{\frac{\pi}{2}} \Delta C_z(\varphi)\, d\varphi - \frac{1}{2\pi}\int_{\varphi_\Delta}^{\varphi_{\Delta 1}} \Delta C_z(\varphi)\, d\varphi \\ \Delta C_{zVs} &= \frac{2}{\pi}\int_{\varphi_\Delta}^{\frac{\pi}{2}} \Delta C_z(\varphi)\, \sin\varphi\, d\varphi - \frac{1}{\pi}\int_{\varphi_\Delta}^{\varphi_{\Delta 1}} \Delta C_z(\varphi)\, \sin\varphi\, d\varphi \\ \Delta C_{zVc} &= -\frac{1}{\pi}\int_{\varphi_\Delta}^{\varphi_{\Delta 1}} \Delta C_z(\varphi)\, \cos\varphi\, d\varphi \end{aligned} \tag{D.4}$$

Here, φ_Δ is the non-dimensional time in φ corresponding to the stall angle α_Δ while $\varphi_{\Delta 1}$ represents the non-dimensional time at which actual stall starts after the stall delay. Using the relation 5.3 these can be expressed as

$$\varphi_\Delta = \begin{cases} \frac{\pi}{2} \text{ (no stall)} & \text{if } \frac{\alpha_\Delta - \alpha_0}{\alpha_V} > 1 \\ -\frac{\pi}{2} \text{ (full stall)} & \text{if } \frac{\alpha_\Delta - \alpha_0}{\alpha_V} < -1 \\ \sin^{-1}(\frac{\alpha_\Delta - \alpha_0}{\alpha_V}) \text{ (partial stall)} & \text{elsewhere} \end{cases} \tag{D.5}$$

$$\varphi_{\Delta 1} = \begin{cases} \varphi_\Delta \text{ (no stall)} & \text{if } \frac{\alpha_\Delta - \alpha_0}{\alpha_V} > 1 \\ \varphi_\Delta \text{ (full stall)} & \text{if } \frac{\alpha_\Delta - \alpha_0}{\alpha_V} < -1 \\ \varphi_\Delta + 10\,k \text{ (partial stall)} & \text{elsewhere} \end{cases} \tag{D.6}$$

It is noted that there is no stall delay effect in the full stall case. Also, φ_Δ and $\varphi_{\Delta 1}$ are set equal to $\frac{\pi}{2}$ if $\varphi_{\Delta 1} > \pi - \varphi_\Delta$; in this case the stall delay time is long enough

not to initiate the stall and no stall is introduced. After substituting the deviations D.3 into the integrals D.4 and using the noted non-dimensional times φ_Δ, $\varphi_{\Delta 1}$, one obtains the first harmonics of the deviations as follows

$$
\begin{aligned}
\Delta C_{z0} &= \frac{a_{11z}}{\pi}[(\alpha_0 - \alpha_\Delta)\{\frac{\pi}{2} - \frac{1}{2}(\varphi_\Delta + \varphi_{\Delta 1})\} \\
&\quad + \frac{\alpha_V}{2}(\cos\varphi_\Delta + \cos\varphi_{\Delta 1})] \\
\Delta C_{zVs} &= -\frac{a_{11z}\alpha_V}{\pi}[\frac{1}{2}\sin\varphi_\Delta\cos\varphi_\Delta + \cos\varphi_{\Delta 1}(\sin\varphi_\Delta \\
&\quad - \frac{1}{2}\sin\varphi_{\Delta 1}) - \frac{\pi}{2} + \frac{1}{2}(\varphi_{\Delta 1} + \varphi_\Delta)] \\
\Delta C_{zVc} &= \frac{a_{11z}\alpha_V}{\pi}[\sin\varphi_\Delta(\sin\varphi_{\Delta 1} - \sin\varphi_\Delta) \\
&\quad + \frac{1}{4}(\cos 2\varphi_{\Delta 1} - \cos 2\varphi_\Delta)]
\end{aligned} \tag{D.7}
$$

To further account for negative stall, a symmetric aerodynamic force curve can be employed by including a second stall angle at $-\alpha_\Delta$. The resultant formula is not shown here.

For the drag stall part, the Fourier integral expressions 5.6 of the drag deviation D.2 reduce, to

$$
\begin{aligned}
\Delta C_{D0} &= \frac{2}{\pi}[-a_{D1}(-\alpha_0\varphi_1 + \alpha_V\cos\varphi_1) - \frac{\pi}{2}a_{D2} \\
&\quad (\alpha_0^2 + \frac{1}{2}\alpha_V^2) - a_{D3}\{-\alpha_0^3\varphi_1 + 3\alpha_0^2\alpha_V\cos\varphi_1 \\
&\quad + \frac{3}{2}\alpha_0\alpha_V^2(-\varphi_1 + \sin\varphi_1\cos\varphi_1) \\
&\quad + \frac{\alpha_V^3}{3}\cos\varphi_1(\sin^2\varphi_1 + 2)\}] \\
\Delta C_{DVs} &= \frac{4}{\pi}[-a_{D1}\{\alpha_0\cos\varphi_1 + \frac{\alpha_V}{2}(-\varphi_1 + \sin\varphi_1\cos\varphi_1)\} \\
&\quad - \frac{\pi}{2}a_{D2}\alpha_0\alpha_V - a_{D3}\{\alpha_0^2\cos\varphi_1 + \frac{3}{2}\alpha_0^2\alpha_V \\
&\quad (-\varphi_1 + \sin\varphi_1\cos\varphi_1) + \alpha_0\alpha_V^2\cos\varphi_1(\sin^2\varphi_1 + 2) \\
&\quad + \alpha_V^3(-\frac{3}{8}\varphi_1 + \frac{1}{2}\sin\varphi_1\cos\varphi_1 - \frac{1}{8}\sin\varphi_1\cos\varphi_1 \\
&\quad \cos 2\varphi_1)\}] \\
\Delta C_{DVc} &= 0
\end{aligned} \tag{D.8}
$$

These expressions are valid both for positive and negative angle of attack provided that a proper definition of φ_1 is used.

For positive α:

$$\varphi_1 = \begin{cases} -\frac{\pi}{2} & \text{if } \alpha_V < |\alpha_0| \\ -\sin^{-1}(\frac{\alpha_0}{\alpha_V}) & \text{if } \alpha_V > |\alpha_0| \end{cases}$$

For negative α:

$$\varphi_1 = \begin{cases} \frac{\pi}{2} & \text{if } \alpha_V < |\alpha_0| \\ -\sin^{-1}(\frac{\alpha_0}{\alpha_V}) & \text{if } \alpha_V > |\alpha_0| \end{cases}$$

Appendix E

Definitions of Aerodynamic Coefficients

Definitions of various coefficients in section 5.2 are given.

$$
\begin{aligned}
F_z(k) &= \frac{\lambda_z^2 + \gamma_z k^2}{\lambda_z^2 + k^2} \\
G_z(k) &= -\frac{\lambda_z k (1 - \gamma_z)}{\lambda_z^2 + k^2}
\end{aligned}
\tag{E.1}
$$

$$
\begin{aligned}
L_{zs}(k) &= a_{z0} V_{3s} + \sigma_z b \dot{\epsilon}_s \\
L_{zc}(k) &= a_{z0} V_{3c} + \sigma_z b \dot{\epsilon}_c
\end{aligned}
\tag{E.2}
$$

$$
\begin{aligned}
k_{z1} &= 1 + d^2 - \frac{k^2}{w^2} \\
k_{z2} &= 2 d \frac{k}{w} \\
k_{z3} &= -(1 + d^2)(\Delta\Gamma_{zs} - e_z k \Delta\Gamma_{zc}) \\
k_{z4} &= -(1 + d^2)(\Delta\Gamma_{zc} + e_z k \Delta\Gamma_{zs})
\end{aligned}
\tag{E.3}
$$

$$
\begin{aligned}
m_1 &= r_D - k^2 \\
m_2 &= a_D k \\
m_3 &= -r_D \Delta\Gamma_{Ds} + k e_D V_{3c} \\
m_4 &= -r_D \Delta\Gamma_{Dc} - k e_D V_{3s}
\end{aligned}
\tag{E.4}
$$

where

$$
\begin{aligned}
d &= \frac{a_L}{\sqrt{4r_L - a_L^2}} \\
w &= \frac{a_L}{2d}
\end{aligned}
\tag{E.5}
$$

$$
\begin{aligned}
\Delta\Gamma_{z0} &= V_0\,\Delta C_{z0} + \frac{1}{2}(V_s\,\Delta C_{zs} + V_c\,\Delta C_{zc}) \\
\Delta\Gamma_{zs} &= V_0\,\Delta C_{zs} + V_s\,\Delta C_{z0} \\
\Delta\Gamma_{zc} &= V_0\,\Delta C_{zc} + V_c\,\Delta C_{z0} \\
\Delta\Gamma_{D0} &= V_0\,\Delta C_{D0} + \frac{1}{2}(V_s\,\Delta C_{Ds} + V_c\,\Delta C_{Dc}) \\
\Delta\Gamma_{Ds} &= V_0\,\Delta C_{Ds} + V_s\,\Delta C_{D0} \\
\Delta\Gamma_{Dc} &= V_0\,\Delta C_{Dc} + V_c\,\Delta C_{D0}
\end{aligned}
\tag{E.6}
$$

and after converting back to the real time domain

$$
\begin{aligned}
\Delta C_{zs} &= \Delta C_{zVs}\cos\xi - \Delta C_{zVc}\sin\xi \\
\Delta C_{zc} &= \Delta C_{zVs}\sin\xi + \Delta C_{zVc}\cos\xi \\
\Delta C_{Ds} &= \Delta C_{DVs}\cos\xi - \Delta C_{DVc}\sin\xi \\
\Delta C_{Dc} &= \Delta C_{DVs}\sin\xi + \Delta C_{DVc}\cos\xi
\end{aligned}
\tag{E.7}
$$

where ξ has been defined in equation 5.4.